

On the Theory of Surface Diffusion in InAs/GaAs(001) Heteroepitaxy

vorgelegt von
Diplom-Physiker
Evgeni Stefanov Penev

von der Fakultät II – Mathematik und Naturwissenschaften
der Technischen Universität Berlin
zur Erlangung des akademischen Grades

Doktor der Naturwissenschaften
– Doctor rerum naturalium –


genehmigte Dissertation

Promotionsausschuß:

Vorsitzender: Prof. Dr. Wolfgang Richter
Berichter: Prof. Dr. Eckehard Schöll
Berichter: Prof. Dr. Matthias Scheffler

Tag der wissenschaftliche Aussprache: 18. Januar 2002

Berlin 2002
D 83

This thesis is typeset on a  **SuSE** Linux PC and an AIX IBM workstation at the Fritz-Haber-Institut der Max-Planck-Gesellschaft in Berlin using $\text{\LaTeX}2_{\epsilon}$.

On the theory of surface diffusion in InAs/GaAs(001) heteroepitaxy

Evgeni S. Penev

February 1, 2002

*На Вера, семейството ми и моя учител Тодор Мишов
с искрена признателност за тяхното търпение и подкрепа.*

Preface

Looking at the human history, one may realize that our progress ever was determined by success and failures in finding solutions to all those riddles put by the nature, and sometimes emerging as a result of the social evolution.

In the cradle of the civilization along the banks of the Nile River, about 3 000 years BC, our predecessors buried the pharaohs in monumental tombs having the shape of one of the simplest polyhedrons—the pyramid, Figure 1 (a). Intriguingly, there is a question still not answered satisfactory about who and how built the giant pyramids, the largest one among them—the Great (or Khufu’s) Pyramid—being originally 147 m high with a base covering area of 53 000 m²!

Nowadays, fifty centuries since those times, man has reached unfathomable perfection in exploring the secrets of matter. Yet, about only a decade ago, one of the branches of the physical science, the so-called *mesoscopics*, offered a puzzle, perhaps as astonishing as the secrets of the Egyptian pyramids—a puzzle which, however, emerged from a world where the characteristic length scale is just as tiny as the white bar in Figure 1 (b): 10^{-6} – 10^{-9} m, *i.e.* 1 μ m–1 nm.

In the pursuit of further miniaturization of the fundamental semiconductor devices [1], such as transistors or diodes, the nanometer technology made it possible that the spatial motion of the quantum objects, like the electrons in crystals, was confined to lower dimensions. Thus, terms as *two-dimensional electron gas* (2DEG) or *one-dimensional* (1D) *quantum wires* were brought to live in materials science, device and fundamental physics. We can even count electrons, letting them through the so called *quantum point contacts* (QPCs), and use them to control single-electron devices.

A new epoch in this ongoing miniaturization appeared, however, when the charge carriers were confined to zero-dimensions (0D), *i.e.* in quantum “boxes”. Of course, the characteristic

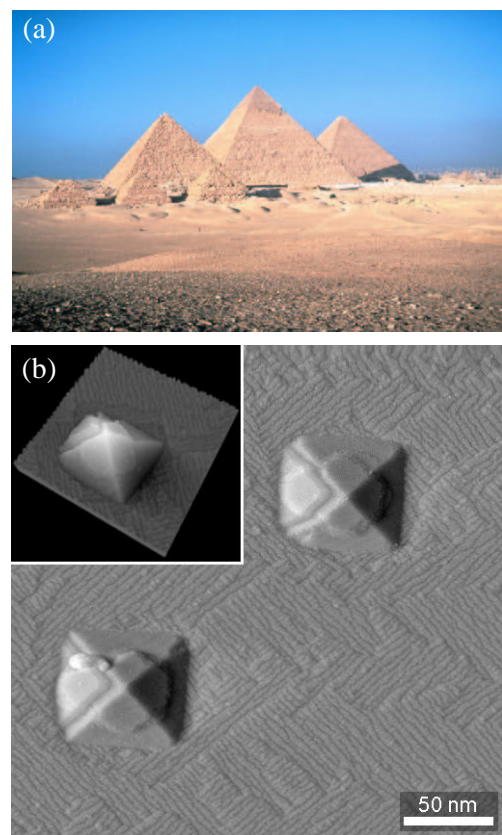


Figure 1: Pyramids, big ones and little ones: (a) (color) Pyramids of al-Jizah (Giza), Egypt, built during the 4th dynasty (*c.* 2575–*c.* 2465 BC); (b) STM image of Ge pyramidal islands, grown on the Si(001) surface—an experiment carried out on the brink of the new millennium (image courtesy of Dr. O. Leifeld, Paul-Scherrer-Institute, Villigen, Switzerland).

size l of the latter in the three spatial dimensions needs to be of the order of the de Broglie's wavelength of the particle(s) confined, $l \sim \lambda = 2\pi\hbar/p$, where p is the particle quasi-momentum, \hbar being the Planck's constant. Such "boxes" are so small, that another term has been widely adopted as well: *quantum dots*, or briefly QDs. One of the technological tools which allowed this stupendous trick is known as molecular beam epitaxy¹ (MBE). Now, the striking fact we are about to discuss hereafter, was that in the heteroepitaxial growth of the so-called lattice-mismatched semiconductor systems upon certain conditions such QDs can self-organize in regular arrays on the substrate surface. In fact, these tiny objects are three-dimensional (3D) and can have different shapes: pyramids, "hut" clusters, dome clusters etc. A sample image of Ge little pyramids, acquired by means of *in situ* scanning tunneling microscopy (STM) [2, 3], is shown in Figure 1 (b).

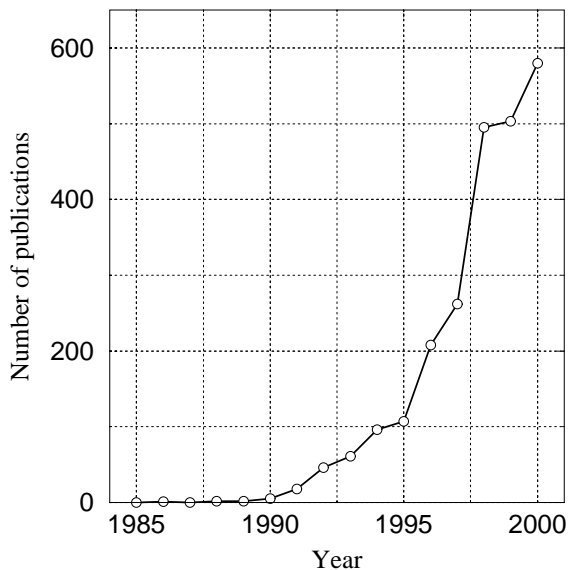


Figure 2: Number of articles published in the period 1985–2000, containing the terms 'quantum dot(s)' & 'InAs' or 'GaAs' in the title, abstract or the list of key words according to the Science Citation Index Expanded database (wos.isiglobalnet.com).

Thus, on the brink of the new millennium, another kind of pyramids is provoking our knowledge. How these pyramidal islands arrange in regular arrays? Why do they have very similar size and shape within a given array...? The answer to these and other related questions would decide to the utmost our success in developing the new generation semiconductor device technologies. Being of exclusive importance, this topic has triggered an immense experimental effort, motivating in parallel numerous theoretical studies. As a result, an avalanche of publications have appeared over the past years. One can get some insight into the time evolution of the scientific activity in this field just by browsing any of the related citation databases available on Internet. It would be perhaps fair to say that the trend observed in Figure 2 bares the imprint of a "scientific rush". Many research groups around the world have contributed to this process, advancing substantially our understanding of the basic physical phenomena in the QDs self-organization. It is therefore

necessary for us to precise, even on a mundane level, the place of the present work in this enormous scientific production.

This thesis gives an account of the recent progress made at the Theory Department of the Fritz-Haber-Institut der Max-Planck-Gesellschaft (Berlin, Germany) towards understanding on the atomic level one of the fundamental processes in QDs formation and crystal growth in general termed *surface diffusion*.

From theoretical point of view the diffusion problem has been extensively studied in virtually every field of the physical science, from colloid physics to stellar dynamics [4]. In the context of heteroepitaxial growth of semiconductor compounds, whose bulk lattice parameters substantially differ, a new physical situation emerges, which could be briefly phrased as 'diffusion on strained semiconductor surfaces'. Then the question naturally poses itself as to how the new physical conditions affect the adatom migration on such surfaces? In the following we shall further precise this question and will attempt to give an answer as complete as possible.

¹Literally translated: "ordered on" (from the Greek words $\varepsilon\pi\iota$ - "on", and $\tau\alpha\acute{\xi}\iota\varsigma$ - "order").

Offering an essentially theoretical work, the reader will find certainly those standard chapters where the basic method used is briefly described. We feel it appealing, however, a few words about the latter to be said in the preface. In this thesis the diffusion problem is addressed within a parameter-free approach based upon the Density-Functional Theory (DFT). In this respect we have greatly benefited from the tradition established at the Theory Department of the Fritz-Haber-Institute in exploiting DFT in surface science.

DFT and based on it computational methods² have become an indispensable tool in the theoretical treatment of crystal growth. Its ability to provide hints to the experimentalists turns out to be of extreme importance. As an excellent example we would mention the collaboration between the Theory Department of the Fritz-Haber-Institute and both experimental and theoretical groups in the field of semiconductor science and technology which led to resolving the atomic structure of the technologically important GaAs(001)-(2 × 4) surface, Figure 3.

This thesis appears after two excellent theses dedicated to diffusion on GaAs surfaces and the shape and stability of QDs, respectively: A. Kley’s “*Theoretische Untersuchungen zur Adatomdiffusion auf niederindizierten Oberflächen von GaAs*” [5] and N. Moll’s “*Theorie der Form und Stabilität von Quantenpunkten auf III-V-Halbleitern*” [6]. It is the author’s hope that the present study will not be an exception to the tradition and would be just as informative to the people working in this field. Yet, only the reader decides. . .



Figure 3: Typical title on the Science Daily Web page reflecting the joint effort between experimental and theoretical groups.

Berlin, December 1999–September 2001

²The foundations of the density-functional theory and the computational methods in quantum chemistry were put forward in the pioneering works of Walter Kohn and John Pople, respectively, for which they were awarded with the 1998 Nobel Prize in chemistry (<http://www.nobel.se/chemistry/laureates/1998/index.html>).

Acknowledgments

The writing of this thesis, as often happens in the physics community, is a typical example of a “collective phenomenon” ;-), and considerable number of people have contributed to this years-long process. Thus, I feel obliged to express my gratitude to them in the very beginning.

First of all I am much indebted to Prof. Dr. Matthias Scheffler who offered me an excellent opportunity to work at the Fritz-Haber-Institute and for his continuous support.

I would like also to acknowledge the indispensable help of my supervisor Dr. Peter Kratzer who in fact made the completion of this thesis possible. It was Peter’s suggestion that I consider the effect of strain on adatom diffusion. He introduced me to the minute details in the physics of self-organized nanostructures on semiconductor surfaces and with the time I somehow managed to extend his original idea to the present form.

This, on the other hand, would not be possible without the training in theoretical physics I had due to my teacher at the Sofia University St. Kliment Ohridski (Sofia, Bulgaria) Prof. Dr. Todor Mishonov. The lengthy discussions I had with him over the past three years turned out to be crucial for the final stages of my PhD study.

In the everyday work at the Fritz-Haber-Institute however I benefited enormously from the discussions with two of my former colleagues—Ari Seitsonen and Martin Fuchs. Ari practically introduced me to the world of UNIX, and Martin did his best to make the pseudopotential concept much clearer to me. It was a real luck that I had the chance to consult with them. Martin also proofread the final draft of the thesis and made a great deal of valuable suggestions.

I also express my gratitude to my ‘Betreuer’ from Technical University Berlin, Prof. Dr. Eckehard Schöll, as well as to Dr. Sumit Bose and Dr. Matthias Meixner for the numerous discussions we had in the course of our collaborative research within the framework of Sonderforschungsbereich 296 of Deutsche Forschungsgemeinschaft (DFG) concerning the physics of self-organized nanostructures.

It is a pleasure to acknowledge also the help of my friends Dr. Nevena Arsenova, Dr. Rossitza Pentcheva, and Mira Todorova. Given my German language skills they were patient enough so as to provide the vital “language support” which I sometimes desperately needed.

I am much indebted to Prof. Dr. Caroline Morgan from Wayne State University (Detroit, USA) who did the final fine-tuning of my “brilliant” written English.

Last but not least, I need to mention all my colleagues at the Theory Department of the Fritz-Haber-Institute, who really made me enjoy my stay there.

Contents

1	Introduction	1
1.1	The challenge of “self-fabrication”	1
1.2	Lattice-mismatched heteroepitaxy and the role of surface diffusion	2
1.3	Overview	4
2	Elements of computational materials science	5
2.1	Hierarchy of approximations	5
2.2	Density-Functional Theory (DFT) in a nutshell	8
2.2.1	Basic formalism	8
2.2.2	Approximations to $E_{\text{XC}}[n]$: LDA, GGA	9
2.3	Practical aspects of DFT implementation schemes	12
2.3.1	Supercell approximation & plane-wave basis set	12
2.3.2	<i>Ab initio</i> pseudopotentials, the fhi98PP package	14
2.3.3	Brillouin zone sampling	16
2.3.4	Assembling all together: the fhi98md program	17
3	Continuum elasticity theory	19
3.1	Basic concepts	19
3.2	Elastic properties of bulk III-V semiconductors: GaAs, InAs	22
3.3	Surface elasticity: thermodynamic aspects	24
3.3.1	Surface energy and surface stress	24
3.3.2	Strain distribution and shape of InAs QDs	27
3.4	The “flat island” approximation	28
4	Surface diffusion	31
4.1	General background	31
4.1.1	Diffusion PES	31
4.1.2	Surface diffusion tensors	32
4.2	Random walk formalism for the tracer diffusion tensor	34
4.2.1	Master equation of a 2D random walk	34
4.2.2	The hydrodynamic limit	36
4.3	Transition-State Theory	38
5	Early stages of InAs/GaAs(001) heteroepitaxy	43
5.1	Introduction	43
5.2	The clean (001) surfaces of GaAs and InAs	45
5.2.1	Surface reconstruction and relaxation: basic principles	45
5.2.2	Atomic structure	46
5.2.3	Surface stability	49

5.3	Structure and energetics of InGaAs alloy wetting layer	55
5.3.1	Structural models	55
5.3.2	Energetics	56
5.4	Indium diffusion on InGaAs(001)-(2 × 3) wetting layer	61
5.4.1	PES	61
5.4.2	Diffusion coefficients	63
6	Indium diffusion on the bare GaAs(001)-c(4 × 4) substrate	67
6.1	Introduction	67
6.2	Diffusion on the unstrained substrate	69
6.2.1	PES	69
6.2.2	Diffusion coefficients	70
6.2.3	Comparison with Ga diffusion on GaAs(001)-c(4 × 4)	71
6.3	Interaction of indium with As-As bonds	73
6.4	Effect of strain	76
7	Consequences for growth	81
7.1	Introduction	81
7.2	Growth on a capping layer with buried islands	82
7.3	Diffusion limitations in island growth kinetics	82
	Summary	89
	Kurzfassung	91
	Резюме	93
A	Structural and cohesive properties of Ga, In, As, GaAs and InAs	95
B	Scaling hypothesis for corrections to total energy and pressure	97
C	Calculation of elastic moduli	99
D	Geometry of the In_{2/3}Ga_{1/3}As(001)-(2 × 3) surface	105
	References	107
	Index	119

Chapter 1

Introduction

1.1 The challenge of “self-fabrication”

Undoubtedly, semiconductor optoelectronic devices and the technological tools for their fabrication form the tandem that is the heart of today’s communications industry [7]. A classic example are the omnipresent quantum-well laser diodes. The appearance of these devices marked a new stage in energy-level engineering and has reflected the new optical properties pertinent to a two-dimensional (2D) system, having a step-like density of states (DOS). It was realized, however, that two-dimensionality, being initially an advantage, poses natural restrictions towards improvement of quantum-well lasers. As a result, nanostructures of lower dimensionality, *i.e.* 0D quantum dots (QDs) and 1D quantum wires, which may serve as an active region (layer) in semiconductor lasers, have recently been attracting unprecedented interest. It is theoretically predicted [8] that the dramatic change of DOS in these systems compared to a bulk 3D material¹ will drastically improve the basic device characteristics, leading to much larger optical gain, differential gain and narrower gain bandwidth. These would thus result in a highly desired low operation threshold current at room temperature.

It turned out, however, that the standard patterning techniques such as optical lithography or etching used so far to fabricate QDs and quantum wires did not provide the needed, especially lateral, confinement of the charge carriers at room temperature. Some of the methods also introduce various imperfections which may act as nonradiative recombination centers, thus limiting device performance.

The breakthrough came first with the observation that in the heteroepitaxial growth of lattice-mismatched semiconductors under certain growth conditions defect-free, or *coherent*, islands may spontaneously form on the substrate surface. It seems that the first report of this phenomenon appeared as early as in 1985 [9]. Goldstein *et al.* observed “...In-rich clusters, whose sizes are less than 100 Å” during molecular-beam epitaxial growth of InAs/GaAs strained-layer superlattices. Shortly after, Eaglesham and Cerullo [10] and Mo *et al.* [11] observed self-assembled coherent islands in the Ge/Si(100) system; Guha *et al.* [12] achieved coherent islands in the $\text{In}_x\text{Ga}_{1-x}\text{As}/\text{GaAs}(001)$ system. The remarkable feature which put these novel structures in the limelight of materials science was, however, revealed in the analysis of the statistics on the sizes and arrangement of the islands. By Atomic Force Microscopy (AFM) measurements, Moison *et al.* [13] showed for InAs QDs on GaAs that their distribution in sizes displays remarkably low dispersion, $\pm 10\%$, and that their arrangement is rather regular. Similar results were reported also by Leonard *et al.* [14].

¹For a bulk material the DOS per unit volume $D(E) \sim \sqrt{E}$, while the corresponding for a quantum wire $D(E) \sim 1/\sqrt{E}$. The structure of the energy spectrum of a quantum dot is completely atom-like with $D(E) \sim \delta(E)$.

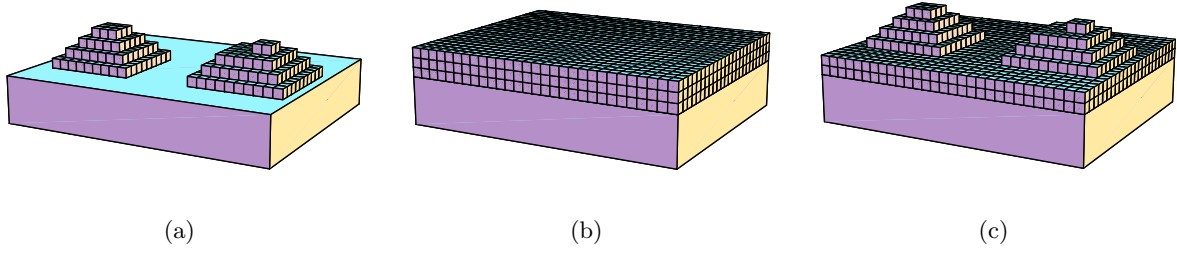


Figure 1.1: Crystal growth modes (schematic) according to the classification given by Bauer [22]: (a) Volmer-Weber mode, or island growth; (b) Frank-van der Merwe mode, or layer-by-layer growth; (c) Stranski-Krastanov mode, or layer-then-island growth.

Thus the early 1990s brought into focus a novel class of nanostructures, “that could, in effect, fabricate themselves” [15], with properties making them ideal candidates for applications in optoelectronic devices. The proof of lasing from III-V QDs [16, 17] only quickened to the utmost the interest, and now the first self-assembled InGaAs/GaAs QD lasers are a reality. It was clear, however, that as a prerequisite for achieving the theoretical predictions for the device performance [8], a thorough understanding of the mechanism(s) of self-organization is required. This motivated enormous experimental and theoretical activity towards understanding the basic processes in the heteroepitaxial growth of lattice-mismatched semiconductors with particular emphasis on direct-gap systems, a typical example being In(Ga)As/GaAs.

For an excellent introduction to the field the reader is further referred to the recent comprehensive reviews and monographs [18–20].

1.2 Lattice-mismatched heteroepitaxy and the role of surface diffusion

Generally in heteroepitaxial growth of thin films, the cohesive/adhesive properties of the deposit differ from that of the substrate [21]. The lattice constant of the bulk phase of the deposited material a_f may also be different from that of the substrate a_s , thus defining the relative lattice mismatch of the heteroepitaxial system

$$\varepsilon_0 = 1 - \frac{a_f}{a_s}. \quad (1.1)$$

These factors, in turn, determine the functional dependence of the chemical potential of the film $\mu_f(\theta)$ on its thickness θ , which hereafter is assumed to be measured in monolayers (ML). It is the μ - θ dependence that determines the three types of temporal evolution of the film morphology, *i.e.* the growth modes, schematically presented in Figure 1.1.

The thermodynamic criterion that allows one to determine which mode would be adopted was given by Bauer in 1958 [22] on the basis of considerations of the relation between the surface energies of the substrate γ_s , of the epilayer γ_f , and that of the interface between them γ_i :

- ✧ Volmer-Weber (VW) mode [23], if $\gamma_f + \gamma_i > \gamma_s$;
- ✧ Frank-van der Merwe (FvdM) mode [24], if $\gamma_f + \gamma_i < \gamma_s$, $\forall \theta$;
- ✧ Stranski-Krastanov (SK) mode [25], $\gamma_f + \gamma_i \leq \gamma_s$.

An equivalent thermodynamic criterion can be formulated [21] in terms of $\mu_f(\theta)$, respectively: $d\mu_f/d\theta < 0$, $d\mu_f/d\theta > 0$, and $d\mu_f/d\theta \leq 0$. It should be also noted that Bauer's classification refers to the thermodynamic equilibrium situation. However, in experimental work the terms VW, FvdM, and SK are often used in a purely phenomenological sense.

It has been established that the formation of strained coherent islands occurs in SK growth of semiconductor systems with large lattice mismatch, $|\varepsilon_0| \gtrsim 2\%$. Up to now self-assembled QDs have been achieved in this growth regime for a variety of systems based on III-V compound semiconductors, such as InAs/GaAs(001), InGaAs/GaAs(001), InAs/InP(001) to name a few, for $\text{Si}_x\text{Ge}_{1-x}/\text{Si}(001)$, and even for "exotic" materials like PbSe/Pb_{1-x}Eu_xTe [26].

In the following, we shall be particularly concerned with the InAs/GaAs(001) material system for which $\varepsilon_0 \simeq -7\%$. As mentioned already, its electronic structure and transport properties has made it of primary technological importance. InAs QDs are typically fabricated by both conventional MBE and Metal-Organic Chemical Vapor Deposition (MOCVD). The initial "delivery" of InAs to the GaAs(001) surface leads to formation of a 2D film usually referred to as a wetting layer (WL). Because of the large lattice misfit the WL is metastable, and above a critical coverage of $\theta_c = 1.5\text{--}1.8$ ML 3D coherent islands form, as they provide an efficient way to relieve the strain-induced elastic energy. However, still there is no consensus about the mechanism underlying this 2D \rightarrow 3D transition and the island ordering in sizes, and a number of both thermodynamic and kinetic models have been proposed so far in the literature.

Detailed measurements of mass transfer in the SK growth of InAs on GaAs however strongly indicated that "strain-dependent kinetics must be a key ingredient of an appropriate theoretical framework describing the QD formation", cf. Ref. [28]. On the other hand, in the MBE growth of arsenide compound semiconductors it is the *surface diffusion*² that mainly governs the incorporation of the cation species, *e.g.*, Ga, In, Al, whereas the kinetics of arsenic incorporation is dominated by adsorption/desorption of As₂ or As₄ molecules at surface sites with enhanced local population of cations [30]. The latter realization dates back to the dawn of MBE experiments and has been best demonstrated in the studies of As₂-Ga interaction kinetics on GaAs(001), Figure 1.2: the sticking coefficient of As₂ approaches unity for adequate Ga population and, vice versa, is zero if no Ga atoms are present on the surface.

When put together these experimental findings constitute the essence of a problem whose theoretical treatment is the main goal of the present work: how diffusion properties of a cation change on a semiconductor surface that supports strain, and what are, eventually, the morphological consequences for the heteroepitaxial growth of self-assembled QDs? It is somewhat surprising that this question has not been given due attention so far, and the impact of strain on the surface diffusion process still remains elusive, although attempts to make its effect clearer date back to the last decade [31]. Scarce information on the influence of strain is available recently from molecular dynamics (MD) simulations based on empirical potentials [32]. Therefore

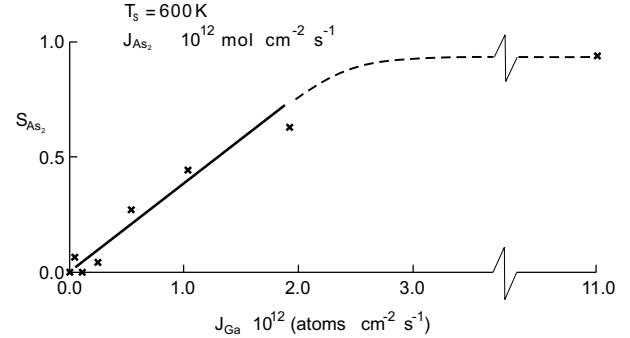


Figure 1.2: Sticking coefficient of As₂ on a GaAs(001) surface at 600 K as a function of the Ga flux after Foxon and Joyce [27] (reproduced with the kind permission of the authors, ©1977 North-Holland Publishing Company).

²The notion of *surface diffusion*, interestingly, has been deduced in the early experiments in the field of crystal growth. It seems that Volmer and Estermann were the first to invoke surface diffusion arguments to rationalize the experimentally observed growth kinetics of Hg crystals [29].

there is a clear need for rigorous analysis of the problem that, apart from qualitative trends, would be able to provide quantitative estimates for the strain renormalization of adatom diffusivity, and thus will shed light on the relevance of strain-induced limitations in growth kinetics of strained islands. The results from such an analysis would also allow for a more detailed comparison to adatom diffusivity on metal surfaces and bulk materials, where the effect of strain has already gained substantial understanding [33–37].

The problem of surface adatom diffusion in InAs/GaAs(001) heteroepitaxy turns out to be even more intricate than it appears at first sight. As we have just mentioned the growth mode classifications dating back to Bauer [22], Figure 1.1, tend to be used to indicate the type of resultant growth morphology. Thus, if one sticks to the original “taxonomy”, the SK growth of InAs on GaAs(001) should be characterized first by formation of a pure, or nearly pure InAs WL, and further nucleation and growth of islands of the same composition. However, a body of experimental evidence (we shall consider it in detail in Chapter 5) has appeared that the actual growth process deviates from the classical notion of SK growth, both in its initial and later stages. The distinguishing characteristic of this “quasi-SK” mode is the substantial InAs-GaAs alloying taking place once InAs is delivered to the GaAs substrate within the experimentally relevant temperature range and not too low deposition rate. As a result, the WL is to be more appropriately described as a *strained ternary* $\text{In}_x\text{Ga}_{1-x}\text{As}$ *alloy*. Such a realization, by itself, entails a number of questions that need be clarified by any theoretical scheme attempting a microscopic description of InAs/GaAs(001) heteroepitaxy: What is the atomic structure of the WL surface? How does the adatom migration on such a WL compare to that on the clean substrate etc...? Current specialized literature, admittedly, does not provide an unambiguous answer to these points. Thus, we find it of particular interest, but also regard it as a crucial prerequisite to cover this issue within the framework of the powerful first-principles approach mentioned in the Preface. The QD self-assembly in this heteroepitaxial system certainly contains far more rich physics, thus we have tried to put emphasis on those problems where the *ab initio* treatment is particularly valuable in providing information hardly accessible from other theoretical methods or experiment. A brief survey of the present work’s contents is given in the next section.

1.3 Overview

In what follows we have attempted a more topical structure of the thesis rather than following the actual computational steps taken during the period of completion of the study. Thus, original results may be found also in the introductory chapters.

We start first with a description of the theoretical grounds of this study: density-functional theory and the plane-wave pseudopotential method (Chapter 2), elasticity theory (Chapter 3), and the theory of diffusion on regular lattices (Chapter 4). In Chapter 5 a detailed analysis of the early stages of InAs deposition on GaAs(001) is carried out. We address the clean (001) surfaces of GaAs and InAs in Sec. 5.2 as a first step, and then the stability of the InGaAs(001) alloy wetting layer is discussed in Sec. 5.3. Indium diffusion on the (2×3) -reconstructed InGaAs(001) WL is considered in Sec. 5.4. Chapter 6 is dedicated to the microscopic analysis of In diffusivity on the bare GaAs(001) substrate. For the example of In/GaAs(001)- $c(4 \times 4)$, we calculate the microscopic characteristic of the migration potential in the conventional case of an unstrained substrate. Then we consider a situation where the latter surface is subject to isotropic strain, and the resulting renormalization of In diffusivity is discussed in detail in Sec. 6.4. The possible implications for the growth kinetics of strained islands in lattice-mismatched heteroepitaxy are discussed in Chapter 7, where we critically reexamine the microscopic results from the previous analysis. Finally, we provide a brief Summary of the results obtained in the present work.

Chapter 2

Elements of computational materials science

Modeling of complex systems and phenomena is a powerful method towards understanding, predicting, and eventually controlling different aspects of the latter. In materials science, the systems of interest typically consist of many particles (electrons, nuclei, atoms, molecules etc.), of the order of Avogadro's constant $N_A = 6.022 \times 10^{23} \text{ mol}^{-1}$.

In a pure state, the N -particle quantum-mechanical system is described by a generally complex-valued function of the particles' spatial and spin coordinates $\Psi(\xi_1, \xi_2, \dots, \xi_N)$, with $\xi_i = (\mathbf{r}_i, s_i)$ being, respectively, the position and the spin of the i th particle. Solving the Schrödinger equation for Ψ when $N \sim N_A$ is neither useful nor possible.¹ Our aim is to explore the basic processes in semiconductor heteroepitaxy. But for these we would be inevitably bound to solve a problem of a similar size. Fortunately the Lord is merciful and enabled us to develop *approximate methods* which in conjunction with today's powerful computing machinery allow the principles of quantum mechanics, which we usually call *first*, or *ab initio*, *principles*, to be applied to real poly-atomic systems [38].

2.1 Hierarchy of approximations

Consider a system consisting of N_e electrons with coordinates $\mathbf{r} \equiv \{\mathbf{r}_i\}$ and N_i ions at points $\mathbf{R} \equiv \{\mathbf{R}_I\}$, in absence of external fields. When relativistic effects are negligible, its Hamiltonian has the well-known structure

$$H = \sum_i^{N_e} \frac{\mathbf{p}_i^2}{2m} + \sum_I^{N_i} \frac{\mathbf{P}_I^2}{2M_I} + V_{ee}(\mathbf{r}) + V_{ei}(\mathbf{r}, \mathbf{R}) + V_{ii}(\mathbf{R}), \quad (2.1)$$

where the first two terms are the kinetic energies, T_e and T_i , of the electronic and ionic subsystem, respectively, and the contributions by the electron-electron, electron-ion and ion-ion Coulomb interaction are denoted V_{ee} , V_{ei} , and V_{ii} .

Early in 1927, Born and Oppenheimer already realized that the Hamiltonian of Eq. (2.1) can be treated perturbatively [39] because of the usually small T_i due to the large masses of the

¹In one of his lectures given at the Fritz-Haber-Institute, E. K. U. Gross used the following example to illustrate the typical size of the full many-particle problem. Consider the nitrogen atom having 7 electrons ($1s^2 2s^2 2p^3$) described by $7 \times 3 = 21$ spatial coordinates. Let us estimate now the size of a rough table of the corresponding wave function. Assuming only 10 entries per coordinate and 4 bytes per entry would give 4×10^{21} bytes. If we want to store such a table on compact disks (CDs), say, each of 6.5×10^8 bytes size, then we would need $\approx 6 \times 10^{12}$ CDs. Taking into account that a CD weighs about 10 g we end up with a demand of 6×10^7 tons of CDs... :-)

atomic nuclei; recall that the mass of a nucleon $\sim 10^3 \times m_{\text{electron}}$. In the spirit of perturbation theory [40], H is cast in the form

$$H \equiv \underbrace{T_e + V_{ee} + V_{ei} + V_{ii}}_{H_0} + T_i = H_0 + \lambda^4 H_1, \quad (2.2)$$

with $\lambda = (m/M_0)^{1/4}$ being the small parameter introduced by Born and Oppenheimer, where M_0 is some of the nuclear masses or their mean. Suppose that we have found the spectrum $\{U_n(\mathbf{R})\}$ and eigenstates $\{\psi_n(\mathbf{r}, \mathbf{R})\}$ of the zero-order approximation H_0 for some $\mathbf{R} = \mathbf{R}_0$, which is nothing but the Hamiltonian of the system for fixed nuclei. The complete neglect of the T_i term, *i.e.* setting $\lambda \equiv 0$ in (2.2), yields the *Born-Oppenheimer* (BO) *approximation*. The total energy of the many-particle system in this case is simply $U_n(\mathbf{R}_0) = E_n(\mathbf{R}_0) + V_{ii}(\mathbf{R}_0)$, where $E_n(\mathbf{R}_0)$ is the spectrum of the *many-electron* Hamiltonian $H_e = T_e + V_{ee} + V_{ei}$, depending parametrically on the nuclear coordinates. However, in the BO approximation the assumption is usually made that the electronic component stays in its ground state, $n = 0$, thus in the following the term (ground-state) *total energy* for a particular configuration \mathbf{R} of the nuclei will refer to the quantity

$$E(\mathbf{R}) \equiv U_0(\mathbf{R}) = E_0(\mathbf{R}) + V_{ii}(\mathbf{R}). \quad (2.3)$$

In fact $E(\mathbf{R})$ is a hypersurface in the configurational space spanned over the $3N_i$ nuclear degrees of freedom and is usually termed the *potential energy surface* (PES).

Beyond the zero-order approximation solution to the exact Hamiltonian (2.1), for some \mathbf{R} close to \mathbf{R}_0 , $\mathbf{R} - \mathbf{R}_0 = \lambda \mathbf{u}$, is sought in the form

$$\mathcal{E} = U_n^{(0)} + \lambda \mathcal{E}_n^{(1)} + \lambda^2 \mathcal{E}_n^{(2)} + \dots, \quad \Psi(\mathbf{r}, \mathbf{u}) = \Psi_n^{(0)} + \lambda \Psi_n^{(1)} + \lambda^2 \Psi_n^{(2)} + \dots. \quad (2.4)$$

Born and Oppenheimer have shown [39, 41] that the zero-order approximation to the wave function simply factors into a product of the zero-order electronic $\psi_n^{(0)}(\mathbf{r})$ and nuclear wave functions $\Phi^{(0)}(\mathbf{u})$, *i.e.* $\Psi_n^{(0)}(\mathbf{r}, \mathbf{u}) = \Phi^{(0)}(\mathbf{u})\psi_n^{(0)}(\mathbf{r})$, and the nuclear wave function satisfies the Schrödinger equation,

$$\lambda^2 \left[- \sum_I^{N_i} \left(\frac{M_0}{M_I} \right) \frac{\hbar^2}{2m} \nabla_{\mathbf{u}_I}^2 + U_n^{(2)} + \mathcal{E}_n^{(2)} \right] \Phi^{(0)}(\mathbf{u}) = 0, \quad (2.5)$$

where the second-order term $\lambda^2 U_n^{(2)} \sim \lambda^2 \mathbf{u}^2$ in the expansion of $U_n(\mathbf{R}_0 + \lambda \mathbf{u})$ plays the role of an effective potential for the nuclear motion. It is immediately apparent that Eq. (2.5) describes harmonic nuclear oscillations around \mathbf{R}_0 , and the electrons move as if the nuclei are fixed at \mathbf{R}_0 . Thus, if the wave function in Eq. (2.4) is truncated up to the first order one obtains the *harmonic approximation*. For the understanding of many features of condensed systems one needs to go to higher approximations, but it turns out that no more than a step can be made further that still preserves the simplicity of the harmonic approximation and yet is an improvement over the latter. Indeed, if the perturbative expansion is only made up to terms $O(\lambda^2)$, the wave function can be written as

$$\Psi_n(\mathbf{r}, \mathbf{u}) = [\Phi^{(0)}(\mathbf{u}) + \lambda \Phi^{(1)}(\mathbf{u}) + \lambda^2 \Phi^{(2)}(\mathbf{u})] \psi_n(\mathbf{r}, \mathbf{R}). \quad (2.6)$$

The physical picture that emerges in the interpretation of (2.6) is the *adiabatic approximation*: the motion of the nuclei is described by the first factor and the electronic component *adiabatically* follows the nuclear motion by adapting to the instantaneous nuclear configuration, as it follows from the presence of \mathbf{R} in the argument of the electronic wave function ψ_n . The PES

determined within the adiabatic approximation, *i.e.* $E(\mathbf{R})$ for all possible \mathbf{R} , is the commonly termed adiabatic PES. It is the PES that contains all the important information for the diffusion process of adatoms on surfaces (Sec. 5.4, Sec. 6.2, and Sec. 6.3 present particular examples of PES “mapping”).

The adiabatic picture is no longer applicable once we take into account terms $O(\lambda^3)$ or higher orders. On the other hand, the BO approximation itself is inapplicable when T_1 is not negligible as in high-energy atom-surface collisions, or when electron-phonon coupling and electronic transitions to excited states are important. The properties of the systems and phenomena discussed here can be, however, understood on the basis of the BO and the adiabatic approximation. Furthermore the latter provide quite simple concept towards *ab initio* molecular dynamics (MD), especially if the nuclei can be treated as classical charged particles:²

- ✧ For a particular fixed configuration \mathbf{R} one solves the Schrödinger equation for the electronic ground state, $H_e\psi_0(\mathbf{r}, \mathbf{R}) = E_0(\mathbf{R})\psi_0(\mathbf{r}, \mathbf{R})$, or

$$\left[-\sum_i^{N_e} \frac{\hbar^2}{2m} \nabla_{\mathbf{r}_i}^2 + \frac{1}{2} \frac{1}{4\pi\epsilon_0} \sum_{i,k}' \frac{e^2}{|\mathbf{r}_i - \mathbf{r}_k|} - \frac{1}{4\pi\epsilon_0} \sum_i^{N_e} \sum_I^{N_i} \frac{(Z_I e)e}{|\mathbf{r}_i - \mathbf{R}_I|} \right] \psi_0(\mathbf{r}, \mathbf{R}) = E_0(\mathbf{R})\psi_0(\mathbf{r}, \mathbf{R}), \quad (2.7)$$

where \sum' indicates that the double summation includes only terms with $i \neq k$, ϵ_0 is the dielectric permeability of vacuum, and $Z_I e$ is the charge of the I th nucleus;

- ✧ The ions are then moved classically according to the forces \mathbf{F} calculated from $E_0(\mathbf{R})$,

$$M_I \ddot{\mathbf{R}}_I = -\nabla_{\mathbf{R}_I} U_0(\mathbf{R}) = -\nabla_{\mathbf{R}_I} [E_0(\mathbf{R}) + V_{ii}(\mathbf{R})] \equiv \mathbf{F}_I. \quad (2.8)$$

The next level in the hierarchy of approximations appears when treating the many-electron problem, Eq. (2.7). The latter by itself is of the same order as the one for the total Hamiltonian H and is practically intractable for the systems under consideration. Dramatic reduction of the degrees of freedom thus can be achieved if the many-electron problem is reformulated in terms of an effective one-electron picture. The classic example described in all textbooks on quantum mechanics is the *Hartree-Fock* (HF) approximation, where one employs a Slater determinant of one-electron orbitals $\varphi_i(\xi_i)$, $\psi(\xi) = (1/\sqrt{N_e!}) \sum_{P\{p_1, p_2, \dots\}} (-1)^P \varphi_{p_1}(\xi_1) \varphi_{p_2}(\xi_2) \dots \varphi_{p_{N_e}}(\xi_{N_e})$ (P being the parity of the permutation of state indices $\{p_1, p_2, \dots\}$, and the sum is over all permutations) as a trial wave function, and the ground state of H_e is determined from a variational principle. The HF approximation and its extensions have served as the ground for the majority of the state-of-the-art computational methods in quantum chemistry, but when applied to extended systems, such as crystals, one encounters principle problems. Suffice it to say that it does not describe the electronic screening properly [38], which is a fundamental property of the interacting electron systems.

Another “approach to the quantum many-body problem”, however, substantially increased the scope of system sizes and phenomena complexity that can be treated from first principles. It is the *Density-Functional Theory* (DFT) that allows for a maximum reduction in the degrees of freedom by reformulating the many-body problem in terms of the single particle density [43, 44].

DFT-based calculations have proven to be an efficient tool to explore the elementary processes of crystal growth. Recent reviews provide quite a comprehensive account of the progress in this field: please see, for example, the works by Ruggerone *et al.* [45], Ratsch *et al.* [46], Kratzer *et al.* [30]. In the rest of this chapter, we briefly outline the main framework of the DFT formalism and discuss features of the particular implementation used in the present work.

²See, for example, Sec. 3 in Ref. [42] for more detailed discussion on the applicability of classical and quantum description.

2.2 Density-Functional Theory (DFT) in a nutshell

2.2.1 Basic formalism

The origins of the density-functional formalism can be traced back to the Thomas-Fermi model and its extensions. The “basic variable” in such an approach is the electron density $n(\mathbf{r})$.³ The rigorous foundations of DFT were put forward in the pioneering work by P. Hohenberg and W. Kohn [47] that appeared in 1964. They have originally established the following theorem [43, 47].

THEOREM 1 (HOHENBERG-KOHN) *Given an arbitrary number of electrons N_e moving under the influence of static, local, and spin-independent external potential $v(\mathbf{r})$, leading to the Hamiltonian*

$$H_e = T_e + V_{ee} + v, \quad (2.9)$$

with non-degenerate ground state ψ_0 , and corresponding ground-state density $n_0(\mathbf{r})$, being a functional of $v(\mathbf{r})$,

$$n_0(\mathbf{r}) \equiv \left\langle \psi_0 \left| \sum_i^{N_e} \delta(\mathbf{r} - \mathbf{r}_i) \right| \psi_0 \right\rangle, \quad (2.10)$$

it follows then that

- ① *[invertability] $v(\mathbf{r})$, and therefore ψ_0 are (to within a constant) unique functionals of $n_0(\mathbf{r})$;*
- ② *[variational access & universality] The energy functional*

$$E_v[n] \equiv \int v(\mathbf{r})n(\mathbf{r})d\mathbf{r} + \mathcal{F}[n], \quad (2.11)$$

where $\mathcal{F}[n] \equiv \langle \psi_0 | T_e + V_{ee} | \psi_0 \rangle$ is a universal functional, assumes its minimum value for the correct $n(\mathbf{r})$,

$$E_0 = \min_n E_v[n], \quad (2.12)$$

if the admissible functions are restricted by the condition

$$N[n] \equiv \int n(\mathbf{r})d\mathbf{r} = N_e, \quad n(\mathbf{r}) \geq 0. \quad (2.13)$$

The Hohenberg-Kohn theorem asserts the existence of the universal functional $\mathcal{F}[n]$, but “it does not tell us how to construct” it formally [43]. Shortly after, in 1965, Kohn and Sham [48] proposed an equivalent orbital scheme to treat the variational problem (2.12)–(2.13) that has turned out to be the crucial step towards applications of the DFT.

The gist of their scheme is the existence of an auxiliary problem for *non-interacting* particles, with kinetic-energy functional $T_s[n]$, and local single-particle potential $v_s(\mathbf{r})$, such that the ground-state density of the interacting system $n_0(\mathbf{r})$ is reproduced by that of the auxiliary problem $n_{s,0}(\mathbf{r})$, $n_0(\mathbf{r}) = n_{s,0}(\mathbf{r})$. Then from the “auxiliary” one-particle Schrödinger equation $[-(\hbar^2/2m)\nabla_{\mathbf{r}}^2 + v_s(\mathbf{r})]\varphi_{s,i}(\mathbf{r}) = \epsilon_i\varphi_{s,i}(\mathbf{r})$ one gets a representation of $n_0(\mathbf{r})$, $n_0(\mathbf{r}) = \sum_i^{N_e} |\varphi_{s,i}(\mathbf{r})|^2$. By virtue of the Hohenberg-Kohn theorem $\varphi_{s,i}(\mathbf{r}) = \varphi_{s,i}[n; \mathbf{r}]$, and therefore $T_s[n]$ is also a unique functional of $n(\mathbf{r})$. The major advantage thus achieved was the exact representation of the kinetic energy term, $T_s[n] = \sum_i^{N_e} \int \varphi_{s,i}(\mathbf{r})^* [-(\hbar^2/2m)\nabla_{\mathbf{r}}^2] \varphi_{s,i}(\mathbf{r}) d\mathbf{r}$.

³In what follows \mathbf{r} denotes a single Cartesian vector and should not be confused with the same notation used in the context of Sec. 2.1.

With this central assertion, for a particular external potential $v(\mathbf{r})$ leading to ground-state density $n_0(\mathbf{r})$, Eq. (2.11) can be written in the form

$$E_v[n] = \int v(\mathbf{r})n(\mathbf{r})d\mathbf{r} + \frac{1}{2} \frac{e^2}{4\pi\epsilon_0} \iint \frac{n(\mathbf{r})n(\mathbf{r}')}{|\mathbf{r} - \mathbf{r}'|} d\mathbf{r}d\mathbf{r}' + \mathcal{G}[n], \quad \mathcal{G}[n] \equiv T_s[n] + E_{\text{XC}}[n], \quad (2.14)$$

where, by definition, $E_{\text{XC}}[n]$ is the exchange-correlation energy functional of the *interacting* system with density $n(\mathbf{r})$. From the stationarity of $E_v[n]$ upon density variations δn , such that $\int \delta n(\mathbf{r})d\mathbf{r} = 0$ (cf. Eqs. (2.12)–(2.13)) and the orbital representation of the kinetic term and n_0 , Kohn and Sham have derived the system of equations to determine the auxiliary potential $v_s(\mathbf{r})$ “generating” the quantity $n_0(\mathbf{r})$. The Kohn-Sham equations read [43, 48]:

$$n_0(\mathbf{r}) = \sum_{i=1}^{N_e} |\varphi_{0,i}(\mathbf{r})|^2 \quad (2.15)$$

$$H_{\text{KS}} \varphi_{0,i}(\mathbf{r}) \equiv \left[-\frac{\hbar^2}{2m} \nabla_{\mathbf{r}}^2 + v_s([n_0]; \mathbf{r}) \right] \varphi_{0,i}(\mathbf{r}) = \epsilon_i \varphi_{0,i}(\mathbf{r}) \quad (2.16)$$

$$v_s([n_0]; \mathbf{r}) = v(\mathbf{r}) + \frac{e^2}{4\pi\epsilon_0} \int \frac{n_0(\mathbf{r}')}{|\mathbf{r} - \mathbf{r}'|} d\mathbf{r}' + v_{\text{XC}}([n_0]; \mathbf{r}), \quad (2.17)$$

where the exchange-correlation potential is defined as the functional derivative of $E_{\text{XC}}[n]$,

$$v_{\text{XC}}([n_0]; \mathbf{r}) = \left. \frac{\delta E_{\text{XC}}[n(\mathbf{r})]}{\delta n(\mathbf{r})} \right|_{n_0(\mathbf{r})}. \quad (2.18)$$

It is immediately apparent that the Kohn-Sham equations need to be solved *self-consistently* due to the density dependence of the effective Kohn-Sham potential v_s . In contrast to the HF scheme, however, v_s is common for all one-particle Kohn-Sham orbitals $\varphi_{0,i}(\mathbf{r})$. Thus, starting from some initial guess for the density, $n^{[0]}(\mathbf{r})$, the effective Kohn-Sham potential is set up according to Eqs. (2.17), (2.18) and the new density $n^{[1]}(\mathbf{r})$ is generated by Eqs. (2.16), (2.15) and so forth. This procedure is repeated until a certain *convergence* criterion is fulfilled.

Once the self-consistent density is obtained, the ground-state total energy is computed from Eq. (2.3), where E_0 is given by the exact (alternative to (2.14)) expression

$$E_0 = \sum_i^{N_e} \epsilon_i - \frac{1}{2} \frac{e^2}{4\pi\epsilon_0} \iint \frac{n_0(\mathbf{r})n_0(\mathbf{r}')}{|\mathbf{r} - \mathbf{r}'|} d\mathbf{r}d\mathbf{r}' + E_{\text{XC}}[n_0] - \int v_{\text{XC}}([n_0]; \mathbf{r})n_0(\mathbf{r})d\mathbf{r}. \quad (2.19)$$

Equation (2.19) is, in fact, the one given originally by Kohn and Sham in Ref. [48], and tied to the original formulation of the Hohenberg-Kohn theorem. Subsequently the latter has been generalized for degenerate ground state, spin-polarized systems, relativistic systems etc., thus different modifications of Eq. (2.19) are available in the literature [43, 44].

It should be stressed once again that the DFT formalism is exact in principle, only $E_{\text{XC}}[n]$ must be approximated. Over the years a bunch of approximate expressions have appeared and we shall briefly discuss them. Another stream of approximations have developed for the needs of *numerical* treatment of Eq. (2.19) and will be addressed later in this chapter.

2.2.2 Approximations to $E_{\text{XC}}[n]$: LDA, GGA

Already in their original work Ref. [48] Kohn and Sham considered the limiting case of slowly varying densities, exploiting the Hohenberg-Kohn result [47],

$$E_{\text{XC}}[n] \approx E_{\text{XC}}^{\text{LDA}}[n] = \int \epsilon_{\text{XC}}^{\text{unif}}(n(\mathbf{r})) n(\mathbf{r}) d\mathbf{r}, \quad (2.20)$$

with $\epsilon_{\text{XC}}^{\text{unif}}(n) = \epsilon_{\text{X}}^{\text{unif}}(n) + \epsilon_{\text{C}}^{\text{unif}}(n)$ being the exchange & correlation energy per electron of a uniform electron gas of density n . In calculating the integral (2.20) the function $\epsilon_{\text{XC}}^{\text{unif}}$ is evaluated for the local density $n(\mathbf{r})$ of the inhomogeneous system under consideration. The approximation thus defined is the well-known *Local-Density Approximation* (LDA), or local spin-density approximation (LSDA) for spin-polarized systems, respectively, in which case $\epsilon_{\text{XC}}^{\text{unif}}(n_{\uparrow}, n_{\downarrow})$ takes as arguments the spin-up and spin-down densities, n_{\uparrow} and n_{\downarrow} , $n_{\uparrow}(\mathbf{r}) + n_{\downarrow}(\mathbf{r}) = n(\mathbf{r})$. The exchange part of $\epsilon_{\text{XC}}^{\text{unif}}$ in atomic units (used hereafter) reads $\epsilon_{\text{X}}^{\text{unif}}(n) = -\frac{3}{4\pi}(3\pi^2 n)^{1/3}$. The correlation part $\epsilon_{\text{C}}^{\text{unif}}$ is available explicitly as an asymptotic expansion in the low [49] and high-density [50] limits. In practice, more recently one makes use of different parameterizations of the quantum Monte-Carlo results of Ceperley and Alder [51]. For the LDA results reported here we have used the one proposed by Perdew and Zunger [52]. It employs Ceperley's parameterization [53] for $r_s \geq 1$, $r_s = (\frac{4\pi}{3}n)^{-1/3}$ being the local Wigner-Seitz radius, which is smoothly tailored at $r_s = 1$ to Gell-Mann and Brueckner's result for high densities [50], $0 \leq r_s \leq 1$. For spin-unpolarized densities, *i.e.* $\zeta \equiv (n_{\uparrow} - n_{\downarrow})/n = 0$, it is given by

$$\epsilon_{\text{C}}^{\text{LDA}}(n) = \begin{cases} \frac{-0.1423}{1 + 1.0529\sqrt{r_s} + 0.3334 r_s}, & r_s \geq 1 \\ -0.048 + 0.0311 \ln r_s - 0.0116 r_s + 0.002 r_s \ln r_s, & 0 \leq r_s \leq 1 \end{cases}. \quad (2.21)$$

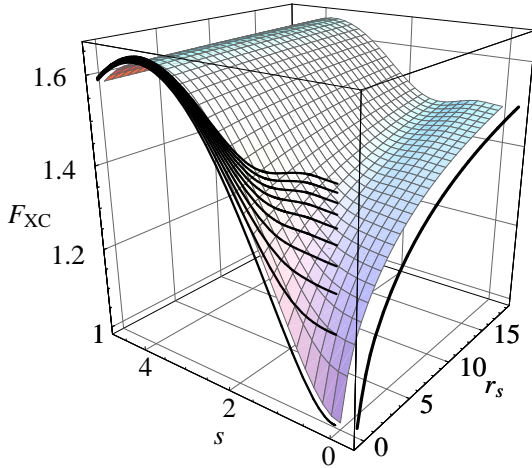


Figure 2.1: Enhancement factor $F_{\text{XC}}(r_s, s)$ for the PW91 exchange-correlation functional (image courtesy of Martin Fuchs). Projections for 10 equidistant values of r_s are made onto the $F_{\text{XC}}-s$ face of the plot. The local-density limit, $s \rightarrow 0$ is given as the projection onto the $F_{\text{XC}}-r_s$ face, $F_{\text{XC}}(r_s, 0) = F_{\text{XC}}^{\text{LDA}}(r_s)$.

to Sec. IV of Ref. [54] and Secs. 7.1 and 7.2 of Ref. [43].

A number of methods have been developed to remedy the deficiencies of the LDA. For a system of nonuniform density E_{XC} may no longer be adequately represented by Eq. (2.20), thus one immediate modification appears to be the inclusion of gradient terms ∇n , which leads to the *Generalized Gradient Approximation* (GGA),

$$E_{\text{XC}}^{\text{GGA}}[n] = \int f(n, \nabla n) d\mathbf{r}. \quad (2.22)$$

The LDA is the most widely used approximation, and a number of its properties are now known and understood. It performs best for (simple) metals, while for semiconductors and insulators the band gap is underestimated by up to 50 % in some cases, but this problem, admittedly, is rather pertinent to the DFT in principle. As regards cohesion and binding, the LDA is found to “overbind”. As a result, the calculated cohesive energies of solids and atomization energies of molecules come out larger compared to experiment, while lattice constants and bond lengths are, respectively, smaller. Though, LDA provides a rather adequate description of bulk elastic properties for the systems under consideration. Section 3.2 gives more details concerning GaAs and InAs. Systematic deviations are additionally found in the energetics of surface chemical reactions; some trends are exemplified below for the hydrogen passivation of the Si(001) surface. For a comprehensive overview of LDA/LSDA the reader is referred, for instance,

Research is being carried out by many groups and various recipes for constructing $f(n, \nabla n)$ have been proposed. Commonly used forms of $E_{\text{XC}}^{\text{GGA}}$ are, for example, those by Becke [55] (exchange part) and Perdew [56] (correlation part) (BP), Becke [55] (exchange part) and Lee-Yang-Parr [57] (correlation part) (BLYP), Perdew and Wang [58, 59] (PW91, known also as GGA-II), or the new revision of PW91 by Perdew, Burke and Ernzerhof [60] (PBE).

The operation of the GGA is conveniently described using as variables r_s and the reduced (dimensionless) density gradient $s(\mathbf{r}) = |\nabla n|/2k_{\text{F}}n|_{n \rightarrow n(\mathbf{r})}$, where k_{F} is the Fermi wave vector, $k_{\text{F}} = (3\pi^2 n)^{1/3}$; the typical range for s , *e.g.*, in Al is $s \simeq 0\text{--}3$ [61], and for Si its average value is $\simeq 0.66$ [62]. The non-locality of the GGA is then expressed in terms of an *enhancement factor* F_{XC} over the local exchange [60], and Eq. (2.22) is rewritten as (absence of spin polarization is implied, $\zeta = 0$)

$$E_{\text{XC}}^{\text{GGA}}[n] = \int \epsilon_{\text{X}}^{\text{unif}}(n) F_{\text{XC}}^{\text{GGA}}(r_s, s) d\mathbf{r}. \quad (2.23)$$

The characteristic shape of F_{XC} , *i.e.* the non-locality, is shown in Figure 2.1 for the PW91 exchange-correlation functional; cf. also Figure 1 in Ref. [60] and the corresponding discussion therein. For all results reported in this work, obtained within the GGA, we employ the PBE functional, which is numerically very similar, but simpler, compared to the PW91 functional. As features, shared by the PW91 and PBE functional, being in principle common for the GGA's, and particularly relevant to the present work, one can mention the improved cohesive energies of solids compared to LDA. Anticipating the further discussion, the lattice constants of GaAs and InAs, calculated with the PBE E_{XC} , however, are found bigger than the experimental values (see Table 3.1 on page 23). In the context of the present study we note also that the surface free energies within GGA are typically lower than the LDA-calculated values.

An example where the GGA is expected to improve over the LDA is the energetics of surface chemical reactions. In an earlier work [63] we have studied the performance of different functionals in the case of molecular hydrogen desorption and dissociative adsorption on the Si(001) surface. The quantities of importance have meaning of relative energies—usually small differences of two large energies. The reaction energetics (adsorption, desorption barriers E_a^{ads} , E_a^{des} , and reaction enthalpy E_{rxn}) was calculated for three cluster models of the clean Si(001) surface, Si_9H_{12} , $\text{Si}_{15}\text{H}_{16}$, $\text{Si}_{21}\text{H}_{20}$, and then compared to a reference extended 5-layer slab model, assuming the so-called *pre-pairing scenario* for the $\text{H}_2/\text{Si}(001)$ reaction mechanism (for an overview, see for example Ref. [64]). The tests employed the LDA, BP, PW91 and BLYP functionals and results are summarized in Figure 2.2. What is to be noticed is (*i*) the well-pronounced

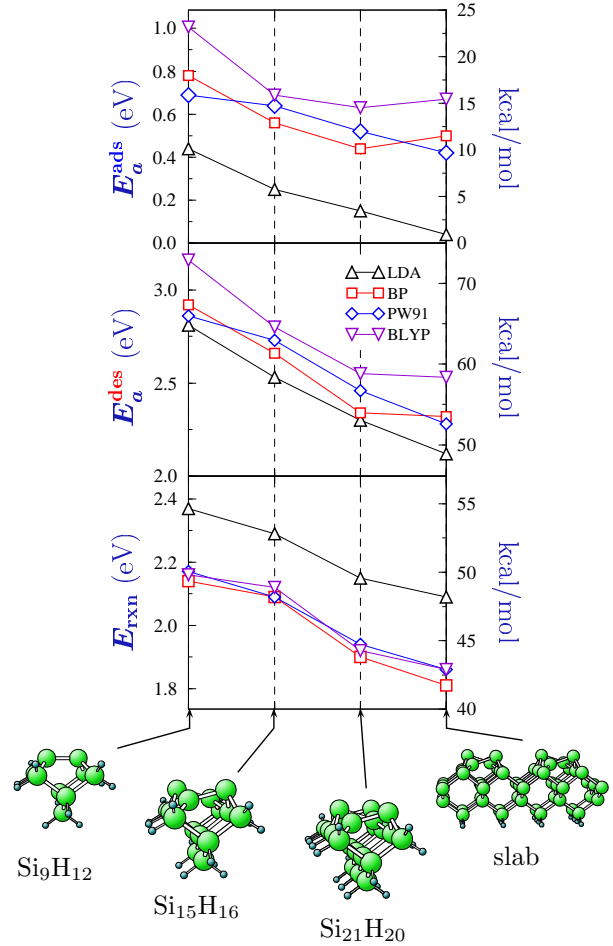


Figure 2.2: Performance of different exchange-correlation functionals studied for the reaction energetics of H_2 dissociative adsorption and desorption at the Si(001) surface.

effect of the size of the system used to model the clean Si(001) surface; (ii) noticeable interplay between the system size and E_{XC} ; (iii) different performance of the LDA and GGA functionals. For discussion on the first two points we refer to Ref. [63]. Concerning the performance of the functionals, we found that LDA underestimates the barrier to adsorption E_a^{ads} . This is in accord with the established picture that LDA tends to underestimate the adsorption barriers at surfaces [65, 66]. For the slab model E_a^{ads} is just vanishing, so the use of a GGA functional is crucial for getting the correct qualitative behavior, complying with the experiment. The LDA calculations provided also the lower bound for the desorption barrier E_a^{des} . The heat of reaction within LDA is larger than in GGA and, as seen from the bottom panel of Figure 2.2, the GGA functionals give very similar results for E_{rxn} . Thus the major effect in the change of the latter quantity for the models considered comes from the type of approximation scheme used for E_{XC} , LDA *versus* GGA, while details in constructing $f(n, \nabla n)$ seem to have only minor influence.

Besides the GGA scheme there exist other methods to go beyond the local-density approximation: the Self-Interaction Correction (SIC), the Optimized Effective Potential (OEP) method etc., and the method of choice is often determined by the aspects of the process and properties that need to be described. For an overview of these schemes, please see for example Section 2.7 in Ref. [38].

2.3 Practical aspects of DFT implementation schemes

2.3.1 Supercell approximation & plane-wave basis set

DFT allows the many-body problem, Eq. (2.7), to be mapped onto an effective single-particle picture. Nonetheless, one could hardly solve the Kohn-Sham equations for 10^{23} electrons moving in certain effective potential. This difficulty can be overcome if we consider only a “minimum representation” of the system to be studied: *e.g.*, the bulk unit cell for crystals, a slab representing a surface (including eventually adsorbate structures) etc. This “proto-image” is put in a *supercell* with certain size and symmetry properties, Figure 2.3. The supercell is a prism spanned by three basis vectors \mathbf{a}_1 , \mathbf{a}_2 , and \mathbf{a}_3 , and its volume is given by⁴ $\Omega = \mathbf{a}_1 \cdot (\mathbf{a}_2 \times \mathbf{a}_3) = \varepsilon_{ijk} a_{1,i} a_{2,j} a_{3,k}$, where ε_{ijk} is the unit fully antisymmetric (Levi-Civita’s) tensor. Periodic images of the supercell are generated by translations $\mathbf{t} = n_1 \mathbf{a}_1 + n_2 \mathbf{a}_2 + n_3 \mathbf{a}_3$, with $n_i = \text{integer}$.

A surface can be viewed as a defect in the bulk crystal structure which destroys the perfect periodicity in a certain crystallographic direction \mathbf{n} . Such an aperiodic system is modeled within the supercell approach by a *slab* representing a given number of atomic layers Δ_s along the surface normal \mathbf{n} which are separated by a vacuum region Δ_v . The values of Δ_s and Δ_v are system specific but generally Δ_s should be chosen large enough so that the interaction between the two surfaces of the slab is negligible; the thickness of the vacuum “layer” Δ_v also needs to be sufficient not to introduce artifacts from the artificial periodicity along \mathbf{n} . In the following we explicitly specify details for the supercell used in each particular calculation. Supercells for three typical classes of systems are sketched in Figure 2.3.

The treatment of electronic states in an external periodic potential, $v(\mathbf{r} + \mathbf{t}) = v(\mathbf{r})$, is a standard problem in solid state physics (see, for example, Chapter VI in Ref. [67]). The wave function of a stationary state must satisfy the same translation invariance (within a phase factor), $\varphi(\mathbf{r} + \mathbf{t}) = \text{const} \times \varphi(\mathbf{r})$. The Bloch theorem states that a wave function with such a property has the form

$$\varphi_{n,\mathbf{k}}(\mathbf{r}) = e^{i\mathbf{k}\cdot\mathbf{r}} u_{n,\mathbf{k}}(\mathbf{r}), \quad \text{where} \quad u_{n,\mathbf{k}}(\mathbf{r} + \mathbf{t}) = u_{n,\mathbf{k}}(\mathbf{r}), \quad (2.24)$$

n is the band index, \mathbf{k} is the electron quasi-momentum, and $\langle \varphi_{n',\mathbf{k}'} | \varphi_{n,\mathbf{k}} \rangle = \delta_{nn'} \delta_{\mathbf{k}\mathbf{k}'}$. Being a

⁴In the following we use the Einstein summation convention: $\sum_i A_i B_i \equiv A_i B_i \equiv A_1 B_1 + A_2 B_2 + \dots$.

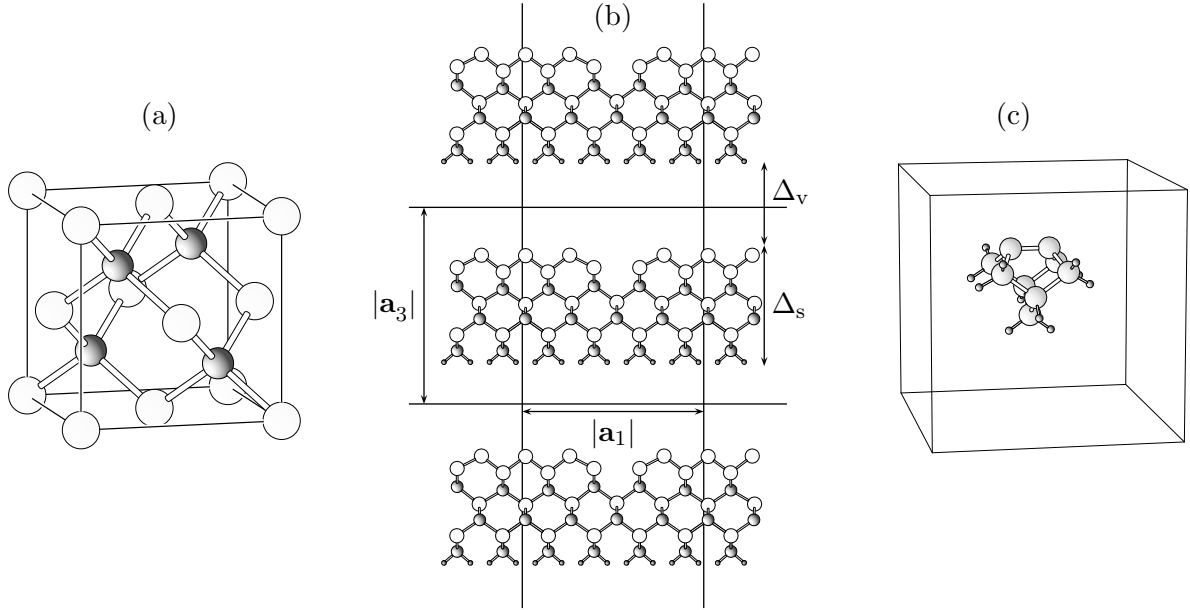


Figure 2.3: Schematic representation of three basic types of systems: (a) Simple cubic unit cell for bulk zincblende structure; (b) Slab representing GaAs(001) surface (2D projection onto the x - z plane) with Δ_s equal to 7 atomic layers and Δ_v equivalent to $\simeq 6$ interlayer distances; (c) large supercell for an isolated cluster (Si_9H_{12}).

periodic function, $u_{n,\mathbf{k}}$ can be expanded in a Fourier series, $u_{n,\mathbf{k}}(\mathbf{r}) = (1/\sqrt{\Omega}) \sum_{\mathbf{G}} c_{n,\mathbf{k}+\mathbf{G}} \exp(i\mathbf{G} \cdot \mathbf{r})$, where in principle the sum goes over an infinite number of reciprocal lattice vectors $\mathbf{G} = m_1\mathbf{b}_1 + m_2\mathbf{b}_2 + m_3\mathbf{b}_3$, with $(\mathbf{b}_1, \mathbf{b}_2, \mathbf{b}_3)$ being the basis in the reciprocal space and $m_i = \text{integer}$. Substituting the expansion for $u_{n,\mathbf{k}}$ into Eq. (2.24) we obtain

$$\varphi_{n,\mathbf{k}}(\mathbf{r}) = \frac{1}{\sqrt{\Omega}} \sum_{\mathbf{G}} c_{n,\mathbf{k}+\mathbf{G}} e^{i(\mathbf{k}+\mathbf{G}) \cdot \mathbf{r}}. \quad (2.25)$$

This representation of the single-particle state $\varphi_{n,\mathbf{k}}$ is referred to as a *plane-wave expansion*. Using the above expression for the Kohn-Sham orbitals, Eq. (2.16) takes a simpler secular form with a diagonal kinetic term, and including the Fourier images of the potentials in the right-hand side of Eq. (2.17),

$$\sum_{\mathbf{G}'} \left[\frac{1}{2} |\mathbf{k} + \mathbf{G}|^2 \delta_{\mathbf{G}\mathbf{G}'} + v(\mathbf{G} - \mathbf{G}') + v_{\text{H}}(\mathbf{G} - \mathbf{G}') + v_{\text{XC}}(\mathbf{G} - \mathbf{G}') \right] c_{n,\mathbf{k}+\mathbf{G}'} = \epsilon_n(\mathbf{k}) c_{n,\mathbf{k}+\mathbf{G}}. \quad (2.26)$$

In practice, however, instead of the infinite series (that has to be made for each \mathbf{k}) one uses a truncated plane-wave expansion to include terms with kinetic energies only up to certain cutoff $E_{>\epsilon}$,

$$\frac{1}{2} |\mathbf{k} + \mathbf{G}|^2 \leq E_{>\epsilon}. \quad (2.27)$$

The “quality” of the so produced finite basis set is entirely controlled by the energy cutoff—the higher the $E_{>\epsilon}$, the better the plane-wave representation. Note also that, by virtue of Eq. (2.27), the number of \mathbf{G} vectors, *i.e.* the number of plane-wave basis states N_{PW} , is generally different for each \mathbf{k} , thus an alternative description in terms of the mean number of plane waves \bar{N}_{PW} can be also employed. One says that an absolute convergence with respect to $E_{>\epsilon}$ is achieved when the total energy E no longer changes with increasing $E_{>\epsilon}$. For this, in principle, very high cutoffs

are required. Many of the quantities of interest are obtained as differences between total energies (*e.g.*, diffusion barriers) and it turns out that they “converge” much faster with respect to E_{∞} , thus calculations at lower cutoffs can be performed, and the value of E_{∞} , ensuring “convergence” of the calculated quantity, is determined by tests. For most of the results obtained in this work we use $E_{\infty} = 10 \text{ Ry} = 136.058 \text{ eV}$. The principle factor, however, that allows significant reduction of the energy cutoff in calculations using plane-wave basis set is the pseudopotential concept, briefly outlined in the next subsection.

2.3.2 *Ab initio* pseudopotentials, the fhi98PP package

The external potential v for the electrons is the superposition of the nuclear Coulomb potentials, $v(\mathbf{r}) := -\sum_I Z_I/|\mathbf{r} - \mathbf{R}_I|$. The electron wave functions in such a singular potential are rapidly oscillating due to orthogonality, which leads to high kinetic energies. Very large E_{∞} would be required to reproduce these rapid oscillations in the plane-wave expansion (2.25). Since the number of matrix elements $(H_{\text{KS}}(\mathbf{k}))_{\mathbf{G}\mathbf{G}'}$ increases as the squared number of plane-wave basis states, N_{PW}^2 , then the “all-electron” problem may well become intractable for large systems (in fact, already diamond is too hard), at first, because of high memory demands.

On the other hand, most properties of the condensed systems can be well described by the valence electrons while the highly localized core electrons have only minor influence. The concept of a *pseudopotential* (for an overview please see, for example, Ref. [68]) exploits these features and within the frozen-core approximation eliminates the core electrons. This provides a “softer” potential for the valence electrons which are described by nodeless pseudo wavefunctions. Thus, a crucial parameter in the construction of atomic pseudopotentials is the cutoff radius r^{∞} , dividing the electron shell into a (chemically inert) core region ($r \leq r^{\infty}$), and a valence region ($r > r^{\infty}$) responsible for the chemical bonding. The choice of r^{∞} should ensure that the pseudopotential describes adequately the scattering properties of the ion in diverse atomic environments, a property usually referred to as *transferability*. Yet, they have to be *efficient* in reducing the overall computational effort.

Generally a norm-conserving pseudopotential is represented in the “semilocal” operator form

$$\langle \mathbf{r} | v^{\text{ps}} | \mathbf{r}' \rangle = v_{\text{loc}}(r) \delta(\mathbf{r} - \mathbf{r}') + \sum_{l=0}^{l_{\text{max}}} \sum_{m=-l}^l Y_{lm}^*(\Omega_{\mathbf{r}}) \delta v_l^{\text{ps}}(r) \frac{\delta(r - r')}{r^2} Y_{lm}(\Omega_{\mathbf{r}'}), \quad (2.28)$$

where the local pseudopotential $v_{\text{loc}}(r)$ is independent of the angular momentum component l , whereas the semilocal part contains components $\delta v_l^{\text{ps}}(r) = v_l^{\text{ps}}(r) - v_{\text{loc}}(r)$ for each l , Y_{lm} being the spherical harmonics, and $\Omega_{\mathbf{r}}$ is the body angle in the direction of \mathbf{r} .

In this work, we use the plane-wave basis set in conjunction with *ab initio* pseudopotentials generated and tested with the **fhi98PP** program package written by Martin Fuchs [69], which provides as tools the pseudopotential generator **psgen** and an excellent testing utility **pswatch**. The **fhi98PP** code implements the Hamann [70] and the Troullier-Martins [71] schemes for generating norm-conserving pseudopotentials (different schemes have been proposed, *e.g.*, in Refs. [72, 73]).

As a first step, **psgen** solves the all-electron atom in a given reference configuration, obtaining the all-electron potential and valence states. Then, within the selected scheme (Hamann or Troullier-Martins) it creates intermediary *screened* pseudopotential $v_l^{\text{ps,scr}}(r)$ by inverting the Schrödinger equation for the radial pseudo wavefunction R_l^{ps} . The pseudo wavefunction is subject to the requirements:

- ✧ for given l the corresponding eigenvalue should reproduce that of the reference state, $\epsilon_l^{\text{ps}} \equiv \epsilon_{nl}$, and the logarithmic derivatives of the pseudo and all-electron wavefunction R_{nl} match for $r > r_l^{\infty}$;

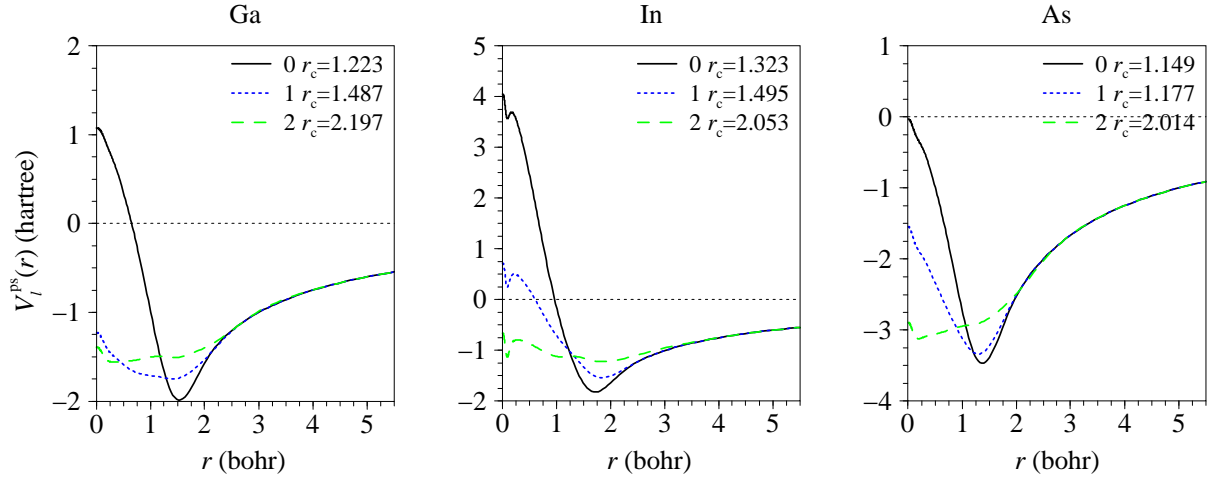


Figure 2.4: Hamann-type ionic pseudopotentials used in the present work, generated with the PBE E_{XC} (graphical output from **psgen**). The valence configurations are, respectively, Ga: $4s^2 4p^1$, In: $4s^2 5s^1$, and As: $4s^2 4p^3$. The legends give the core cutoff radii $r_l^>e$ for each momentum component, $l = 0, 1, 2$, as used by **psgen**.

◇ meets the *norm-conservation* requirement:

$$\int_0^r |R_l^{\text{ps}}(\epsilon_l^{\text{ps}}, r')|^2 r'^2 dr' \equiv \int_0^r |R_{nl}(\epsilon_{nl}, r')|^2 r'^2 dr' \quad \text{for } r \geq r_l^>e;$$

◇ $R_l^{\text{ps}}(r)$ is nodeless.

The actual ionic pseudopotential does not depend on the valence configuration, and is produced by “unscreening”,

$$v_l^{\text{ps}}(\mathbf{r}) = v_l^{\text{ps,scr}}(r) - v_{\text{H}}([n_0^{\text{v}}]; r) - v_{\text{XC}}([n_0^{\text{v}}]; r), \quad (2.29)$$

i.e. subtracting the Hartree and exchange-correlation contribution of the *valence* shell with density $n_0^{\text{v}}(r) = \frac{1}{4\pi} \sum_l f_l |R_l^{\text{ps}}(\epsilon_l^{\text{ps}}, r)|^2$, where the occupation numbers f_l are those for the all-electron reference problem. This procedure implies a linear exchange-correlation interaction between the core and the valence electrons, thus only $n_0^{\text{v}}(r)$ enters as argument in v_{XC} . When required, however, the core-valence nonlinearity is formally accounted for by considering dependence on the *total* density $n_0 = n_0^{\text{v}} + n_0^{\text{core}}$. Though, in practice one can include only a *partial core density* $\tilde{n}_0^{\text{core}}$ [74] set up according to a cutoff radius $r_{\text{nl}}^>e$, so that it is a smooth function for $r < r_{\text{nl}}^>e$ and $\tilde{n}_0^{\text{core}} \equiv n_0^{\text{core}}$ beyond $r_{\text{nl}}^>e$ (see Ref. [75] and the extensive list of references therein). In such a case the exchange-correlation term in Eq. (2.29) is replaced: $v_{\text{XC}}([n_0^{\text{v}}]; r) \rightarrow v_{\text{XC}}([n_0^{\text{v}} + \tilde{n}_0^{\text{core}}]; r)$. In the **psgen** tool the explicit treatment of the core-valence nonlinearity is activated by a non-zero input value of the $r_{\text{nl}}^>e$ parameter.

In practice, to reduce the computational effort in the calculations, the semilocal part of the so constructed pseudopotentials is further brought to a fully nonlocal, separable form following Kleinman and Bylander [76], and one of the semilocal pseudopotential components is taken for the local potential,

$$v_l^{\text{ps}}(\mathbf{r}, \mathbf{r}') := v_{\text{loc}}(r) \delta(r - r') + \frac{\langle \mathbf{r} | \delta v_l R_l^{\text{ps}} \rangle \langle \delta v_l R_l^{\text{ps}} | \mathbf{r}' \rangle}{\langle R_l^{\text{ps}} | \delta v_l R_l^{\text{ps}} \rangle}, \quad (2.30)$$

The Kleinman-Bylander form, however, may induce artificial, *ghost* states in the spectrum of the pseudoatom, thus leading to a non-transferable pseudopotential. The **pswatch** utility allows

a thorough test for detecting such ghost states, which involves also the analysis by Gonze *et al.* [77], and provides additional functionalities to assess the pseudopotential quality. With its help, the transferability of all pseudopotentials used here was carefully tested. Further details on the `fhi98PP` program can be found in the original work by Fuchs and Scheffler [69].

The actual PBE-GGA pseudopotentials employed in the present work are shown in Figure 2.4. For all species, the d component of the ionic pseudopotential was used as local, $l_{\text{loc}} = 2$. Cohesive properties of the elemental and compound materials to be considered in the following chapters, calculated within the LDA, are collected in Appendix A.

2.3.3 Brillouin zone sampling

One important consequence stemming from the spatial periodicity within the supercell approach and the Bloch theorem is that all physically inequivalent values of the quasi-momentum \mathbf{k} lie within a single unit cell in the reciprocal space, termed the Brillouin zone (BZ). Thus integrals over momentum space are conveniently reduced to integration over the volume of the BZ, $\Omega_{\text{BZ}} = (2\pi)^3/\Omega$. Hence, the electron density $n(\mathbf{r})$, is given by

$$n(\mathbf{r}) = \Omega \sum_n \int_{\text{BZ}} f(\epsilon_n(\mathbf{k})) |\varphi_{n,\mathbf{k}}(\mathbf{r})|^2 \frac{d\mathbf{k}}{(2\pi)^3}, \quad (2.31)$$

where the summation goes over all bands and the occupancies have the step-like distribution $f(\epsilon_n) = (2s+1)\theta(\epsilon_n(\mathbf{k}) - \epsilon_F)$, with ϵ_F being the Fermi energy, and $s = 1/2$.

In the numerical treatment of (2.31) $\int d\mathbf{k}$ is transcribed into a sum over discrete set of $N_{\mathbf{k}}$ “ \mathbf{k} -points”,

$$\Omega \int_{\text{BZ}} \dots(\mathbf{k}) \frac{d\mathbf{k}}{(2\pi)^3} \rightarrow \frac{1}{N_{\mathbf{k}}} \sum_i^{N_{\mathbf{k}}} \dots(\mathbf{k}_i) \quad (2.32)$$

Strictly speaking, the precise representation of the integral requires summation over a large number of \mathbf{k} -points, corresponding to all allowed values of \mathbf{k} in the irreducible part of first BZ, as determined by the (Born-von Kármán) periodic boundary conditions [78, 79]. In practice, however, one makes use of relatively small set of specially selected \mathbf{k} -points. Generally they are specified as

$$\mathbf{k}_i = k_1^{(i)} \mathbf{b}_1 + k_2^{(i)} \mathbf{b}_2 + k_3^{(i)} \mathbf{b}_3, \quad i = 1, \dots, N_{\mathbf{k}}. \quad (2.33)$$

In this work we use a generalized version of the Monkhorst-Pack scheme [80] to construct the “ \mathbf{k} -mesh”. The three coefficients $k_j^{(i)}$ in Eq. (2.33) have the form

$$k_j^{(i)} = \frac{2p_j^{(i)} + 2q_j - l_j - 2}{2l_j} \quad \begin{cases} q_j = 1, 2, \dots, l_j \\ i = 1, 2, \dots, N_{\mathbf{k}} \end{cases}. \quad (2.34)$$

Figure 2.5 illustrates the essence of the approach as applied to a system with 2D periodicity. In fact, Eqs. (2.33) and (2.34) can be viewed as a rule according to which the BZ is “tiled” into small polyhedra of the same shape, l_j along each basis vector \mathbf{b}_j , resulting to a fragmentation of $l_1 \times l_2 \times l_3$ tiles in total. Then $N_{\mathbf{k}}^s$ \mathbf{k} -points with “local” coordinates $(p_1^{(1)}, p_2^{(1)}, p_3^{(1)}) \dots, (p_1^{(N_{\mathbf{k}}^s)}, p_2^{(N_{\mathbf{k}}^s)}, p_3^{(N_{\mathbf{k}}^s)})$ are generated in each of the tiles. It is the value of $N_{\mathbf{k}}^s$ that is referred to as the number of *special \mathbf{k} -points*. As an alias for the so constructed set of \mathbf{k} -points we shall use here the signature

$$\left\{ \left[\left(p_1^{(1)}, p_2^{(1)}, p_3^{(1)} \right), \dots, \left(p_1^{(N_{\mathbf{k}}^s)}, p_2^{(N_{\mathbf{k}}^s)}, p_3^{(N_{\mathbf{k}}^s)} \right) \right], l_1 \times l_2 \times l_3 \right\}. \quad (2.35)$$

Monkhorst and Pack [80] have originally used a single special \mathbf{k} -point in the center of the tile, thus the corresponding signature reads $\{(\frac{1}{2}, \frac{1}{2}, \frac{1}{2}), l_1 \times l_2 \times l_3\}$.

The two particular realizations of the Monkhorst-Pack scheme, shown in Figure 2.5, also illustrate the concept of *equivalence*: the sampling of the \mathbf{k} -space is equally uniform for the two different BZs. Since one often is interested in comparing results obtained from different setups, the use of equivalent sets of \mathbf{k} -points is one of the prerequisites for achieving comparability (cf., e.g., Sec. 3.2 in Ref. [81]).

Applying the Monkhorst-Pack scheme produces a mesh of $N_{\mathbf{k}} = (l_1 \times l_2 \times l_3) \times N_{\mathbf{k}}^s$ \mathbf{k} -points, but this number can be even further reduced. The point is that the BZ + atomic basis are usually characterized by a certain number of point symmetry elements (e.g., rotations, mirror planes). As a result, the $N_{\mathbf{k}}^r$ symmetry-inequivalent \mathbf{k} -points are only a subset of the $N_{\mathbf{k}}$ points. The sum (2.32) is then taken only over the reduced set with corresponding weighting factors w_i , $\sum_{i=1}^{N_{\mathbf{k}}^r} w_i \dots (\mathbf{k}_i)$.

The actual pattern to be used in sampling the BZ generally depends on the nature of the problem that needs to be solved. Systems with a gap in the energy spectrum typically require fewer $N_{\mathbf{k}}$, whereas in case of metallic systems a much denser \mathbf{k} -mesh is to be employed, ensuring good sampling of the Fermi surface. The “quality” of the \mathbf{k} -mesh should necessarily be tested for each particular system, so that a convergence of the total energy is ensured with respect to $N_{\mathbf{k}}$.

In many problems, however, one operates with total energies obtained for supercells with varying volume V , but using the same value of E_{sc} . In such a situation, changes in V lead to a discontinuous change of \bar{N}_{PW} , inducing errors in the calculated quantities. A few schemes for calculating corrections to energy and pressure have been proposed in the literature [82–84]. In the present work, when necessary, corrections to the total energy are evaluated according to the *scaling hypothesis* due to Rignanese *et al.* [84], described in Appendix B.

2.3.4 Assembling all together: the fhi98md program

All results in the present work have been obtained with the **fhi98md** program [81, 85], developed at the Theory Department of the Fritz-Haber-Institute. The package, including also a starting utility **fhi98start** to generate consistent input files, provides a complex set of functionalities allowing DFT calculations of static, elastic, electronic properties of poly-atomic systems as well as finite-temperature MD simulations. A large part of the runs were carried out with a parallel version of the program on a CRAY T3E shared-memory multiprocessor system (www.cray.com/products/systems/t3e/) using from 8 up to 128 processing elements (PEs).

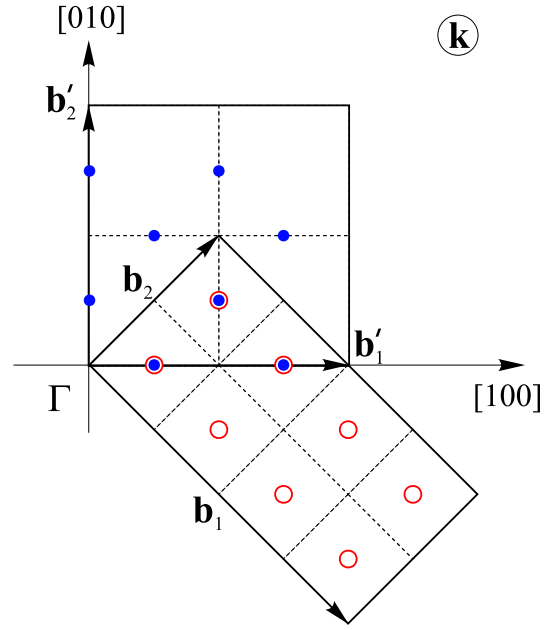


Figure 2.5: BZs for (2×4) (spanned by \mathbf{b}_1 and \mathbf{b}_2) and $c(4 \times 4)$ (spanned by \mathbf{b}'_1 and \mathbf{b}'_2) surface unit cells. The former has (4×2) periodicity and the sampling is the Monkhorst-Pack mesh with signature $\{(\frac{1}{2}, \frac{1}{2}, 0), 4 \times 2 \times 1\}$ (\circ). To obtain an equivalent sampling in the latter case we can use 2 special \mathbf{k} -points in each tile (\bullet) leading to the set $\{[(\frac{1}{2}, 0, 0), (0, \frac{1}{2}, 0)], 2 \times 2 \times 1\}$. Since a surface is modeled by a slab (see Figure 2.3 (b)) we use a single tile along \mathbf{b}_3 .

The preceding sections outlined the main features of the setup used in the **fhi98md** code.

When solving the Kohn-Sham equations (2.15)–(2.17), however, the size of the Kohn-Sham Hamiltonian matrix (cf. Eq. (2.26)) may increase substantially for large systems. Then in the self-consistent iterative procedure of Eq. (2.19) one would face the problem of a large matrix diagonalization in every iteration, the effort for which scales as $O(N_{\text{PW}}^3)$.

In the **fhi98md** code the eigenvalue problem is addressed, instead, on an *iterative* principle having its origin in the Car-Parrinello method [86]. The wave functions $\varphi_{n,\mathbf{k}}(\mathbf{r})$ are considered dynamic variables and are iteratively improved, starting from an initial guess $\varphi_{n,\mathbf{k}}^{[0]}(\mathbf{r})$, by solving a particular equation of motion. The program offers three different schemes to iterate the wave function: steepest descent method, Williams-Soler and damped Joannopoulos algorithms [87]. All operations are performed on a 3D Fourier mesh $n_1 \times n_2 \times n_3$ whose size is determined according to the sampling theorem

$$n_i \geq \frac{2}{\pi} \|\mathbf{a}_i\| \sqrt{E_{\infty}}, \quad (2.36)$$

and an (inverse) fast Fourier transformation (FFT/IFFT) is used to switch between real-space and reciprocal-space representation of the potentials and the wave functions.

In most of the actual problems of interest in materials science, one needs to know the lowest-energy geometrical configuration \mathbf{R}_0 of the atoms in the system. Generally, it is *a priori* unknown, but a hint can always be found to generate some initial, or starting, configuration that is used in the search for \mathbf{R}_0 . This procedure is referred to as structure (geometry) optimization (relaxation), and within the BO approximation it can be realized on the basis of Eqs. (2.7) and (2.8). Similarly, the same two-step scheme can be used in finite-temperature MD simulation. Once the BO surface is reached, the so-called variational forces [88], $\mathbf{F}_I^{\text{var}} = - \int \frac{\delta E}{\delta n} \nabla_{\mathbf{R}_I} n(\mathbf{r}) d\mathbf{r}$, vanish and \mathbf{F}_I in Eq. (2.8) is identified with the physical Hellmann-Feynman force

$$\mathbf{F}_I^{\text{HF}} = - \frac{\partial E(\mathbf{R})}{\partial \mathbf{R}_I}. \quad (2.37)$$

On the other hand, as the plane-wave basis used by the **fhi98md** program is defined by the cutoff energy E_{∞} (input parameter **ecut**), $\mathbf{F}_I^{\text{var}}$ also vanishes [88]. Thus it is the Hellmann-Feynman force (2.37) used in the program to operate on the atoms. In all structure relaxation runs performed in this work, geometries were considered converged if the residual forces $\|\mathbf{F}_I\| \leq 0.0005 \text{ Ha}/a_{\text{B}} \simeq 0.025 \text{ eV}/\text{\AA}$.

Further information about the **fhi98md** program, as well as a growing number of examples for its application to diverse problems in physics, chemistry, and recently to biological systems can be found on the home page of the Theory Department of the Fritz-Haber-Institute:

- ◇ www.fhi-berlin.mpg.de/th/fhimd/
- ◇ www.fhi-berlin.mpg.de/th/Meetings/trieste.html
- ◇ www.fhi-berlin.mpg.de/th/Meetings/FHImd2001/
- ◇ www.fhi-berlin.mpg.de/th/paper.html

Chapter 3

Continuum elasticity theory

The discussion in Section 1.2 already suggested the importance of the elastic degrees of freedom in a lattice-mismatched heteroepitaxial system. Depositing a material with a bulk lattice constant much larger than that of the substrate, which is the case of InAs/GaAs, drives the substrate-WL interface and the WL surface out of their (local) mechanical equilibrium. In order to understand how this new condition will bias the surface adatom diffusion one therefore requires a knowledge of the elastic properties of the InAs/GaAs heteroepitaxial system. The characteristic lengths in the latter are typically much larger than the bulk lattice parameters of the two materials, a_{InAs} and a_{GaAs} , respectively, which allows us to utilize the concept of an elastic continuum. The language to describe the mechanics of a continuous medium is provided by continuum elasticity theory [89].

Apart from the general introductory purposes of this chapter, here we derive results that serve as a groundwork for introducing elastic deformations in the problem of surface adatom diffusion.

3.1 Basic concepts

Generally, under the action of applied forces a point at position $\mathbf{r} = (x_1, x_2, x_3)$ in a continuous medium of volume V gets displaced to a new position $\mathbf{r}' = (x'_1, x'_2, x'_3)$, thus its displacement is simply given by the vector

$$\mathbf{u} = \mathbf{r}' - \mathbf{r}, \quad u_i = x'_i - x_i, \quad i = 1, 2, 3. \quad (3.1)$$

The deformed state of a solid is then completely defined if \mathbf{u} is specified for each $\mathbf{r} \in V$, *i.e.* if we know the vector field $\mathbf{u}(\mathbf{r})$. In fact the “continuity” of the medium requires that a point is considered together with a surrounding infinitesimal neighborhood δV . The displacement at $\mathbf{r} + \delta \mathbf{r}$ within δV can be written as

$$u_i(\mathbf{r} + \delta \mathbf{r}) = u_i(\mathbf{r}) + \frac{\partial u_i(\mathbf{r})}{\partial x_k} \delta x_k. \quad (3.2)$$

The derivatives of the displacement field $\partial_k u_i$ in Eq. (3.2) constitute the components of the (generally non-symmetric) elastic distortions tensor γ_{ik} [90]. In a more formal approach γ_{ik} can be decomposed into a symmetric and an antisymmetric parts, respectively,

$$\varepsilon_{ik} = \frac{1}{2} \left(\frac{\partial u_i}{\partial x_k} + \frac{\partial u_k}{\partial x_i} \right), \quad \text{and} \quad \omega_{ik} = \frac{1}{2} \left(\frac{\partial u_i}{\partial x_k} - \frac{\partial u_k}{\partial x_i} \right). \quad (3.3)$$

In the following we shall always assume that the deformations are small, so that $|\varepsilon_{ik}|, |\omega_{ik}| \ll 1$. Geometrically, the tensor ω_{ik} describes the infinitesimal rotations of the points in δV . Consider

now the change of the volume δV as a result of a small deformation, and let $\delta V'$ be its “deformed” value. Exploiting the smallness of ε_{ik} and after some algebra [89, 90] one can easily show that

$$\delta V = \delta V'(1 + \varepsilon_{ii}) \equiv \delta V'(1 + \text{Tr } \boldsymbol{\varepsilon}). \quad (3.4)$$

The tensor ε_{ik} is called the strain tensor and, as indicated by Eq. (3.4), its trace determines the relative change of the volume $(\delta V' - \delta V)/\delta V$ upon deformation. One important special case is realized when a solid is uniformly compressed or expanded, *i.e.* $\mathbf{r}' = \alpha \mathbf{r}$, with α being a scalar constant. Substituting \mathbf{r}' in Eq. (3.1), and according to the definition Eq. (3.3), the strain tensor adopts its simplest diagonal form

$$\varepsilon_{ik} = \text{const } \delta_{ik} = (\alpha - 1)\delta_{ik}. \quad (3.5)$$

Any deformation leads to the appearance of internal tension, *i.e.* internal *short-range* forces, in the solid attempting to restore its equilibrium state. The total force, acting on a part of the solid of volume V , due to the surrounding parts, can be represented as an integral $\int_V \mathbf{P} dV$ of the volume force density \mathbf{P} . Because of the short-range nature of the internal forces, the surroundings act on V only through its surface, and therefore the volume integral can be transformed into one over the surface of V . According to Gauss’s theorem, this is only possible if \mathbf{P} is the divergence of a second rank tensor, $\mathbf{P} = \text{Div } \boldsymbol{\sigma}$. In continuum elasticity theory, this equality introduces the stress tensor σ_{ik} , and thus

$$\int P_i dV = \int \frac{\partial \sigma_{ik}}{\partial x_k} dV = \oint \sigma_{ik} n_k dA, \quad (3.6)$$

where n_k is the k th component of the unit vector \mathbf{n} normal to surface element dA . In the case of isotropic compression, each part of the solid experiences a constant pressure p , and $\boldsymbol{\sigma}$ takes the simplest form $\sigma_{ik} = -p \delta_{ik}$. It is intuitively clear, however, that the elastic deformations are proportional to the loading applied. In other words, there should be a dependence between the strain and the stress tensors, and for small deformations Hooke’s law asserts its linearity, *i.e.*

$$\varepsilon_{ik} = s_{iklm} \sigma_{lm}, \quad \text{or} \quad \sigma_{ik} = c_{iklm} \varepsilon_{lm}. \quad (3.7)$$

These equations define two material tensors of rank four called the elastic, or stiffness, constants tensor c_{iklm} , and the elastic compliance tensor s_{iklm} . Since the latter relate symmetric tensors of rank two, they are symmetric, too, with respect to the first and second pair of indices as well as with respect to exchange of the pairs.¹ Two consequences of such an inner symmetry are to be pointed out: The number of the different tensor components is reduced from $3^4 = 81$ to $6 \times (6 + 1)/2 = 21$. The symmetries of the crystal lattice may further reduce this number, and we will return to this point later in this section, when discussing elastic properties of bulk GaAs and InAs. Secondly, one can migrate to contracted notations, the so-called Voigt notations, with only two indices, *e.g.*, $c_{iklm} \rightarrow c_{\lambda\mu}$, where $\lambda, \mu = 1, 2, 3, 4, 5, 6$.

In the context of the present work, it is however of primary interest to apply the basic thermodynamic relations to the case of an elastically deformed media. Under the standard assumptions that ensure the reversibility of the deformation process [89], the differentials of the Helmholtz and the Gibbs free energy per unit volume, respectively, read²

$$dF = -S dT + \sigma_{ik} d\varepsilon_{ik}, \quad dG = -S dT - \varepsilon_{ik} d\sigma_{ik}, \quad (3.8)$$

¹For brevity in the specialized literature, the inner symmetry of a rank four tensor with such symmetry properties is designated as $[[V^2]^2]$. In this notation, the inner symmetry of a rank r tensor symmetric with respect to all indices is $[V^r]$, which indicates the fact that the components of such a tensor transform as a product of r components of one and the same vector.

²Note that in these expressions F is a thermodynamic potential in the variables (T, ε_{ik}) , while G is so in (T, σ_{ik}) .

with S being the entropy per unit volume. From Eq. (3.8) it follows, for example, that $\sigma_{ik} = (\partial F / \partial \varepsilon_{ik})_T$. For isothermal deformations, it can also be easily shown that

$$F = \frac{1}{2} \boldsymbol{\sigma} : \boldsymbol{\varepsilon} \equiv \frac{1}{2} \sigma_{ik} \varepsilon_{ik} = \frac{1}{2} c_{iklm} \varepsilon_{ik} \varepsilon_{lm}. \quad (3.9)$$

From a computational point of view, this expression is fairly suitable, as it allows the elastic constants to be easily extracted from total-energy calculations for an appropriately deformed bulk unit cell. The quadratic form in Eq. (3.9) may contain, however, a considerable number of terms, *i.e.* elastic constants, especially for crystals belonging to lower symmetry classes. On the other hand only *two* independent *scalar* constants completely characterize the elastic properties of an *isotropic* material: *e.g.*, the Poisson's ratio ν and Young's modulus Y , or the bulk and the shear moduli, B and G , respectively. Consider, for example, the deformation of an elastic bar under the action of a force p per unit area of its cross-section applied along its axis ($x_3 \parallel z$, $x_{1,2} \parallel x, y$) [89, 90]. Then $1/Y$ is the ratio of the relative stretching of the bar ε_{zz} to the applied loading p ; the ratio of the lateral shrinkage to the longitudinal elongation of the bar is Poisson's ratio ν , and the relative change of the volume of the bar is characterized by $1/B$ (compressibility), *i.e.*

$$\varepsilon_{zz} = \frac{1}{Y} p, \quad \varepsilon_{xx} = -\nu \varepsilon_{zz}, \quad \text{Tr } \boldsymbol{\varepsilon} = -\frac{1}{B} p. \quad (3.10)$$

The notions introduced in Eq. (3.10) can be generalized for anisotropic bodies, as real crystals are, and ν , Y etc. have to be considered as functions of the crystallographic direction \mathbf{n} with certain Miller indices $[hkl] \parallel \mathbf{n}$: $\nu = \nu(\mathbf{n})$, $Y = Y(\mathbf{n})$ etc. In the next section, this is demonstrated for bulk GaAs and InAs.

With the above remarks we can proceed to the issue of the mechanical equilibrium of a semi-infinite elastic continuum. One can think, for instance, of the (001) surface of a GaAs substrate. When the InAs islands form in heteroepitaxy, they can be considered as the “loading” that creates forces with certain distribution $\mathbf{P} = \mathbf{P}(\mathbf{r}_{\parallel})$, \mathbf{r}_{\parallel} being the surface coordinate, under the action of which the substrate gets elastically deformed. The objective is therefore to work out the resulting displacement field $\mathbf{u}(\mathbf{r})$ in the substrate, which in principle allows us to obtain the “elastic” parts of the thermodynamic quantities. From a mathematical point of view, the problem reduces to finding the surface elastic Green's tensor $\boldsymbol{\chi}$, which determines the response of the medium to the applied loading (assuming that the z axis is along the surface normal),

$$u_i(\mathbf{r}) = \int \chi_{ik}(\mathbf{r}_{\parallel} - \mathbf{r}'_{\parallel}, z) P_k(\mathbf{r}'_{\parallel}) d\mathbf{r}'_{\parallel}. \quad (3.11)$$

Solving this problem is a rather formidable task, and we shall provide only the final results for the isotropic case to be used in the further discussion. If a force \mathbf{F} is applied to a point \mathbf{r}_{\parallel}^0 on the free surface, one can formally take its distribution to be $\mathbf{P}(\mathbf{r}_{\parallel}) = \mathbf{F} \delta(\mathbf{r}_{\parallel} - \mathbf{r}_{\parallel}^0)$. We may further assume \mathbf{r}_{\parallel}^0 to be the coordinate origin, and the components of the displacement field at the surface ($z = 0$) are then given by [89]:

$$u_x = \frac{1 + \nu}{2\pi Y} \frac{1}{r} \left\{ -\frac{(1 - 2\nu)x}{r} F_z + 2(1 - \nu)F_x + \frac{2\nu x}{r^2} (xF_x + yF_y) \right\} \quad (3.12)$$

$$u_y = \frac{1 + \nu}{2\pi Y} \frac{1}{r} \left\{ -\frac{(1 - 2\nu)y}{r} F_z + 2(1 - \nu)F_y + \frac{2\nu y}{r^2} (xF_x + yF_y) \right\} \quad (3.13)$$

$$u_z = \frac{1 + \nu}{2\pi Y} \frac{1}{r} \left\{ 2(1 - \nu)F_z + \frac{1 - 2\nu}{r} (xF_x + yF_y) \right\}, \quad (3.14)$$

where $r = \|\mathbf{r}_{\parallel}\| = \sqrt{x^2 + y^2}$, which implicitly define the surface Green's tensor $\chi_{ik}(\mathbf{r}_{\parallel}, 0)$. Using the latter from Eq. (3.11), one can find the solution to the problem for an arbitrary force distribution $\mathbf{P}(x, y)$. In Sec. 3.4, we shall apply the above prescriptions to the particular case of an isolated long flat island.

3.2 Elastic properties of bulk III-V semiconductors: GaAs, InAs

In this section, we describe how to employ DFT calculations to predict the elastic constants, using the zincblende semiconductors GaAs and InAs as an example. These III-V compounds have a face-centered Bravais lattice, space group $F\bar{4}3m$, and provide the simplest example of a crystal as an anisotropic body, from the viewpoint of Eq. (3.9). Indeed, their crystal symmetry reduces the number of different c_{iklm} components from 21 to only 3:

$$c_{1111} \rightarrow c_{11}, \quad c_{1122} \rightarrow c_{12}, \quad c_{1212} \rightarrow c_{44}, \quad (3.15)$$

where we have used the contracted Voigt notations in the right-hand sides. With the help of Eqs. (3.7) and (3.15), the elastic energy density F , Eq. (3.9), takes the form

$$F(\varepsilon) = \frac{1}{2}c_{11}\varepsilon_{ii}^2 + c_{12}(\varepsilon_{xx}\varepsilon_{yy} + \varepsilon_{xx}\varepsilon_{zz} + \varepsilon_{yy}\varepsilon_{zz}) + 2c_{44}(\varepsilon_{xy}^2 + \varepsilon_{xz}^2 + \varepsilon_{yz}^2). \quad (3.16)$$

The computational strategy dictated by the above functional dependence relies on the simple observation that one may nullify some of the terms in Eq. (3.16) by properly straining the unit cell used to represent the bulk material. If, for instance, a hydrostatic pressure p is simulated, changing the equilibrium bulk lattice constant $a_0 \rightarrow a = a_0 + \delta a$, then both the strain and stress tensor are constant, and $\alpha = a/a_0$ in Eq. (3.5). Inserting $\varepsilon_{ik} = (a/a_0 - 1)\delta_{ik} = (\delta a/a_0)\delta_{ik} \equiv \varepsilon\delta_{ik}$ in Eq. (3.16) gives the well known result for isotropic and cubic media under hydrostatic stress $F = \frac{3}{2}(c_{11} + 2c_{12})\varepsilon^2$. On the other hand, by a uniaxial deformation, say, along any of the C_4 axes of the cubic system, we can directly get c_{11} from $F = c_{11}\varepsilon^2/2$.

When performing the DFT calculations with the `phi98md` program one has to pay attention to a few technical points: (i) The deformations realized in the actual calculations should not drive the system out of the linear elastic regime where Eq. (3.16) is no longer applicable. (ii) Secondly, one needs to handle in this case a plane-wave basis set whose quality changes because of the change in the volume of the supercell used. For GaAs and InAs, especially for calculations employing $E_{\infty} \lesssim 10$ Ry, corrections to the total energy, *e.g.*, using the scaling hypothesis (cf. Appendix B and Appendix C) are required in order for a good fit of $F(\varepsilon)$ to be achieved. (iii) In principle, the calculation of the total energy for a strained material should proceed via relaxation of the atomic positions, because of the concomitant bonds bending/stretching. In the case of the zincblende structure, however, internal atomic displacements for any diagonal strain $\varepsilon\delta_{ik}$ are not allowed by symmetry, so one can perform relaxation of the electronic component only. For shear strains (ε_{ik} with $i \neq k$ and $\varepsilon_{ii} = 0$) along the $[111]$ direction, used when calculating c_{44} , the $[111]$ bond is no longer equivalent to the other three bonds, and symmetry does allow internal displacements of the anion and cation sublattices [91].

Taking into account the above points, we have carried out a set of calculations to determine c_{11} , c_{12} , Poisson's ratio ν and the bulk and Young's moduli B , Y of GaAs and InAs. Practical aspects of the calculations are described in Appendix C, and the results are collected in Table 3.1. Note, however, that from c_{11} and c_{12} only the isotropic parts of ν and Y are accessible, which are, in effect, the quantities tabulated in the reference literature [92]. Complete expressions for ν and Y can be derived from Eq. (3.16) (see, for example, § 10, problem 3 in Ref. [89], and

Table 3.1: Calculated values of the lattice constant a_0 and elastic parameters for bulk GaAs and InAs within LDA and PBE-GGA using four different cutoff energies. Young’s modulus and the bulk modulus, Y , B and the stiffnesses c_{11} , c_{12} are given in 10^{11} dyn cm $^{-2}$. Experimental values are taken from Ref. [92].

	E_{∞} [Ry]	a_0 [Å]		c_{11}		c_{12}		ν		Y		B	
		LDA	GGA	LDA	GGA	LDA	GGA	LDA	GGA	LDA	GGA	LDA	GGA
GaAs	8	5.53	5.77	12.15	9.16	5.68	3.82	0.32	0.29	8.46	7.06	7.47	5.42
	10	5.54	5.78	12.34	8.96	5.36	3.67	0.30	0.29	9.22	6.85	7.19	5.13
	16	5.54	5.77	12.46	9.30	5.51	3.69	0.31	0.28	8.92	7.34	7.44	5.33
	32	5.53	5.77	12.51	9.44	5.37	3.79	0.30	0.29	9.30	7.15	7.43	5.36
Experiment		5.65		12.11		5.48		0.31		8.77		7.69	
InAs	8	6.02	6.32	8.13	5.87	4.29	3.10	0.35	0.35	5.01	4.45	5.26	3.80
	10	6.04	6.33	7.92	6.05	4.24	3.24	0.35	0.35	4.92	3.76	5.22	4.04
	16	6.02	6.30	8.51	6.44	4.41	3.33	0.34	0.34	5.55	4.19	5.52	4.18
	32	6.01	6.29	8.51	6.06	4.54	3.10	0.35	0.34	5.28	3.92	5.55	4.10
Experiment		6.06		8.33		4.53		0.35		5.22		5.80	

Ref. [90]) and read:

$$Y^{-1}(\mathbf{n}) = \frac{c_{11} + c_{12}}{(c_{11} + 2c_{12})(c_{11} - c_{12})} + \left(\frac{1}{c_{44}} - \frac{2}{c_{11} - c_{12}} \right) (n_x^2 n_y^2 + n_x^2 n_z^2 + n_y^2 n_z^2), \quad (3.17)$$

$$\nu(\mathbf{n}) = \frac{1}{2} \left[1 - \frac{Y(\mathbf{n})}{c_{11} + 2c_{12}} \right]. \quad (3.18)$$

The two index surfaces, $Y(\mathbf{n})$ and $\nu(\mathbf{n})$, are rendered in Figure 3.1 using the experimental elastic constants for GaAs and InAs (cf. the “Experiment” rows in Table 3.1). Both quantities reach their extremal values along the (elastically soft) $\langle 100 \rangle$ and (elastically hard) $\langle 111 \rangle$ directions of the cubic crystal, *e.g.*,

$$\nu(\langle 100 \rangle) = \frac{c_{12}}{c_{11} + c_{12}}, \quad Y(\langle 100 \rangle) = \frac{c_{11} + c_{12}}{(c_{11} + 2c_{12})(c_{11} - c_{12})}. \quad (3.19)$$

Thus, Eq. (3.19) was used to calculate ν and Y in Table 3.1. It is worth noting that both LDA and GGA give a rather good representation of Poisson’s ratio for GaAs and InAs, while systematic (with respect to E_{∞}) under- or overestimation is observed for Young’s modulus and the bulk modulus Y , B . The LDA calculated values are generally closer to the experimentally determined ones though, and they also agree fairly well with Nielsen and Martin’s results for GaAs [91] based on the microscopic stress theorem [93]. The (dimensional) elastic moduli within the GGA (in our case employing the PBE exchange-correlation functional) turn out to be underestimated by $\lesssim 30$ %. This trend has been documented [75,94,95] for the bulk modulus of GaAs and some elemental semiconductors (Si, Ge) as well, both in pseudopotential and all-electron studies [75,94,95]. It can be, in fact, anticipated from the trend in the equilibrium lattice constant a_0 , which is typically found to be larger in GGA (*e.g.*, here by 2 % for GaAs and about 4 % for InAs, see Table 3.1).

A way to partly correct the errors from the “pseudoization” sometimes lies in taking into account the nonlinear core-valence exchange and correlation [75] (Sec. 2.3.2). We have compared the lattice constant of InAs calculated with an In pseudopotential incorporating a partial core

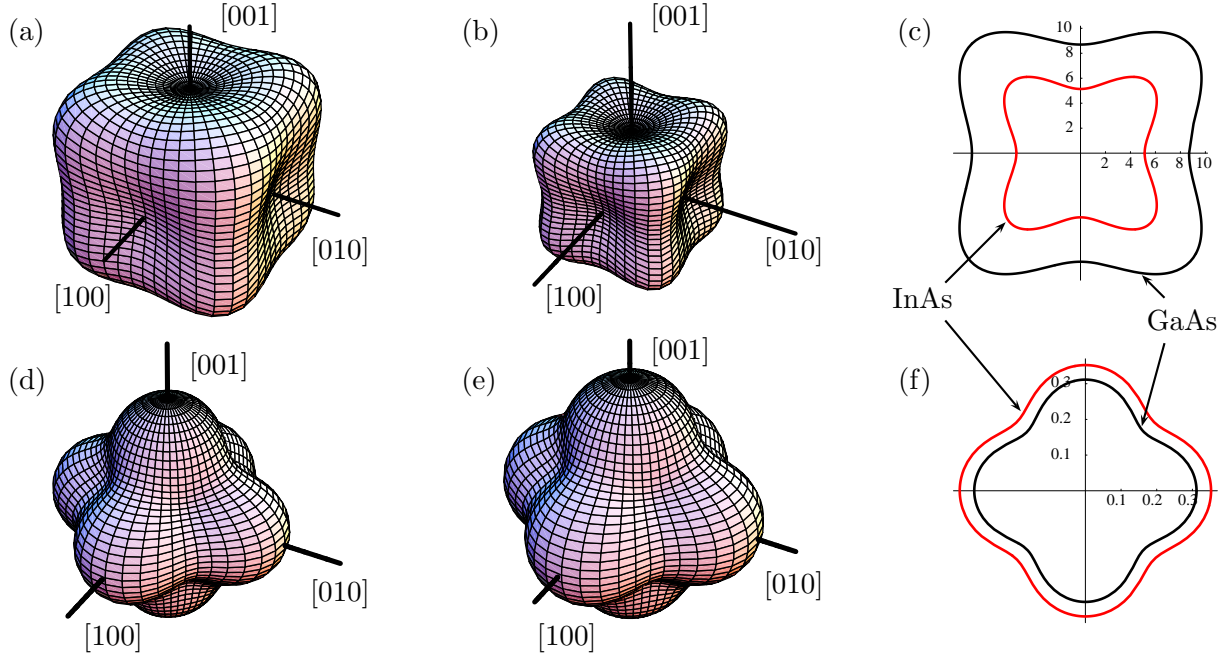


Figure 3.1: (a), (b) Young's modulus $Y(\mathbf{n})$ as a function of crystallographic direction \mathbf{n} for GaAs and InAs, respectively, with equatorial cut given in (c); Similarly for Poisson's ratio $\nu(\mathbf{n})$: (d) GaAs; (e) InAs and the corresponding equatorial cut (f).

density $\tilde{n}_0^{\text{core}}$ with a cutoff radius $r_{\text{nl}}^{\infty} = 1.4$ Bohr to the values in Table 3.1. For the reference cutoff energies E_{∞} , a_0 was still found to be too small by 2–3 % within the LDA. The GGA figures did not improve either, although a_0 is only ~ 0.1 % larger than the values in Table 3.1 for $E_{\infty} = 16$ and 32 Ry. Note that, in principle, the quite localized partial core density requires higher E_{∞} , thus the bulk calculations converge poorly for the lower energy cutoffs, and are generally more expensive computationally. As taking account of the nonlinear core-valence exchange and correlation in the In pseudopotential did not produce an improvement in the elastic properties, we inferred that the error in the latter stems from the exchange-correlation functional itself. It should be noted also that with the calculated equilibrium bulk lattice constants of GaAs and InAs, Table 3.1, the intrinsic lattice misfit of an InAs/GaAs heteroepitaxial system, according to Eq. (1.1), would be $\varepsilon_0 \approx 8.5$ %, which is somewhat larger than the experimental value of ≈ 7 %.

3.3 Surface elasticity: thermodynamic aspects

3.3.1 Surface energy and surface stress

Let us consider now the passage from an infinite to a semi-infinite elastic continuum having a free surface, or in general, to a heterogeneous system incorporating different phases and the interfaces between them. Besides the volume V of the total system, a new parameter characterizing its state is the area A of the interfaces. The corresponding “generalized force” γ is called the surface energy and the total internal energy takes the form [96]

$$E = TS - pV + \mu N + \gamma A, \quad (3.20)$$

where p is the pressure, and S , μ , N are, respectively, the entropy, chemical potential and number of particles in the system. Furthermore, in analogy with bulk elasticity considerations, one can define the *surface strain* and *surface stress* tensors $\varepsilon_{\alpha\beta}$ and $\tau_{\alpha\beta}$, respectively. Assume the system is now perturbed so that the area A changes by a small amount dA . The differential change in the energy dE then takes the form, similar to Eq. (3.8),

$$dE = TdS - pdV + \mu dN + A\tau_{\alpha\beta}d\varepsilon_{\alpha\beta}. \quad (3.21)$$

Taking the full differential of Eq. (3.20) and comparing with the last equation we get the Gibbs-Duhem relation for the total system [96],

$$Ad\gamma + SdT - Vdp + Nd\mu + A(\gamma\delta_{\alpha\beta} - \tau_{\alpha\beta})d\varepsilon_{\alpha\beta} = 0, \quad (3.22)$$

where we have used the 2D analog to Eq. (3.4), $dA/A = \text{Tr}(d\boldsymbol{\varepsilon}) = \delta_{\alpha\beta}d\varepsilon_{\alpha\beta}$. In equilibrium one can think of a crystal, its surface, and vapor as a system consisting of three distinct phases: two bulk phases and an “interphase”, the latter, actually, being characterized by certain set of extensive quantities, *e.g.*, $S^{(s)}$, $V^{(s)}$, $N^{(s)}$. On the other hand, for each of the two bulk phases one has $SdT - Vdp + Nd\mu = 0$, which allows us to “extract” the surface analog to Eq. (3.22), known as the Gibbs adsorption equation,

$$Ad\gamma + S^{(s)}dT - V^{(s)}dp + N^{(s)}d\mu + A(\gamma\delta_{\alpha\beta} - \tau_{\alpha\beta})d\varepsilon_{\alpha\beta} = 0. \quad (3.23)$$

In many respects, the guidelines for establishing surface thermodynamics, were laid by J. Willard Gibbs in his masterpiece “*On the Equilibrium of Heterogeneous Substances*”, which appeared in 1877 [97]. He introduced the notion of a *dividing surface* between two phases and showed that a particular fraction of the extensive quantities had to be ascribed to that geometric model object in order that the equivalence to the real system be retained. According to the Gibbs approach $V^{(s)} \rightarrow 0$, and we arrive at the fundamental result

$$d\gamma = -s^{(s)}dT + (\tau_{\alpha\beta} - \gamma\delta_{\alpha\beta})d\varepsilon_{\alpha\beta}, \quad s^{(s)} = S^{(s)}/A, \quad (3.24)$$

which tells us that the surface energy and surface stress obey the relation

$$\tau_{\alpha\beta} = \gamma\delta_{\alpha\beta} + \left(\frac{\partial\gamma}{\partial\varepsilon_{\alpha\beta}} \right)_T. \quad (3.25)$$

This was established by Shuttleworth in 1950 [98], and has brought out clearly the subtle difference between γ and τ in the case of solids. For liquids, because of the absence of long-range order and the mobility of its molecules, the surface energy does not change upon deformation, which nullifies the derivative in Eq. (3.25) and $\tau_{\alpha\beta} = \gamma\delta_{\alpha\beta}$. For a crystal, however, this is impossible and τ cannot be identified with γ . A comprehensive discussion of the relation between surface energy and surface stress was given, *e.g.*, by Herring [99] as well as in the monograph by Defay, Prigogine and Bellemans [100].

The knowledge of γ and τ is of particular importance, as it is well understood that the equilibrium shape of a crystal for a given volume is determined by the minimum of its surface free energy $\int \gamma dA$ [101, 102]. On the other hand, the interplay between γ and τ is a driving force towards surface reconstructions [103], and has been also shown to have influence on the equilibrium shape of QDs in InAs/GaAs lattice-mismatched heteroepitaxy [104].

The computational strategy for obtaining γ is usually based upon the original definition [97, 99, 100],

$$\gamma A = F^{(s)} - \sum_{i=1}^c \mu_i N_i^{(s)}. \quad (3.26)$$

In this expression, $N_i^{(s)}/A$ is the surface density of the i th component of the system ($i = 1, 2, \dots, c$), and $F^{(s)} = E^{(s)} - TS^{(s)}$ is the Helmholtz surface free energy. The chemical potential μ_i of the i th component is defined in both bulk phases,

$$\mu_i = \left(\frac{\partial F^{(v)}}{\partial N_i} \right)_{T, V, N_{k \neq i}} = \left(\frac{\partial G^{(v)}}{\partial N_i} \right)_{T, \sigma, N_{k \neq i}}, \quad v = \begin{cases} \text{bulk crystal} \\ \text{vapor} \end{cases}, \quad (3.27)$$

where $F^{(v)}$ and $G^{(v)}$ are, respectively, the Helmholtz and Gibbs free energies of the bulk phases, where in the second case the bulk stress should be also kept constant when taking the partial derivative (indicated by the subscript “ σ ”).

Thus, in practice [105, 106], for a GaAs surface ($c = 2$) at zero temperature and pressure, Eq. (3.26) takes the form

$$\gamma A = E^{(s)} - \mu_{\text{Ga}} N_{\text{Ga}} - \mu_{\text{As}} N_{\text{As}}. \quad (3.28)$$

In thermodynamic equilibrium, however,

$$\mu_{\text{Ga}} + \mu_{\text{As}} = \mu_{\text{GaAs}} = \mu_{\text{Ga(bulk)}} + \mu_{\text{As(bulk)}} + \Delta H_{\text{f}}^{\text{GaAs}}, \quad (3.29)$$

where $\Delta H_{\text{f}}^{\text{GaAs}}$ is the heat of formation of GaAs at $p, T = 0$. This equation can be used to reduce the number of variables, *e.g.*, by expressing μ_{Ga} via μ_{As} , and one obtains the expression to calculate γ ,

$$\gamma A = E - \mu_{\text{GaAs}} N_{\text{Ga}} - \mu_{\text{As}} \underbrace{(N_{\text{As}} - N_{\text{Ga}})}_{\Delta N}, \quad (3.30)$$

where E is just the total energy of the slab representing the GaAs surface, and ΔN is the surface stoichiometry. From Eq. (3.30) it follows that for a nonstoichiometric GaAs surface, $\Delta N \neq 0$, the surface energy displays dependence on μ_{As} . The range of physically allowed variation for μ_{As} is set up by $\Delta H_{\text{f}}^{\text{GaAs}}$, and its upper limit is the chemical potential of the bulk crystal phase of As, $\mu_{\text{As(bulk)}}$. Thus, introducing $\mu'_{\text{As}} = \mu_{\text{As}} - \mu_{\text{As(bulk)}}$, we can write

$$-|\Delta H_{\text{f}}^{\text{GaAs}}| \leq \mu'_{\text{As}} \leq 0, \quad \mu'_{\text{As}} = \mu_{\text{As}} - \mu_{\text{As(bulk)}}. \quad (3.31)$$

Details on the cohesive properties of the elemental and compound materials involved in the present work are given in Appendix A. In order to relate Eqs. (3.30)–(3.31) to the real experimental conditions, where p and T are essentially nonzero quantities, one needs to consider the corresponding temperature and pressure dependence of the chemical potentials. It can be shown [5], however, that for the experimentally relevant range of p and T , $|\delta(\Delta H_{\text{f}}^{\text{III-V}}(p, T))| \lesssim 0.05$ eV, which is negligible compared to $\Delta H_{\text{f}}^{\text{III-V}}(0, 0)$, and will be disregarded in the following discussion.

As regards the surface stress tensor $\tau_{\alpha\beta}$, one can calculate its components on the basis of the microscopic stress theorem due to Nielsen and Martin [93] or, in a more direct way, using Eq. (3.25). Two points are in order now: (i) the latter equation is derived for an *unstrained* surface, $\varepsilon_{\alpha\beta} = 0$, and (ii) one needs to know the slope $(\partial\gamma/\partial\varepsilon_{\alpha\beta})_{\varepsilon=0}$, which obviously requires the knowledge of $\gamma = \gamma(\varepsilon)$. For small strains, γ can be represented as an expansion [19, 103],

$$\gamma(\varepsilon) = \gamma_0 + \left(\frac{\partial\gamma}{\partial\varepsilon_{\alpha\beta}} \right)_{\varepsilon=0} \varepsilon_{\alpha\beta} + \frac{1}{2} \left(\frac{\partial^2\gamma}{\partial\varepsilon_{\alpha\beta}\partial\varepsilon_{\mu\nu}} \right)_{\varepsilon=0} \varepsilon_{\alpha\beta}\varepsilon_{\mu\nu}, \quad (3.32)$$

where $\gamma_0 = \gamma(\varepsilon = 0)$ is the free energy of the unstrained surface. From (3.32) one can formally make a “linear-elastic extension” of Eq. (3.25),

$$\tau_{\alpha\beta}(\varepsilon) = \underbrace{\gamma_0 \delta_{\alpha\beta} + \left(\frac{\partial\gamma}{\partial\varepsilon_{\alpha\beta}} \right)_{\varepsilon=0}}_{\tau_0} + S_{\alpha\beta\mu\nu} \varepsilon_{\mu\nu}, \quad (3.33)$$

where $S_{\alpha\beta\mu\nu} = \partial^2\gamma/\partial\varepsilon_{\alpha\beta}\partial\varepsilon_{\mu\nu}$ is the tensor of “surface excess elastic constants” [103].

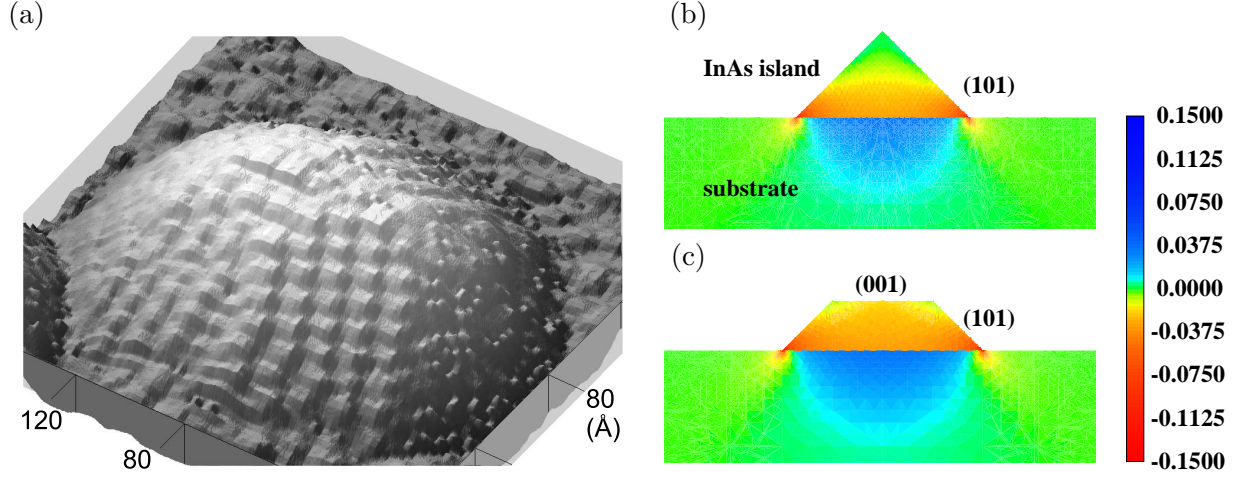


Figure 3.2: (a) Atomic-resolution STM image of an InAs island grown on GaAs(001)-c(4×4) by MBE. Four of the bounding facets are found to be the high-index $\{137\}$ planes [108] (image courtesy of Dr. J. Márquez and Dr. L. Geelhaar, FHI). The average aspect (height/base) ratio of these QDs was only $\simeq 1/6$; (color) $\text{Tr } \epsilon$ for a pyramidal (b) and truncated pyramidal island (c) ((010) cross sections), calculated by Moll *et al.* [104] within the finite-element approach (reproduced with the kind permission of the authors, ©1998 APS).

3.3.2 Strain distribution and shape of InAs QDs

Since we are going to be mainly concerned with the effect of strain on the adatom diffusion in the process of QD formation, it is of particular interest for us to know details about the strain field in the substrate $\epsilon_{\alpha\beta}(\mathbf{r}_{\parallel})$ induced by the growing island. On the other hand, the shape of the island determines the force density distribution $\mathbf{P}(\mathbf{r}_{\parallel})$ which, in turn, is needed to calculate the resulting displacement field in the substrate.

The *equilibrium* shape of InAs islands on the GaAs(001) surface has recently become available from first-principles calculations reported in a sequence of publications, Refs. [6, 104, 106, 107] and can be described as “hills bounded by $\{110\}$, $\{111\}$, and $\{\bar{1}\bar{1}\bar{1}\}$ facets and a (001) surface on top” [106]. Detailed analysis of the island energetics has also revealed that islands of larger volume display a bigger height-to-base (aspect) ratio [104, 107], which implies that the island shape changes continuously with volume. The experimentally observed island shapes, however, are rather diverse, including pyramids and “plano-convex” lenses, as well as shapes bound by high-index facets [108, 109] with small aspect (height-to-base) ratios; such an island is shown in Figure 3.2 (a). These shapes are clearly different from the theoretically determined equilibrium ones, and this has been considered as indication that kinetics may also play role. This is still a highly debated issue [19]. Essentially planar shapes were also reported in the cross-sectional STM studies of stacked InAs QDs [110, 111], being discussed also in the context of heteroepitaxy of the Ge/Si(001) materials system [112].

Analysis of the strain distribution for a free-standing InAs island on GaAs substrate, employing a finite-element method, was reported by Moll *et al.* [104], Figure 3.2 (b,c). They have considered initially a pyramidal island bound by $\{101\}$ facets. In terms of $\text{Tr } \epsilon = \epsilon_{ii}$ the substrate around the island edges was found to be compressed up to $\simeq 4\%$, while it was under tensile strain beneath the island. The top of the island, on the other hand, is almost completely relaxed.

In the growth of 3D stacked arrays (multisheet arrays) of QDs, the islands are further buried and thus act as “stressors” for the GaAs capping layer. The calculation of the strain field in the

latter usually relies on an approximation scheme where the QDs are considered as elastic point defects in an isotropic medium. In such a case one can make use of the result by Maradudin and Wallis [113], and the hydrostatic part of the surface strain due to an island at depth L and $\mathbf{r}_{\parallel}^0 = \mathbf{0}$ is given by

$$\varepsilon_{ii}(x, y, z = 0) = -\frac{C}{(x^2 + y^2 + L^2)^{3/2}} \left(1 - \frac{3L^2}{x^2 + y^2 + L^2} \right). \quad (3.34)$$

C in this expression is a material constant $\propto \varepsilon_0, V_{\text{island}}$, and $C > 0$ for InAs/GaAs as well for Ge/Si, *i.e.* when the matrix has a smaller lattice constant. One can easily realize that (3.34) has an extremum just above the island, $\mathbf{r}_{\parallel} \equiv (x, y) = \mathbf{0}$, $\varepsilon_{ii}(0) = 2C/L^3$ which implies *maximum* tensile strain. Consequences of such a strain profile for In adatom diffusion on the GaAs capping layer have been discussed, for example, by Xie *et al.* [114, 115], Tersoff *et al.* [15] considered its effect on the island nucleation process for Ge/Si(001), and a semiquantitative kinetic model for InAs/GaAs was proposed by Ledentsov *et al.* [116].

Thus in different stages of growth of a nanostructure, different regimes of strain may come into focus. The strain field at a step or island edge varies slowly on the scale of the substrate lattice constant. We can thus treat the inhomogeneously strained surface by performing DFT calculations with a locally adjusted lattice parameter. Further details will be given in Chapter 6.

3.4 The “flat island” approximation

Let us illustrate now the use of Eqs. (3.12)–(3.14) on the example of a flat island, Figure 3.3. This approximation to the real shape of a free-standing island has been considered in detail by Tersoff and Tromp [112] in the context of quasi-1D quantum wires, self-assembly in Ge/Si(001), and Ag/Si(001) lattice-mismatched heteroepitaxy. The typical geometry of a flat (or planar) island is sketched in Figure 3.3.

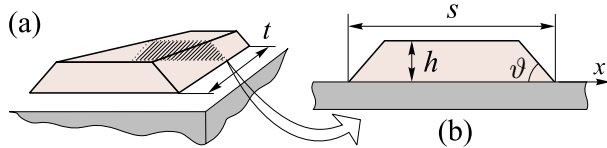


Figure 3.3: (a) Schematic view of a flat island of rectangular shape. The geometry of the island cross-section is given in panel (b). The width and height are denoted, respectively, by s and h , and the tilt angle of the side facets is ϑ .

As we shall see now, this approximation allows a simple analytic expression to be derived for the strain field induced in the substrate by such an island. The “flatness” of the island implies that the lattice constant of material a and the characteristic dimensions of the island are related via the inequality $a \ll h \ll s, t$. We make, however, another simplifying supposition, that the island is long enough and standing on an isotropic substrate, so that variations in the strain field along the extended island edges are negligible away from the corners. Thus we may formally write $s \ll t$ and concentrate on the effective 1D problem as depicted in Figure 3.3 (b). Note that such an assumption has a model character and is particularly valuable when putting the further discussion in Chapter 7 in a more general framework.

As a first step, let us employ Eqs. (3.12)–(3.14) in order to determine the strain field due to a continuous line of point force sources, having length L , *i.e.* a force density \mathbf{P} with distribution

$$\mathbf{P}(\mathbf{r}_{\parallel}) = \mathbf{F}\delta(x)[\theta(y) - \theta(y - L)], \quad \text{with } \mathbf{F} = (F_x, 0, 0), \quad (3.35)$$

schematically shown as a solid line in Figure 3.4 (a), where formally the finite length of the line is represented as a difference of two step-like functions $\theta(y)$. The solution to this problem can be viewed as a Green’s function in a more restricted sense, that would allow us to find the

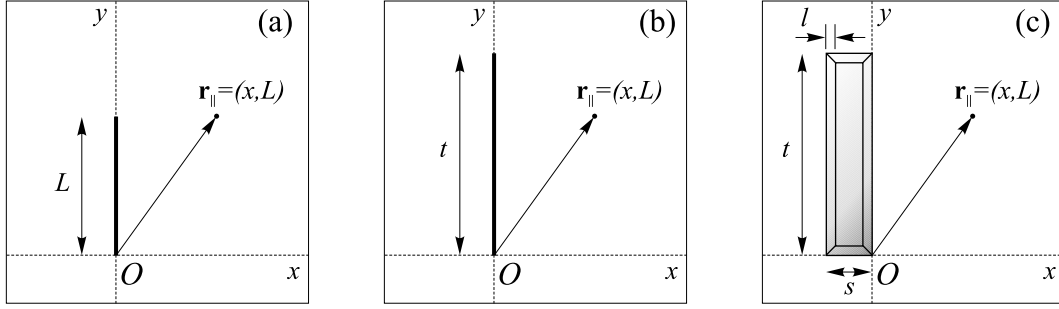


Figure 3.4: Towards the derivation of the strain field of a long flat island.

strain field of a force with an arbitrary distribution in x direction by solving integral of the type (3.11). Note, however, that by convention Eqs. (3.12)–(3.14) give the displacement field at point $\mathbf{r}_{\parallel} = (x > 0, y > 0)$, therefore we locate the “line of forces” in the way shown in Figure 3.4 (a) (cf. also Eq. (3.35)), and consider the strain field $\tilde{\varepsilon}_{xx}$ along x at the point (x, L) . It can be found as a superposition of the fields $\varepsilon_{xx}(x, y)$ due to all “point forces” along the line, *i.e.*

$$\tilde{\varepsilon}_{xx}(x; L) = \int_0^L \varepsilon_{xx}(x, y) dy. \quad (3.36)$$

The integrand can be easily worked out by differentiating Eq. (3.12) with respect to x , $\varepsilon_{xx} = \partial u_x / \partial x$. In the evaluation of Eq. (3.36) one has to calculate integrals of the type

$$I_n(x, l) = \int_0^l \frac{dy}{r^n} = \int_0^l \frac{dy}{(x^2 + y^2)^{n/2}}.$$

The corresponding indefinite integrals $I_n(x)$ are straightforward to solve by differentiation with respect to a parameter. Taking the x coordinate as the parameter, one finds the recurrence relation,

$$\frac{\partial I_n(x)}{\partial x} = -n x I_{n+2}(x), \quad I_0 = l, \quad I_1(x) = \ln |y + \sqrt{x^2 + y^2}|, \quad I_n(x, l) = I_n(x)|_0^l,$$

and Eq. (3.36) takes the final form

$$\tilde{\varepsilon}_{xx}(x; L) = \frac{1 + \nu}{\pi Y} F_x [(3\nu - 1)x I_3(x, L) - 3\nu x^3 I_5(x, L)]. \quad (3.37)$$

On the basis of this result, one can consider the general situation, shown in Figure 3.4 (b), where the point for which the strain is to be calculated does not have a special position along the y axis, as in Figure 3.4 (a). One can therefore partition the length t into L ($L < t$) and $t - L$, and apply the previous considerations to both fragments, as a result redefining $\tilde{\varepsilon}_{xx}(x; L)$ as

$$\tilde{\varepsilon}_{xx}(x; L, t) := \tilde{\varepsilon}_{xx}(x; L) + \tilde{\varepsilon}_{xx}(x; t - L). \quad (3.38)$$

The meaning of $\tilde{\varepsilon}_{xx}(x; L, t)$ is simple: it plays the role of a Green’s function with respect to the xx strain component. Thus, for an arbitrary force density distribution in the x direction $P_x(x)$, say in the interval $x \in [-s, 0]$, we can work out the strain field in analogy to Eq. (3.11),

$$\varepsilon_{xx}(x; L, t) = \int_{-s}^0 \tilde{\varepsilon}_{xx}(x - x'; L, t) P_x(x') dx', \quad (x' < x). \quad (3.39)$$

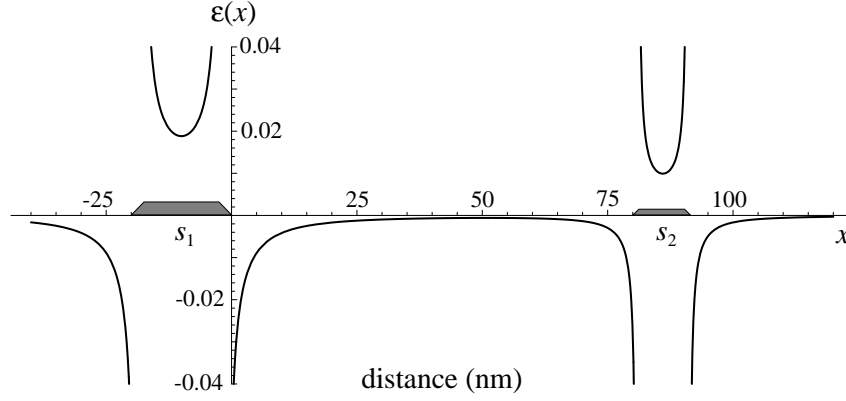


Figure 3.5: Strain field $\varepsilon(x)$ in the substrate, according to Eq. (3.41), for two flat islands of width $s_1 = 20$ nm and $s_2 = 12$ nm, whose edges are separated by distance $L = 80$ nm. The island/substrate system is assumed to be InAs/GaAs, and $\vartheta = 45^\circ$.

In particular, this equation is immediately applicable to the case of a planar island, as shown in Figure 3.4 (c). If we consider points close to the island edge $x = 0$, one can formally neglect the island corners. This corresponds to the short-range asymptotic regime $x/t \ll 1$, as well as to $x/L \ll 1$. The behavior of the integrals in Eq. (3.37) is then very simple,

$$I_3(x, L \gg x) \simeq \frac{1}{x^2}, \quad \text{and} \quad I_5(x, L \gg x) \simeq \frac{2}{3} \frac{1}{x^4}.$$

and from Eqs. (3.37)–(3.39) we obtain finally

$$\varepsilon(x) \equiv \varepsilon_{xx}(x \ll t) = -2 \frac{(1+\nu)(1-\nu)}{\pi Y} \int_{-s}^0 \frac{P_x(x')}{|x-x'|} dx', \quad (x \ll t). \quad (3.40)$$

Let us now estimate $P_x(x)$ for the assumed island shape, Figure 3.3 (b). Following Tersoff and Tromp [112], and according to Eq. (3.6), one can write $P_x = \sigma dh(x)/dx$, where σ is the xx component of the stress tensor of the island’s material uniformly strained to match the lattice constant of the substrate, and $h(x)$ is the “height function” of the island cross-section. From Figure 3.4 (c) it is obvious that P_x is non-vanishing only within the projections of the (long) side facets, $l = h \cot \vartheta$, *i.e.* for $x \in (-s, -s + h \cot \vartheta) \cup (-h \cot \vartheta, 0)$, where $h(x) = x \tan \vartheta$, and therefore the force density is a constant, $P_x = -\sigma \tan \vartheta \equiv P_0$. The integral (3.40) is thus taken over the above specified range of x and the resulting strain field reads

$$\varepsilon(x) = \frac{2(\nu^2 - 1)}{\pi Y} P_0 \ln \left| \frac{(h \cot \vartheta + x)(s - h \cot \vartheta + x)}{x(s + x)} \right|. \quad (3.41)$$

Strictly speaking, this expression diverges at the island edges, and therefore we have to exclude from consideration unphysical stripes of width a around the island edges that should be taken to be of the order of the lattice constant of the substrate material, cf. Ref. [117]. In Figure 3.5, the actual profile of $\varepsilon(x)$ is plotted for two flat islands having similar aspect ratios: $h : s = 1 : 8$ for the larger and $h : s = 1 : 10$ for the smaller one.

Chapter 4

Surface diffusion

4.1 General background

4.1.1 Diffusion PES

Surface diffusion is the ultimate process through which mass transport occurs on surfaces. It can be viewed as a particular case of diffusion in media with reduced dimensionality. The possibility for a 2D diffusive motion of adparticles (*e.g.*, atoms, molecules, small clusters, but eventually vacancies as well) is intimately related to the specifics of the adsorbate-surface interaction. The latter by itself is a complex collision problem for an atom hitting large-mass target [118]. Similarly to the discussion in Sec. 2.1, let us denote the surface (target’s) degrees of freedom \mathbf{R} , and those of the “incidon” (adatom etc.) $\mathbf{R}^{\text{ad}} = (X, Y, Z)$. The atom-surface collision mechanics is then governed by the corresponding interaction potential energy hypersurface $U(\mathbf{R}, \mathbf{R}^{\text{ad}})$. In most situations of interest, however, it turns out that the BO and adiabatic approximations are well justified for the surface, and therefore one can consider the interaction potential restricted to the spatial degrees of freedom of the adsorbate, $U(X, Y, Z)$. Thus the problem reduces to a single-particle dynamics in $U(\mathbf{R}^{\text{ad}})$.

Perpendicular to the surface, $U(Z)$ is usually represented as long-range attractive and short-range repulsive part whose superposition gives rise to a local minimum for a certain $Z = Z_0$, Figure 4.1. An atom colliding with the surface may lose enough energy so that it gets adsorbed in this minimum. $U(X, Y)$ displays qualitatively different behavior—it is an *oscillatory* (periodic) and bound quantity in the surface plane. This is schematically shown in Figure 4.1, of course, only for a single “in-plane” degree of freedom X . It is this feature of $U(X, Y)$ that makes the diffusive motion possible. In a more strict way, denoting by \mathbf{a}_1 and \mathbf{a}_2 the basis of the surface unit cell, we can write down

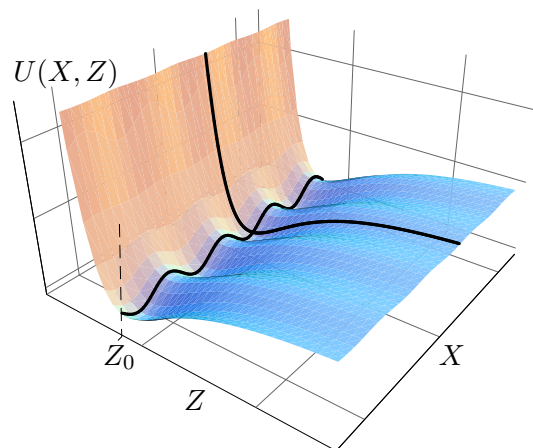


Figure 4.1: Schematic of a two-dimensional “slice” $U(X, Z)$ through the multidimensional potential energy hypersurface for the adatom-surface interaction. Z is the distance to the surface, and X is the adatom coordinate along given surface direction.

$$U(\mathbf{R}_{\parallel}^{\text{ad}} + \mathbf{t}) = U(\mathbf{R}_{\parallel}^{\text{ad}}), \quad \mathbf{R}_{\parallel}^{\text{ad}} = (X, Y), \quad (4.1)$$

where $\mathbf{t} = n\mathbf{a}_1 + m\mathbf{a}_2$ ($n, m = \text{integer}$) is arbitrary translation within the surface plane. This equation is a simple expression of the translational invariance (regularity) of the surface crystal structure. The knowledge of the latter is therefore the most important prerequisite for studying surface diffusion. Furthermore $U(X, Y)$ will “inherit” the point-group symmetry properties as determined by the *plane* Bravais lattice of the crystal surface (*e.g.*, oblique, p -rectangular, c -rectangular, square, or hexagonal), which property, as we shall see, reduces greatly the computational effort in determining $U(X, Y)$. The minima of $U(X, Y)$ will generally provide stable, or eventually metastable, adsorption sites for the adatom, and we shall denote them in the following $\mathbf{A}_i = (X_i, Y_i)$, $i = 1, 2, \dots, N_b$, with N_b being the number of such sites within a single surface unit cell.

Within the computational scheme outlined in Chapter 2, $U(X, Y)$ is defined as the minimized difference

$$U(X, Y) = \min_{\mathbf{R}' \subseteq \mathbf{R}} \min_Z E(\mathbf{R}, \mathbf{R}^{\text{ad}}) - E^{\text{slab}} - E^{\text{atom}}. \quad (4.2)$$

In this expression $E(\mathbf{R}, \mathbf{R}^{\text{ad}})$ stands for the total energy of the adatom + surface system; E^{slab} and E^{atom} are, respectively, the energies of the bare surface (modeled by a slab) and the isolated atom. Minimization is carried out with respect to the “height” of the adatom Z , and a given subset \mathbf{R}' or eventually all coordinates \mathbf{R} of the substrate atoms. This is accomplished in practice via constrained atomic relaxation, and specific details will be given in all particular cases in the following. The definition (4.2) gives, in fact, the binding energy of the adatom with lateral coordinate $\mathbf{R}_{\parallel}^{\text{ad}}$, and is usually referred to as the (diffusion) adiabatic PES (compare also with the discussion in Sec. 2.1).

4.1.2 Surface diffusion tensors

Tracer diffusion tensor

The PES, as introduced in Eq. (4.2), emerges from a ground-state formalism. At finite temperature, a realistic description of the adatom-surface system requires taking account of the adatom coupling to the phonon modes of the substrate. As a result of the latter, an adatom adsorbed at some site \mathbf{A}_i may escape from the local minimum to a neighboring site \mathbf{A}_f . The nature of such a jump motion is determined by the relation of a few time scales: the time $1/\Gamma$ an adatom “waits” before escaping the potential well, the characteristic period $1/\Gamma^{(0)}$ of the adatom oscillations in the well, and the time it takes to cross the potential barrier, τ_d . Then if $1/\Gamma, \tau_d \gg 1/\Gamma^{(0)}$, the adatom motion will be a stochastic process [4] and can be described as a 2D random walk on the regular network of sites \mathbf{A}_i [119, 120]. An example of such a network is given in Figure 4.2. Thus, a random walker at site \mathbf{A}_2 may jump to any of the \mathbf{A}_1 , \mathbf{A}_3 , and $\mathbf{A}_{3'}$ sites. We shall assign to each of these possibilities corresponding jump, or transition, *rates*, *i.e.* probability that the event occurs per unit time. If the initial site of the transition is \mathbf{A}_i and the final one is \mathbf{A}_f , then we shall denote the corresponding escape rate

$$\Gamma_{fi} \equiv \Gamma_{f \leftarrow i}. \quad (4.3)$$

In Sec. 4.3 we discuss some properties of Γ ’s and outline a method commonly employed to determine them.

Systematic description of a stochastic process requires determination of its statistical properties. The central quantity of interest is the mean square displacement $\langle |\mathbf{R}_{\parallel}^{\text{ad}}(t)|^2 \rangle$ of the adatom, which is a (finite, positive) non-vanishing quantity, and especially its long time limit, $t \rightarrow \infty$. Here $\langle \dots \rangle$ implies averaging over an equilibrium ensemble of adatoms. In terms of $\langle |\mathbf{R}_{\parallel}^{\text{ad}}(t)|^2 \rangle$ one defines in the most general case the *tracer diffusion tensor* $D_{\alpha\beta}^*$ [33] (see also Part 1 in

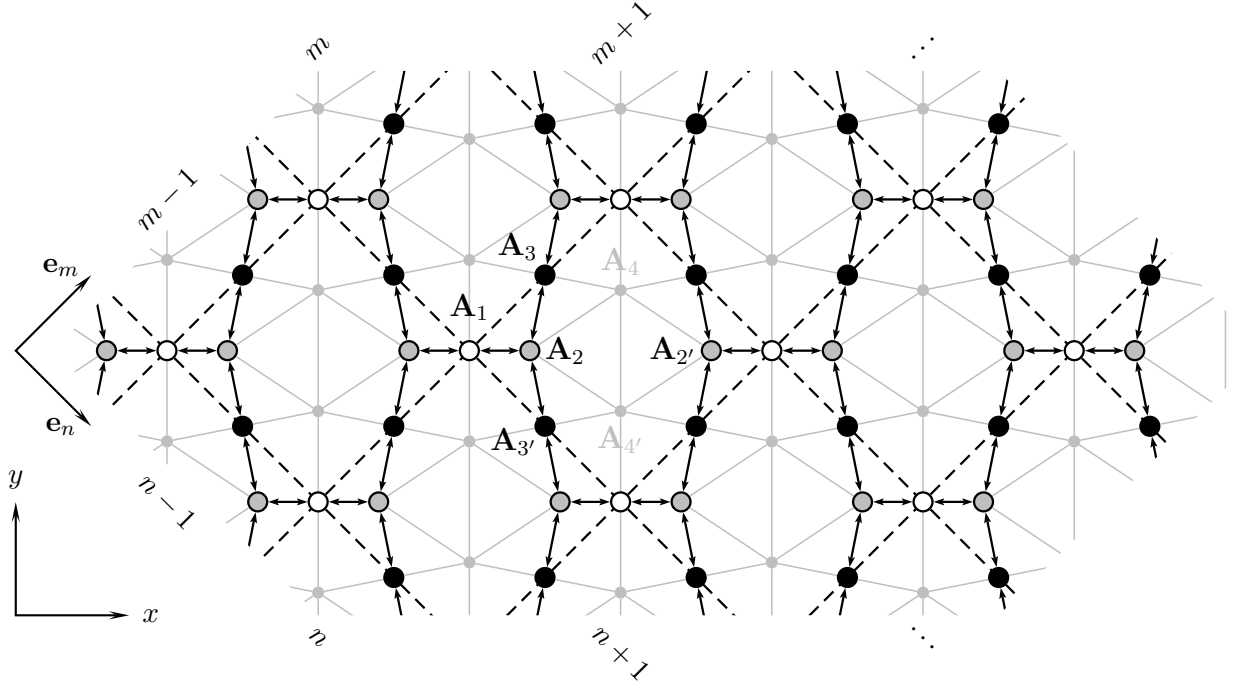


Figure 4.2: Schematic representation of random walk on a 2D lattice with $N_b = 5$. The stable adsorption sites for the adatom are shown as circles and transitions between them are denoted by arrows: $\Gamma_{fi} := \mathbf{A}_i \rightarrow \mathbf{A}_f$. Symmetry equivalent sites are denoted by primed indices, *e.g.*, \mathbf{A}_2 and $\mathbf{A}_{2'}$. The dashed boxes outline the unit cell of the 2D lattice (in this example it belongs to the $mm2$ symmetry class, c -rectangular Bravais lattice). The basis associated with the lattice coordinate system is $(\mathbf{e}_n, \mathbf{e}_m)$, while that of the Cartesian one is (x, y) , and the vector index $\mathbf{n} = (n, m)$ labels the unit cell. The network connectivity could be substantially complicated (see the gray lines) if two more sites (\mathbf{A}_4 and $\mathbf{A}_{4'}$) are added, $N_b = 7$.

Ref. [121] and Chapter 16 in Ref. [118]):

$$D_{\alpha\beta}^* = \lim_{t \rightarrow \infty} \frac{1}{4t} \left\langle \left[R_{\alpha}^{\text{ad}}(t) - R_{\alpha}^{\text{ad}}(0) \right] \left[R_{\beta}^{\text{ad}}(t) - R_{\beta}^{\text{ad}}(0) \right] \right\rangle, \quad (4.4)$$

where we have suppressed the “||” subscript to simplify the notation, but we will use it explicitly when necessary. In the following, we use Greek letters to denote tensor in-plane components, *i.e.* in Eq. (4.4) $\alpha, \beta = x, y$, $R_x^{\text{ad}} \equiv X$, etc. In the case of isotropic surface diffusion,

$$D_{\alpha\beta}^* = D^* \delta_{\alpha\beta}, \quad (4.5)$$

where D^* is the tracer diffusion coefficient. Tensor notations will be used in the following only in the cases where diffusion anisotropy is to be highlighted.

It is imperative to point out that the definition (4.4) applies strictly only to the random walk of an *isolated* adatom, the so-called *tracer*. In relation to the experimental situation, it therefore corresponds to a low adatom concentration and/or a vanishing interaction between the adatoms. The most important consequence of the rate description of the tracer diffusivity is that D^* should be a function of the transition rate(s),

$$D^* \propto \Gamma. \quad (4.6)$$

An efficient scheme to work out the functional dependence (4.6) rests on the random walk formalism described in Sec. 4.2.

Chemical diffusion tensor

The simple “jump” picture pertinent to tracer diffusion becomes far more complicated, or even not meaningfully defined, if one considers an adsorbate layer of interacting adatoms. A gradient of the surface adatom density $n(\mathbf{r})$ will cause the system support a non-vanishing current density \mathbf{j} . Then a simple linear response relation follows,

$$\mathbf{j} = -\mathbf{D} \cdot \nabla n(\mathbf{r}), \quad j_\alpha = -D_{\alpha\beta} \nabla_\beta n(\mathbf{r}) \quad (4.7)$$

known as the Fick’s first law. This phenomenological equation introduces the *chemical diffusion tensor* $D_{\alpha\beta}$ (or chemical diffusion coefficient D in the isotropic case). Combining Eq. (4.7) with the continuity equation $\partial n / \partial t = -\nabla \cdot \mathbf{j}$ leads us to the Fick’s second law, which is nothing but the diffusion equation,

$$\frac{\partial}{\partial t} n(\mathbf{r}, t) = \nabla \cdot \mathbf{D} \cdot \nabla n(\mathbf{r}, t) = D_{\alpha\beta} \nabla_\alpha \nabla_\beta n(\mathbf{r}, t), \quad (4.8)$$

where the second equality holds for a position-independent chemical diffusion tensor.

In most cases, when applied to surface phenomena, the above approach is based on a generalized version of Eq. (4.7) in terms of the gradient of the surface chemical potential $\mu(\mathbf{r})$. If the latter is assumed to change only due to variation of $n(\mathbf{r})$, then one readily gets the generalization

$$\mathbf{j} = \frac{n}{k_B T} \left(\frac{\partial(\mu/k_B T)}{\partial \ln n} \right)_T^{-1} \mathbf{D} \cdot \nabla \mu, \quad (4.9)$$

where the quantity $[\partial(\mu/k_B T)/\partial \ln n]_T$ is usually referred to as the “thermodynamic factor”. In the very special case when the adparticles’ velocities are completely uncorrelated [33], it can be shown that

$$\frac{D}{D^*} = \text{thermodynamic factor} \equiv \left(\frac{\partial(\mu/k_B T)}{\partial \ln n} \right)_T, \quad (4.10)$$

which is known as the Darken relation [33]. This last result unequivocally points to the nonequivalence of the chemical and tracer diffusion coefficients in the general case. In the “dilute” limit (low adatoms concentration) when interactions between adatoms can be neglected, these two quantities coincide. Indeed, this is a trivial consequence of the fact that in this case $\mu = \mu_0 + k_B T \ln n$, where μ_0 depends on temperature T and external parameters.

In conclusion, we should stress that the diffusion coefficient/tensor calculated within the supercell approach (Sec. 2.3.1) can be endowed with the physical meaning of a tracer diffusion coefficient. Everywhere in Chapters 5 and 6 this will be implied.

4.2 Random walk formalism for the tracer diffusion tensor

4.2.1 Master equation of a 2D random walk

We turn now to the problem defined by Eq. (4.6). The natural language to derive the general form of the D^* - Γ relation is that of probability theory. The method outlined in this section builds upon the underlying assumption that the stochastic motion of an adatom on the 2D regular lattice of sites \mathbf{A}_i is a *Markoff process* (for a concise classification of stochastic processes see, *e.g.*, Sec. 2.4.1 in Ref. [122]). That is, the “state” of the random walker at time t may depend on the “next earlier time” $t' < t$, but not on more detailed prehistory of the adatom motion. Let now the “state” of the adatom be its coordinate. Then the central quantity we most want to know is the probability $P_i(\mathbf{n}, t)$ of finding the adatom at the site \mathbf{A}_i in the \mathbf{n} th unit cell at time

t . If the random walk takes place on a 2D lattice of size $N \times M$ ($n = 1..N, m = 1..M$) and the common Born-von Kármán periodic boundary condition is imposed, then $P_i(\mathbf{n}, t)$ would satisfy a relation similar to Eq. (4.1). Let us remember that $P_i(\mathbf{n}, t)$ is subject to the fundamental requirement to fall into the “physical region”

$$0 \leq P_i(\mathbf{n}, t) \leq 1, \quad \text{and} \quad \sum_{i, \mathbf{n}} P_i(\mathbf{n}, t) \equiv \sum_i \sum_{n=1}^N \sum_{m=1}^M P_i(n, m, t) = 1. \quad (4.11)$$

For a Markoff process, the dynamics of the N_b quantities $P_i(\mathbf{n}, t)$ are governed by the *master equation*

$$\frac{d}{dt} P_i(\mathbf{n}, t) = \underbrace{\sum_{j=1}^{N_b} \sum_{\mathbf{n}'} \Gamma_{ij}(\mathbf{n} - \mathbf{n}') P_j(\mathbf{n}', t)}_{\text{rate in}} - \underbrace{P_i(\mathbf{n}, t) \sum_{j=1}^{N_b} \sum_{\mathbf{n}'} \Gamma_{ji}(\mathbf{n}' - \mathbf{n})}_{\text{rate out}}, \quad i = 1, 2, \dots, N_b, \quad (4.12)$$

where $\Gamma_{ij}(\mathbf{n} - \mathbf{n}')$ is just the rate at which an adatom jumps from site \mathbf{A}_j in the \mathbf{n}' th cell to site \mathbf{A}_i in the \mathbf{n} th neighbor cell. A very comprehensive account of the method to obtain a solution to the master equation in the form (4.12) is given, for instance, by Natori and Godby [123] and Kley [5], where applications to diffusion, respectively, on stepped surfaces and low-index GaAs surfaces were considered.

Here we want to notice the formal correspondence (upon the replacement $t \rightarrow t/i\hbar$) of the N_b coupled linear differential equations with constant coefficients to the Schrödinger equation for the tight-binding electron spectrum especially of 2D systems, *e.g.*, CuO₂ and RuO₂ planes in the superconducting cuprates and ruthenates, respectively [124]. With the help of the Fourier transform

$$P_j(\mathbf{n}, t) = \frac{1}{\sqrt{NM}} \sum_{\mathbf{q}} e^{i\mathbf{q} \cdot \mathbf{n}} P_j(\mathbf{q}, t) \quad \begin{cases} \mathbf{q} = 2\pi \left(\frac{p}{N}, \frac{q}{M} \right) \\ p = 1..N \\ q = 1..M \end{cases}, \quad (4.13)$$

the system (4.12) can be brought to the compact form

$$\frac{d}{dt} \mathbf{P}(\mathbf{q}, t) = \mathbf{\Gamma}(\mathbf{q}) \cdot \mathbf{P}(\mathbf{q}, t) \quad \begin{cases} \mathbf{P} \equiv (P_1, P_2, \dots, P_{N_b})^T \\ \mathbf{\Gamma} \equiv [\Gamma_{ij}] \end{cases}, \quad (4.14)$$

where the (generally *non-symmetric*) $N_b \times N_b$ matrix

$$\Gamma_{ij}(\mathbf{q}) = \sum_{\mathbf{n}} e^{-i\mathbf{q} \cdot \mathbf{n}} \Gamma_{ij}(\mathbf{n}) - \delta_{ij} \sum_{k=1}^{N_b} \sum_{\mathbf{n}} \Gamma_{ki}(\mathbf{n}). \quad (4.15)$$

is commonly termed the transition rate matrix [119]. If $\mathbf{P}(\mathbf{q}, 0)$ is the initial condition for the probability state vector, then the solution to Eq. (4.14) can be written in terms of the corresponding Green's tensor G_{ik} , in a similar fashion to the way it was done in Sec. 3.1, $\mathbf{P}(\mathbf{q}, t) = \mathbf{G}(\mathbf{q}, t) \cdot \mathbf{P}(\mathbf{q}, 0)$, where formally $\mathbf{G}(\mathbf{q}, t) = \exp[\mathbf{\Gamma}(\mathbf{q})t]$.¹ However, if $\mathbf{\Gamma}$ has N_b *non-degenerate* eigenvalues γ_k , then a complete, biorthogonal set $\{\xi^{(k)}, \zeta^{(k)}\}$ exists,² and one can

¹The matrix exponent exists in the sense of the series $\sum_n \mathbf{\Gamma}^n t^n / n! = \mathbf{1} + \mathbf{\Gamma} t + \frac{1}{2!} \mathbf{\Gamma} \cdot \mathbf{\Gamma} t^2 + \dots$.

² $\xi^{(k)}$ and $\zeta^{(k)}$ are solution of the eigenvalue problem and its adjoint, respectively:

$$\Gamma_{ij} \xi_j^{(k)} = \gamma_k \xi_i^{(k)}, \quad \text{and} \quad \zeta_j^{(k)} \Gamma_{ji} = \gamma_k \zeta_i^{(k)},$$

satisfying the completeness and orthogonality relations, $\sum_k \xi_i^{(k)} \zeta_j^{(k)} = \delta_{ij}$, and $\xi^{(i)} \cdot \zeta^{(j)} = \delta_{ij}$.

employ the spectral decomposition $\Gamma_{ij} = \sum_{k=1}^{N_b} \gamma_k \xi_i^{(k)} \zeta_j^{(k)}$.³ Hence, the most general form of the solution to Eq. (4.14) reads

$$\mathbf{P}(\mathbf{q}, t) = \mathbf{G}(\mathbf{q}, t) \cdot \mathbf{P}(\mathbf{q}, 0), \quad \text{with} \quad \mathbf{G}(\mathbf{q}, t) = \sum_k^{N_b} e^{\gamma_k(\mathbf{q})t} \boldsymbol{\xi}^{(k)}(\mathbf{q}) \boldsymbol{\zeta}^{(k)}(\mathbf{q}). \quad (4.16)$$

Substituting (4.16) back into Eq. (4.13), we get the real-space solution to the master equation (4.12),

$$\mathbf{P}(\mathbf{n}, t) = \sum_{\mathbf{n}'} \mathbf{G}(\mathbf{n} - \mathbf{n}', t) \cdot \mathbf{P}(\mathbf{n}', 0), \quad \text{with} \quad \mathbf{G}(\mathbf{n}, t) = \frac{1}{NM} \sum_{\mathbf{q}} e^{i\mathbf{q} \cdot \mathbf{n}} \mathbf{G}(\mathbf{q}, t). \quad (4.17)$$

The passage to an infinite lattice, $N, M \rightarrow \infty$, in this equation can be simply accomplished by the replacement $\sum_{\mathbf{n}'} \rightarrow \sum_{\mathbf{n}', m'=-\infty}^{\infty}$, and using the integral representation for the Green's tensor

$$\mathbf{G}(\mathbf{n}, t) = \sum_{k=1}^{N_b} \int_{-\pi}^{\pi} \frac{d\mathbf{q}}{(2\pi)^2} e^{\gamma_k(\mathbf{q})t + i\mathbf{q} \cdot \mathbf{n}} \boldsymbol{\xi}^{(k)}(\mathbf{q}) \boldsymbol{\zeta}^{(k)}(\mathbf{q}), \quad (4.18)$$

where the continuous variable $\mathbf{q} = (p, q)$, and $d\mathbf{q} = dpdq$. This expression is the major result of the above considerations, and has a simple physical meaning. Indeed, at the initial moment $t = 0$, the exponent in the integrand becomes purely imaginary, and we can immediately take advantage of the completeness of the biorthogonal set (see the footnotes on page 35). Furthermore, the principle contribution to the integral over \mathbf{q} comes from the region $\mathbf{q} \simeq \mathbf{0}$, and therefore the integration can be extended over the range $(-\infty, \infty)$, thus recognizing the Fourier integral representation of the delta function $\delta(\mathbf{n})$. These remarks show that $G_{ik}(\mathbf{n} - \mathbf{n}', 0) = \delta_{ik} \delta(\mathbf{n} - \mathbf{n}')$, *i.e.* the Green's tensor “starts” at $t = 0$ as a delta-like peak centered at \mathbf{n}' , and the time evolution of its profile, according to Eq. (4.18), is governed by relaxation times $|1/\gamma_k(\mathbf{q})|$ of the N_b modes.

4.2.2 The hydrodynamic limit

In order to calculate $D_{\alpha\beta}^*$, according to Eq. (4.4), one needs to consider the long-time asymptotics of the Green's tensor (4.18). From simple qualitative arguments, it is clear that its behavior for $t \rightarrow \infty$ will be determined only by the mode γ_k with the longest relaxation time $1/\gamma_k$. The stability of this mode implies that only small “wave-vectors” $\mathbf{q} \simeq \mathbf{0}$ are essential, so we can refer to it also as being in the long-wavelength limit, where the discreteness of the lattice is no longer important. In fact, a stability analysis of the solution to the master equation (4.12) with any initial condition $\mathbf{P}(\mathbf{n}, 0)$ starting in the “physical region” (4.11) tells us [125] that there is one and only one (say, that corresponding to $k = 1$) vanishing eigenvalue, and the real parts of the rest of the spectrum are negative:

$$\gamma_1(\mathbf{0}) = 0, \quad \text{and} \quad \text{Re}[\gamma_k(\mathbf{q})] < 0, \quad \forall k \geq 2. \quad (4.19)$$

Therefore the long-time asymptotic behaviour of (4.18) will be governed by the “highest” branch of the spectrum, γ_1 .

$$\lim_{t \rightarrow \infty} \mathbf{G}(\mathbf{n}, t) = \lim_{t \rightarrow \infty} \int_{-\pi}^{\pi} \frac{d\mathbf{q}}{(2\pi)^2} e^{\gamma_1(\mathbf{q})t + i\mathbf{q} \cdot \mathbf{n}} \boldsymbol{\xi}^{(1)}(\mathbf{q}) \boldsymbol{\zeta}^{(1)}(\mathbf{q}) \quad (4.20)$$

³This decomposition follows immediately from the completeness of the biorthogonal set.

The principal part of the integral in Eq. (4.20) comes from the region $\mathbf{q} \simeq \mathbf{0}$, and can be extracted via saddle-point integration [126] (for a rigorous derivation,⁴ see Ref. [5]). We provide here the final asymptotic result, which has the familiar Gaussian shape,⁵

$$\mathfrak{G}(\mathbf{n}, t) = \frac{1}{\sqrt{4\pi\sigma_1 t}} \exp\left(-\frac{|\mathbf{s}_1 \cdot \mathbf{n}|^2}{4\sigma_1 t}\right) \frac{1}{\sqrt{4\pi\sigma_2 t}} \exp\left(-\frac{|\mathbf{s}_2 \cdot \mathbf{n}|^2}{4\sigma_2 t}\right) \boldsymbol{\xi}^{(1)}(\mathbf{0}) \boldsymbol{\zeta}^{(1)}(\mathbf{0}) \quad (4.21)$$

$$= \mathfrak{G}(\mathbf{n}, t) \boldsymbol{\xi}^{(1)}(\mathbf{0}) \boldsymbol{\zeta}^{(1)}(\mathbf{0}). \quad (4.22)$$

In this expression, $\{\mathbf{s}_1, \mathbf{s}_2\}$ and $\{\sigma_1, \sigma_2\}$ are respectively the eigenvectors and eigenvalues of the “Hessian” matrix \mathbf{H} of the diffusion mode γ_1 at $\mathbf{q} = \mathbf{0}$,

$$\mathbf{H} = \mathbf{S} \cdot \tilde{\mathbf{H}} \cdot \mathbf{S}^{-1}, \quad \mathbf{H} = -\frac{1}{2!} \nabla_{\mathbf{q}} \nabla_{\mathbf{q}} \gamma_1(\mathbf{q}) \Big|_{\mathbf{q}=\mathbf{0}}. \quad (4.23)$$

Equation (4.23) is just the eigenvalue decomposition of \mathbf{H} , *i.e.* $S_{\mu\nu} = s_{\mu,\nu}$ ($\mu, \nu = 1, 2$) is the matrix of the eigenvectors, and $\tilde{H}_{\mu\nu} = \sigma_{\mu} \delta_{\mu\nu}$ the corresponding matrix of eigenvalues.

We can make now the final step and define an adatom density $n(\mathbf{n}, t)$ in terms of $\mathbf{P}(\mathbf{n}, t)$ [5],

$$n(\mathbf{n}, t) \stackrel{\text{def}}{=} \frac{1}{A} \sum_{k=1}^{N_b} P_k(\mathbf{n}, t) \equiv \frac{1}{A} \boldsymbol{\zeta}^{(1)}(\mathbf{0}) \cdot \mathbf{P}(\mathbf{n}, t), \quad (4.24)$$

where we have used the fact that $\boldsymbol{\zeta}^{(1)}(\mathbf{0}) = (1, 1, \dots, 1)$ (this can be immediately verified by considering the adjoint eigenvalue problem for $[\Gamma(\mathbf{0})]^T$ and the definition Eq. (4.15)) and A is the area of the unit cell of the 2D lattice. In the long-wavelength (hydrodynamic) limit $\mathbf{n} = (n, m)$ can be considered as continuous variable, and we obtain

$$n(\mathbf{n}, t) = \int d\mathbf{n}' \mathfrak{G}(\mathbf{n} - \mathbf{n}', t) n(\mathbf{n}', 0). \quad (4.25)$$

Because of the integral operator form of Eq. (4.25), $\mathfrak{G}(\mathbf{n}, t)$ is sometimes called the diffusion kernel. On the other hand, it can be readily verified that $n(\mathbf{n}, t)$ satisfies Fick’s second law, Eq. (4.8), but including the tracer diffusion tensor $D_{\alpha\beta}^*$,

$$\frac{\partial}{\partial t} n(\mathbf{n}, t) = D_{\alpha\beta}^* \nabla_{\alpha} \nabla_{\beta} n(\mathbf{n}, t), \quad \alpha, \beta = n, m. \quad (4.26)$$

From Eqs. (4.25) and (4.26) we obtain the final form of the tracer diffusion tensor in lattice coordinates (see Figure 4.2), which, remarkably, is just given by Eq. (4.23)

$$\mathbf{D}^* = \mathbf{S} \cdot \tilde{\mathbf{H}} \cdot \mathbf{S}^{-1}. \quad (4.27)$$

This simple result has, in fact, rather general basis. It was obtained by Festa and Galleani d’Agliano [127] for the Smoluchowski equation [128] with periodic external potential (see also Sec. 12.7.2 in Ref. [122]). The latter will be discussed in more details later in Sec. 7.3.

Alternatively, with the help of the coordinate transformation matrix $\mathbf{B}_{\alpha\beta} = \mathbf{e}_{\alpha,\beta}$, the diffusion tensor (4.27) reads in Cartesian coordinates

$$\mathbf{D}^* = \mathbf{B} \cdot \mathbf{H} \cdot \mathbf{B}^T. \quad (4.28)$$

⁴The method employs essentially the properties (4.19), as well as the vanishing of the gradient $\nabla_{\mathbf{q}} \gamma_1(\mathbf{q})|_{\mathbf{0}} = \mathbf{0}$.

⁵cf. also any 10 DM banknote from the pre-Euro era ;-).

Equation (4.28) is the final expression for the diffusion tensor of an isolated random walker, and we shall use it in what follows to calculate diffusion coefficients of indium adatoms on an InGaAs(001) wetting layer (Chapter 5) and a bare GaAs(001) substrate (Chapter 6). The above prescription is an N_b -dimensional eigenvalue problem for the transition matrix $\Gamma_{ij}(\mathbf{q})$, and we need to determine only the “highest energy” branch $\gamma_1(\mathbf{q})$, which is vanishing for $\mathbf{q} \simeq \mathbf{0}$. However for some adsorbate/substrate systems, N_b may well be as large as 5 or even bigger, which makes it impossible to write down an analytical solution of the eigenvalue problem in closed form. A workaround can exploit the hydrodynamic limit itself—we can work with accuracy not exceeding $O(|\mathbf{q}|^2)$ [123]. On the other hand, γ_1 satisfies the characteristic polynomial of $\mathbf{\Gamma}$, $\det[\Gamma_{ij} - \gamma_1 \delta_{ij}] = \sum_{n=0}^{N_b} a_n \gamma_1^n = 0$. Thus we can truncate the latter up to terms $O(\gamma_1)$ and obtain simpler, approximate expression for \mathbf{H} ,

$$\left. \begin{aligned} \sum_{n=0}^{N_b} a_n \gamma_1^n &\simeq a_0(\mathbf{q}) + a_1(\mathbf{q})\gamma_1(\mathbf{q}) + O(\gamma_1^2) = 0 \\ \gamma_1(\mathbf{q} \simeq \mathbf{0}) &\simeq -\frac{a_0(\mathbf{q})}{a_1(\mathbf{q})} \end{aligned} \right\} \Rightarrow \mathbf{H} \simeq \frac{1}{2a_1(\mathbf{0})} \nabla_{\mathbf{q}} \nabla_{\mathbf{q}} a_0(\mathbf{q}) \Big|_{\mathbf{q}=\mathbf{0}}. \quad (4.29)$$

Hence, the calculation of the diffusion tensor, Eq. (4.28), reduces to working out the first two coefficients in the characteristic polynomial of the transition matrix $\mathbf{\Gamma}(\mathbf{q})$. Equations (4.28) (or Eq. (4.27) in lattice coordinates) and (4.29) represent the desired functional form of the relation (4.6).

4.3 Transition-State Theory

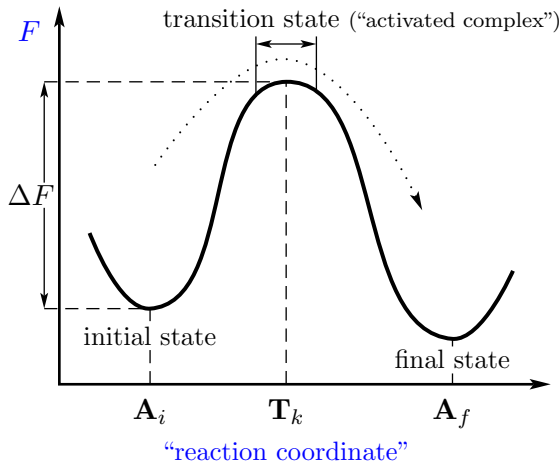


Figure 4.3: Schematic of the lowest free energy path for a thermally activated jump of an adatom from \mathbf{A}_i to \mathbf{A}_f over the saddle point \mathbf{T}_k , $\mathbf{A}_i \xrightarrow{\mathbf{T}_k} \mathbf{A}_f$.

It turns out to be rather discouraging (especially from the viewpoint of a PhD student; see, for example, A. Kley’s discussion in Sec. 5.1 of Ref. [5]). In this work we shall use a computationally expedient and efficient (statistical) tool known as transition-state theory (TST) [129–131]. The TST has its origin in Eyring’s absolute rate theory [130,132].

The underlying idea of the transition-state theory is illustrated in Figure 4.3. Let the initial state of our adatom/surface system be represented on the free-energy diagram by the \mathbf{A}_i point. The highest point along the lowest free-energy path to the next (meta)stable point \mathbf{A}_f

The formulation of the diffusion coefficient(s) in terms of the transition rates Γ_{ij} opens another, even more challenging question as to how can one calculate Γ ’s? Being intimately related to the fundamental problem of a particle in potential well, the latter question has attracted exclusive interest in almost all natural sciences, and a number of methods have been developed. For a nice review on the subject, we refer the reader to the excellent essay by Hänggi, Talkner, and Borkovec [129].

Different schemes for calculating Γ represent different levels of complication in the treatment of the adatom/surface system [121]. The simplest, and apparently straightforward approach is to employ MD simulations of the diffusion process. A rough estimate of the feasibility of this approach within first-principles schemes turns

is the “activated point” \mathbf{T}_k . Eyring has dubbed the system at the activated point an “activated complex” [132]. In considering the *absolute* rate Γ_{fi} for the transition $\mathbf{A}_i \xrightarrow{\mathbf{T}_k} \mathbf{A}_f$ the underlying assumption has been made that the initial state and the activated complex are at *thermal equilibrium*.⁶ Eyring showed then that the absolute rate Γ_{fi} is given by

$$\Gamma_{fi} = \kappa(T) \frac{k_B T}{2\pi\hbar} \frac{Z_k}{Z_i}, \quad (4.30)$$

where $Z_k \equiv Z(\mathbf{T}_k)$, and $Z_i \equiv Z(\mathbf{A}_i)$ are the *canonical* partition function of the system, respectively, for the activated complex and for the initial state. The factor κ is introduced to account for “transition state recrossing” events, reducing the absolute rate, and thus $\kappa \leq 1$. The other simplifying assumption specific for the TST is that all activated complexes reach the final state, *i.e. recrossings of the saddle point \mathbf{T}_k are neglected*, so $\kappa \equiv 1$, and we arrive at the simpler version of (4.30),

$$\Gamma_{fi}^{\text{TST}} = \frac{k_B T}{2\pi\hbar} \frac{Z_k}{Z_i} = \frac{k_B T}{2\pi\hbar} \exp\left(-\frac{\Delta F}{k_B T}\right), \quad \Delta F = F(\mathbf{T}_k) - F(\mathbf{A}_i). \quad (4.31)$$

In the second equality, we have used the canonical expression for the Helmholtz free energy, $F = -k_B T \ln Z$. ΔF is usually referred to as the free energy of activation. In the following, we shall drop the superscript “TST” and the expression (4.31) will be always implied by Γ_{fi} . The above consideration points directly to one of the limitations for the applicability of the TST: the equilibrium assumption requires that $\Delta F \gg k_B T$. The latter condition will be therefore used to estimate whether an adsorption site is diffusion “active”, *i.e.* has to be included in the random walk formalism from the preceding section.

In the practical application of Eq. (4.31) to surface diffusion, one usually considers the surface as a heat bath of harmonic oscillators. In this approximation, the partition functions entering Eq. (4.31) can be expressed via the normal modes of the system. At \mathbf{A}_i , the latter is described by N normal modes with angular frequencies $\omega_n^{(i)}$. At the saddle point \mathbf{T}_k , however, the mode related to the reaction coordinate has an imaginary frequency and has to be excluded from the summation when setting the partition function. Note, that such a statement implies that the reaction coordinate can be separated from all other degrees of freedom of the system, which is another important approximation in the transition state theory. Thus, at \mathbf{T}_k there are $N - 1$ normal modes with frequencies $\omega_n^{(k)}$.

The Helmholtz free energy of a crystal lattice considered as “collection of N independent oscillators” ω_n has the form [41]

$$F = \underbrace{U}_{\text{static part}} + \underbrace{\sum_{n=1}^N \frac{1}{2} \hbar \omega_n + k_B T \sum_{n=1}^N \ln(1 - e^{-\hbar \omega_n / k_B T})}_{\text{vibrational part}}, \quad (4.32)$$

where U is the total energy of the static lattice. For the adatom/surface system, U is identified to be its ground state total energy. It is that quantity accessible through the DFT computational scheme, Chapter 2. A similar expression can be written for the transition state, in which case the summation has to be made over the $N - 1$ normal modes $\omega_n^{(k)}$. Substituting $F(\mathbf{T}_k)$ and $F(\mathbf{A}_i)$ in Eq. (4.31) with (4.32), and taking into account the basic thermodynamic relation between

⁶It seems that Arrhenius was the first to introduce the equilibrium argument in the reaction-rate theory [129, 133].

the (vibrational) entropy of the system S_{vib} and the Helmholtz free energy, $S_{\text{vib}} = -(\partial F/\partial T)_V$, we obtain the harmonic approximation for Γ_{fi} ,

$$\Gamma_{fi} = \Gamma_{fi}^{(0)} \exp\left(-\frac{\Delta U}{k_B T}\right), \quad (4.33)$$

$$\Gamma_{fi}^{(0)} = \frac{k_B T}{2\pi\hbar} \exp\left(-\frac{\Delta U_{\text{vib}}}{k_B T} + \frac{\Delta S_{\text{vib}}}{k_B}\right). \quad (4.34)$$

The static total energy difference ΔU in Eq. (4.33) is the quantity commonly referred to as *diffusion barrier*; ΔU_{vib} and ΔS_{vib} in Eq. (4.34) stand, respectively, for the differences between vibrational energy and entropy of the saddle point \mathbf{T}_k and the initial state \mathbf{A}_i . The prefactor $\Gamma_{fi}^{(0)}$ is usually interpreted as an attempt-to-escape frequency of the adatom in the metastable site \mathbf{A}_i (but see the discussion by Wahnström in Sec. 16 of Ref. [118]).

One important particular case of Eq. (4.34) occurs in the classical limit $T \gg \Theta_D$, Θ_D being the Debye temperature [41]. InAs and GaAs have relatively low Θ_D ($\Theta_D^{\text{InAs}} = 247$ K, $\Theta_D^{\text{GaAs}} = 344$ K [92]), thus at the typical growth conditions $T \simeq 400\text{--}600$ °C, all vibrational modes ω_n will be populated, so we can take the classical limit in Eq. (4.34). For $\hbar\omega_n/k_B T \ll 1$, expanding the logarithm in Eq. (4.32),

$$\ln\left[1 - \exp\left(-\frac{\hbar\omega_n}{k_B T}\right)\right] \approx \ln\left(\frac{\hbar\omega_n}{k_B T}\right) - \frac{\hbar\omega_n}{2k_B T}, \quad (4.35)$$

it is easily worked out that

$$\frac{\Delta U_{\text{vib}}}{k_B T} = \sum_{n=1}^{N-1} 1 - \sum_{n=1}^N 1 = -1, \quad (4.36)$$

$$\frac{\Delta S_{\text{vib}}}{k_B} = \sum_{n=1}^N \ln\left(\frac{\hbar\omega_n^{(i)}}{k_B T}\right) - \sum_{n=1}^{N-1} \ln\left(\frac{\hbar\omega_n^{(k)}}{k_B T}\right) - 1. \quad (4.37)$$

As a result we obtain the well-known expression [129, 131, 132]

$$\Gamma_{fi}^{(0)} = \frac{1}{2\pi} \frac{\prod_{n=1}^N \omega_n^{(i)}}{\prod_{n=1}^{N-1} \omega_n^{(k)}}. \quad (4.38)$$

Notice that all T -factors that appear in the expansion of (4.34) cancel out to give a temperature independent frequency prefactor (4.38) in the classical, harmonic limit.⁷ This simple formula represents, by itself, a prescription towards calculating $\Gamma_{fi}^{(0)}$ in DFT [5, 136], where the frequencies ω_n are evaluated from the force-constant matrix of the adatom/surface system in the particular configuration (*e.g.*, \mathbf{A}_i , \mathbf{T}_k , etc.).

It is usually believed, and for a number of systems it has been demonstrated, that the frequency prefactor $\Gamma^{(0)}$ obeys the so-called Meyer-Neldel rule [137, 138]. This rule establishes a subtle relation between the prefactor $\Gamma^{(0)}$ and the activation barrier ΔU in a Van't Hoff-Arrhenius type of temperature dependence (4.33): activated processes with higher ΔU are characterized by higher $\Gamma^{(0)}$. This phenomenon is known also as the *compensation effect*, and

⁷Valuable discussion on these points can be found in the Letter [134] and the follow-up Comment [135].

a simple graphical illustration is shown in Figure 4.4 (cf. also Ref. [136]). In mathematical notation, the Meyer-Neldel rule can be written in the general form [138]

$$\Gamma^{(0)} = \Gamma_0^{(0)} \exp\left(\frac{\Delta U}{\Delta_0}\right)^\alpha, \quad \frac{1}{2} \leq \alpha \leq 1, \quad (4.39)$$

where Δ_0 is the Meyer-Neldel energy, and α is a constant exponent specific for the mechanism of activation.

We would like to note, however, that even in the specialized literature the Meyer-Neldel rule “still tends to exist in a sort of limbo between fully accepted physical law and unexplained correlation ...” [137]. In theoretical studies on surface diffusion, the effect has been analyzed mainly for diffusion rates on metal surfaces [138]. In the context of adatom diffusion on strained surfaces, Ratsch and Scheffler [136] conducted a first-principles study of $\Gamma^{(0)}$ for Ag/Ag(111). They found, however, that the latter system obeys rather an anticompensation rule. For surface diffusion in lattice-mismatched semiconductor heteroepitaxy we are unaware of similar studies. In Chapter 6, we briefly discuss the relevance of the Meyer-Neldel effect for the indium diffusion on strained GaAs(001)- $c(4 \times 4)$ surface.

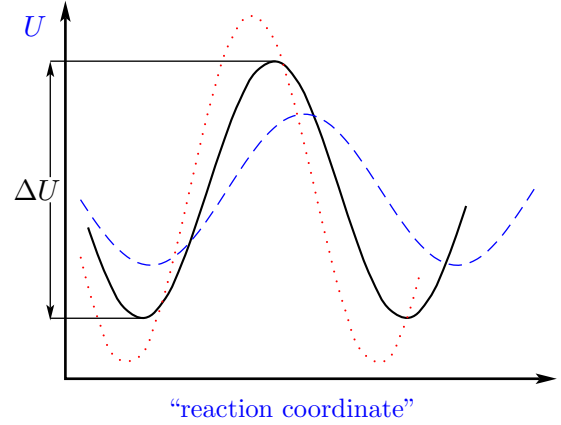


Figure 4.4: Simple qualitative sketch of the Meyer-Neldel effect (the full line corresponds to a “reference” process). The process occurring with lower barrier (dashed curve) will exhibit lower attempt rates as well, because of the smoother potential relief. And vice versa, the higher potential “corrugation” (dotted curve) is compensated by higher attempt-to-escape frequencies.

Chapter 5

Early stages of InAs/GaAs(001) heteroepitaxy

5.1 Introduction

MBE growth of InAs on the (001) surface of GaAs follows, in terms of the observed surface morphology, the SK mode (see Figure 1.1 (c) on page 2). The first stage of this process, up to coverages $\theta \leq \theta_c \simeq 1.8 \text{ ML} \pm 10 \%$, is characterized by the formation of a pseudomorphic [21] InAs film—wetting layer (WL)—fully strained to match the lattice constant of the GaAs substrate. Recent experimental studies focusing on this early stage of InAs/GaAs(001) deposition, however, revealed that the WL formation (for not too low deposition rate [139]) has a more complex nature than that given in the plain SK picture. This has been captured quite aptly by Joyce *et al.* [140]: “...Wetting layer formation is a very complex issue, where it is much easier to state what does not happen than what does.”

The first important deviation from the conventional SK growth mode is that the WL does not consist of pure InAs but is rather of mixed $\text{In}_x\text{Ga}_{1-x}\text{As}$ composition, *i.e.* it is a surface alloy with (dependent of temperature and deposition rate) $x = 0.2\text{--}0.6$ [140]. This has been found in a number of RHEED (Reflection High-Energy Electron Diffraction) and STM *in situ* measurements [140–146]. A schematic diagram of surface phases as a function of substrate temperature, reconstruction and amount of InAs deposited as given by Belk *et al.* [142] (see also Fig. 1 in Ref. [145]) is shown in Figure 5.1. It is immediately apparent that, for example, a complete (1×3) -reconstructed monolayer forms even for submonolayer delivery of InAs, which is only possible if the film is an $\text{In}_x\text{Ga}_{1-x}\text{As}$ alloy. Notably, for substrate temperatures $T < 450 \text{ }^\circ\text{C}$ and small InAs coverage the (1×3) structure coexists with surface domains having the same RHEED pattern as the clean GaAs(001)- $c(4 \times 4)$ substrate. On increasing the temperature, the (1×3) phase becomes incommensurate, reflecting the increased disorder in the film morphology. Note also that in the temperature window $T \simeq 450\text{--}500 \text{ }^\circ\text{C}$, a (2×4) phase is observed for high InAs coverages.

The other remarkable feature is related to the dependence of the integrated island volume V_f on the InAs coverage beyond the 2D→3D transition. Surprisingly, it was found that V_f substantially exceeds the amount of material deposited after the islands have nucleated [143, 144, 146, 147]. This was interpreted as a clear indication for the active role of the WL in supplying extra material (and/or serving as a “conductor” for material from the substrate) to be incorporated into the islands.

Thus the presence of an (In,Ga)As “active WL” renders the classical SK mode not fully adequate to describe the MBE of InAs on GaAs(001). Very recently, however, Wang *et al.*

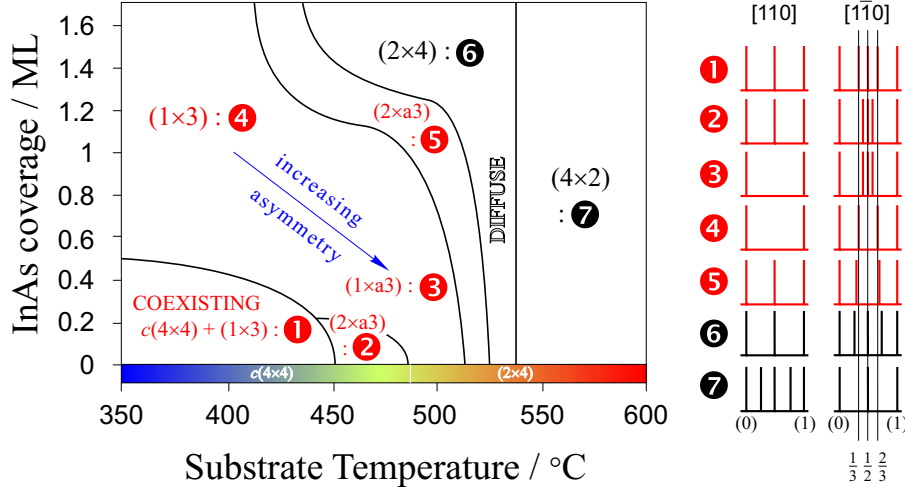


Figure 5.1: Diagram of surface phases during InAs deposition on GaAs(001) substrate as derived from RHEED patterns, according to Belk *et al.* [142]. The symbol “a” in the reconstruction patterns stands for “asymmetric (incommensurate)” (reproduced with the kind permission of the authors, ©1998 Elsevier; colors added by E.P.). Note the domination of triple-period surface structures (**1–5**) for deposition on GaAs(001)- $c(4 \times 4)$.

[107, 148] extended the notion of a SK growth mode to systems in a constrained, rather than a full, thermodynamic equilibrium, and showed that material transfer from the WL to the growing islands may be a key process for understanding the island size distribution. Nevertheless, up to now, our knowledge of the importance of alloying and the pseudomorphism¹ for the mechanism of strain relief and island growth kinetics in InAs/GaAs(001) heteroepitaxy is far from being complete. In fact, the interplay between surface strain, alloying, and surface mass transport is an issue of rather general interest. These are directly related, *e.g.*, to the indium segregation process, which is a main point of concern in technology and fabrication of high-quality InAs films and InAs/GaAs heterostructures, or, in general, to the problem of compositional modulation and ordering in semiconductor compounds [149].

In this chapter, we shall consider the effect of strain on alloying and indium mobility in the initial stages of InAs/GaAs(001) heteroepitaxy. In relation to the “phase” diagram in Figure 5.1, we focus on the triple-period structures (regions **1–5**) thus extending the previous work, Refs. [107, 148, 150], that concentrated mainly on the (2×4) -phase (region **6**) of the WL. Experimentally InAs is deposited on a few hundred nm thick GaAs buffer layer, grown at higher $T \sim 550\text{--}650$ °C. The substrate is then cooled down to $T \sim 450$ °C, where the MBE growth is performed typically under As-rich conditions. Thus, the first question to be answered concerns the morphology of the (001) substrate surface under these growth conditions. In Sec. 5.2, we address the structure and thermodynamic stability of the clean (001) surfaces of GaAs and InAs, which is, in principle, one of the most fundamental and intensely studied problems in surface science [96, 151, 152]. In contrast to GaAs(001) and InAs(001), available structural information about the WL is very scarce, to say the least. No atomic models for the triple-period reconstructions were proposed in either of the STM experimental studies Refs. [140–144, 146], perhaps because of the difficulties in obtaining high resolution STM images, as well as in preparing sufficiently large well-ordered single-phase domains on the WL to be scanned. Therefore, in Sec. 5.3, we discuss in detail a few possible atomic geometries for the $\text{In}_x\text{Ga}_{1-x}\text{As}(001)$ surface alloy, suggested in other experimental studies, and compare their thermodynamic stability and intrinsic

¹That is, “enforced isomorphism” [21].

surface properties to those of the clean binary (001) surfaces. The energetics of the (most energetically favorable) $\text{In}_x\text{Ga}_{1-x}\text{As}(001)-(2 \times 3)$ film as a function of its thickness is compared to the previous studies on the (2×4) -reconstructed WL [107, 150]. Finally, in Sec. 5.4, we consider the specifics of indium diffusion on the pseudomorphic $\text{InGaAs}(001)-(2 \times 3)$ -alloy WL.

5.2 The clean (001) surfaces of GaAs and InAs

5.2.1 Surface reconstruction and relaxation: basic principles

GaAs and InAs crystals are characterized by sp^3 -hybrid-type bonding of partial ionic character [79]. Consider now a process of dividing the infinite crystal into two semi-infinite parts bounded by the (001) crystal plane. This can be achieved, *e.g.*, by the hypothetic cleaving process sketched in Figure 5.2. Cutting of anion-cation bonds leaves at least one unpaired orbital per atom, the so-called dangling bond. Such an electronic configuration is very energetically unfavorable, and the surface undergoes a transition into a lower energy state. The two main processes which occur are atomic displacements from the ideal bulk positions *and/or* rebonding, eventually (but not necessarily) leading to lowered surface translational symmetry; in general, however, adding/removing/substituting of atoms is also possible. The former is usually referred to as surface relaxation, and the latter as surface reconstruction. Since the reconstruction process also naturally includes atomic displacements, we use it here in a more general sense to indicate any structural changes at surfaces [151, 152]. A rigorous treatment can be found, for example, in Ref. [153]. In order to designate a reconstructed surface with Miller indices (hkl) , whose unit cell is spanned by vectors $\mathbf{a}_1 = n\mathbf{a}'_1$, $\mathbf{a}_2 = m\mathbf{a}'_2$, $(\mathbf{a}'_1, \mathbf{a}'_2)$ being the primitive vectors of the ideal surface, we use the (slightly modified) Wood's notations [154],

$$\text{A}_{\text{III}}\text{B}_{\text{V}}(hkl)\text{-}[identifier](n \times m). \quad (5.1)$$

The majority of the experimentally observed semiconductor surface reconstructions, in particular those of the (001) surfaces of GaAs and InAs, have been rationalized in terms of a few principles.² In brief, reconstructions lower the

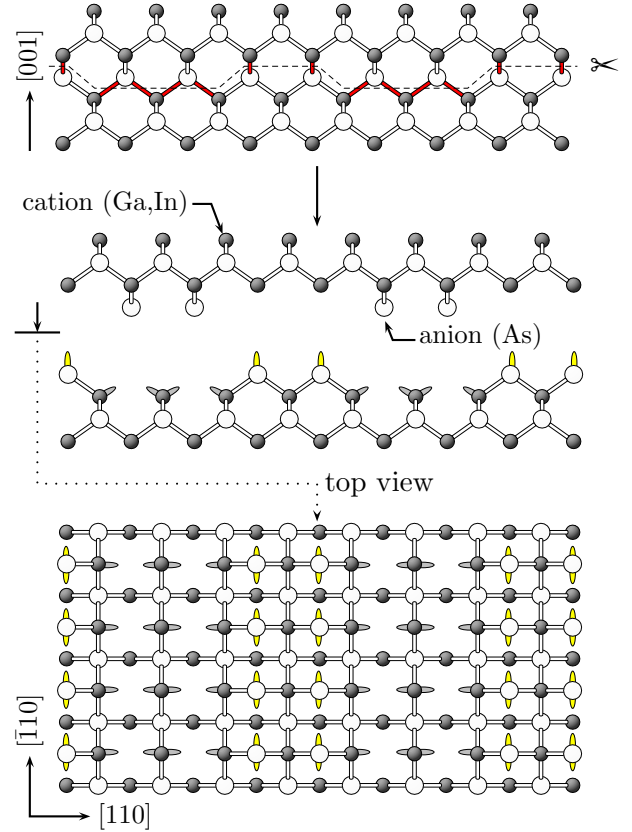


Figure 5.2: Schematic of a process of (001) surface creation by “cleaving” the bulk arsenide compound along the dashed line, *i.e.* cutting the shaded bonds (top panel). As a result, the periodicity of the so created surface is 4 times larger along $[110]$ crystallographic direction as compared to the ideal bulk terminated surface (*e.g.*, if cutting was done with an ideal (001) plane). Brighter little ellipses represent the As dangling bonds, and the darker ones—those of the cations (Ga, In).

²An explicit formulation and a comprehensive discussion was given by Duke [151]:

① “Reconstructions tend either to saturate surface ‘dangling’ bonds via rehybridization or to convert them into nonbonding electronic states.”

Table 5.1: Structural chemistry parameters of the (001) reconstructed surface. N_{ad} and N_{cd} denote, respectively, the number of anion and cation dimers per surface unit cell, and N_{adb} , N_{cdb} , similarly, the number of the dangling bonds.

reconstruction	stoichiometry $[1/A_{1 \times 1}]$	N_{ad}	N_{cd}	N_{adb}	N_{cdb}
$c(4 \times 4)$	$5/4$	15	0	10	0
$\beta 2(2 \times 4)$	$1/4$	3	0	6	4
$\alpha 2(2 \times 4)$	0	2	2	4	4
$\zeta(4 \times 2)$	$-1/4$	0	3	8	10

surface energy by rendering the surface ground state semiconducting, and preserving the surface charge neutrality. The latter is known also as the electron counting rule (ECR) [155]. It effectively means that the surface dangling bonds of the electronegative element (*e.g.*, Ga, In) tend to be empty (thus merging with the conduction band), while those of the electropositive element (As) are filled, and fall into the valence band. It should be emphasized, however, that these empirical principles give only a guideline towards the most likely route of surface stabilization. It is then the minimal property of the surface free energy γ (see Sec. 3.3.1) that determines which one out of a few possible reconstructions will be observed ideally in *thermodynamic equilibrium* (a typical example where the ECR is not fulfilled are the Sb-rich $(n \times 5)$ reconstructions of the GaSb(001) surface [156]). In the next subsection, we briefly discuss the reconstructions of the GaAs(001) and InAs(001) surfaces which are currently believed to be the most stable ones, relevant for the InAs/GaAs(001) heteroepitaxy.

5.2.2 Atomic structure

GaAs(001)

The MBE-grown GaAs(001) surface has been found to form a relatively large number of reconstructions as a function of growth temperature T and As:Ga flux ratio (or beam-equivalent pressure, $\text{BEP}_{\text{As}}/\text{BEP}_{\text{Ga}}$) [151, 157–161]. In order of decreasing BEP_{As} , three basic types of equilibrium reconstruction patterns are observed: $c(4 \times 4)$ (\equiv centered (4×4)), (2×4) , and (4×2) . This sequence, coincidentally, gives also the chronological order in which their atomic geometries were identified.

$c(4 \times 4)$ The $c(4 \times 4)$ reconstruction is the one prepared under the most As-rich conditions, usually by cooling the substrate under As_2 or As_4 flux. The early RHEED [162] and X-ray experiments [163] gave evidence for a As-stabilized double-layer structure consisting of As-As dimers, with the dimer bond being along the $[110]$ direction, adsorbed on a full As monolayer. A few possible geometries were proposed, containing from one to three

- ② “In many cases (and in all quasi-one-dimensional ones) surfaces can lower their energies by atomic relaxations leading to semiconducting (as opposite to metallic) surface state eigenvalue spectra.”
- ③ “The surface structure observed will be the lowest free-energy structure kinetically accessible under the preparation condition.”
- ④ “Surfaces tend to be autocompensated.”
- ⑤ “For a given surface stoichiometry, the surface atomic geometry is determined primarily by a rehybridization-induced lowering of the surface state bands associated with either surface bonds or (filled) anion dangling bond states.”

As dimers in the surface unit cell. The STM experiments by Biegelsen *et al.* [157] have provided unambiguous evidence only for the three-dimer model, shown in Figure 5.3 (a). The latter was supported also by subsequent theoretical work [5, 6], and is adopted in the present work. Accordingly, the GaAs(001)- $c(4 \times 4)$ reconstruction can be described as rows of As dimers (adsorbed on complete As monolayer) running in the $[\bar{1}10]$ direction, with units of three As dimers interrupted by a dimer vacancy. The X-ray diffraction measurements [163] reported a dimer bond length of $d = 2.59 \pm 0.06$ Å. The excessive As content leads to a fractional surface stoichiometry $\Delta N/A = 5/4 A_{1 \times 1}^{-1}$ (see Table 5.1 and Eq. (3.30) on page 26). On the basis of Table 5.1 (cf. also Figure 5.3 (a)) one can easily verify that the $c(4 \times 4)$ reconstruction fulfills the ECR: the $15 \times \frac{1}{2}$ electrons available from the 3 surface dimer bonds and the 12 dimer back-bonds equal exactly the $10 \times \frac{3}{4}$ electrons needed to fill the 10 As dangling bonds. Most importantly, as seen from Figure 5.1, GaAs(001)- $c(4 \times 4)$ forms the substrate for the initial stages of InAs deposition for temperatures $T \lesssim 500$ °C.

(2×4) Under typical MBE growth conditions, the GaAs(001) surface forms the As-rich (2×4) reconstruction, which is of primary technological importance. The “2-by” periodicity was understood to be due to the As-As dimerization along $[\bar{1}10]$ taking place in the topmost As layer (see, *e.g.*, Figure 5.2), while the “by-4” pattern in $[110]$ direction was interpreted as stemming from one or two missing dimers (“As-dimer-vacancy”) [164]. Farrell and Palmström [165] have found that the RHEED patterns along this direction provided evidence for three different phases as a function of temperature (maintaining the As_4 flux constant): α ($T \gtrsim 595$ °C), β ($T \sim 550$ °C), and γ ($T \gtrsim 505$ °C). Details on the atomic geometry of the possible models have been largely debated, but only very recently the structure of the GaAs(001)- (2×4) surface was finally resolved by LaBella *et al.* [166] in favor of the so-called β_2 reconstruction, shown in Figure 5.3 (b).

$\beta_2(2 \times 4)$ The atomic geometry of the β_2 reconstruction was first theoretically proposed by Chadi [164]. It has two As dimers in the topmost and one in the third atomic layer (trench dimer), Figure 5.3 (b). Its “construction” can be easily understood when compared with the top view in Figure 5.2. The number of dangling bonds is first reduced by dimerizing topmost As atoms along $[\bar{1}10]$ direction, leading to the $2 \times$ periodicity. The next modification is to remove the twofold coordinated Ga atom in the second atomic layer, and again dimerize the exposed third-layer As atoms in the same $[\bar{1}10]$ direction.³ Such an atomic configuration satisfies the ECR as $N_{\text{cdb}} \times \frac{3}{4} e^- = N_{\text{adb}} \times \frac{1}{2} e^-$ (cf. Table 5.1), and is found to be energetically more favorable than the similar β model having three coplanar As-dimers [5, 150, 167]. Precise X-ray diffraction measurements [168] have found almost identical bond lengths for the top and trench As dimers—2.51 Å and 2.49 Å, respectively.

$\alpha_2(2 \times 4)$ The α_2 model, Figure 5.3 (c), has been recently considered as a possible structure of the high-temperature α “phase” [165, 169]. It is derived from β_2 by removing one of the top As dimers, after which rebonding of the two exposed Ga atoms leads to Ga-Ga bonds (dimers) along $[110]$ direction. This reconstruction, just like α , is stoichiometric ($\Delta N = 0$, Table 5.1) and fulfills the ECR. Very recently a number of groups [170–174] have found in first-principles calculations that the α_2 reconstruction is energetically more favorable than the α structure by a few meV/Å². Their results, however, suggest that its stability is restricted to a very narrow region

³See also the slide collection available at w3.rz-berlin.mpg.de/~kratzer/lectures/cargese1/index.html.

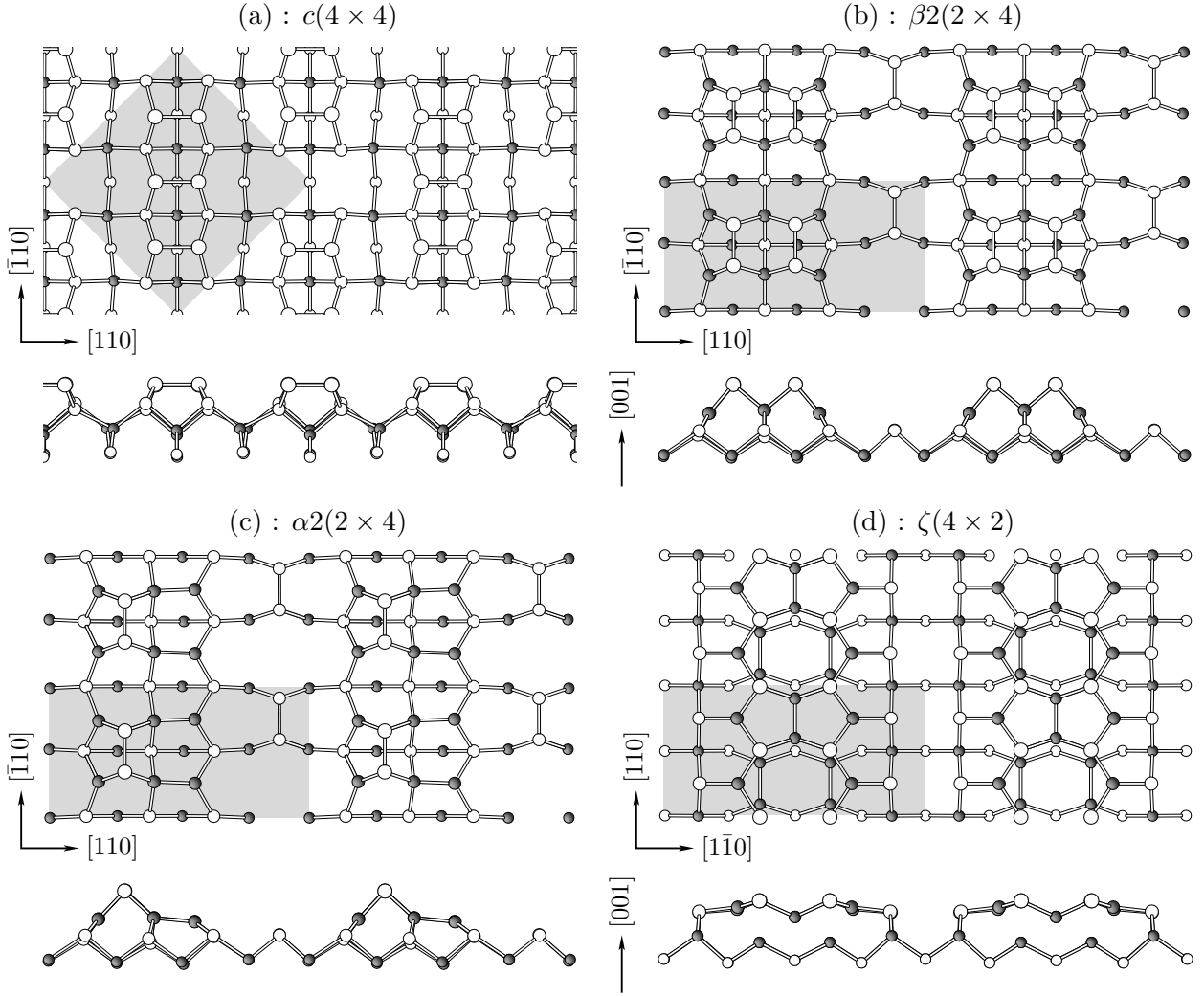


Figure 5.3: Atomic structure of stable reconstructions of GaAs(001) and InAs(001) surfaces. Only the topmost 4 atomic layers are shown (Ga, In: shaded circles, As: open circles). Shaded polygons indicate the surface unit cell. All top views represent a surface area A equivalent to 4 unit cells, *i.e.* $A = 16a_0^2$, a_0 being the lattice constant of the bulk compound. Side views are provided in the lower part of each panel.

of As pressures before the GaAs(001) exhibits the typical (4×2) pattern at As-poor conditions. On the other hand, combined STM and RHEED measurements by Hashizume *et al.* [175] lend support for the α model. Thus, although theoretical work finds the $\alpha 2$ geometry preferable, it may not be kinetically accessible under the preparation conditions [176] (see also the footnote on page 45). In contrast, on InAs(001), it is the stable reconstruction for intermediate-to-As-poor conditions.

(4×2) Under As-poor (Ga-rich) conditions the (001) surface develops a (4×2) , or $c(8 \times 2)$ reconstruction pattern, the latter being a centered combination of (4×2) structural units. It was originally believed that the $\beta 2$ model accounts for the observed features in the STM images [151,157,177]; the Ga-rich counterpart is a 90° -rotated $\beta 2(2 \times 4)$ unit (because of the zincblende registry in [001] direction), where the dimerization occurs between Ga atoms. This model has been recently dethroned by the DFT calculations by Lee *et al.* [174]. These

authors proposed the so-called $\zeta(4 \times 2)$ structure whose geometry is radically different from all considered so far for the III-V(001) surfaces, in that it displays subsurface dimerization of the group-III atoms, Figure 5.3 (d). The ζ model complies with the ECR, and was found to result in 0.44 eV lower surface energy per unit cell. Kumpf *et al.* [178] also demonstrated its uniqueness in interpreting the X-ray diffraction measurements of the metal-rich GaAs, InAs, and InSb (001) surfaces. In the present work we adopt the $\zeta(4 \times 2)$ model, Figure 5.3 (d), as the most stable reconstruction of the GaAs(001) surface in an As-poor environment.

It should be noted that in addition to the above described geometries, the GaAs(001) surface displays a number of kinetically driven reconstructions. For example, Däweritz and Hey [158] reported 14 different reconstruction patterns for the vicinal GaAs(001) surface. Majority of them are transient disordered “phases” existing in the transition region between the equilibrium reconstructions. In the typical temperature range where GaAs(001) is used as a substrate for InAs deposition [142], as seen from Figure 5.1, a (2×4) - $c(4 \times 4)$ transition occurs at $T \sim 480$ – 500 °C. Detailed analysis [179, 180] shows that no other “phases” are involved in the latter.

InAs(001)

On the basis of simple electrostatic arguments by Northrup and Froyen [167], one can anticipate similarities between the reconstructed InAs(001) and GaAs(001) surfaces. In the larger region of experimentally relevant conditions, the InAs(001) surface forms a (2×4) pattern, but, unlike GaAs(001), the $c(4 \times 4)$ reconstruction has never been observed experimentally, except for very low temperatures, $T \lesssim 300$ °C [180]. Instead, in the As-rich limit, STM and X-ray diffraction experiments [171, 181, 182] as well as first-principles calculations [6, 104, 106, 150, 171] support the $\beta 2$ structural model, Figure 5.3 (b). The bond lengths of the top and trench dimers (2.47 Å and 2.44 Å, respectively [182]) are very similar to those on GaAs(001)- $\beta 2(2 \times 4)$, thus, because of the larger lattice constant of InAs, one might expect more strained surface bonds.

The atomic structure for moderate As coverages is less clear. Upon annealing an As-stabilized InAs(001)- (2×4) surface at 340 °C, Yamaguchi and Horikoshi [181] observed a dominant single As-dimer structure, interpreted as the $\alpha 2$ reconstruction, Figure 5.3 (c), formed by desorption of one top As dimer from the $\beta 2$ unit. Recently Ratsch *et al.* [171] came to the same conclusion in a combined DFT and STM study.

In the In-rich limit, the InAs(001) surface develops, similar to GaAs(001), a $(4 \times 2)/c(8 \times 2)$ reconstruction pattern [178, 181, 183, 184]. At present, however, the most stable atomic arrangement in the (4×2) unit is still being debated, but it appears that the most likely geometry is provided by the novel ζ model, Figure 5.3 (c). In fact, Kumpf *et al.* [178] have already established experimentally (a slightly modified version of the $\zeta(4 \times 2)$ for GaAs(001)) this model for the InAs(001) in In-rich conditions. Theoretical work so far has not convincingly found any stable (4×2) reconstruction in this limit [104, 106, 150, 171], which is probably because the ζ structure was unknown at the time. Indeed, in the next section, we shall show that the $\zeta(4 \times 2)$ model is a possible reconstruction of InAs(001) for low As pressure.

5.2.3 Surface stability

Technical details

The equilibrium phase diagrams for all the surfaces considered in the present work are calculated on the basis of the theoretical scheme outlined in Sec. 3.3.1. Within the supercell approximation (Sec. 2.3.1), the (001) surface is modeled by a slab, whose “top” side represents (an initial guess

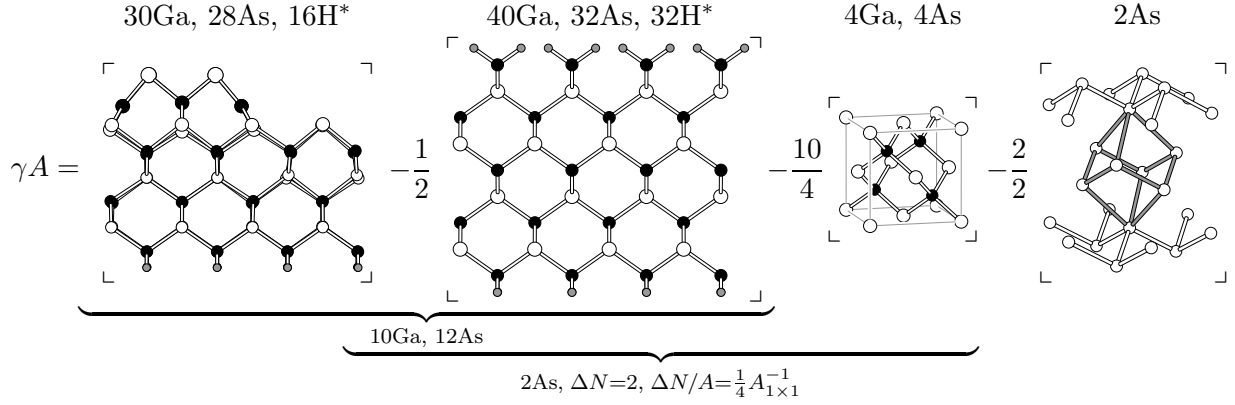


Figure 5.4: Pictorial representation of the procedure for calculating the surface energy of GaAs(001)- $\beta_2(2 \times 4)$. Number of atoms per species in the supercell used in the actual calculation is given above each system. Total energies of the corresponding systems are symbolically given by small corners. Thus the right-hand side of the “equation” reads from left to right: E^{slab} , $E^{\text{H}^*-\text{slab}}$, E^{GaAs} , and E^{As} .

to) the atomic geometries in Figure 5.3. The thickness of the slab Δ_s , depending on the particular reconstruction, is chosen so that the “bottom” side is always terminated by a group-III atomic layer, *i.e.* Ga or In. The 2×8 cation dangling bonds of this layer are then passivated by fictitious hydrogen atoms (H^*) (in tetrahedral coordination) of fractional charge $Z_{\text{H}^*} = 1\frac{1}{4}$, in order to mimic the missing $\Delta_s + 1\text{st}$ As layer [185]. This choice is easily rationalized in terms of the ECR, according to which a group-III cation contributes $\frac{3}{4} e^-$ to a bond, whereas the group-V anion contributes $\frac{5}{4} e^-$. This procedure has proven to be computationally very expedient as it allows an efficient decoupling of the two slab surfaces, and thereby using relatively “thinner” slabs (see Figure 5.5 below).

As a first step in calculating the surface energy γ of a particular reconstruction, one needs to compute the total energy of the corresponding slab E^{slab} . Towards this end, the atomic geometry for each reconstruction, Figure 5.3, is optimized by relaxing all atomic spatial degrees of freedom except those of the bottom cation layer and the passivating H^* ’s (see also Subsection 2.3.4). Since the LDA gave a better representation of the bulk elastic properties of GaAs and InAs (see Table 3.1 on page 23), it is used in all total-energy calculations of surface energies, employing $E_\infty = 10$ Ry, and working at the “theoretical” bulk lattice constant a_0 as given in Table 3.1. As we attempt to compare relative stability of structures with different plane symmetries, it is also imperative to ensure equivalent sets of \mathbf{k} -points (Sec. 2.3.3) in sampling the surface BZ. The equivalent Monkhorst-Pack sets for the $c(4 \times 4)$ and (2×4) reconstructions used throughout this work are illustrated in Figure 2.5 on page 17.

Within such a scheme, Eq. (3.30) is no longer directly applicable, as E^{slab} contains contributions from $c = 3$ components: cation (Ga or In), anion (As), and H^* . Thus, as a second step, one needs to subtract the contribution from the H^* -passivated bottom slab surface. This is achieved here by calculating the total energy of a thick slab with the same lateral size ($n \times m$) and both surfaces H^* -passivated, identically to the slab representing the reconstructed surface; we shall term it hereafter a H^* -slab. Symmetry equivalence between the two hydrogenated slab surfaces (within the zincblende $F\bar{4}3m$ space group) requires an odd number of atomic layers ($4n + 1$, $n = 1, 2, \dots$) and a 90° relative rotation of the terminating H^* pairs on both sides (see Figure 5.4). Thus, we can use Eq. (3.30) with the substitution $E \rightarrow E^{\text{slab}} - \frac{1}{2}E^{\text{H}^*-\text{slab}}$, where $E^{\text{H}^*-\text{slab}}$ is just the total energy of the *unrelaxed* H^* -slab, and the factor $\frac{1}{2}$ appears because we need to subtract the contribution from only one H^* -passivated surface (note, that this step

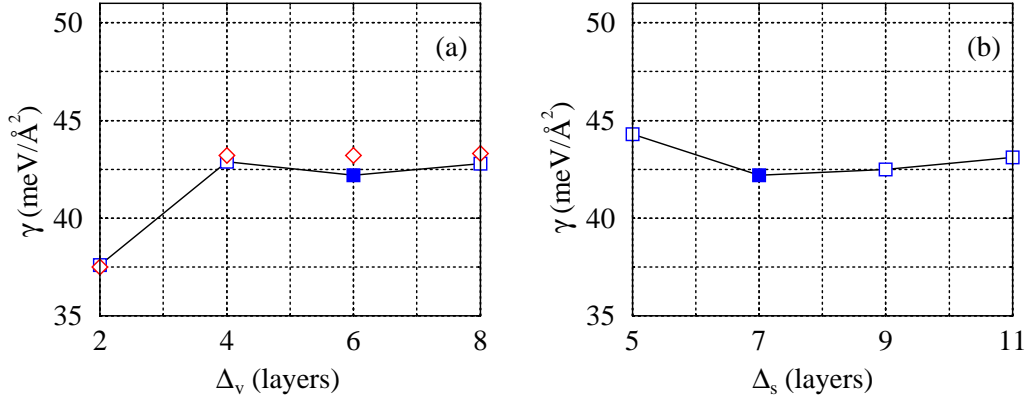


Figure 5.5: A test case: surface energy γ of GaAs(001)- $c(4 \times 4)$ as a function of Δ_v (a) and Δ_s (b) (see also Figure 2.3 (b) on page 13) for $\mu_{\text{As}} = \mu_{\text{As(bulk)}}(p = 0, T = 0)$. The square symbols on both panels represent the “raw” values of γ calculated according to the scheme of Figure 5.4. The abscissae of the full square (■) shows the value of the parameter that is kept fixed, *e.g.*, $\gamma(\Delta_v)$ was calculated for a slab of 7 atomic layers, $\Delta_s = 7$. The open diamonds (◇) on panel (a) indicate the values of $\gamma(\Delta_v)$ corrected according to the scaling hypothesis (Appendix B).

results also in a partial subtraction of the contribution from the bulk material). Furthermore, at zero temperature and pressure, $\mu_{\text{GaAs,InAs}}$ is identified with the total energy per pair of the bulk compound $E_2^{\text{III-V}}$

$$\mu_{\text{GaAs}}(0, 0) := E_2^{\text{GaAs}}, \quad \mu_{\text{InAs}}(0, 0) := E_2^{\text{InAs}} \quad (5.2)$$

(see also Appendix A). The extra As for the nonstoichiometric reconstructions is assumed to be in equilibrium with a reservoir of bulk As metal with the rhombohedral A7 structure (see Appendix A and Subsection 3.3.1). Figure 5.4 represents a step-by-step description of the above procedure for the GaAs(001)- $\beta 2(2 \times 4)$ surface.

In order to determine Δ_s of the slab representing the reconstructed surface and the thickness of the vacuum region in the supercell, Δ_v , a set of test calculations was carried out, and the output for the example of GaAs(001)- $c(4 \times 4)$ is summarized in Figure 5.5. Since the reconstructions considered here (Figure 5.3) have different registries of the topmost atomic layers, the corresponding slabs comprised $\Delta_s = 7$ atomic layers for $c(4 \times 4)$ and $\zeta(4 \times 2)$, whereas the (2×4) slabs were built up from $\Delta_s = 8$ layers; $\Delta_s = 9$ was used for the H^* slabs. Vacuum spacing in all cases was kept to $\Delta_v = 6$ interlayer distances. Figure 5.5 also provides an estimate for the error bar of the calculated relative values of the surface energies within the above described scheme: $\delta\gamma \sim \pm 1\text{--}2 \text{ meV}/\text{\AA}^2$ (see the footnote on page 47). Within this accuracy, present figures for the (001) surface are found to be in excellent agreement with the results in Refs. [5, 6, 105, 150], where very similar settings have been used. The absolute values, however, may be strongly affected by the exchange-correlation functional. As already mentioned in Subsection 2.2.2, the use of the GGA leads to (in some cases much) lower γ . For example, while LDA gives at the As-rich limit $\mu'_{\text{As}} = 0$ (cf. Eq. (3.31)) for GaAs(001)- $c(4 \times 4)$ $\gamma_{\text{LDA}} \simeq 43 \text{ meV}/\text{\AA}^2$, Figure 5.5, the PBE-GGA results in $\gamma_{\text{PBE}} \simeq 11 \text{ meV}/\text{\AA}^2$. Tests were made also with a very thick “symmetric” slab with $\Delta_s = 15$ atomic layers and both sides representing the GaAs(001)- $c(4 \times 4)$ reconstruction so the necessity of H^* -termination was eliminated; all atoms, except those in the middle layer, were allowed to freely relax. Results of these tests were found to be practically identical to the previously cited numbers, which demonstrated nicely the reliability of the computational scheme from Figure 5.4. As the LDA leads to higher cohesive energies for the reference bulk materials,

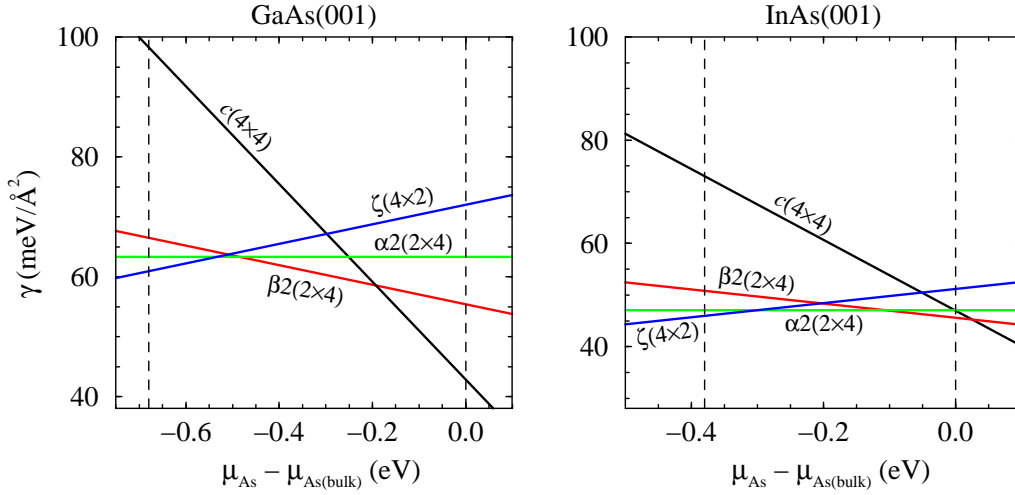


Figure 5.6: Calculated equilibrium phase diagrams of the clean GaAs(001) and InAs(001) surfaces using the LDA. Dashed lines indicate the physical range of variation of $\mu_{\text{As}} - \mu_{\text{As(bulk)}}$, which is given by the formation enthalpy $\Delta H_{\text{f}}^{\text{III-V}}$ of the corresponding binary compound, Appendix A.

the difference in γ reflects the fact that creating a surface by bond cutting is less costly in GGA than in LDA. Relative stability, however, being determined by differences in γ , is similarly well described in both exchange-correlation schemes.

Surface phase diagrams

Calculated surface energies γ of the four phases, considered for the clean GaAs(001) and InAs(001) surfaces, Figure 5.3, are shown as a function of $\mu_{\text{As}}(p = 0, T = 0)$ on Figure 5.6. In the case of GaAs(001), this set of reconstructions has been discussed, to our knowledge, only by Lee *et al.* [174] (see Fig. 2 in Ref. [174]). Apart from the rigid shift of the whole phase diagram and a difference ~ 0.1 eV in $\Delta H_{\text{f}}^{\text{GaAs}}$ (because of the use of PBE-GGA by those authors⁴) we find very good agreement between Figure 5.6 and Ref. [174]. Thus, under very As-rich conditions, the $c(4 \times 4)$ reconstruction is prominently the most stable one, while in the moderate-to-As-rich region, the $\beta 2(2 \times 4)$ phase is lowest in energy. This sequence is well-established in most theoretical work [5, 6, 105, 150, 167, 171]. At the Ga-rich side of the phase diagram, Lee *et al.* [174] demonstrated that taking into account the $\zeta(4 \times 2)$ model is crucial for determining the equilibrium reconstruction of the GaAs(001) surface. No conclusive answer, however, can be given as regards stability of the $\alpha 2(2 \times 4)$ phase. While found stable by Ratsch *et al.* [171] and Schmidt *et al.* [170], who did not consider the ζ structure, it is apparent that the stoichiometric $\alpha 2$ is always higher in energy than ζ for μ'_{As} lower than the value at which $\beta 2$, $\alpha 2$, and ζ are nearly energetically degenerate. In principle, one can speculate that, because of the degeneracy, entropic contributions to γ at realistic growth temperatures may render $\alpha 2$ preferable, but so far no clear experimental evidence has been found in favor of such an argument.

The calculated phase diagram for the InAs(001) surface displays a similar order of stable phases as a function of decreasing μ_{As} : $\beta 2(2 \times 4)$, $\alpha 2(2 \times 4)$, and $\zeta(4 \times 2)$. We do not find the $c(4 \times 4)$ reconstruction stable, in contrast to the results by Ratsch *et al.* [171]. Apparently taking into account the $\alpha 2(2 \times 4)$ and $\zeta(4 \times 2)$ reconstructions significantly reduces the range of stability

⁴Strictly speaking, for a given reconstruction, LDA and GGA should result in different stoichiometries $\Delta N/A_{1 \times 1}$, due to the difference in the equilibrium bulk lattice constant a_0 . A simple estimate using values for a_0 from Table 3.1, however, gives $|\delta(\Delta N/A_{1 \times 1})| \sim O((\delta a_0/a_0)^2) \sim 0.1\%$, which is a negligible quantity.

of the $\beta 2(2 \times 4)$ phase [6, 104, 150]. The $\alpha 2$ reconstruction, having only one top dimer in the unit cell (Figure 5.3 (c)), is also believed to be the one observed in the STM experiments [171, 181] under As-poor conditions. In the very In-rich limit, the $\zeta(4 \times 2)$ reconstruction becomes the most favorable one. Insofar as our phase diagram could be compared to that in Ref. [171], the so-called $\alpha 3(2 \times 4)$, predicted to be stable by those authors, seems to be higher in energy than $\zeta(4 \times 2)$. Thus, in agreement with Kumpf *et al.* [178], we predict that the ζ model might account for the (4×2) pattern commonly observed in As-deficient environment. This statement, however, is subject to the following proviso. The atomic arrangement/stoichiometry for InAs(001)- $\zeta(4 \times 2)$ as reported by Kumpf *et al.* differs slightly from that of the GaAs(001)- $\zeta(4 \times 2)$ surface. The best fit to the X-ray diffraction data was obtained if only 13 % of the higher In subsurface dimers were present, and all four-fold coordinated hollow sites were almost fully occupied by In atoms (cf. Fig. 5 in Ref. [178]). Our tests of a few such structures, however, resulted only in higher surface energies. On the other hand, a different model for the In-rich InAs(001)- (4×2) reconstruction was proposed earlier by Ohkouchi and Ikoma [183]. The STM experiment by Kendrick *et al.* [184] also provided support for the same structure. Wang *et al.* [150], however, calculated γ for this reconstruction (called I (4×2) in Ref. [150]) to be about 5 meV/Å² higher than the $\beta 2(4 \times 2)$, having the same stoichiometry. Thus, more detailed investigations are needed to single out the most stable reconstruction of InAs(001) under In-rich conditions. This regime in case of InAs/GaAs(001) heteroepitaxy would correspond to region ⑦ in Figure 5.1, and is beyond the scope of the present work.

In comparison, surface energies of InAs(001) reconstructions, except $c(4 \times 4)$, are lower in absolute values, which is due to the smaller $E_{\text{coh}}^{\text{InAs}}$, and the bigger bulk lattice constant a_{InAs} as compared to GaAs (cf. Table 3.1 on page 23, and Appendix A); *e.g.*, for the stoichiometric $\alpha 2(2 \times 4)$ reconstruction $\gamma_{\text{GaAs}} - \gamma_{\text{InAs}} = 16 \text{ meV}/\text{\AA}^2$. Furthermore, at $\mu_{\text{As}} = \mu_{\text{As(bulk)}}$, all four stoichiometries/reconstructions for InAs(001) lie within a surface energy range of only 5 meV/Å², while for GaAs(001), they cover much a wider range of $\simeq 30 \text{ meV}/\text{\AA}^2$. The difference in the bulk lattice constants also leads to a relative difference in the surface stoichiometries $\sim 2\varepsilon_0$ (*i.e.* less steep lines for InAs). Thus, one can read off Figure 5.6 that the $\beta 2$, $\alpha 2$, and ζ reconstructions for InAs share a surface energy band of $\sim 5 \text{ meV}/\text{\AA}^2$ in the whole allowed range of μ_{As} values. This is an important point which implies a bigger sensitivity of the InAs(001) phase diagram in general. In particular, as discussed by Ratsch [186] very recently, deviations from mechanical equilibrium could thereby significantly change the relative stability of the surface phases. We address this aspect below in fuller detail.

Surface stress

For a lattice-mismatched heteroepitaxial system like InAs/GaAs(001), as follows from the discussion in Sec. 3.3, the relative stability of the surface phases depends on the strain. In the linear elastic regime, it is the surface stress tensor $\tau_{\alpha\beta}$ that determines the γ - ε functional relation. The calculation of $\tau_{\alpha\beta}$ carried out in this work relies on Eq. (3.25), and therefore reduces to finding $(\partial\gamma/\partial\varepsilon_{\alpha\beta})_{\varepsilon=0}$. It should be emphasized, however, that, except for calculating stress differences [187], the computational scheme outlined in the beginning of this subsection (cf. also Figure 5.4) leads to major difficulties in working out individual tensor components $\tau_{\alpha\beta}$, mostly because of the need to subtract the contribution due to the H*-passivated surface of the slab. Recall that the two sides of the H*-slab are related via a mirror rotation symmetry. We have thus focused only on isotropic compressive and tensile strains.

Isotropic strain $\varepsilon_{\alpha\beta} = \varepsilon\delta_{\alpha\beta}$ for a particular reconstruction of the clean (001) surfaces is realized by rescaling the lateral size of the supercell and the atomic coordinates according to ε . The same procedure is applied also to the H*-slab and the bulk material. In calculating total

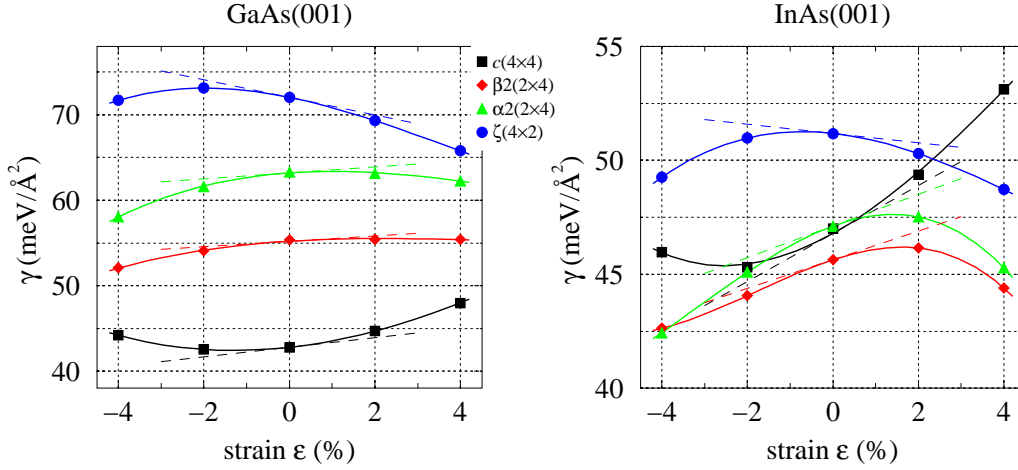


Figure 5.7: Surface energy of reconstructed GaAs(001) and InAs(001) surfaces as a function of isotropic strain for $\mu_{\text{As}} = \mu_{\text{As}(\text{bulk})}$ calculated within the LDA. Full curves are third-order least-square fits to the calculated points (symbols). Tangents to the fits at $\varepsilon = 0$ are indicated by dashed lines.

energies of the strained slabs, no atomic relaxations were performed, as the energy contributions due to relaxations are $O(\varepsilon^2)$, and thus do not affect the first derivative [6,187]. Surface energies of the considered reconstructions are calculated for $\varepsilon \in \{\pm 4\%, \pm 2\%, 0\}$, and corrected according to the scaling hypothesis, Appendix B and Appendix C.

Figure 5.7 shows the calculated $\gamma(\varepsilon)$ dependence. In order to determine its slope at $\varepsilon = 0$, the calculated points are fitted by a third-order polynomial $\gamma(\varepsilon) = \sum_{n=0}^3 \gamma^{(n)} \varepsilon^n$. The free term in the latter $\gamma^{(0)} \equiv \gamma_0 \equiv \gamma(\varepsilon = 0)$; because of the isotropic deformations, however, the coefficient $\gamma^{(1)}$ in the linear term, according to Eq. (3.25), gives the *intrinsic* part of the trace $\text{Tr } \tau_{\alpha\beta}$,

$$\gamma^{(1)} = \text{Tr } \tau_{\alpha\beta} - 2\gamma_0 = \underbrace{\left(\frac{\partial \gamma}{\partial \varepsilon_{xx}} + \frac{\partial \gamma}{\partial \varepsilon_{yy}} \right)_{\varepsilon=0}}_{\sigma_x + \sigma_y} \quad (5.3)$$

It should be pointed out that this method for determining surface stress is subject to substantial uncertainty due to the residual forces acting on the atoms in the supercell. Hence, the typical error bar in calculating $\partial \gamma / \partial \varepsilon_{\alpha\beta}$ is $\pm 20 \text{ meV}/\text{\AA}^2$ [6]. For present purposes, “exact” quantification of $|\sigma_x + \sigma_y|$ is not crucial, as the qualitative trends for γ upon applied isotropic strain are well reflected by $\text{sign}(\sigma_x + \sigma_y)$. From Figure 5.7, having the above reservations in mind, we can conclude that the *dominant* component of the intrinsic stress of the $c(4 \times 4)$, $\beta 2(2 \times 4)$, and $\alpha 2(2 \times 4)$ reconstructions for both GaAs(001) and InAs(001) is *tensile*, *i.e.* $\sigma_x + \sigma_y > 0$ (cf. the slopes of the tangents in Figure 5.7). In contrast, for the $\zeta(4 \times 2)$ reconstruction, again for both surfaces, it is *compressive*, $\sigma_x + \sigma_y < 0$. On the other hand, $\gamma(\varepsilon)$ for $c(4 \times 4)$ is a concave function at $\varepsilon = 0$, whereas for all other reconstructions it is convex. Combining Figures 5.6 and 5.7, *i.e.* working out $\gamma = \gamma(\mu_{\text{As}}, \varepsilon)$, one can build up a diagram of the stable surface phases as a function of μ_{As} and ε , Figure 5.8.

For GaAs(001), as seen from Figure 5.8, isotropic strain in the considered range of $\pm 4\%$ reduces the $c(4 \times 4)$ domain, while $\beta 2(2 \times 4)$ gets shifted symmetrically to more As-rich conditions. In the As-poor limit, isotropic strain has more profound effect. Compressive strain, $\varepsilon < 0$, enlarges the $\alpha 2(2 \times 4)$ domain, while for $\varepsilon > 0$, $\alpha 2$ disappears, and $\zeta(4 \times 2)$ becomes the dominant phase. In the case of InAs(001), the conjecture made for $\varepsilon = 0$ that the $c(4 \times 4)$ reconstruction is energetically unfavored can now be extended to $\varepsilon \neq 0$. Remarkably, compressive strain favors

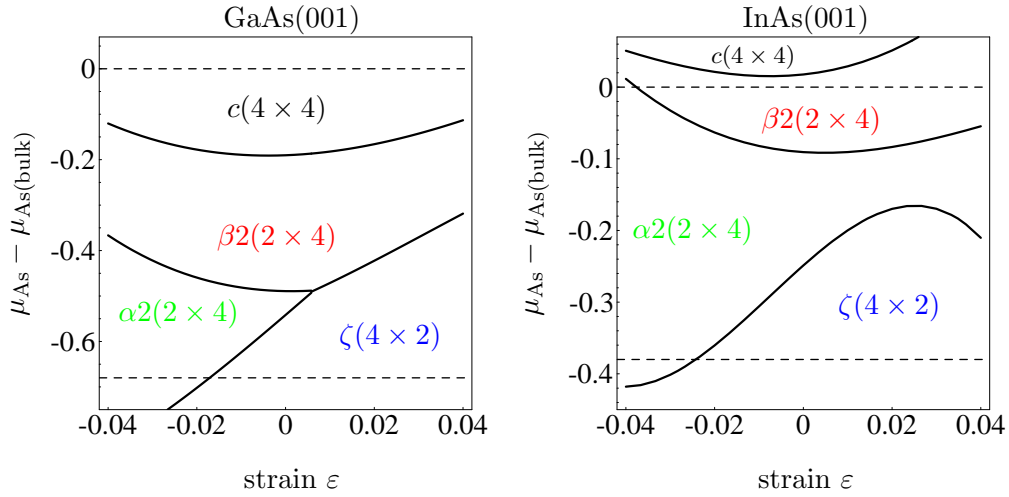


Figure 5.8: Diagram of surface phases as a function of μ_{As} and isotropic strain ε .

exclusively the $\alpha 2$ phase, and at about -4% compressive strain, it appears to be the only stable reconstruction of the InAs(001) surface. This is a clearly different situation from GaAs(001) as was recently also pointed out by Ratsch [186]. On the other hand, under tensile strain, the range of stability of $\zeta(4 \times 2)$ increases at the expense of the $\alpha 2$ and $\beta 2$ phases which are still favored but shifted towards the more As-rich limit.

These features are interpreted [186] in terms of the effect of strain on dimer bonds at the (001) surfaces, which are strengthened by collinear to the dimer bond compression and weakened, respectively, by expansion. On the unreconstructed (001) surface, Figure 5.2, the atoms that would form a dimer are not nearest neighbors, so a large relaxation (“buckling”) occurs upon dimer formation. On the $c(4 \times 4)$ and $\zeta(4 \times 2)$, dimers are oriented along $[110]$ direction, while for $\beta 2(2 \times 4)$, they are 90° rotated. The $\alpha 2(2 \times 4)$ reconstruction displays dimers in both directions: As dimers along $[\bar{1}10]$ and In dimers along $[110]$, cf. Figure 5.3. Thus it is generally argued (cf. Ref. [187]) that the stress component parallel to the dimer bond σ_{\parallel} is due to individual dimers. If we map $x \parallel [\bar{1}10]$, and $y \parallel [110]$, then $\sigma_x + \sigma_y$ in Eq. (5.3), *e.g.*, for the $c(4 \times 4)$ and $\zeta(4 \times 2)$ reconstructions, should be dominated by σ_y . Indeed, Silveira and Briones [188] have followed the $\sigma_x \equiv \sigma_{[\bar{1}10]}$ evolution during the $c(4 \times 4) \rightarrow (2 \times 4) \rightarrow (4 \times 2)$ phase transition on the GaAs(001), and found almost identical low σ_x stress levels for the $c(4 \times 4)$ and (4×2) phases. For InAs(001), Ratsch [186] also noted the similarity between tensile isotropic and tensile uniaxial strain along $[110]$ direction. Details in the overall effect of strain, however, cannot be rationalized solely using the above arguments, and one should include in the analysis other structural motifs present at the surface; *e.g.*, the $\zeta(4 \times 2)$ reconstruction displays three-fold coordinated As atoms in the top layer, which are not present in the other reconstructions.

5.3 Structure and energetics of InGaAs alloy wetting layer

5.3.1 Structural models

Discussion in the current literature on the structure of the WL in InGa/GaAs(001) heteroepitaxy is rather speculative. As mentioned in Sec. 5.1, there is a growing amount of strong experimental evidence that the WL is an InGaAs ternary alloy characterized by triple-periodicity patterns in diffraction experiments, Figure 5.1. In another group of experiments, a (2×4) -reconstructed WL was reported [109, 161, 189, 190]. The limited number of theoretical publications also found

the $\alpha(2 \times 4)$ [6] or $\beta(2 \times 4)$ [107, 148, 150] phases to be stable for the WL. Those authors, however, did not consider $(n \times 3)$ reconstructions, though they were cautious to mention such a possibility. The typical difficulties in determining atomic arrangement on the WL were brought out clearly recently by Márquez in combined STM and LEED (Low-Energy Electron Diffraction) measurements [161]. Intriguingly, the LEED pattern from a 1 ML thick InAs film grown on GaAs(001)- $c(4 \times 4)$ indicated a (1×3) reconstruction, while the high-resolution STM image was interpreted as a $\gamma(2 \times 4)$ -like phase [165]. The explanation to reconcile these observations is given in Figure 5.9, and suggests *significant structural disorder* in the underlying (2×4) structure, thus leading to small domains of local (1×3) , (2×3) , or $c(4 \times 4)$ symmetry.

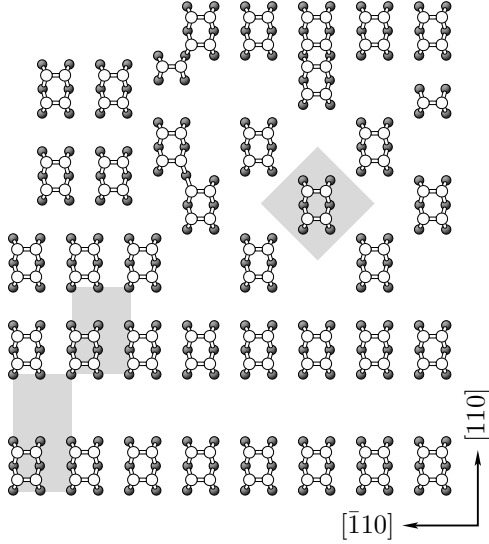


Figure 5.9: Illustration of As dimers arrangement on 1 ML thick InAs film on GaAs(001) leading to a mixed (1×3) and $c(4 \times 4)$ LEED pattern as suggested by Márquez [161]. Shaded boxes indicate local periodicity.

suggested by RDS (Reflectance-Difference Spectroscopy) measurements [196, 197]: (1×3) , Figure 5.10 (a), and $\alpha(2 \times 3)$, Figure 5.10 (c).

For an indium concentration $x = \frac{2}{3}$, the (1×3) and (2×3) models are characterized by continuous top-layer rows of “chemisorbed” As dimers running along $[\bar{1}10]$ direction. In the third layer, $x \times (n \times m)$ cation positions are occupied by In and $(1 - x) \times (n \times m)$ by Ga atoms, the latter preferentially occupying the site below the As dimers. The doubled periodicity along $[\bar{1}10]$ for the (2×3) reconstruction is due to the structural motif comprising an As dimer back-bonded to the four third-layer In atoms, Figure 5.10 (b) (see also Appendix D). The (1×3) model is simply derived from (2×3) by removing these dimers and dimerizing In atoms along $[110]$ direction, Figure 5.10 (a). The $\alpha(2 \times 3)$ reconstruction is very similar to the $\alpha(2 \times 4)$ for the clean binary surfaces, Figure 5.3 (c): the second-layer dimers along $[110]$ are now formed by In atoms, and no trench dimers are present giving the $\times 3$ periodicity in the same direction. The (4×3) reconstruction is obtained from (2×3) by removing every fourth As dimer in the topmost layer leading to doubled periodicity in $[\bar{1}10]$ direction.

5.3.2 Energetics

In order to determine the most favored reconstruction of the WL, we first consider the thermodynamic stability of the $(n \times 3)$ reconstructions from Figure 5.10 for the reference amount

A qualitatively different driving force for the observed triple periodicity is the interplay between compositional modulation and ordering. While never observed for clean binary III-V surfaces, a (2×3) reconstruction is known to form for pseudomorphic $\text{In}_x\text{Ga}_{1-x}\text{As}$ films [191, 192]. Sauvage-Simkin *et al.* [193] demonstrated by X-ray diffraction that In-Ga ordering stabilizes the (2×3) reconstruction under As-rich conditions, leading to an indium surface concentration of $x = \frac{2}{3}$. The structural model they deduced from the X-ray data is shown in Figure 5.10 (b). It was also confirmed by subsequent experimental studies [145, 194]. Detailed analysis further revealed that In “depletion”, $x < 2/3$, leads to *incommensurate* $(2 \times m)$ reconstruction with $m < 3$, while $m > 3$ for $x > 2/3$ [145, 194] (cf. Appendix D). Similar geometry was proposed by Ohkouchi and Gomyo [195] for an ordered GaInAs overlayer on InP(001), shown in Figure 5.10 (d). In the present work, we include also two other models

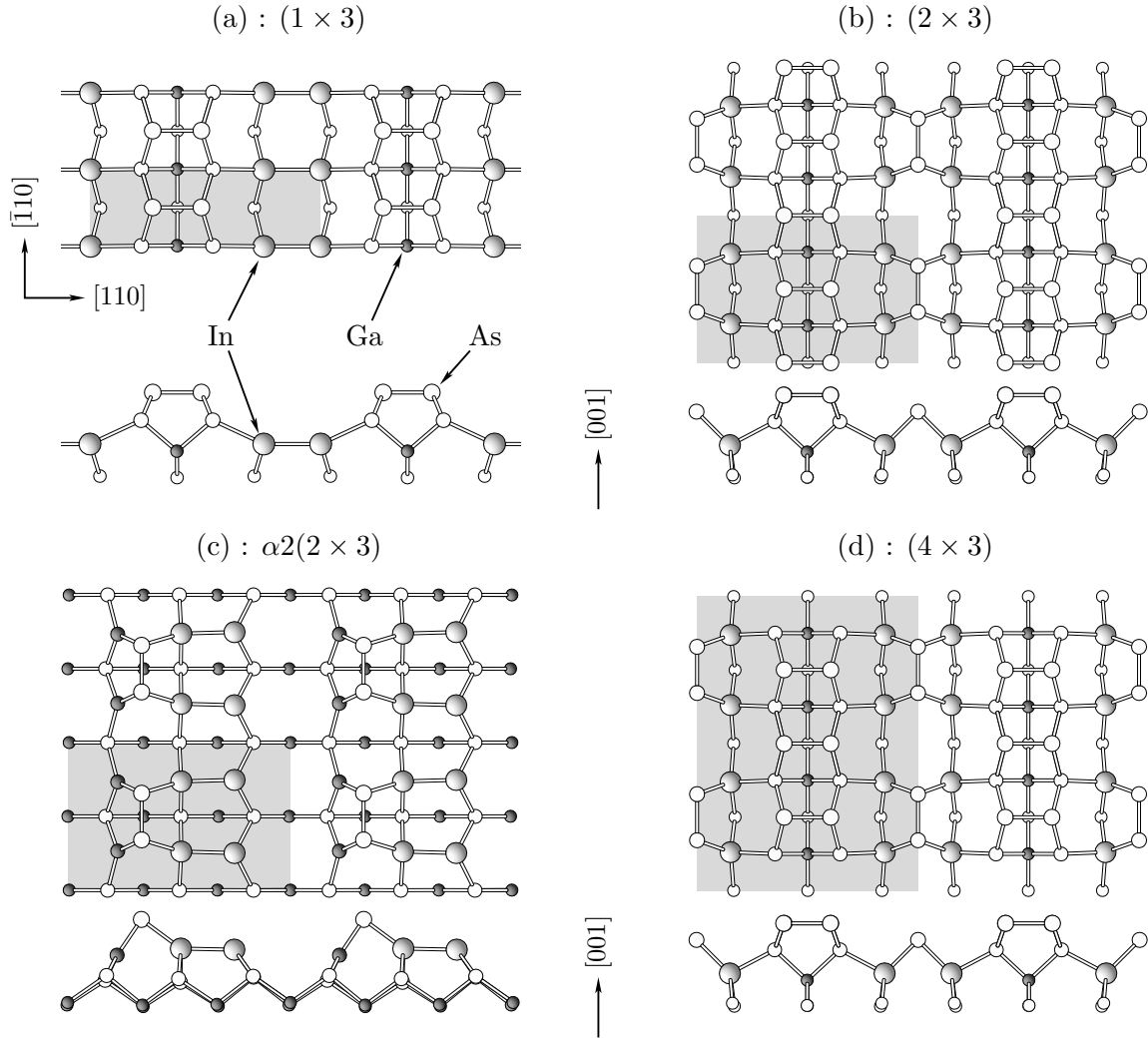


Figure 5.10: Structural models for the $(n \times 3)$ -reconstructed $\text{In}_x\text{Ga}_{1-x}\text{As}(001)$ alloy WL for $\theta = 2/3$ ML of indium. Only the topmost 4 atomic layers are shown (In,Ga: shaded circles, As: open circles). Shaded polygons indicate the surface unit cell. All top views represent a surface area equivalent to 4 unit cells, except for (4×3) , corresponding to 2 unit cells. Side views are provided in the lower part of each panel.

$\theta = 2/3$ ML of InAs deposited. This set of reconstructions was further extended by including $\alpha 2(2 \times 4)$ which our calculations from the previous section, Figure 5.8, showed to be the dominant phase on the compressively strained InAs(001) surface. In fact, for a sufficiently thick WL, one would expect the reconstruction to be the one of the clean InAs(001) surface; this is indeed the case also for region ⑥ in Figure 5.1. The $\alpha 2$ reconstruction, on the other hand, has not been considered in previous theoretical work [6, 107, 148, 150]. Therefore it is interesting to compare its energetics under As-rich conditions to that of both the $\times 3$ - and the previously studied $\beta 2(2 \times 4)$ -reconstructed WL [107], which is important especially for the later stages of the WL formation or after the 2D \rightarrow 3D growth mode crossover.

The technical settings for the calculations were already described in Sec. 5.2.3. Slabs with $\Delta_s = 7$ atomic layers were used for the $(n \times 3)$, $n = 1, 2, 4$ reconstructions, and $\Delta_s = 8$ for $\alpha 2(2 \times 3)$ and $\alpha 2(2 \times 4)$. The equivalent Monkhorst-Pack \mathbf{k} -point sets used for the $(n \times 3)$ unit cells read as follows: (1×3) — $\{(\frac{1}{2}, \frac{1}{2}, 0), 8 \times 3 \times 1\}$; (2×3) — $\{(\frac{1}{2}, \frac{1}{2}, 0), 4 \times 3 \times 1\}$; (4×3) —

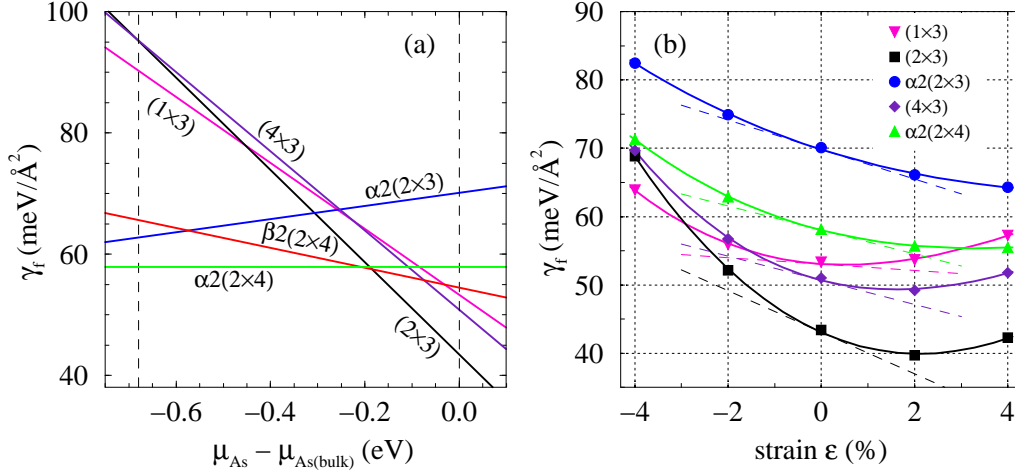


Figure 5.11: Formation energy of In_{2/3}Ga_{1/3}As(001) film with different reconstructions (a) as a function of μ_{As} , and (b) as a function of isotropic strain ϵ at $\mu_{\text{As}} = \mu_{\text{As(bulk)}}$. $\gamma_f(\mu_{\text{As(bulk)}})$ of the $\beta 2(2 \times 4)$ reconstruction on panel (a) is obtained from Ref. [107] by extrapolation to $\theta = 2/3$, and shifting by $-0.2 \text{ eV} \times \frac{1}{4} A_{1 \times 1}^{-1}$ to account for the fact that γ_f has been calculated therein at $\mu_{\text{As}} = \mu_{\text{As(bulk)}} - 0.2 \text{ eV}$.

$\{(\frac{1}{2}, \frac{1}{2}, 0), 2 \times 3 \times 1\}$. Since coverage of $2/3$ ML cannot be trivially realized for the $\alpha 2(2 \times 4)$, reconstruction we have made a linear interpolation from a set of calculations at $1/2$ ML and $3/4$ ML. The procedure for creating the thicker slabs needed for the study of the WL energetics as a function of its thickness θ will be described later in this subsection. Since we have to deal with an InGaAs ternary compound, special care should be paid to defining the energy quantities for its surface.

The notion of a surface energy γ was derived from a *gedanken* experiment of cleaving a binary bulk compound. Such a procedure, however, is not formally applicable for a *strained surface alloy*, such as the pseudomorphic In_xGa_{1-x}As(001) WL. The quantity which in this case can be “safely” defined through a procedure similar to that in Figure 5.4, as discussed in detail by Wang *et al.* [107, 148, 150], is the *formation energy* γ_f of the InGaAs(001) film with definite thickness θ . In analogy to Eq. (3.30),

$$\gamma_f A = E - \mu_{\text{GaAs}} N_{\text{Ga}} - \mu_{\text{InAs}} N_{\text{In}} - \mu_{\text{As}} \underbrace{(N_{\text{As}} - N_{\text{Ga}} - N_{\text{In}})}_{\Delta N}, \quad (5.4)$$

which is derived from Eq. (3.26) for $c = \text{Ga}, \text{In}, \text{As}$, assuming equilibrium conditions with the bulk binary compounds,

$$\mu_{\text{Ga}} + \mu_{\text{As}} = \mu_{\text{GaAs}}, \quad \mu_{\text{In}} + \mu_{\text{As}} = \mu_{\text{InAs}} := \mu_{\text{InAs}}^{\text{unstrained}}. \quad (5.5)$$

The “:=” equality in Eq. (5.5) implies that the so defined γ_f is a *total* quantity including the elastic energy of the WL.

Figure 5.11 shows the calculated formation energy γ_f of the In_xGa_{1-x}As(001) for the reference thickness $\theta = 2/3$ ML. There are a few remarkable features to be pointed out for γ_f of the pseudomorphic In_{2/3}Ga_{1/3}As(001) film strained to match the lattice constant of the GaAs(001) substrate, Figure 5.11 (a): (i) under (very) As-rich conditions none of the reconstructions considered can compete with the (2×3) model; (ii) very importantly, within the computational accuracy, In_{2/3}Ga_{1/3}As(001)- (2×3) is energetically degenerate to the GaAs(001)- $c(4 \times 4)$ bare substrate in the As-rich limit (stoichiometries of these reconstructions differ by only $\simeq 7 \%$, $\Delta N_{(2 \times 3)} = \frac{7}{6} A_{1 \times 1}^{-1}$); (iii) with the As chemical potential decreasing, the $\alpha 2(2 \times 4)$ reconstruction

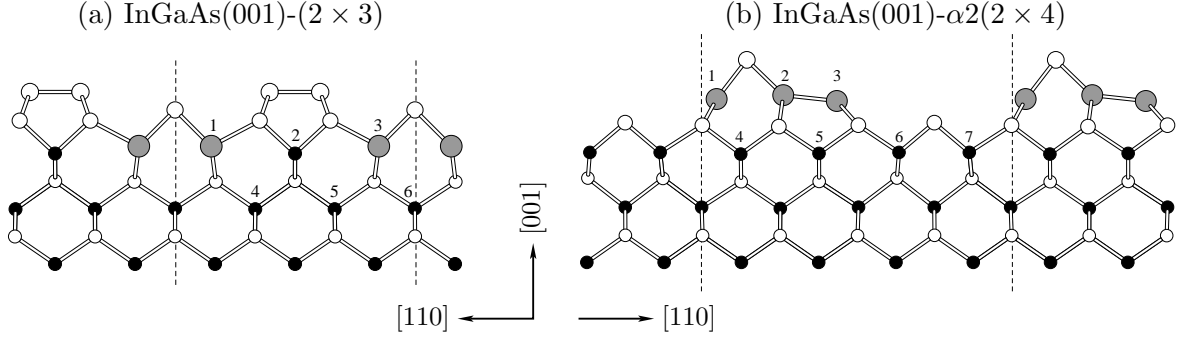


Figure 5.12: Configuration of pairs of sites occupied by In atoms tested in the calculation of $\gamma_f = \gamma_f(\theta)$. Every index represents two atomic positions along the $[\bar{1}10]$ direction, *e.g.*, 1-1', 2-2' etc. Dashed lines mark the supercell.

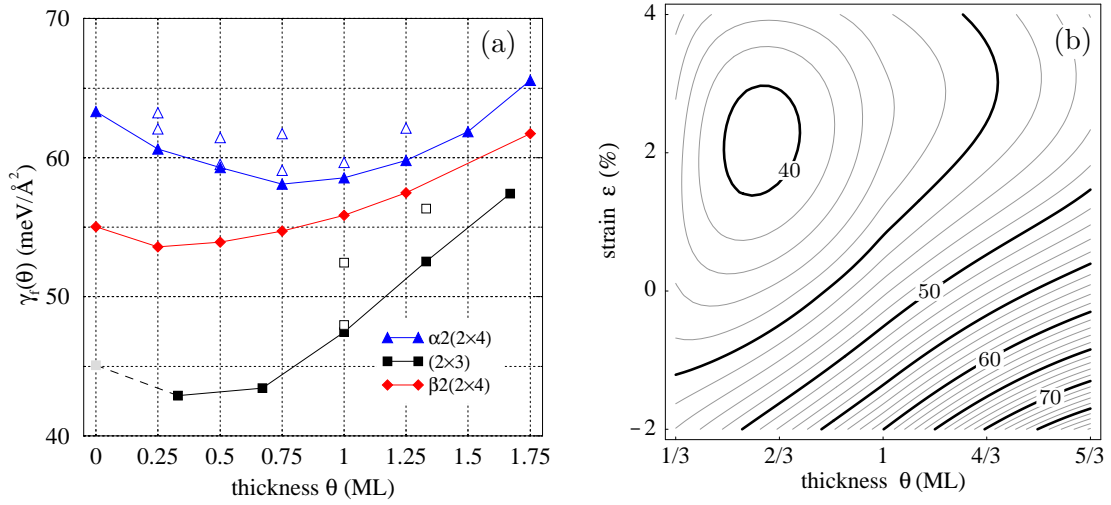


Figure 5.13: (a) Formation energy of WL as a function of its thickness θ . $\gamma_f(\theta)$ for the $\beta 2(2 \times 4)$ reconstruction is taken from Ref. [107]. The gray symbol corresponds to the surface energy of a fictitious GaAs(001)-(2 x 3) reconstructed surface obtained as the $(x \rightarrow 0)$ -limit of $\text{In}_x\text{Ga}_{1-x}\text{As}(001)-(2 \times 3)$. Full symbols give the minimum γ_f for a fixed θ , while the other tested configurations are indicated by open symbols. (b) Strain-thickness dependence of γ_f of $\text{In}_x\text{Ga}_{1-x}\text{As}(001)-(2 \times 3)$ WL. Contour labels are given in $\text{meV}/\text{\AA}^2$.

becomes the most favorable; (iv) at the $(2 \times 3) \rightarrow \alpha 2(2 \times 4)$ transition, the $\beta 2(2 \times 4)$ phase appears to be nearly degenerate in energy.

The low γ_f of the (2×3) reconstruction is somewhat unexpected, because none of the $(n \times 3)$ models fulfills the ECR, and they are therefore of metallic character. This surface, however, displays strong tendency towards dimerization, leading to 1 dangling bond per 1×1 area. Thus, our result seems to be in accord with the recent studies on the high-index GaAs(2511) surface by Geelhaar *et al.* [198], who revealed that “the minimization of the number of the dangling bonds” is a superior process to the ECR in stabilizing semiconductor surfaces (further aspects will be discussed in the next section). It also lends credibility for the (2×3) structural model as proposed by Sauvage-Simkin *et al.* [193], Figure 5.10 (a).

Another important feature of the pseudomorphic $\text{In}_{2/3}\text{Ga}_{1/3}\text{As}(001)$ film shows up upon considering γ_f as a function of the applied isotropic strain ϵ , Figure 5.11 (b). The dominant component of the intrinsic surface stress, Eq. (5.3), for all reconstructions is *compressive*, *i.e.* $\sigma_x + \sigma_y < 0$, in contrast to the As-rich reconstructions of GaAs(001) and InAs(001), Figure 5.7.

This is understood as to be due to the insertion of the indium atoms, having larger ionic radius, and attempting to form longer bonds to As (see Table A.2 in Appendix A). Clearly the (2×3) reconstruction has the lowest formation energy over almost the entire range of strain. At the reference thickness $\theta = 2/3$ ML, however, a $(2 \times 3) \rightarrow (1 \times 3)$ transition might occur for isotropic compression $|\varepsilon| \gtrsim 3\%$. One can also note the apparent similarity in $\gamma_f(\varepsilon)$ for the $\alpha 2$ reconstructions; removal of the trench dimer from the $\alpha 2(2 \times 4)$ phase to form the cation-rich $\alpha 2(2 \times 3)$ does not lead to any significant change in the qualitative behavior. On the basis of the above first-principles results we single out the (2×3) reconstruction as the most preferable one for the $\text{In}_{2/3}\text{Ga}_{1/3}\text{As}(001)$ film under As-rich conditions.

The next question to be answered is how the energetics of the (2×3) reconstruction compares to that of $\alpha 2(2 \times 4)$ and $\beta 2(2 \times 4)$ [107] as a function of the WL thickness θ . This problem is approached here in analogy to Refs. [107, 150]. For given x , In atoms occupy $x(n \times m)$ sites in the cation sublattice. Thus, the formation energy $\gamma_f(\theta)$ of the (2×3) and $\alpha 2(2 \times 4)$ -reconstructed WL is calculated as the minimum of γ_f over a few possible configuration of In atoms. Figure 5.12 shows the sites included in the tests. We consider only pairwise occupation of the two cation sites along the $[\bar{1}10]$ direction of the unit cell, also ensuring that the substrate is represented by at least 4 atomic layers of GaAs. It is interesting to note that for the (2×3) reconstruction, the sites marked ‘2’ in Figure 5.12 (a), below the As dimer, are unfavorable for In insertion. While for $x = 1/3$ the three symmetry inequivalent pairs (*e.g.*, 1-1', 1-3, and 1-3') that can be formed out of the two pairs 1-1' and 3-3' are energetically degenerate, we find that $\theta = 1$ ML is realized by occupying pairs 1, 3, and 6. Once pair 6 is occupied the next two In atoms ($\theta = 1\frac{1}{3}$ ML) are incorporated into sites 4-4', or 5-5' as these are symmetry equivalent. The $\alpha 2(2 \times 4)$ reconstruction follows different pattern, favoring formation of complete cation layers, and is thus very similar to $\beta 2(2 \times 4)$ [107]. For example, 6 In atoms ($\theta = 0.75$ ML) occupy pairs 1-3, and at $\theta = 1.75$ ML In forms two complete cation layers, *i.e.* pairs 1-7.

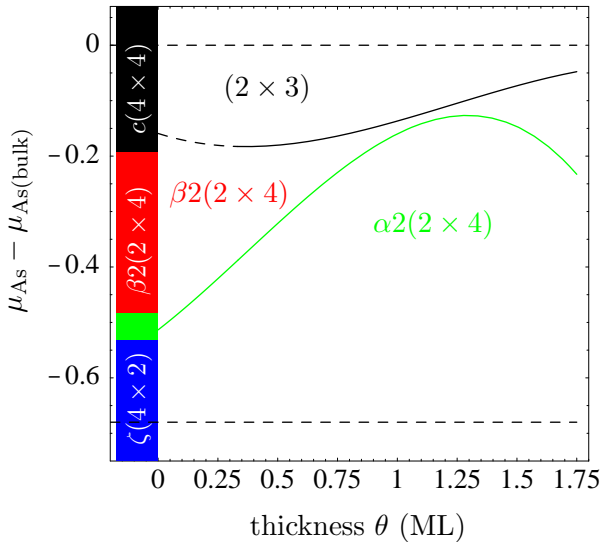


Figure 5.14: Diagram of the (2×3) , $\beta 2(2 \times 4)$, and $\alpha 2(2 \times 4)$ reconstructions of the WL as a function of its thickness θ and μ_{As} .

to a good accuracy, a linear function of θ . In Figure 5.13 (b), we also present its dependence on isotropic strain. As can be seen, compressive strain strongly destabilizes the (2×3) films beyond $\theta \sim 1/3$ ML, while under tensile strain $\varepsilon \gtrsim 2\%$, γ_f varies little as a function of θ ; within the range of parameters considered, γ_f has a global minimum for the $\text{In}_{2/3}\text{Ga}_{1/3}\text{As}(001)$ film under

The thickness dependence of γ_f is shown in Figure 5.13 (a), where we have also added the curve for the $\beta 2(2 \times 4)$ reconstruction, previously calculated by Wang *et al.* [107] using very similar computational settings (note that $\gamma(\mu_{\text{As}})$ of the $\text{GaAs}(001)$ - $\beta 2(2 \times 4)$ surface from Figure 5.6 coincides with that calculated in Ref. [150]). Clearly, at the (very) As-rich limit, formation of a (2×3) -reconstructed $\text{InGaAs}(001)$ surface alloy is the most advantageous process for the entire range of θ considered. This conclusion seems not to be affected by the accuracy of the calculations, as the (2×4) reconstructions lie higher in energy, well beyond the typical error bar. Interestingly, γ_f for $\alpha 2(2 \times 4)$ displays a minimum at $\theta = 3/4$ ML, while the minima for $\beta 2(2 \times 4)$ and (2×3) are shifted to lower “coverages” by about $1/2$ ML. Furthermore, for $\theta \gtrsim 2/3$ ML, $\gamma_f(\theta)$ of $\text{InGaAs}(001)$ -(2×3) is,

2 % tensile strain.

The trend from Figure 5.13 (a), however, corresponds to the extreme case of very As-rich conditions. In order to obtain γ_f in the whole experimentally relevant range of μ_{As} , we take into account the effect of surface stoichiometry, Figure 5.11 (a), which results in the $\mu_{\text{As}}-\theta$ “phase” diagram shown in Figure 5.14. Thus, within the reconstructions considered, we find that a submonolayer InAs deposition on the GaAs(001)- $c(4 \times 4)$ substrate under As-rich conditions leads to the formation of an InGaAs(001)- (2×3) WL. In order to compare with the experimentally derived diagram of surface phases due to Belk *et al.* [142] (cf. Sec. 5.1), we note that the μ'_{As} -axis in Figure 5.14 can be mapped onto the (substrate temperature) T -axis in Figure 5.1, with lower temperatures corresponding to higher $|\mu'_{\text{As}}|$ values. It is then easily established that Figure 5.14 reproduces another experimentally observed trend: in the low-temperature growth regime the range of the (2×3) phase retracts at higher θ , where the (2×4) phase becomes the dominant one. As mentioned already, the commensurate (2×3) reconstruction develops only for an In surface concentration $x = 2/3$ ML, while deviations from this amount result in incommensurate “phases” [145].

On the other hand, the resolution in the STM experiments [141–143] did not allow for resolving the atomic arrangement between the continuous As dimer rows characteristic for both the (1×3) and (2×3) models, Figure 5.10 (a,b). Distinction between the latter two is further made ambiguous, as the half-order X-ray diffraction lines indicative of the $2 \times$ periodicity were impossible to measure, cf. Ref. [194]. Our results also show that for somewhat less As-rich growth conditions, the (2×4) reconstruction is to be expected for the WL. For lower coverages, $\beta 2$ appears to be dominant. On increasing θ , interestingly, the $\alpha 2$ domain increases mostly at the expense of $\beta 2$, to reach a “maximum” range of stability at 1–1.5 ML. Beyond this thickness, we expect that the range of the $\beta 2(2 \times 4)$ WL reconstruction increases again. In conclusion, Figure 5.14 shows that surface alloying induces a new type of reconstruction(s) that should be taken into account in analyzing the kinetics/thermodynamics of the growth processes in the InAs/GaAs(001) heteroepitaxy.

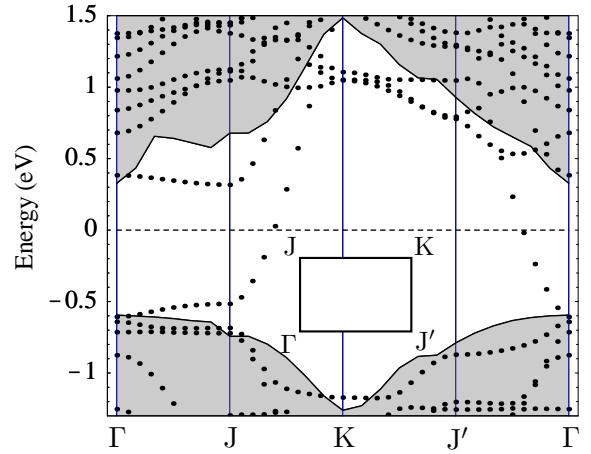


Figure 5.15: LDA band structure of the $\text{In}_{2/3}\text{Ga}_{1/3}\text{As}(001)-(2 \times 3)$ surface. High-symmetry lines in the surface 2×3 Brillouin zone are shown in the inset. Shaded regions represent the projected GaAs bulk bands and the Fermi energy is indicated by a dashed line.

5.4 Indium diffusion on InGaAs(001)- (2×3) wetting layer

5.4.1 PES

In order to investigate the specifics of cation surface diffusion related to the alloying discussed in the previous section, we consider as a representative system $\text{In}/\text{In}_{2/3}\text{Ga}_{1/3}\text{As}(001)-(2 \times 3)$. This choice was dictated by the stability analysis as shown in Figures 5.11, 5.13, and 5.14. Furthermore, as mentioned already, the $\text{In}_{2/3}\text{Ga}_{1/3}\text{As}(001)-(2 \times 3)$ reconstruction does not fulfill the ECR. This shows up nicely in its electronic spectrum, Figure 5.15. Clearly, one band, associated with the continuous As dimer rows in $[\bar{1}10]$ direction, crosses the Fermi level along the J-K and J'- Γ symmetry lines in the surface BZ, leading to a metallic state. Thus, In diffusion

Table 5.2: Binding energy E_b (eV) of an In adatom at the sites on the $\text{In}_{2/3}\text{Ga}_{1/3}\text{As}(001)$ -(2×3) surface, denoted in Figure 5.16.

	Site								
	\mathbf{A}_1	\mathbf{A}_2	\mathbf{A}_3	\mathbf{T}_1	\mathbf{T}_2	\mathbf{T}_3	\mathbf{T}_4	\mathbf{T}_5	\mathbf{T}_6
E_b	-1.61	-1.56	-1.46	-1.48	-1.39	-1.37	-1.32	-1.29	-1.27

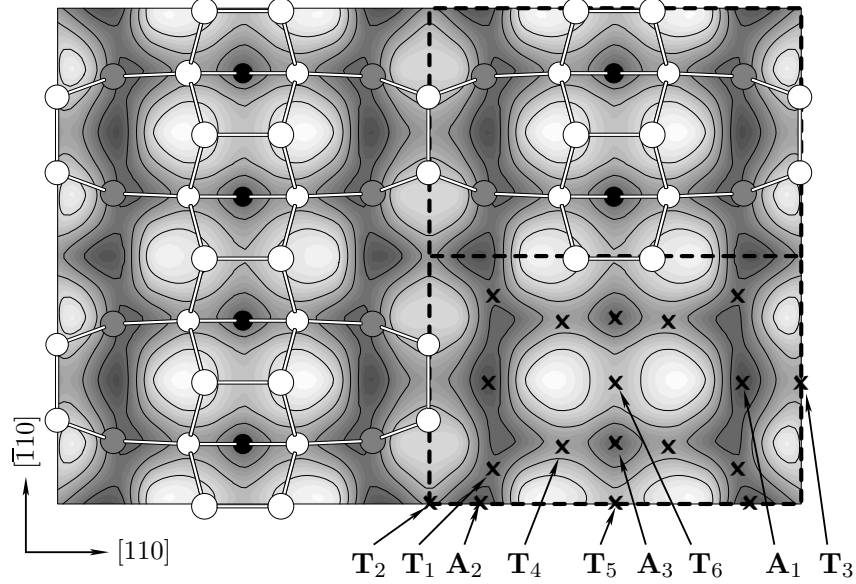


Figure 5.16: Potential-energy landscape for an In adatom on the $\text{In}_{2/3}\text{Ga}_{1/3}\text{As}(001)$ -(2×3) surface. Contour-line spacing is 0.1 eV; atomic positions in the unit cell (dashed rectangles) of the clean surface are indicated for atoms in the upper three layers, cf. also Figure 5.10 (b).

on a metallic, ternary surface alloy may also be considered as a problem on its own merits.

The diffusion problem for an In adatom on the $\text{In}_{2/3}\text{Ga}_{1/3}\text{As}(001)$ -(2×3) surface is pursued within the framework of the method outlined in Chapter 4. Unlike the previous section, now we model the surface by taking 2 surface unit cells stacked in $[\bar{1}10]$ direction, thereby forming a supercell with 4×3 , periodicity and using the Monkhorst-Pack set $\{(\frac{1}{2}, \frac{1}{2}, 0), 2 \times 3 \times 1\}$. This is required in order for us to decouple periodic images of the adsorbate. For the sake of achieving an improved description of substrate-adsorbate binding energy, the PBE-GGA was employed as well. Comparison of the surface geometries as obtained from LDA and PBE optimization is provided in Appendix D, along with the one derived from the X-ray diffraction experiment Ref. [193].

As a first step, we map the PES, Eq. (4.2), as explained in Sec. 4.1, relaxing the indium adatom from $Z \simeq 2 \text{ \AA}$ above the surface, and keeping the bottom double-layer of the slab and the terminating H^* fixed. Since the clean surface symmetry has two mirror planes, we need to map only $1/4$ of the (2×3) unit cell. Accordingly, the constrained relaxation was performed for an equidistant grid of 35 points, and surface symmetry was exploited to assemble the whole PES. For plotting, the set of points has been fitted by a third-order polynomial in the X and Y variables, and the resulting PES is shown in Figure 5.16. Binding energies of the In adatom E_b calculated according to Eq. (4.2) are collected in Table 5.2. The remarkable feature of the PES for indium diffusion is its small “corrugation”. Notice that the maximum difference in calculated binding energy $\max \Delta E_b \simeq 0.5 \text{ eV}$. Within this energy interval, we find 3 (symmetry

inequivalent) potential minima connected via 6 saddle points, which implies small energy barriers ΔE . From the PES and Table 5.2, we conclude that indium adatoms are preferentially adsorbed at the \mathbf{A}_1 site, between the center chemisorbed As dimer and the dimer bound to the third-layer In atoms. Another adsorption site, \mathbf{A}_2 , appears on both sides of the edge chemisorbed As dimer. The troughs between the chemisorbed As dimers give rise to a shallower site \mathbf{A}_3 .

It should be stressed out that the so mapped PES, Figure 5.16, is the lowest energy surface resulting from our particular relaxation procedure. As brought out clearly by Kley *et al.* [199], the interaction of the adatom with the dimer structural motif typical for reconstructed semiconductor surfaces is a crucial process in establishing the relevant diffusion PES. In particular, Kley *et al.* showed that E_b of a Ga adatom coupling to an As dimer on the GaAs(001)- $\beta 2(2 \times 4)$ surface can be significantly increased when the dimer bond splits so as to allow Ga to be inserted in between the two As atoms. The underlying mechanism has been identified to be the replacement of the rather weak surface As-As dimer bond by stronger cation-As bonds, cf. Ref. [5, 199].

The atomic geometry of the $\text{In}_{2/3}\text{Ga}_{1/3}\text{As}(001)-(2 \times 3)$ pseudomorphic film, on the one hand, is characterized by a relatively high density of As dimers. On the other hand, the X-ray diffraction experiment by Sauvage-Simkin *et al.* [194] provided evidence for a highly disordered distribution of the As dimers bonded to the subsurface In atoms. These authors rationalized the observation in terms of a tendency for exposing *nondimerized* As atoms, which would cause the ECR to be obeyed, and thus render the surface semiconducting. For a valid description of In diffusion by the PES shown in Figure 5.16, we therefore have to check if reaction of In with the As-As bonds can lead to more stable binding sites for In than the minima of the PES. To this end, we have recalculated E_b at the \mathbf{T}_3 , \mathbf{T}_5 , and \mathbf{T}_6 sites. As a result, it turned out that dimer splitting indeed lowered the energy at the \mathbf{T}_3 site to $E_b = -1.5$ eV, but such an effect was not found for either of the \mathbf{T}_5 and \mathbf{T}_6 sites related to the topmost layer (“chemisorbed”) As dimers. Even though bonding at the \mathbf{T}_3 is strengthened this process does not lead to appearance of a new stable adsorption site; in fact, an In adatom that has been caught in such a bonding configuration would rather “tip” in the [110] direction and fall into the most stable \mathbf{A}_1 site. Detailed analysis of the reaction of In with surface As-As bonds will be carried out later on, in Sec. 6.3. On the basis of the above remarks, we justify the use of the “conventional” PES in Figure 5.16 in applying the random walk formalism.

5.4.2 Diffusion coefficients

The procedure for working out the diffusion characteristics of a single adatom was described in Sec. 4.2. Accordingly we map a 2D translationally invariant lattice onto the set of adsorption sites as located in Figure 5.16. Because of the $mm2$ plane symmetry of the (2×3) surface unit cell there are $N_b = 6$ adsorption sites in total: \mathbf{A}_1 , $\mathbf{A}_{1'}$, \mathbf{A}_2 , \dots , $\mathbf{A}_{3'}$ (notice that in Figure 5.16 the primed site labels were omitted for the sake of clarity). The random walk process on the network thus defined is sketched in Figure 5.17. Therefore, in order to derive the diffusion tensor $D_{\alpha\beta}^*$ of the In adatom, we have to deal with the six-dimensional eigenvalue problem of the transition rate matrix Γ_{ij} , Eq. (4.15). The master equation for the probability vector $\mathbf{P} = (P_1, P_{1'}, \dots, P_{3'})^T$, set up according to Figure 5.17, leads to the following rather general form of Γ_{ij} ,

$$\Gamma_{ij}(\mathbf{q}) = \begin{pmatrix} -\Sigma_1 & e^{ip}\Gamma_{11} & (1 + e^{-iq})\Gamma_{12} & 0 & \Gamma_{13} & \Gamma_{13} \\ e^{-ip}\Gamma_{11} & -\Sigma_1 & 0 & (1 + e^{-iq})\Gamma_{12} & \Gamma_{13} & \Gamma_{13} \\ (1 + e^{iq})\Gamma_{21} & 0 & -\Sigma_2 & e^{ip}\Gamma_{22} & \Gamma_{23} & e^{iq}\Gamma_{23} \\ 0 & (1 + e^{iq})\Gamma_{21} & e^{-ip}\Gamma_{22} & -\Sigma_2 & \Gamma_{23} & e^{iq}\Gamma_{23} \\ \Gamma_{31} & \Gamma_{31} & \Gamma_{32} & \Gamma_{32} & -2\Sigma_3 & (1 + e^{iq})\Gamma_{33} \\ \Gamma_{31} & \Gamma_{31} & e^{-iq}\Gamma_{32} & e^{-iq}\Gamma_{32} & (1 + e^{-iq})\Gamma_{33} & -2\Sigma_3 \end{pmatrix}, \quad (5.6)$$

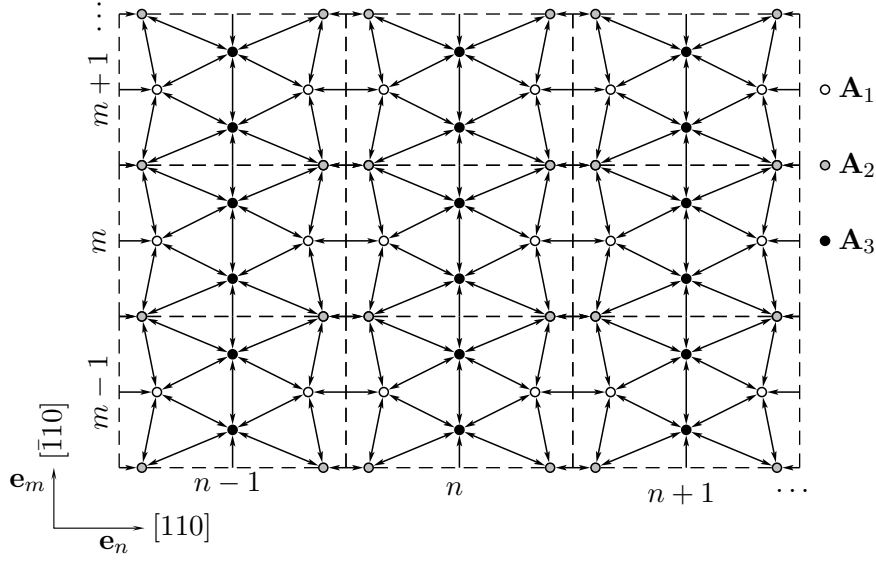


Figure 5.17: Network of binding sites for In adatom on the In_{2/3}Ga_{1/3}As(001)- (2×3) surface according to Figure 5.16, cf. also Figure 4.2 on page 33.

where the diagonal terms read

$$\Sigma_1 = \Gamma_{11} + 2\Gamma_{21} + 2\Gamma_{31}, \quad \Sigma_2 = 2\Gamma_{12} + \Gamma_{22} + 2\Gamma_{32}, \quad \text{and} \quad \Sigma_3 = \Gamma_{13} + \Gamma_{23} + \Gamma_{33}.$$

According to Eq. (4.29), we need to work out the first two coefficients in the characteristic polynomial of (5.6). Although this is a tractable problem for software like MATHEMATICA[®] [200], the result is rather lengthy for any analytic analysis, and one has to seek for simplifying arguments requiring knowledge of all transition rates Γ_{ij} , which is beyond the scope of the present work. Nevertheless, we can assume that, *e.g.*, it is more likely for an In adatom at site A_3 to escape towards a neighboring A_1 site rather than A_2 when crossing the saddle point T_4 , as the latter route also requires crossing of T_1 . By the same token, we neglect reverse jumps, thus setting $\Gamma_{32} = \Gamma_{23} = 0$ in Eq. (5.6). Furthermore, the coordinate transformation matrix $B_{\alpha\beta} = e_{\alpha,\beta}$ has the simple diagonal form

$$\mathbf{B} = \begin{pmatrix} 3 & 0 \\ 0 & 2 \end{pmatrix} \frac{a_0}{\sqrt{2}}, \quad (5.7)$$

where, since the InGaAs(001)- (2×3) film is pseudomorphic to the GaAs substrate, a_0 is the equilibrium bulk lattice constant of GaAs, Table 3.1. Hence, from Eqs. (4.29), (4.28), and (5.7) within the assumptions made, we obtain the In diffusion coefficients in Cartesian coordinates,

$$D_{[110]}^* \simeq \frac{9\Gamma_{12}\Gamma_{13}\Gamma_{31}[\Gamma_{21}\Gamma_{22} + \Gamma_{11}(\Gamma_{12} + \Gamma_{22})]}{4[\Gamma_{21}\Gamma_{22} + \Gamma_{11}(\Gamma_{12} + \Gamma_{22}) + \Gamma_{31}(\Gamma_{12} + \Gamma_{22})][\Gamma_{13}\Gamma_{21} + \Gamma_{31}(\Gamma_{13} + \Gamma_{31})]} a_0^2 \quad (5.8)$$

$$D_{[110]}^* \simeq \frac{\Gamma_{12}[\Gamma_{21}\Gamma_{13}^2 + (2\Gamma_{21} + \Gamma_{31})\Gamma_{33}\Gamma_{13} + 3\Gamma_{31}\Gamma_{33}^2]}{[\Gamma_{13}\Gamma_{21} + \Gamma_{12}(\Gamma_{13} + \Gamma_{31})][\Gamma_{13} + 2\Gamma_{33}]} a_0^2. \quad (5.9)$$

The structure of these expressions could be described as a ratio between the rates for different sequences of jump processes. Consequently, further simplifications may result from the smallness of any Γ_{ij}/Γ_{kl} terms in Eqs. (5.8)–(5.9). For example, let us consider the $A_1 \rightarrow A_3$, $A_1 \rightarrow A_2$, and $A_3 \rightarrow A_1$ transitions. From Table 5.2, one can estimate the corresponding diffusion barriers,

$$\Delta E(A_1 - T_4) \simeq 0.3 \text{ eV}, \quad \Delta E(A_1 - T_1) \simeq 0.1 \text{ eV}, \quad \Delta E(A_3 - T_4) \simeq 0.15 \text{ eV}.$$

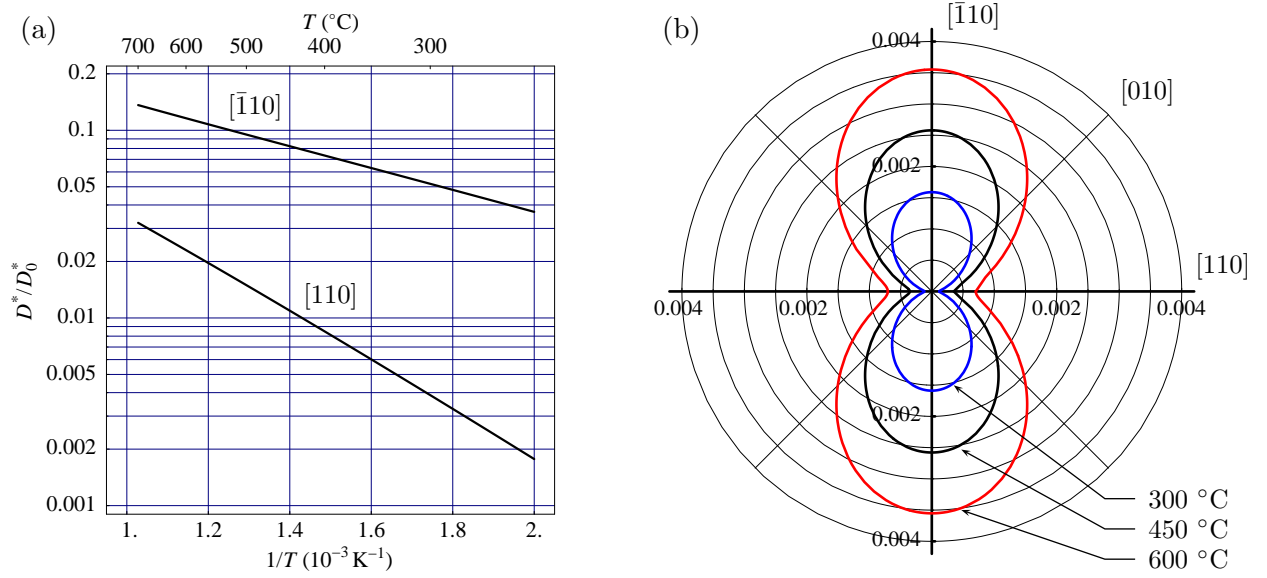


Figure 5.18: (a) Van't Hoff-Arrhenius plot of D^* normalized to $D_0^* = a_0^2 \Gamma^{(0)} \simeq 3 \times 10^{-2} \text{ cm}^2/\text{s}$; (b) Polar plot of $D_{eff}^*(\mathbf{n})$ according to Eq. (5.14) for three different temperatures.

For simplicity we may assume that the attempt frequencies $\Gamma_{fi}^{(0)}$ for these jumps are of the same order of magnitude. It is then easy to work out that at $T = 450 \text{ }^\circ\text{C}$

$$\Gamma_{31}/\Gamma_{13} \sim 0.1, \quad \Gamma_{31}/\Gamma_{21} \sim 0.05,$$

which, in principle, can be used for getting a more approximate analytic form of $D_{[110]}^*$ and $D_{[\bar{1}10]}^*$.

It is, however, more instructive and useful to provide a numerical estimate based on expressions (5.8)–(5.9). The problem one encounters in such an evaluation is related to the necessity of knowing the numerical values of the frequency prefactors $\Gamma_{fi}^{(0)}$. But even they were *a priori* known accurately, the uncertainty in the calculated binding energies $\sim \pm 0.01 \text{ eV}$ would result in an “exponentially large” uncertainty $\exp(\pm 0.02/k_B T)$ in the jump rates Γ_{fi} , which at the typical growth temperatures is a factor ~ 2 . Therefore for the qualitative analysis, it is more important to obtain an order estimate for $\Gamma_{fi}^{(0)}$. This can be achieved, *e.g.*, from the Debye temperature Θ_D of the substrate material, as $\Gamma_{fi}^{(0)} \sim k_B \Theta_D / 2\pi \hbar$, or from the maximum phonon frequency, which are typically quantities $\sim 10^{13} \text{ s}^{-1}$. In the following, we shall use this value in order to calculate the jump rates involved in Eqs. (5.8)–(5.9),

$$\Gamma_{fi} := 10^{13} \text{ s}^{-1} \times \exp \left[-\Delta E(\mathbf{A}_i \xrightarrow{\mathbf{T}_k} \mathbf{A}_f) / k_B T \right], \quad (5.10)$$

with diffusion barriers ΔE read from Table 5.2. For example, at $T = 450 \text{ }^\circ\text{C}$ we find from (5.10) for the Γ 's (in s^{-1}):

Γ_{11}	Γ_{12}	Γ_{21}	Γ_{22}	Γ_{13}	Γ_{31}	Γ_{33}
2.1×10^{11}	2.8×10^{12}	1.2×10^{12}	6.5×10^{11}	1.1×10^{12}	9.5×10^{10}	4.7×10^{11}

Now substituting Eq. (5.10) in (5.8) and (5.9), it is straightforward to obtain the temperature dependence of $D_{[110]}^*$ and $D_{[\bar{1}10]}^*$, which allows us to determine the effective energy barriers ΔE^{eff} associated with In diffusion along the $[110]$ and $[\bar{1}10]$ directions from the Van't

Hoff-Arrhenius-type relations

$$D_{[110]}^*(T) = D_0^* \exp\left(-\Delta E_{[110]}^{\text{eff}}/k_B T\right), \quad D_{[\bar{1}10]}^*(T) = D_0^* \exp\left(-\Delta E_{[\bar{1}10]}^{\text{eff}}/k_B T\right), \quad (5.11)$$

with $D_0^* = a_0^2 \Gamma^{(0)} = \text{const.}$ A semilogarithmic plot of (5.11) over the experimentally relevant temperature range is given in Figure 5.18 (a). As can be seen, within the assumptions made, indium diffusion on the $\text{In}_{2/3}\text{Ga}_{1/3}\text{As}(001)-(2 \times 3)$, is essentially anisotropic, with $[\bar{1}10]$, *i.e.* along the continuous As dimer rows (Figure 5.16), being the fast diffusion direction. From the slopes of the lines, Figure 5.18 (a), we determine

$$\Delta E_{[110]}^{\text{eff}} = 0.29 \text{ eV}, \quad \Delta E_{[\bar{1}10]}^{\text{eff}} = 0.13 \text{ eV}. \quad (5.12)$$

Visual inspection of Figure 5.18 (a) also shows that within the temperature range considered $D_{[110]}^*$ is always smaller in value than $D_{[\bar{1}10]}^*$. For example, at $T = 450^\circ\text{C}$, the diffusion anisotropy ratio, defined as $D_{[110]}^*/D_{[\bar{1}10]}^*$, is about 0.1.

Now let us recall that by definition, Eq. (4.4), $D_{\alpha\beta}^*$ is *symmetric* tensor of rank 2. In analogy to vector analysis, one can consider the *normal component* of $D_{\alpha\beta}^*$ along an arbitrary unit vector \mathbf{n} within the (001) surface plane, defined as

$$\mathbf{n} \cdot \mathbf{D}^* \cdot \mathbf{n} = D_{\alpha\beta}^* n_\alpha n_\beta, \quad \|\mathbf{n}\| = 1. \quad (5.13)$$

On the other hand, we showed that $x \parallel [110]$ and $y \parallel [\bar{1}10]$ are the principle axes of the $D_{\alpha\beta}^*$ tensor. Therefore the normal component (5.13) reaches extremal values in these crystallographic directions, being equal to the eigenvalues $D_{[110]}^*$ and $D_{[\bar{1}10]}^*$, as given by Eqs. (5.8) and (5.9), respectively. Thus, if ϕ is the polar angle in the (001) surface plane measured with respect to the $[110]$ direction, $\mathbf{n} = (n_x, n_y) = (\cos \phi, \sin \phi)$, we can rewrite Eq. (5.13) as

$$\mathbf{n} \cdot \mathbf{D}^* \cdot \mathbf{n} = D_{[110]}^* \cos^2 \phi + D_{[\bar{1}10]}^* \sin^2 \phi.$$

As a result, with the help of this quantity we can conveniently reformulate the problem of In adatom diffusion on the (001) plane in terms of a single, angle-dependent “effective” diffusion coefficient D_{eff}^* (see also the contribution by H. Bonzel in Ref. [121]), identified with the normal component of the tracer diffusion tensor,

$$D_{\text{eff}}^*(\mathbf{n}) := \mathbf{n} \cdot \mathbf{D}^* \cdot \mathbf{n}. \quad (5.14)$$

A representative plot of this simple expression is given in Figure 5.18 (b) for three different temperatures.

Finally, we should mention that all considerations in this section referred to In diffusion on the *commensurate* (2×3) reconstruction for which the In-Ga ordering “locks” the In composition in the first subsurface cation layer to $x = 2/3$ [145]. We thus expect that as long as the same cation configuration is preserved in this subsurface layer, the PES in Figure 5.16 would approximately describe In diffusion on thicker layers as well, $\theta > 2/3$ ML. The above results, however, are not applicable to the case of *incommensurate* $(2 \times m)$ “phases”, with $m \leq 3$, that are believed to be realized through local “stacking faults” in the local ordering of the In-rich blocks (see Appendix D). Given also the overall disorder in the InGaAs(001) WL, any more detailed analysis appears to be hardly achievable. Yet, as we shall see in Chapter 7 these results are of particular value when comparing with In diffusion on the bare GaAs(001).

Chapter 6

Indium diffusion on the bare GaAs(001)- $c(4 \times 4)$ substrate

6.1 Introduction

From the technological point of view, formation of the pseudomorphic WL, discussed in Chapter 5, is the “elementary” process preceding the formation of 3D coherent islands during InAs/GaAs(001) heteroepitaxy. As it is homogeneously strained to match the lattice constant of the underlying GaAs(001) substrate, diffusion on such a film is only a particular case of adatom migration where the strain ε enters the problem as a *constant* parameter. However, once the islands are nucleated they continue to grow, incorporating material also from the WL. As discussed in Sec. 3.3.2, these islands are themselves under compressive strain, whereas the substrate beneath is expanded. As a consequence of this expansion, the substrate surface *around* an island is under *compressive* strain. These features were also clearly demonstrated in the elastic problem for a long flat island considered in Sec. 3.4, see Figure 3.5 on page 30. Supply of further material to the growing island would be then governed by diffusion through this ring-shaped area of compressive strain. On the other hand, in the growth of multisheet arrays of QDs, the *tensile* strain on the capping layer in the regions above the buried islands [115, 170] may again affect the growth kinetics of the next layer of islands to be formed on the capping layer.

From the limited published data about strain effects on diffusion, it appears surprising that compressive surface strain could lead to a self-limiting effect on the island growth. First-principles calculations for diffusion on close-packed metal surfaces, in particular Ag/Ag(111), Ref. [35, 201], have demonstrated that compressive strain increases the adatom diffusivity by reducing the diffusion barrier. Schroeder and Wolf [202] have extended this finding to diffusion

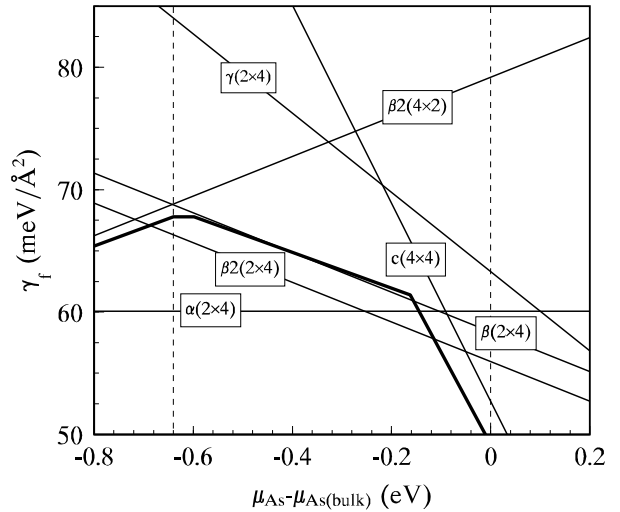


Figure 6.1: Formation energy γ_f of InAs film with $\theta = 1$ ML on the GaAs(001) surface (thin lines). Formation energy of 3D pyramidal islands + γ of the bare reconstructed GaAs(001) surface is indicated with the thick line (reproduced from Ref. [150] with the kind permission of the authors, ©2000 JSAP).

on (001) surfaces of simple cubic, fcc, and bcc lattices. Recent molecular dynamics (MD) simulations using empirical potentials showed the same trend for Ga, In, and As adatom diffusion on a (2×1) -reconstructed GaAs(001) surface [32]. These results also agree with an earlier study of Ga kinetics on the strained GaAs(001) surface [31]. A different strain dependence of diffusion was found, however, for Si adatom [203, 204] and dimer [205] diffusion on the Si(001) surface, where tensile strain leads to an overall decrease in the diffusion barriers. Yet, the majority of the theoretical studies on semiconductor systems provide only scarce quantitative information about the influence of strain on the diffusion process.

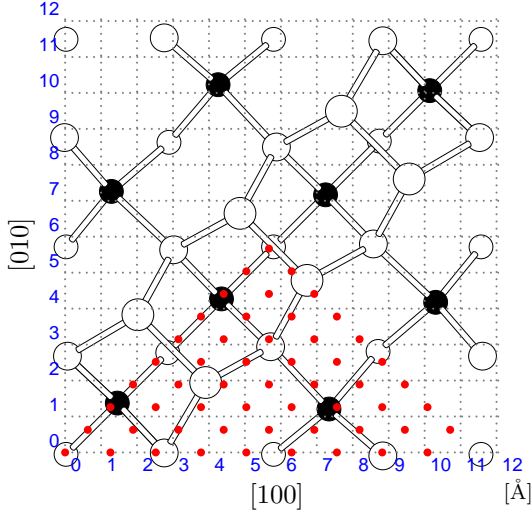
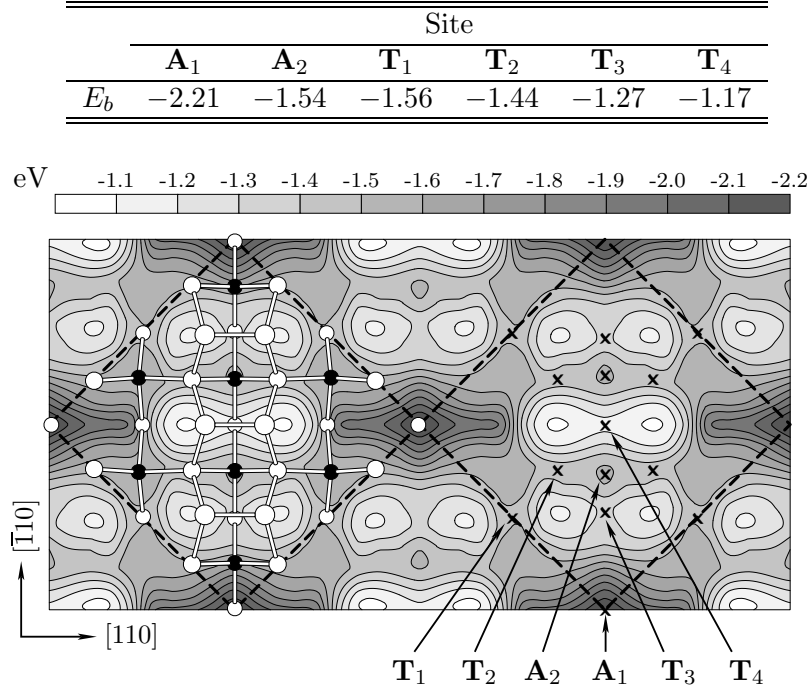


Figure 6.2: Equidistant grid of 54 points (X, Y) used for mapping the PES for In on the GaAs(001)- $c(4 \times 4)$ surface. Because of the $mm2$ plane symmetry (c -rectangular Bravais lattice) one needs to sample only $1/4$ of the surface unit cell. The final “map” is then assembled by applying the symmetry operations, *e.g.*, two reflections in the $m_{[110]}$ and $m_{[\bar{1}\bar{1}0]}$ mirror planes.

According to Figure 6.1, In deposition under high As overpressure is expected to lead to direct formation of 3D InAs islands: notice that for $\mu_{\text{As}} - \mu_{\text{As(bulk)}} \in (-0.12, 0)$ eV the energy of InAs islands + bare GaAs(001)- $c(4 \times 4)$ substrate (the thick line) is lower than γ_f of 1 ML thick InAs film with either the $\beta 2(2 \times 4)$ or $c(4 \times 4)$ reconstruction.

The mapping of the PES for In diffusion on the unstrained GaAs(001)- $c(4 \times 4)$ surface was performed with identical settings as in Sec. 5.4, and is presented in Sec. 6.2; Figure 6.2 shows the set of equidistant grid points in the (001) plane used in the PES mapping. As a reference for calculating the binding energy of the adatom according to Eq. (4.2) for $\varepsilon \neq 0$ we have used the sum of the total energy of the properly strained bare surface and the energy of a free, spin-polarized In atom (cf. Appendix A). In Sec. 6.3, we discuss in great detail the In adatom interaction with the surface As dimers, thus extending results for the case of In/InGaAs(001)- (2×3) . The effect of strain is then addressed in Sec. 6.4. In order to investigate the influence of strain on surface diffusion, the lateral lattice constant a was uniformly changed in the range of $\pm 8\%$ around its value a_0 calculated for the unstrained material, thus defining the isotropic surface strain tensor $\varepsilon_{\alpha\beta} = \varepsilon \delta_{\alpha\beta}$, with $\varepsilon = a/a_0 - 1$, relaxing the system again in the same manner, and recording the In binding energy for the relevant sites on the PES.

The aim of this chapter is, thus, to report the results of DFT calculations for the *tracer* diffusion of a single In adatom in the presence of a strain field $\varepsilon(\mathbf{r}_{\parallel})$ in the surface [206]. In particular, we investigate the strain dependence of In diffusion on the bare GaAs(001)- $c(4 \times 4)$ surface, cf. Figure 5.3 (a) on page 48. We have chosen this reconstruction because, as seen from Figure 5.1, it forms the substrate for the initial stages of InAs deposition for temperatures $T \lesssim 500$ °C. Therefore, on the one hand, we can use this system to study the conventional diffusion (*i.e.* on a strain-free surface) of the first In atoms in the formation of the WL. On the other hand, we could employ the $c(4 \times 4)$ reconstruction to model also the surface of the strained capping/spacer GaAs layer with buried islands in the growth of 3D stacks of QDs, where the strain field due to the latter is usually approximated by Eq. (3.34). Importantly, from the recent study of Wang *et al.* [150], Figure 6.1, we could further speculate that the problem of In diffusion on the strained bare GaAs(001)- $c(4 \times 4)$ surface appears under very arsenic-rich growth conditions. Ac-

Table 6.1: Binding energy E_b (eV) of an In adatom at the sites on the GaAs(001)- $c(4 \times 4)$ surface, denoted in Figure 6.3.**Figure 6.3:** Potential-energy landscape for an In adatom on the GaAs(001)- $c(4 \times 4)$ surface. The adatom is relaxed from 2 Å above the surface. Atomic positions are indicated for atoms in the upper four layers (As: empty circles; Ga: filled circles), and the dashed squares show the surface unit cell.

6.2 Diffusion on the unstrained substrate

6.2.1 PES

The mapping procedure resulted in the PES shown in Figure 6.3, and the binding energies of the In adatom at the adsorption sites (\mathbf{A}_i) and saddle points (\mathbf{T}_k) are given in Table 6.1. The In adatom, like Ga/GaAs(001)- $c(4 \times 4)$ (cf. Subsection 6.2.3), preferentially adsorbs at the four-fold coordinated hollow site \mathbf{A}_1 (the missing dimer position), where it interacts with the dangling bonds of the second layer As atoms. Two other very shallow minima \mathbf{A}_2 are located in between the center and the two edge dimers. Jumps between the adsorption sites occur through four symmetry-inequivalent saddle points \mathbf{T}_k , with \mathbf{T}_1 being lowest in energy. In comparison to the PES for In diffusion on the $\text{In}_{2/3}\text{Ga}_{1/3}\text{As}(001)-(2 \times 3)$ surface, Figure 5.16, it becomes evident that In migration on the GaAs(001)- $c(4 \times 4)$ substrate is governed by a substantially more “corrugated” PES—as can be easily read off Figure 6.3, in the present case $\max \Delta E_b \simeq 1.1$ eV, about twice that found for the former PES, Figure 5.16.

In a simplified picture, the In adatom migrates by a random walk on a 2D square lattice defined by the \mathbf{A}_1 sites, Figure 6.4. Thus, from the viewpoint of network connectivity, this is the simplest possible case. However, we account for hops between them via both \mathbf{T}_1 and \mathbf{T}_2 - \mathbf{A}_2 - \mathbf{T}_2 (gray arrows in Figure 6.4), with rates Γ_{11} and $\tilde{\Gamma}_{11}$, respectively. Indeed, once the In adatom has reached the \mathbf{A}_2 site, it needs to overcome a barrier $E(\mathbf{T}_2) - E(\mathbf{A}_2)$ of only 0.1 eV in order to move towards a neighboring \mathbf{A}_1 site. As $E(\mathbf{T}_2) - E(\mathbf{A}_2) \lesssim 2k_B T$ for typical growth temperatures, the adatom is unlikely to equilibrate at the shallow well \mathbf{A}_2 before it escapes.

Thus, it is justifiable to use a single rate $\tilde{\Gamma}_{11}$ for the whole path $\mathbf{T}_2\text{-}\mathbf{A}_2\text{-}\mathbf{T}_2$.

6.2.2 Diffusion coefficients

Effective diffusion coefficients can now be extracted by again applying the random walk formalism from Sec. 4.2. Because of the simple diffusion network with $N_b = 1$, Figure 6.4, the problem is now reduced to finding dynamics of a single scalar quantity—the probability P_1 . Accordingly, the transition rate “matrix” (4.15) also reduces to a single element,

$$\Gamma(\mathbf{q}) = -4(\Gamma_{11} + \tilde{\Gamma}_{11}) + 2\Gamma_{11}[\cos(p) + \cos(q)] + 4\tilde{\Gamma}_{11} \cos(p - q). \quad (6.1)$$

Hence, using the coordinate transformation matrix

$$\mathbf{B} = \begin{pmatrix} 1 & 1 \\ -1 & 1 \end{pmatrix} \sqrt{2}a_0, \quad (6.2)$$

and Eqs. (4.29)–(4.28), it is easily shown that the diffusion tensor in Cartesian coordinates reads

$$D_{\alpha\beta}^* = \begin{pmatrix} D_{[110]}^* & 0 \\ 0 & D_{[\bar{1}10]}^* \end{pmatrix} = 4a_0^2 \begin{pmatrix} \Gamma_{11} + 4\tilde{\Gamma}_{11} & 0 \\ 0 & \Gamma_{11} \end{pmatrix}. \quad (6.3)$$

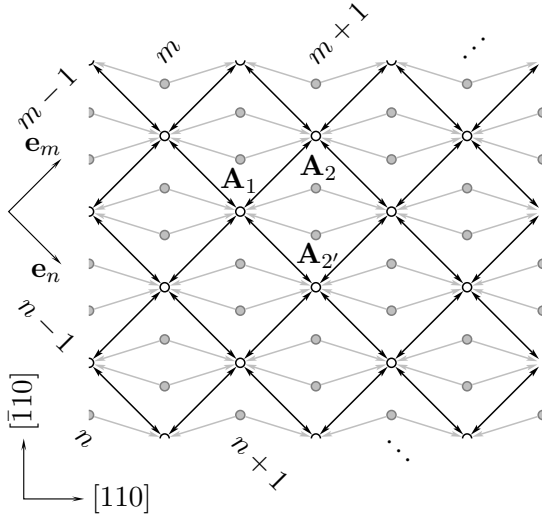


Figure 6.4: Network of binding sites for In adatom on the GaAs(001)-c(4×4) surface, cf. also Figure 6.3.

(cf. Figure 6.3, and Table 6.1). It is now tempting to perform a similar numerical estimate as it was done for In diffusion on the $\text{In}_{2/3}\text{Ga}_{1/3}\text{As}(001)\text{-(}2 \times 3\text{)}$ surface, Subsection 5.4.2. The present case is considerably simpler. One needs to know in addition only the frequency prefactors $\Gamma_{11}^{(0)}$ and $\tilde{\Gamma}_{11}^{(0)}$. Assuming that they differ inessentially, we have calculated $\Gamma_{11}^{(0)}$ using the harmonic approximation (Sec. 4.3) for the lattice vibrations and a force-constant matrix involving only the degrees of freedom [5, 136] of the In adatom, and found $\Gamma_{11}^{(0)} \simeq 1.5 \text{ THz}$ ($\simeq 0.2 \times 10^{13} \text{ s}^{-1}$) which was used to evaluate the diffusion coefficients. The resulting temperature dependence of $D_{[110]}^*$ and $D_{[\bar{1}10]}^*$ is shown in Figure 6.5 (a). It is immediately apparent that diffusion anisotropy is much less pronounced than in the case of diffusion on the $\text{In}_{2/3}\text{Ga}_{1/3}\text{As}(001)\text{-(}2 \times 3\text{)}$ surface, Figure 5.18 (a). This is also well manifested in the polar plot Figure 6.5 (b). For example, at

The factor “4” with $\tilde{\Gamma}_{11}$ is partly due to the fact that there exist two equivalent $\mathbf{T}_2\text{-}\mathbf{A}_2\text{-}\mathbf{T}_2$ paths across the block of three dimers. Another factor two enters because the In adatom travels a $\sqrt{2}$ -times longer distance than along the path crossing the saddle \mathbf{T}_1 , in the $[110]$ direction to reach a neighboring \mathbf{A}_1 site. Equation (6.3) thus implies that an isolated In adatom migrates slightly faster in $[110]$ direction, across the dimer rows, than along the dimer rows in $[\bar{1}10]$ direction, with an anisotropy ratio

$$\frac{D_{[110]}^*}{D_{[\bar{1}10]}^*} = 1 + 4 \frac{\tilde{\Gamma}_{11}}{\Gamma_{11}}. \quad (6.4)$$

The related diffusion barriers entering the rates Γ_{11} , and $\tilde{\Gamma}_{11}$ are, respectively,

$$\Delta E = 0.65 \text{ eV}, \quad \Delta \tilde{E} \simeq 0.8 \text{ eV}$$

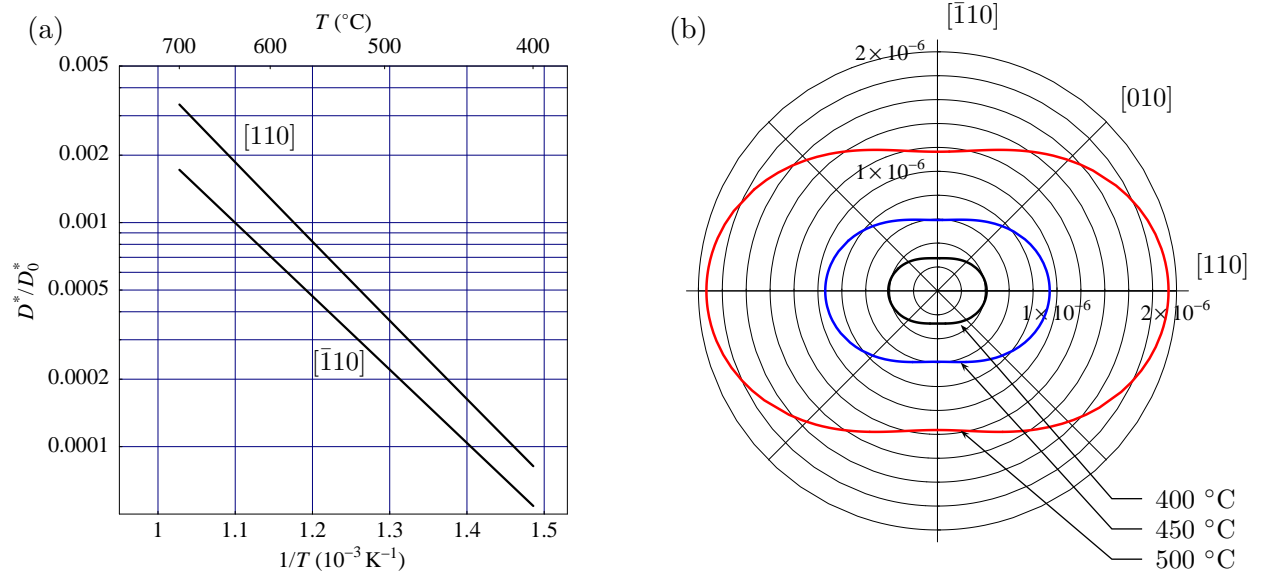


Figure 6.5: (a) Van't Hoff-Arrhenius plot of D^* normalized to $D_0^* = a_0^2 \Gamma^{(0)} \simeq 5 \times 10^{-3} \text{ cm}^2/\text{s}$; (b) Polar plot of $D_{\text{eff}}^*(\mathbf{n})$ according to Eq. (5.14) for three different temperatures with $D_{[110]}^*$ and $D_{[\bar{1}10]}^*$ from Eq. (6.3).

$T = 450 \text{ }^\circ\text{C}$, $D_{[110]}^*/D_{[\bar{1}10]}^*$ exceeds unity by about 50 %, which gives also an estimate for the contribution of the $\mathbf{A}_1 \xrightarrow{\mathbf{A}_2} \mathbf{A}_1$ route. Nevertheless, as can be seen from Figure 6.5 (a), the slopes of the two lines are nearly the same and, therefore we infer similar effective diffusion barriers in both the $[110]$ and $[\bar{1}10]$ directions, being practically that for the $\mathbf{A}_1 \xrightarrow{\mathbf{T}_1} \mathbf{A}_1$ route, $\Delta E^{\text{eff}} \simeq 0.65 \text{ eV}$.

At sufficiently low temperatures, however, one should include \mathbf{A}_2 in the 2D network of sites, Figure 6.4, and consider branching of the diffusion pathways towards neighboring \mathbf{A}_1 or \mathbf{A}_2 sites. Although an analytic result for $D_{\alpha\beta}^*$ can still be derived in this case, the expressions are rather cumbersome and one has to seek for simplifications as already discussed for In diffusion on the $\text{In}_{2/3}\text{Ga}_{1/3}\text{As}(001)-(2 \times 3)$ surface, Subsection 5.4.2.

6.2.3 Comparison with Ga diffusion on GaAs(001)- $c(4 \times 4)$

Recently LePage *et al.* [207] carried out a combined first-principles (within the LDA) and kinetic Monte Carlo (kMC) study of Ga diffusion on the GaAs(001)- $c(4 \times 4)$ surface; cf. also Ref. [208]. The PES for Ga is shown in Figure 6.6 (a), and on panel (b) we have sketched the corresponding network of sites relevant for the random walk formalism. Upon visual inspection of Figure 6.3 and Figure 6.6 (a), it appears that indium diffuses on a less corrugated PES, although the relevant diffusion barriers for In are higher than those for Ga. At the \mathbf{A}_1 site, which is the most stable for both In and Ga, the In adatom is less bound than Ga by $\approx 0.8 \text{ eV}$. Furthermore, the $c(4 \times 4)$ PES provides two additional adsorption sites for Ga as compared to In: between the edge dimers, \mathbf{A}_3 in Figure 6.6 (b), as well as in between the dimer vacancy and the center dimer along $[110]$, \mathbf{A}_2 in Figure 6.6 (b). At the \mathbf{A}_3 site, Ga is more strongly bound than In by 1.0 eV .

These differences can be rationalized easily in terms of the differences in the cation-As bond strength in the corresponding binary compounds (GaAs, InAs) and the larger ionic radius R_{In}^i of indium; for example, at four-fold coordination $R_{\text{In}^{3+}}^i/R_{\text{Ga}^{3+}}^i \simeq 1.3$ [209]. We note, however, that part of the difference is to be attributed to the use of the LDA in Ref. [207]. The cohesive energy per cation-As pair (see also Appendix A) is lowest for InAs ($E_{\text{coh}}^{\text{InAs}} = 6.20 \text{ eV}$), as compared to

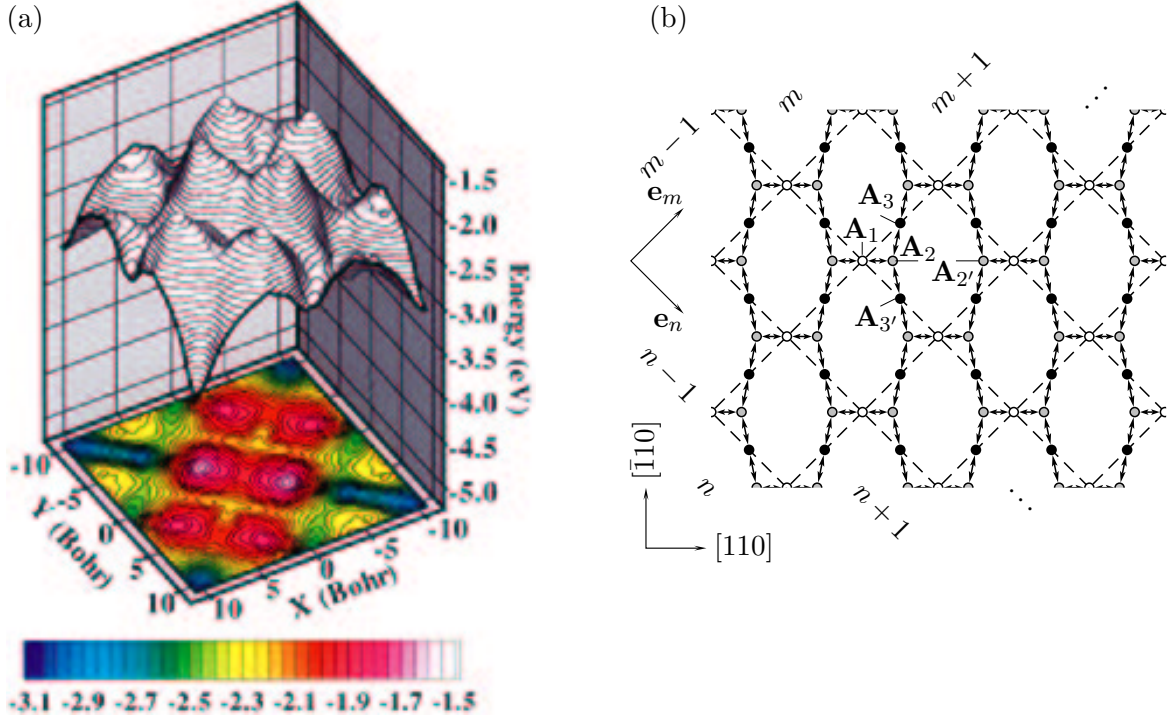


Figure 6.6: (a) (color) Potential-energy landscape for a Ga adatom on the GaAs(001)- $c(4 \times 4)$ surface, calculated by LePage *et al.* [207] (reproduced with the kind permission of the authors, ©1998 APS). (b) Network of binding sites for the Ga adatom as deduced from Ref. [207].

GaAs ($E_{\text{coh}}^{\text{GaAs}} = 6.52$ eV) and AlAs ($E_{\text{coh}}^{\text{AlAs}} = 7.56$ eV). The barriers for diffusion of group-III cations on the GaAs surface generally follow the trend given by the binding energies, as has also been observed in a first-principles study of Ga and Al diffusion on the GaAs(001)- $\beta 2(2 \times 4)$ surface [199].

In analogy to the previous subsection, we can derive the 5×5 transition rate matrix corresponding to the network in Figure 6.6 (b). Note that no jumps between \mathbf{A}_1 and \mathbf{A}_3 are considered, and therefore Γ_{13} , Γ_{31} terms are not present:

$$\Gamma_{ij}(\mathbf{q}) = \begin{pmatrix} -2\Gamma_{21} & \Gamma_{12} & e^{i(p+q)}\Gamma_{12} & 0 & 0 \\ \Gamma_{21} & -(\Gamma_{12} + 2\Gamma_{32}) & 0 & \Gamma_{23} & \Gamma_{23} \\ e^{-i(p+q)}\Gamma_{21} & 0 & -(\Gamma_{12} + 2\Gamma_{32}) & e^{-ip}\Gamma_{23} & e^{-iq}\Gamma_{23} \\ 0 & \Gamma_{32} & e^{ip}\Gamma_{32} & -2\Gamma_{23} & 0 \\ 0 & \Gamma_{32} & e^{iq}\Gamma_{32} & 0 & -2\Gamma_{23} \end{pmatrix}. \quad (6.5)$$

As a result, the tracer diffusion tensor for the Ga adatom in Cartesian coordinates reads

$$\begin{aligned} D_{\alpha\beta}^* &= \begin{pmatrix} D_{[110]}^* & 0 \\ 0 & D_{[\bar{1}10]}^* \end{pmatrix} \\ &= 2a_0^2 \begin{pmatrix} \frac{\Gamma_{12}\Gamma_{21}\Gamma_{23}\Gamma_{32}}{(\Gamma_{12} + 2\Gamma_{32})[\Gamma_{12}\Gamma_{23} + 2\Gamma_{21}(\Gamma_{23} + \Gamma_{32})]} & \\ 0 & \frac{\Gamma_{21}\Gamma_{23}\Gamma_{32}}{\Gamma_{12}\Gamma_{23} + 2\Gamma_{21}(\Gamma_{23} + \Gamma_{32})} \end{pmatrix}. \end{aligned} \quad (6.6)$$

The diffusion anisotropy then adopts the simple form

$$\frac{D_{[110]}^*}{D_{[\bar{1}10]}^*} = \frac{1}{1 + 2\Gamma_{32}/\Gamma_{12}}. \quad (6.7)$$

Note that Eqs. (6.6)–(6.7) are exact within the random walk formalism. On the other hand, numerical values are available from the kMC simulation by LePage *et al.* [207] employing a site-independent frequency prefactor [210], $\Gamma_{fi}^{(0)} \equiv \Gamma^{(0)} := k_B T / \pi \hbar$. At $T = 200$ °C, the diffusion coefficients of Ga on the GaAs(001)-c(4 × 4) surface were found to be

$$D_{[110]}^* = 1.66 \times 10^{-8} \text{ cm}^2/\text{s}, \quad \text{and} \quad D_{[\bar{1}10]}^* = 1.74 \times 10^{-8} \text{ cm}^2/\text{s}, \quad (6.8)$$

which led the authors to infer an isotropic surface diffusion of the Ga adatom, $D_{[110]}^*/D_{[\bar{1}10]}^* \sim 1$.

Now, taking into account that¹ $\Gamma_{32}/\Gamma_{12} \sim 10^{-3}$, we find that the kMC result is compatible with Eq. (6.7), which can also be rewritten as

$$\frac{D_{[110]}^*}{D_{[\bar{1}10]}^*} \simeq 1 - O(\Gamma_{32}/\Gamma_{12}). \quad (6.9)$$

Consequently, given the essentially isotropic Ga migration, the tracer diffusion tensor, Eq. (6.6), reduces to the simple form (4.5) with

$$D^* \approx 2 \frac{\Gamma_{21}\Gamma_{32}}{\Gamma_{12}} a_0^2 \simeq 2.2 \times 10^{-8} \text{ cm}^2/\text{s}. \quad (6.10)$$

This simple quantitative comparison demonstrates clearly the value of having at our disposal analytic expressions derived from the random walk formalism (Sec. 4.2) in validating predictions of the kMC approach.

6.3 Interaction of indium with As-As bonds

Since the c(4 × 4) reconstruction represents a *double* layer of arsenic, of which the top As atoms form As dimers, Figure 5.3 (a), the incorporation of In into the cation sublattice requires the topmost arsenic layer to be eventually replaced by In atoms. One obvious way how this incorporation could occur is by splitting of the As-As bonds in a reaction with an In adatom. For an understanding of heteroepitaxy, it is therefore important to study such processes. It seems that Kley *et al.* [199] were the first to point out that the adatom interaction with the surface As dimers may have important consequences for the cation diffusivity. For a Ga adatom approaching normally a trench dimer on the $\beta 2(2 \times 4)$ -reconstructed GaAs(001), Figure 5.3 (b), they found that $|E_b|$ is increased by about 1 eV, thus amounting to -3.2 eV, when the adatom splits the dimer bond. Our results from Sec. 5.4 also suggested the same trend for In interacting with the $[\bar{1}10]$ -aligned As dimer bonds on the $\text{In}_{2/3}\text{Ga}_{1/3}\text{As}(001)-(2 \times 3)$ surface, although the energy gain from such a process appeared nearly an order of magnitude smaller than that reported for Ga/GaAs(001)- $\beta 2(2 \times 4)$.

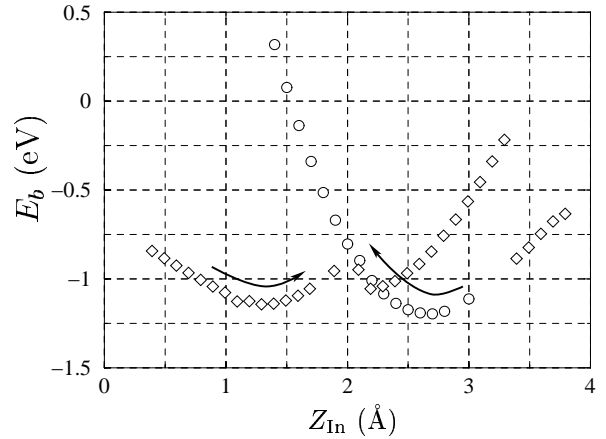


Figure 6.7: Binding energy of an In adatom interacting with the center As dimer as a function of the Z-coordinate of the adatom Z_{In} . The latter is measured from the z-coordinate of the center dimer for the bare surface. Arrows indicate the order in which the calculations were performed: adsorption (○) and desorption (◇).

¹At the simulation temperature ($T = 200$ °C) LePage *et al.* [207] estimated the relevant transition rates to be, respectively, $\Gamma_{21} = 5.4 \times 10^9 \text{ s}^{-1}$, $\Gamma_{12} = 5.1 \times 10^{11} \text{ s}^{-1}$, $\Gamma_{32} = 3.3 \times 10^8 \text{ s}^{-1}$, and $\Gamma_{21} = 5.4 \times 10^{11} \text{ s}^{-1}$.

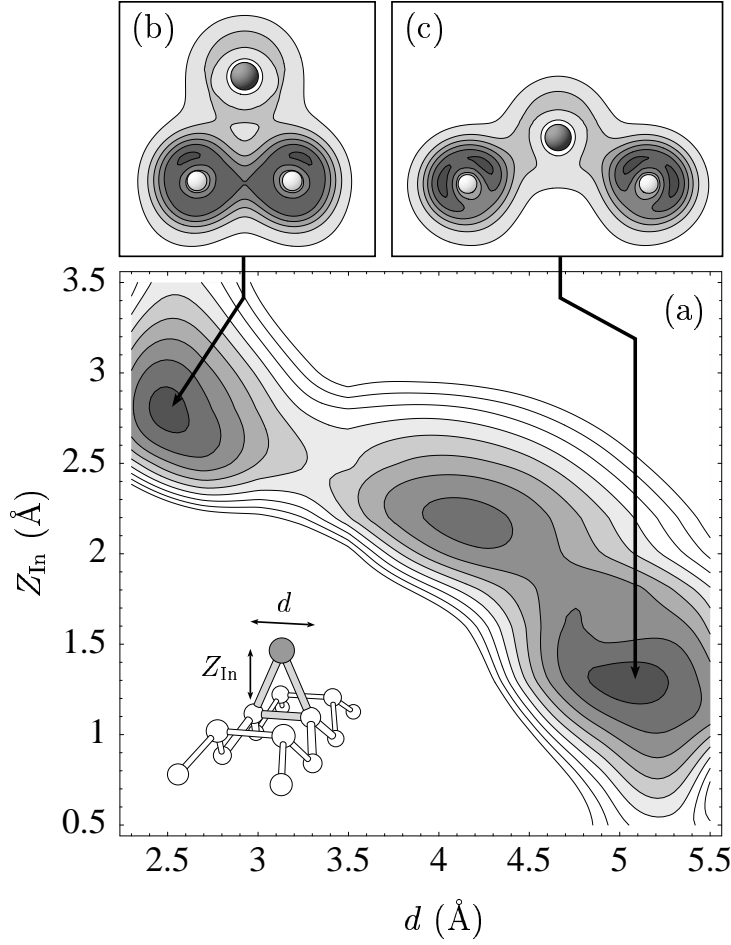


Figure 6.8: (a) Binding energy of an In adatom interacting with the center As dimer as a function of the As-As distance d and the In height above the midpoint of the dimer Z_{In} , as indicated in the inset. (b,c) The bonding configuration and the valence electron density in the plane containing the adatom and the dimer for the two deeper minima of E_b .

In our approach we first sample E_b as a function of the adatom height Z_{In} above the \mathbf{T}_4 site (see the inset in Figure 6.8 (a)), and the resulting E_b - Z_{In} dependence is shown in Figure 6.7. To be more specific, a series of calculations is conducted for a set of predefined values of Z_{In} , where in each calculation the adatom is kept fixed, while the substrate is allowed to freely relax. In subsequent calculations of the series, the geometry of the substrate atoms from the previous calculation is used as input. Thus, if \mathbf{R}'_{in} , and \mathbf{R}'_{out} denote, respectively, the initial guess for the substrate coordinates to be relaxed and their optimized values (cf. also Eq. (4.2)), this means that in the j th run

$$\mathbf{R}'_{\text{in}}[j] = \mathbf{R}'_{\text{out}}[j-1].$$

We find that the outcome of such a series of calculations depends on the initial geometry. While a set of data points modeling adsorption, starting from $Z_{\text{In}} = 3$ Å above the closed dimer, shows an energy minimum at $Z_{\text{In}} \simeq 2.7$ Å, a series of calculations for desorption, starting from an adatom incorporated in between the As dimer atoms at $Z_{\text{In}} \simeq 0.5$ Å, finds a minimum at $Z_{\text{In}} \simeq 1.3$ Å. Both minima have nearly the same depth, $E_b \approx -1.2$ eV. The corresponding bonding configurations and total valence electron densities are shown in Figure 6.8 (b) and (c).

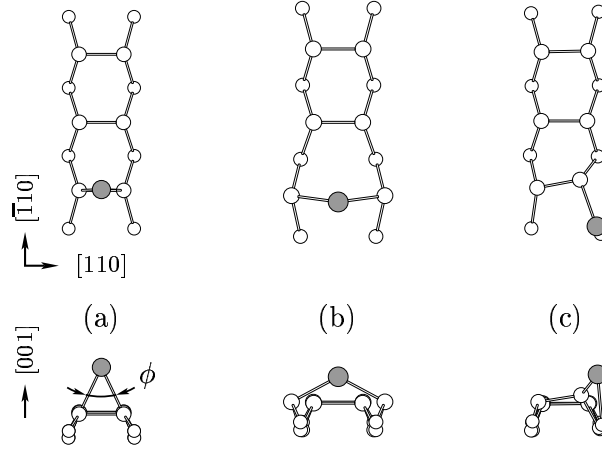


Figure 6.9: Different bonding configurations of an In adatom interacting with the edge As dimer; atomic positions in the topmost two atomic layers are shown (In: shaded circle, As: empty circles). (a) In adatom sitting above the closed edge dimer, similar to Figure 6.8 (b) (configuration corresponding to the \mathbf{T}_3 site). ϕ indicates the As-In-As bond angle; (b) In adatom splitting the dimer, similar to Figure 6.8 (c); (c) In adatom splitting the dimer back-bond.

The discontinuity and hysteresis in E_b seen in Figure 6.7 due to the dimer opening or closing indicates that the information gained from the Z_{In} coordinate alone is insufficient for building up a complete picture of the adatom-dimer interaction. Indeed, the latter poses a multidimensional problem, since not only the adatom itself, but also all degrees of freedom of the surface atoms are involved in this processes. Therefore, even a full relaxation starting from an adatom above the surface may only lead to a local minimum Z_0 , while other minima may exist that can only be reached from different starting configurations. In fact, one could already conclude from the “1D” sampling, Figure 6.7, that the adatom-surface distance Z_{In} and the As-As distance d in the dimer are most important, and the 2D configurational space defined by these coordinates is suitable to image the In-surface dimer interaction.

Towards this end, a special constrained relaxation was carried out, allowing the In adatom and the central As dimer beneath it to be moved as a rigid unit, as sketched in the inset in Figure 6.8 (a). The relative position of these three atoms defines a point in a 2D (d, Z_{In}) -slice through the corresponding multidimensional energy hypersurface. Performing the constrained relaxation, we succeeded in mapping out the 2D PES governing the In-surface interaction in a point-by-point fashion, Figure 6.8 (a). As a result, it becomes evident that the adatom, approaching the dimer, first goes through a minimum of E_b with the dimer bond being $d = 2.56 \text{ \AA}$, Figure 6.8 (b). Upon further pushing towards the surface, the In adatom splits the dimer bond, overcoming a barrier of $\simeq 0.35 \text{ eV}$, and stays shortly within the Z_{In} channel in a second shallower feature of the PES. The formation of directed In-As bonds (see Figure 6.8 (c)) gives rise to a third minimum of E_b at $(d = 5.1, Z_{\text{In}} = 1.3) \text{ \AA}$.

In a similar way, we analyze the adatom interaction with the edge dimers in the $c(4 \times 4)$ unit cell, Figure 6.9. Since the edge dimer has only one neighbor, the second-layer As atoms are expected to relax more efficiently. Indeed, comparing similar bonding configurations for the In atom at the center dimer, Figure 6.8 (c), and at the edge dimer, Figure 6.9 (b), we find $E_b = -1.3 \text{ eV}$ for the latter, which is only slightly lower than $E_b(\mathbf{T}_3)$, Table 6.1. A third possibility, where In attacks the outer back-bond of an edge dimer, is shown in Figure 6.9 (c). This configuration results in $E_b = -1.25 \text{ eV}$.

It is now clear that additional binding sites for In, related to broken As-As bonds,

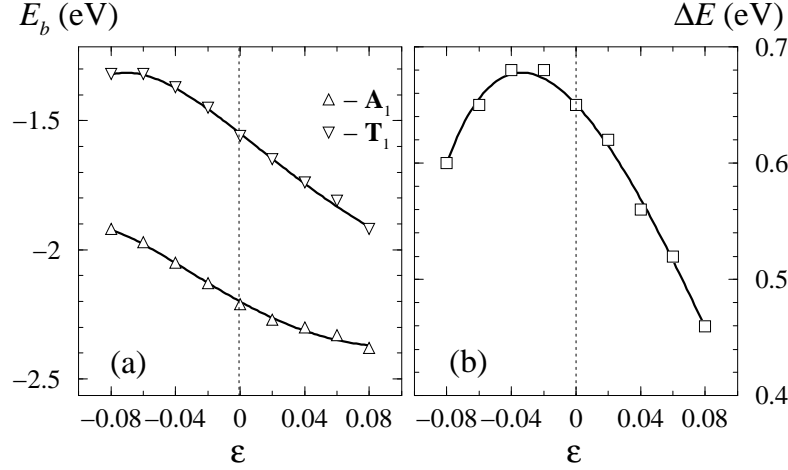


Figure 6.10: (a) Binding energy E_b as a function of isotropic strain ε for an In adatom at the \mathbf{A}_1 and \mathbf{T}_1 sites; (b) diffusion barrier $\Delta E \equiv E_b(\mathbf{T}_1) - E_b(\mathbf{A}_1)$ as a function of ε . Full curves on both panels represent least-squares polynomial fits to the calculated points.

are energetically higher than adsorption on the PES in Figure 6.3, and are therefore not substantially populated in equilibrium. Thus, the mechanism operating in the case of Ga/GaAs(001)- $\beta 2(2 \times 4)$ is strongly suppressed for In/In_{2/3}Ga_{1/3}As(001)- (2×3) , and absent in the In/GaAs(001)- $c(4 \times 4)$ system. Indeed, the more bulky In adatom with an ionic radius larger than that of Ga, when inserted into the As dimer, introduces a substantial elastic distortion of the dimer As back-bonds that cannot be energetically compensated by the gain due to rehybridization. Note that even in the case of an open dimer, the In adatom resides 1.3 Å above it, Figure 6.8 (c), which implies an As-In-As bond angle $\phi \simeq 125^\circ$, while the Ga adatom is incorporated almost collinearly with the two As atoms [199] $\phi \simeq 175^\circ$. This analysis also justifies the use of a single PES, Figure 6.3, for In diffusion in the random walk formalism.

6.4 Effect of strain

The foregoing discussion allows us to single out the main route for the adatom migration: $\mathbf{A}_1 \xrightarrow{\mathbf{T}_1} \mathbf{A}_1$. Hence, the objective in this section is to analyze the influence of surface elastic strain on the Γ_{11} rate. A non-vanishing strain field in the substrate results in a different equilibrium configuration of the topmost atomic layers. Consequently, both the surface phonon spectrum and the PES will experience changes affecting in turn both the frequency prefactor and activation energy in the exponential in Eq. (4.33). The net effect of strain is thus determined by the interplay between the latter two effects. One may expect, however, that the dominant contribution comes from variations in the diffusion barrier

$$\Delta E \equiv E_b(\mathbf{T}_1) - E_b(\mathbf{A}_1), \quad (6.11)$$

for it enters an exponential. This motivated us to concentrate mainly on the strain renormalization of ΔE , but our approach also allows for the influence of $\Gamma^{(0)}$ to be incorporated without detailed knowledge of its functional dependence on strain.

For each particular value of ε the In adatom is placed above the \mathbf{A}_1 and \mathbf{T}_1 sites and the same relaxation scheme as for mapping the PES, Subsection 6.2.1, is applied to obtain the respective binding energy $E_b(\varepsilon)$. The calculated values are shown in Figure 6.10. Interestingly, we find

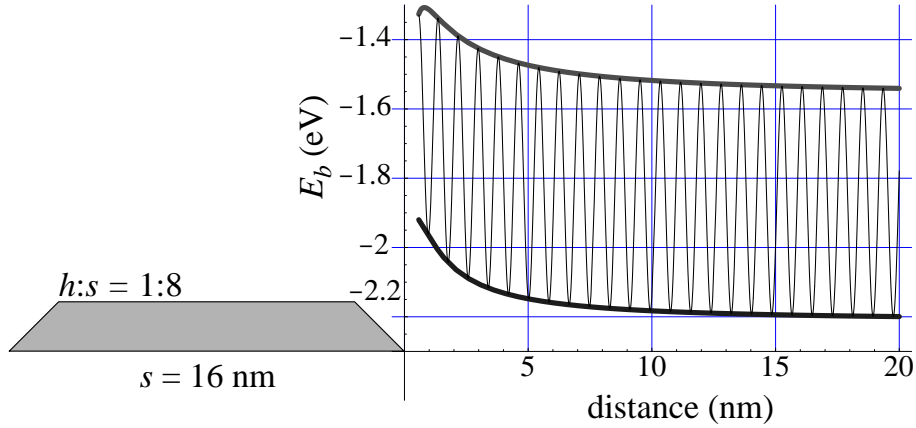


Figure 6.11: Migration potential (oscillating curve) for an In adatom approaching a long, coherently strained InAs island on the GaAs(001)-c(4 × 4) surface, cf. also Figure 3.3. In addition to the diffusion potential due to the atomic structure of the surface, the strain field in the substrate induced by the island gives rise to a repulsive potential that lifts both the binding energies (thick lower line) and transition state energies (thick upper line) close to the island.

that $\Delta E(\varepsilon)$ is a monotonically decreasing function for any tensile strain ($\varepsilon > 0$) employed in the calculations, Figure 6.10 (b). To be specific, this behavior has its onset at $\simeq 3$ % compressive strain, where ΔE reaches a maximum of 0.68 eV. Applying larger compressive strain leads to a reduction of ΔE , with the $\Delta E(0)$ value recovered again for $\varepsilon = -0.06$. The non-monotonic dependence on strain can be rationalized by inspecting the $E_b(\varepsilon)$ curves, given in Figure 6.10 (a). While for $\varepsilon < 0$, E_b at the adsorption site \mathbf{A}_1 follows a linear law [211],

$$E_b(\varepsilon; \mathbf{A}_1) \simeq -2.2 \text{ eV} + |\varepsilon| \times 3.8 \text{ eV}, \quad (6.12)$$

the binding energy at the saddle point \mathbf{T}_1 contains, although small, non-linear terms in strain which do not cancel in the evaluation of ΔE . For an inhomogeneously strained sample, the pronounced strain dependence of E_b for *both* the adsorption site and the saddle point will introduce a position dependence of ΔE . This finding complies with none of the two limiting scenarios of changes of ΔE discussed in the literature [202], where either only $E_b(\mathbf{A}_i)$ or only $E_b(\mathbf{T}_k)$ contributes. Figure 6.11 illustrates a result for a particular geometry obtained by substituting $\varepsilon(x)$ from Eq. (3.41) into Eq. (6.12), for an InAs island on GaAs with height $h = 2$ nm and base length $s = 16$ nm. As can be seen from the figure, the effect of strain leads to a repulsive potential with a strength of up to 0.2 eV, that affects both the binding energy and, to a slightly smaller extent, the diffusion barriers for an In adatom that attempts to approach this island. This repulsive interaction can significantly slow down the speed of growth of strained islands [212].

We would also like to emphasize that the commonly employed linearity [213, 214] for the strain dependence of the diffusion barrier $\delta(\Delta E(\varepsilon))$ is not justified in the case of In/GaAs(001)-c(4 × 4), as clearly seen from Figure 6.10 (b). Thus one needs to go to higher order terms in ε to adequately describe the observed $\delta(\Delta E(\varepsilon))$ behavior. It is also important to point out that strain does not qualitatively change the discussion about the interaction of the In adatom with As-As bonds, based on the PES in Figure 6.8. Extensive tests over the entire range of strain considered here were carried out for E_b of In at the two stable minima, Figure 6.8 (b) and (c), and are shown in Figure 6.12. We found that the binding configuration of Figure 6.8 (b) was always slightly preferable over the one in Figure 6.8 (c), but the strongest binding site for In remains to be \mathbf{A}_1 .

Up to now, reports in the literature about the effect of strain on the diffusion barrier are scarce. A slight lowering of the diffusion barrier upon tensile strain ($\varepsilon > 3.5\%$) has been reported for Ag self-diffusion on a Ag(111) slab within the effective-medium theory [34]. The first-principles treatment of the same system [35] has found instead a linear increase of the barrier with strain. For semiconductors, a lowering of the diffusion barrier upon tensile strain has only been reported for Si adatom and dimer diffusion on Si(001) [203–205], although the underlying binding trends inferred from the MD simulations [203] are opposite to those shown in Figure 6.10 (a).

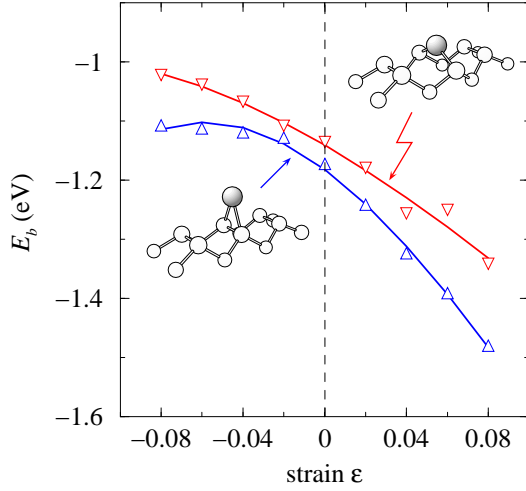


Figure 6.12: Binding energy of an In adatom at the T_4 site (cf. Figure 6.3) for the bonding configurations depicted in Figure 6.8 (b), and (c).

$\varepsilon_{\max} = -3\%$. On the basis of Eq. (6.13), one can write a rather general expression for the diffusion coefficient taking into account the effect of strain,

Given the strain dependence of the diffusion barrier described above, the basic question arises whether diffusion limitations can be observed in the growth kinetics of InAs on GaAs. This would be the case if the adparticle diffusivity is reduced for relevant material parameters and growth conditions. As the substrate around an InAs island, e.g. of pyramidal or truncated pyramidal shape, is under compressive strain (cf. Ref. [104] and Figure 3.5 on page 30), an indium adatom approaching the island samples the $\varepsilon < 0$ branch of $\Delta E(\varepsilon)$. This branch is accurately described by

$$\delta(\Delta E(\varepsilon)) = \delta E_{\max} \left[1 - \left(\frac{\varepsilon}{|\varepsilon_{\max}|} + 1 \right)^2 \right], \quad \varepsilon < 0. \quad (6.13)$$

Equation (6.13) gives the excess diffusion barrier over the one for the unstrained surface $\Delta E(0)$, parameterized by the maximum excess $\delta E_{\max} = 30$ meV, and the strain value at which it occurs,

$$D^*(\varepsilon) = D_0^*(1 + 2\varepsilon) \delta\Gamma^{(0)}(\varepsilon) \exp \left[-\frac{\delta(\Delta E(\varepsilon))}{k_B T} \right], \quad (6.14)$$

where $D_0^* \equiv \text{const}$ is the value of D^* for the unstrained surface, $\delta\Gamma^{(0)} = \Gamma^{(0)}(\varepsilon)/\Gamma^{(0)}(0)$ is the reduction or enhancement factor of the attempt frequency $\Gamma^{(0)}$, and $2\varepsilon \equiv \text{Tr } \varepsilon_{\alpha\beta}$ is the relative change in the surface area. A first estimate of the expected reduction of D^* within the temperature range 350–500 °C used for InAs deposition on the $c(4 \times 4)$ -reconstructed GaAs(001) substrate in Ref. [142], Figure 5.1 can be obtained by inserting Eq. (6.13) in (6.14), setting $\delta\Gamma^{(0)} \equiv 1$. The resulting reduction,

$$D^*(\varepsilon_{\max})/D_0^* \simeq 0.6, \quad (6.15)$$

turns out to be small due to the smallness of δE_{\max} . As a consequence, changes of the prefactor due to the effect of strain on lattice vibrations are equally important in determining the strain renormalization of the In diffusivity on the GaAs(001)- $c(4 \times 4)$ surface in the relevant temperature regime.

Although it is possible to obtain $\delta\Gamma^{(0)}$ from first-principles calculations, it is difficult to get an estimate that is better than a factor of two with reasonable computational effort (see also the discussion in Subsection 5.4.2). Hence we consider $\delta\Gamma^{(0)}$ as an independent parameter in

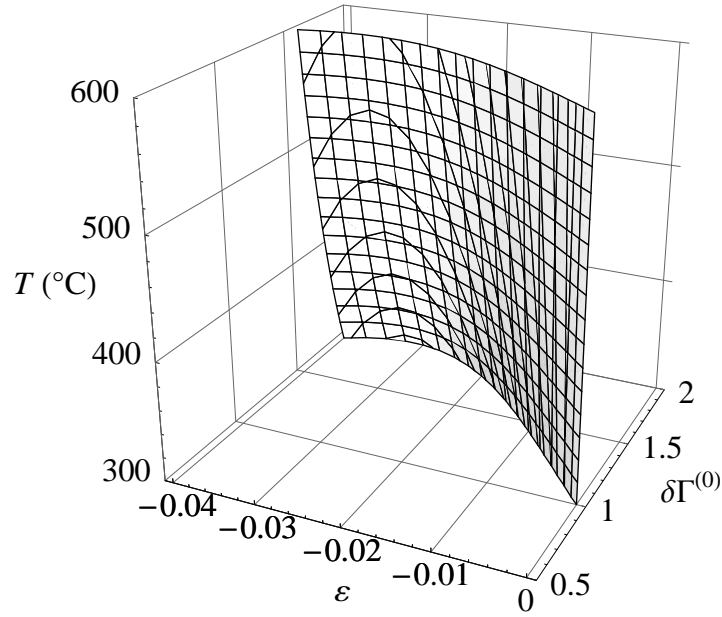


Figure 6.13: The $D^*/D_0^* = 1$ isosurface in the 3D parameter space $(\varepsilon, \delta\Gamma^{(0)}, T)$. The view point is from the side where $D^*/D_0^* < 1$. Points beyond the isosurface correspond to enhanced diffusivity $D^*/D_0^* > 1$.

the following analysis. Thus the right-hand side of Eq. (6.14) is a function of three parameters, ε , $\delta\Gamma^{(0)}$, and T . The region in parameter space where strain-induced growth limitations can be expected is defined by the requirement

$$D^*(\varepsilon; \delta\Gamma^{(0)}, T)/D_0^* < 1. \quad (6.16)$$

Figure 6.13 represents the isosurface $D^*/D_0^* = 1$ in the 3D parameter space of ε , $\delta\Gamma^{(0)}$, and T . We note that the reduction in diffusivity due to positive $\delta(\Delta E)$, especially for lower temperatures, persists even for $\delta\Gamma^{(0)} > 1$, i.e. in presence of the Meyer-Neldel compensation effect [138], cf. also Sec. 4.3. However, for a very strong compensation effect, $\delta\Gamma^{(0)}(\varepsilon) > \delta\Gamma_c^{(0)} \simeq 2$, no decrease in D^* in the relevant range of ε and T values can be expected. Finally, we have performed DFT calculations to obtain an estimate of $\Gamma_{11}^{(0)}(-0.04)$, using the harmonic approximation for the lattice vibrations and a force-constant matrix involving only the degrees of freedom [5, 136] of the In adatom. This estimate indicates ~ 70 % increase of the prefactor for 4 % compressive strain. In this case one cannot expect more than a few percent maximum reduction of D^* , which would in turn make diffusion limitations for the specific example of the GaAs(001)-c(4 × 4) surface rather unlikely.

Chapter 7

Consequences for growth

7.1 Introduction

The QDs self-assembly can be considered as the second stage in the (quasi) SK growth of lattice mismatched heteroepitaxial systems. Now a great number of experiments have shown that these 3D coherent islands often exhibit a rather narrow size distribution. This property was particularly enhanced in the higher layers of 3D stacks of islands obtained from repeated deposition of heteroepitaxial films separated by spacer layers; a sample illustration is given in Figure 7.1. This feature is essential for the usefulness of these nanostructures as QDs, and for their envisaged application in future optoelectronic devices [19, 215].

Considerable theoretical efforts have been made in order to rationalize the observed regularities in island sizes and ordering. Some approaches have attempted to describe the islands as equilibrium structures [19, 148, 216–218]. As an alternative explanation, the role of *kinetics* for the growth of heteroepitaxial islands has been emphasized [213, 214, 219]. It is possible that intrinsic features of the kinetics of the growth process give rise to regular structures. For instance, self-limiting effects in strained island growth could result in a preferred island size, either due to a limitation in material supply [114, 115, 212, 220, 221], or due to nucleation barriers in the growth of the islands' side facets [222, 223].

In this final chapter we would like to discuss the impact of our results from Chapters 5 and 6 for growth in two typical situations, (*i*) nucleation on a strained capping layer for low In concentrations (Sec. 7.2), and (*ii*) diffusion-limited growth of quasi-one-dimensional islands (Sec. 7.3). These topics have been discussed previously in the literature in the context of thermochemical diffusion [114, 115, 212, 220, 224]. Our focus here will be on a *kinetic* description inspired by the results of our atomistic calculations (Chapter 5, Chapter 6), attempting also a more *general* context in the following discussion.

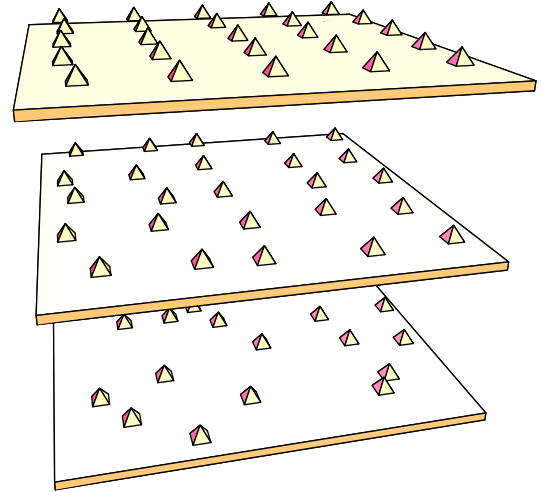


Figure 7.1: Sketch of a vertical stack of 2D QD arrays where ordering in the higher layers is improved.

7.2 Growth on a capping layer with buried islands

As already mentioned in Subsection 3.3.2, in successive stages of growth of vertically stacked QD arrays, different regimes of strain are realized. When a 2D sheet of InAs QDs is completed and capped by a spacer GaAs layer, the GaAs lattice is expanded in the regions above the buried InAs QDs [225, 226]. Let us consider now the onset of In deposition onto the spacer layer before nucleation of the first new islands. In order to employ the results from the previous chapter we assume that the (001) surface of the GaAs capping layer is characterized with a well-defined reconstruction, taken to be $c(4 \times 4)$ [227], Figure 5.3 (a). Then a stationary concentration of adatoms on the surface builds up by the *equilibrium* between supply from an atomic In beam source and loss due to evaporation of In. However, the concentration may vary laterally along the surface. In the stationary state the local concentration $n(\mathbf{r}_{\parallel})$ is given by local equilibrium,

$$n(\mathbf{r}_{\parallel}) = n_0 \exp[-U(\mathbf{r}_{\parallel})/k_B T], \quad (7.1)$$

where $U(\mathbf{r}_{\parallel})$ is the binding energy of the In adatoms at site \mathbf{A}_1 , and \mathbf{r}_{\parallel} is the coordinate within the surface. $U(\mathbf{r}_{\parallel})$ is a function of local strain as given by $E_b(\varepsilon(\mathbf{r}_{\parallel}))$ in Figure 6.10 (a). As can be seen from this figure, the binding strength increases for any tensile strain $\varepsilon > 0$. Thus, the local concentration of adatoms, and hence the nucleation probability for a new island, is increased in the region above a buried island where the capping layer surface is under tensile strain. Our calculations, thus, provide a microscopic foundation for the frequently made assumption [15, 225] that it is easier to nucleate an InAs island on those regions of the capping surface where the GaAs lattice constant increased, and thus more closely matches the InAs lattice constant.

7.3 Diffusion limitations in island growth kinetics

The conditions under which kinetic growth limitations can be expected were discussed already in Sec. 6.4 (see Eq. (6.16) and Figure 6.13). It is interesting to illustrate the possible consequences of such limitations for the island sizes. This is pursued here within the framework of a simple *model problem* based on the flat island approximation [112], Sec. 3.4. One might think, for instance, of adatom diffusion towards the extended edge of a quantum wire.

As a first step, we address the strain renormalization of the adparticle diffusivity due to an isolated island. The strain field it creates in the underlying substrate, within the model adopted, is given by Eq. (3.41). To assess quantitatively the role of diffusion limitations, we insert the numerical values for δE_{\max} and ε_{\max} obtained in Sec. 6.4. We shall further suppose that a low adatom concentration is maintained at the surface, so that the adsorbate-adsorbate interactions are negligible. In such a case, as discussed in Subsection 4.1.2, the tracer diffusion coefficient(s) D^* and the chemical diffusion coefficient(s) D become equivalent, so we suppress hereafter the “*” superscript. For three islands of different sizes, Figure 7.2 shows the spatial dependence of $D(x)$ obtained by inserting Eq. (3.41) into Eq. (6.14), for $\delta\Gamma^{(0)} = 1$ and $T = 450$ °C. As can be seen from the short-range behavior (*i.e.* close to the island edges) of the diffusion coefficient, the larger islands can be about 20–30 % more effective in hindering the adatom migration (due to reduced D) provided that *no substantial compensation* (Meyer-Neldel) effect from the $\Gamma^{(0)}$ prefactor is present, cf. also Sec. 4.3. However, as we have shown in Sec. 6.4, Figure 6.11, the compressive strain field around an island gives rise to an effective repulsive potential. Since this effect is independent of the prefactors and is larger in magnitude, it will bring about a slowdown in adatom migration rate toward the island even if the above mentioned situation is realized. Consequently, as long as the islands grow via strain-dominated surface mass transport, the compressive strain field may lead to retarded growth of the larger islands.

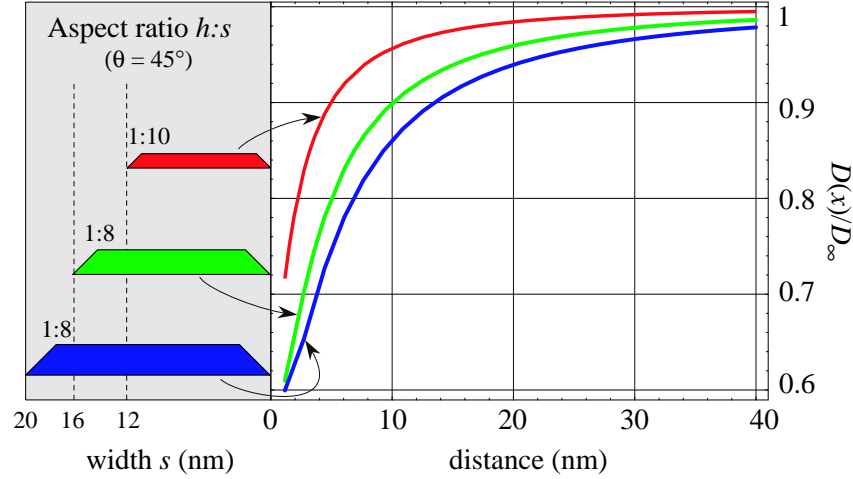


Figure 7.2: Strain renormalization of $D(x)$, according to Eqs. (6.14) and (3.41), versus island size within the 1D flat island approximation (cf. Sec. 3.4) at $T = 450^\circ\text{C}$ and absence of compensation effect, $\delta\Gamma^{(0)} = 1$. D_∞ refers to the asymptotic value of D at an infinitely large distance from the island. The tilt angle of the island side facets is θ and h is the height. The island/substrate system is assumed to be InAs/GaAs.

Consider now two islands of characteristic size s_1 and s_2 , with $s_1 > s_2$, separated by a distance $L \gg s_1, s_2$, Figure 7.3. A supply of adparticles to the surface is maintained by a stationary flux F_0 . One may ask then, what is the steady-state adparticle density distribution $n(x)$ at the surface, and how does it affect the diffusional currents of single adatoms toward the islands, $-j_1$ and j_2 ? This is a standard problem in kinetics [228, 229]; however, we require it to be solved for a spatially varying migration potential $U(x)$ due to the presence of strained islands. Again, we can exploit the results obtained in Sec. 6.4, identifying $U(x)$ with $E_b(\varepsilon(x))$ for the adsorption site \mathbf{A}_1 . The single atom density $n(x, t)$ then satisfies a Smoluchowski equation-type equation [122, 127, 128] that takes explicit account of the field of force due to $U(x)$,

$$\frac{\partial n}{\partial t} = \frac{\partial}{\partial x} \left[D(x) \left(\frac{\partial n}{\partial x} + \frac{n}{k_B T} \frac{dU(x)}{dx} \right) \right] + F_0 \quad (7.2)$$

Since a stationary solution is sought, $\partial n / \partial t = 0$, one can also replace $\partial / \partial x \rightarrow d / dx$, so Eq. (7.2) reduces to

$$\frac{d}{dx} n(x) + \frac{1}{k_B T} \frac{dU(x)}{dx} n(x) = -\frac{F_0}{D(x)} (x - x_0), \quad (7.3)$$

which is a linear inhomogeneous differential equation (x_0 being a constant of integration). The solution of the homogeneous problem has the form of Eq. (7.1), $n(x) = n_0 \exp(-U(x)/k_B T)$, and solution of the inhomogeneous equation can be found just by substituting the latter expression in Eq. (7.3) and varying the constant n_0 , i.e. $n_0 \rightarrow n_0(x)$. In the simplest case, when the island edges act as perfect sinks, we have the trivial boundary conditions

$$n(0) = n(L) = 0, \quad (7.4)$$

thereby the stationary solution finally reads

$$n(x) = F_0 \exp \left(-\frac{U(x)}{k_B T} \right) \int_0^x \frac{x_0 - x'}{D(x')} \exp \left(\frac{U(x')}{k_B T} \right) dx', \quad (7.5)$$

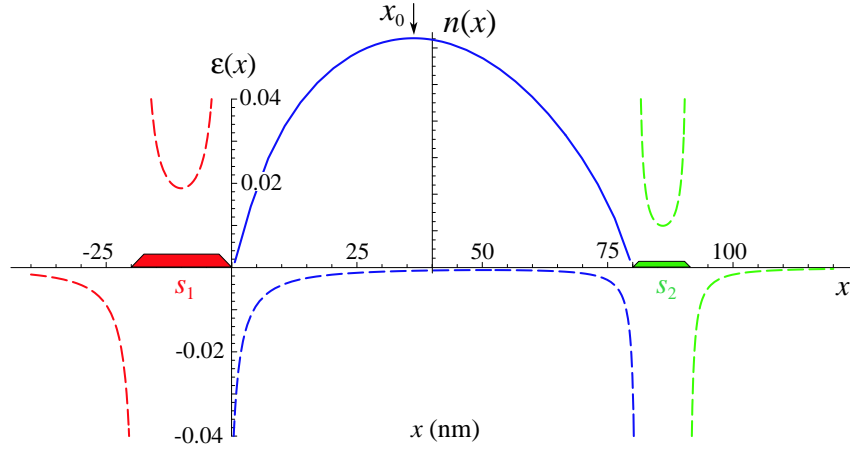


Figure 7.3: Adatom density profile $n(x)$ (full curve, arb. units) between the two long flat islands from Figure 3.5 on page 30. The strain field in the substrate surface is shown as dashed lines. The arrow at $x = x_0$ indicates the maximum of $n(x)$, which is shifted off the midpoint between the islands towards the bigger island s_1 .

with $0 < x_0 < L$ being the position between the two islands where the total adparticle current vanishes,

$$j(x_0) \propto -\left.\frac{dn}{dx}\right|_{x_0} = 0,$$

$$x_0 = \left[\int_0^L \frac{1}{\tilde{D}(x)} dx \right]^{-1} \int_0^L \frac{x}{\tilde{D}(x)} dx, \quad (7.6)$$

with $\tilde{D}(x) = D(x) \exp[-U(x)/k_B T]$. Thus, we can think of x_0 as the marker that divides the space between the islands into two capture areas: j_1 is due to adparticles in the region $x \in (0, x_0)$, while j_2 is determined by those within (x_0, L) . It is now straightforward to obtain the result that relates j_1 with j_2

$$\left| \frac{j_1}{j_2} \right| = \frac{x_0}{L - x_0}. \quad (7.7)$$

Without the effect of strain, the adatom density has a simple parabolic profile,

$$n_0(x) = \frac{F_0}{2D_0} (2x_0 - x)x \quad (7.8)$$

with its maximum being exactly at the midpoint between the two islands, $x_0 = L/2$. The strain renormalization of diffusion shifts x_0 towards the bigger island, Figure 7.3, thus reducing the particle current reaching this island. In order to achieve a rough estimate for the magnitude of this effect, we have evaluated the current ratio (7.7) at $T = 450$ °C, using here the calculated material parameters for the InAs/GaAs system within the PBE-GGA. We have further assumed the right island in Figure 7.3 to be of fixed size and considered Eq. (7.7) as a function of the size s_2 of the left island; aspect ratios of the two islands were kept the same as in Figure 3.3, $h_1/s_1 = 1 : 8$, and $h_2/s_2 = 1 : 10$, respectively. The result is shown in Figure 7.4, where the full curve has been obtained for the case $\delta\Gamma^{(0)} \equiv 1$. Thus it can be seen that doubling the size of the island results in about 40 % reduction of the diffusional current directed to this island. One

should keep in mind, however, that the presented dependence cannot be interpreted as a “time evolution” of Eq. (7.7) for which, in principle, also s_2 and L have to be considered variables.

It is also interesting to test the tendency worked out for $\delta\Gamma^{(0)} \equiv 1$ against inclusion of a compensation effect from the prefactor. From simple physical considerations, one would have

$$\delta\Gamma^{(0)}(\varepsilon) \sim g \text{Tr} \varepsilon \sim g\varepsilon,$$

where the g is to be interpreted as a surface analog to the Grüneisen parameter [41]. With this remark, we have used a simple linear interpolation between the values of $\Gamma_{11}^{(0)}$ calculated for the unstrained surface and for 4 % compressive strain (Subsection 6.2.2, Sec. 6.4). The result is given by the dashed curve in Figure 7.4. Note that the dominant effect stems from the E_b - ε dependence, as shown in Figure 6.11 on page 77, rather than from the diffusion barrier for the adatom, and thus the overall decrease of $|j_1/j_2|$ persists even in the presence of the Meyer-Neldel effect.

This simple 1D model problem demonstrates that the smaller island will grow faster, until x_0 gets shifted back towards the midpoint when the sizes of the two islands have become equal. As a consequence, the strain-limited adatom diffusion will tend to equalize the island sizes by controlling the capture areas for the two islands competing for the deposited material. Thus far we have assumed that the boundary condition (7.4) is fulfilled, which implies that all adatoms that have reached the islands edges got attached. Such a process, however, is energy activated, and the barrier increases monotonically with the island size.¹ Therefore we believe that our results based on these simple model assumptions would not be changed qualitatively if the model is further refined, *e.g.*, by allowing for a *kinetic* barrier to attachment at the island edges, and thereby nonvanishing particle densities at $x = 0, L$.

Finally we would like to comment briefly on a possible scenario for the lattice mismatched heteroepitaxy of InAs on GaAs(001) which attempts to combine our results about the WL stability and In mobility on it (Chapter 5) with the strain dependence of In diffusion on the GaAs(001)- $c(4 \times 4)$ substrate (Chapter 6).

As the MBE growth is usually performed under As-rich conditions, from the diagram in Figure 5.14 one can expect that the initial delivery of InAs to the GaAs(001)- $c(4 \times 4)$ substrate will result in formation of a pseudomorphic InGaAs(001)- (2×3) alloy WL, and above certain coverage the reconstruction changes to (2×4) , Figure 5.14. Beyond the critical coverage θ_c , coherent InAs will nucleate on the (2×4) -reconstructed WL and continue growing at the expense of the WL. If the island density N_i is assumed fixed, the growth process will follow the mechanism proposed by Wang *et al.* [107,148], thereby thinning the WL. According to Figure 5.13 on page 59, for μ_{As} close to $\mu_{\text{As(bulk)}}$ the decrease in θ may proceed to as low as ~ 0.5 ML, where the reconstruction is dominantly (2×3) . At this stage, however, the WL is no longer homogeneously strained as before the onset of islanding. The presence of the InAs islands now appears to be crucial: the compressive strain field in the WL around the islands according to Figure 5.11 on

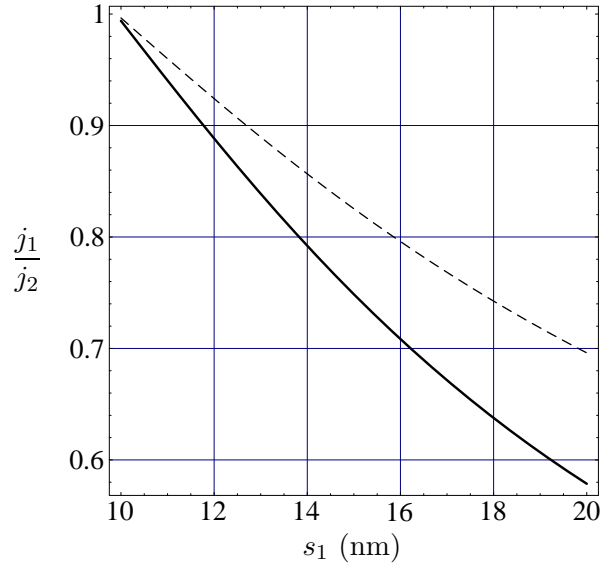


Figure 7.4: Effect of island size (s_1) on the $|j_1/j_2|$ ratio (7.7), cf. Figure 7.3, assuming fixed sized for the right island and distance between the islands, respectively, $s_2 = 12$ nm and $L = 80$ nm. Dashed line refers to the case where a compensation effect is present (see discussion in text).

¹Activated attachment, however in the context of thermo-chemical diffusion, was invoked, *e.g.*, by Chen and Washburn [220] for Ge/Si(001), demonstrating that it can lead to progressive slowdown of the growth of bigger islands thus allowing the smaller ones to catch up in size.

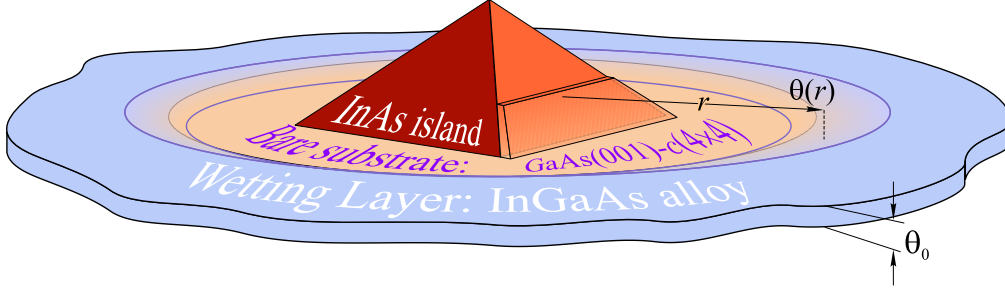


Figure 7.5: Schematic of an isolated pyramidal island decoupled from the WL through a ring-shaped area of exposed bare GaAs(001)- $c(4 \times 4)$ substrate. The WL thickness at distance r from the island is $\theta(r)$, approaching a constant value θ_0 for large r .

page 58 may drive the InGaAs(001) WL unstable so that ring-shaped regions surrounding the islands form, uncovering the bare GaAs(001)- $c(4 \times 4)$ substrate. Figure 7.5 presents a schematic drawing of such a situation. Once such $c(4 \times 4)$ “rings” appear, the In adatom diffusion will be governed by a different PES depending on whether it takes place on the WL or the bare substrate. Thus, we expect reduced In mobility in vicinity of the InAs islands caused by the “decoupling” from the WL. We stress that this slowdown comes from the PES “crossover”. An additional effect of hindering will stem from the compressive strain field in the bare substrate itself as demonstrated in Chapter 6. As a result, one can speculate [176] that the growth rate of the larger InAs islands which have decoupled from the WL will be considerably reduced or even vanish, leading to an equalizing effect on the island sizes, and consequently to a narrow size distribution.

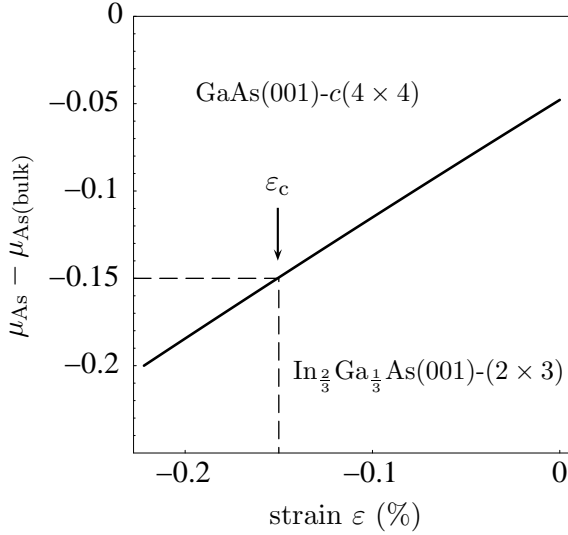


Figure 7.6: Substrate-WL stability diagram as a function of As chemical potential μ_{As} and isotropic compressive strain ϵ . The “critical” strain value for a given chemical potential at which the $(2 \times 3) \rightarrow c(4 \times 4)$ transition occurs is marked by arrow.

substrate depends on the strain, we build up their “phase” diagram as function of μ_{As} and ϵ , just like it was done for the clean GaAs(001) and InAs(001) surface in Figure 5.8 on page 55. It is shown in Figure 7.6. Using this diagram, it is easily established that at $\mu'_{\text{As}} = -0.15$ eV

The plausibility of this hypothesis is, to a large extent, determined by the typical radius \bar{r} of the $c(4 \times 4)$ domains around the islands, or in general, by the validity of the equilibrium assumptions. In principle, the methodology used in Refs. [107,148] should allow such an evaluation to be achieved. In such a case, however, the surface energy of the WL and the energy of the WL-substrate interface (cf. the $\gamma_{\text{WL}}(\theta)$ quantity, *e.g.*, in Ref. [107]) will acquire spatial dependence due to the laterally varying WL thickness $\theta(\mathbf{r}_{\parallel})$.

An estimate for \bar{r} can also be based on the phase equilibrium analysis carried out in Chapter 5. Let us first assume that as a result of the thinning, the WL has reached thickness $\theta \simeq 2/3$ ML, Figure 5.13. Hence, for definiteness, from Figure 5.14 we choose $\mu'_{\text{As}} = -0.15$ eV, which ensures the stability of the (2×3) reconstruction of the WL. Now in order to determine how the equilibrium between the WL and the GaAs(001)- $c(4 \times 4)$

(see the dashed line), a $(2 \times 3) \rightarrow c(4 \times 4)$ reconstruction transition occurs for the “critical” compressive strain $\varepsilon_c = -0.15\%$. Once ε_c is determined from the diagram Figure 7.6, the size of the $c(4 \times 4)$ domain r for a particular island is obtained as the solution of the equation

$$\varepsilon(r) - \varepsilon_c = 0. \quad (7.9)$$

The calculated r thus will be, in fact, determined by the characteristic size of the island s , $r = r(s)$. Details in the $\varepsilon(r)$ profile depend, of course, also on the island shape, but for simplicity we can assume that the latter is the same within the dilute island array in question. If for the given amount of deposited InAs we know the (stationary) distribution of islands in sizes (*i.e.* number of 3D islands of characteristic size s per unit surface area) $f(s)$, then \bar{r} can be obtained by simple averaging,

$$\bar{r} = \int r(s)f(s)ds / \int f(s)ds.$$

Such a procedure in the realistic case of a planar array of 3D islands is a formidable task. However, we can revert again to the simple 1D model, Figure 7.3. In this case we have just a stripe of the uncovered substrate. Consider now the islands of width $s_1 = 20$ nm. Substituting $\varepsilon(x)$ from Eq. (3.41) and $\varepsilon_c = -0.015$ into Eq. (7.9) we find $x \simeq 5$ nm.

Whether such domains of uncovered substrate around the InAs islands can be observed in experiment remains to be seen. Thus far there are no such indications, which may imply that the central local equilibrium assumption in the present theory is not fulfilled under the experimentally relevant growth conditions for the InAs/GaAs(001) material system. Interestingly, however, in the case of Ge/Si(001), such dips in the wetting layer around the Ge islands have been observed; they are also somewhat visible in Figure 1 on page iii (cf. also Ref. [230]).

Summary

The goal of the present work was to provide understanding of surface diffusion in InAs lattice mismatched heteroepitaxy on GaAs(001) on the atomic scale. The self-assembly of coherent 3D islands (QDs) in the Stranski-Krastanov-type growth mode has made this material system of primary technological interest, in view of the potential application of these QDs in optoelectronic devices. The method we have employed to pursue the problem of In surface diffusion is based on density-functional theory (Sec. 2.2), which is nowadays indispensable in exploring microscopic processes in crystal growth in general.

Since the problem of surface diffusion is intimately related to the morphology of the surface on which the diffusion process takes place, we had first to consider (Sec. 5.2) the thermodynamic stability and elastic properties of the clean (001) surfaces of GaAs and InAs. The new element in the present work is the inclusion of the novel $\zeta(4 \times 2)$ model [174] for the InAs(001) surface under In-rich conditions. We showed that this reconstruction is stable, and thus provided first-principles evidence that there exists, indeed, a stable (4×2) reconstruction in the As-poor limit of the surface phase diagram of InAs(001). In Subsection 5.2.3, we calculated the trace of the surface stress tensor for the clean surfaces and showed that for the clean binary (001) surfaces under moderately As-rich conditions, the dominant stress component is tensile, while for the cation-rich $\zeta(4 \times 2)$ phase it is compressive.

In considering the InAs/GaAs(001) growth process itself, we further focused on the alloying which was experimentally found to occur in the initial stages of the wetting layer formation, Sec. 5.3. Our stability analysis supports the experimentally proposed (2×3) structural model for the InGaAs(001) surface. Importantly, we found that the pseudomorphic $\text{In}_{2/3}\text{Ga}_{1/3}\text{As}(001)$ - (2×3) film is considerably destabilized upon compressive isotropic strain, and a $(2 \times 3) \rightarrow (1 \times 3)$ reconstruction transition may occur at about $|\varepsilon| = 3\%$ compression. This part of the work also extended the previous analysis of Wang *et al.* [107, 148, 150] by including the $\alpha 2(2 \times 4)$ reconstruction for the WL. As a result we derived a diagram of the WL surface phases (Figure 5.14), demonstrating that under As-rich conditions the (2×3) reconstruction is the most favorable one for WL thickness up to $\theta \simeq 1\text{--}1.5$ ML, while the $\alpha 2(2 \times 4)$ is dominant for moderate As chemical potential. Surface alloying and pseudomorphism turned out to result in a relatively “smooth” potential-energy surface for indium diffusion on the $\text{In}_{2/3}\text{Ga}_{1/3}\text{As}(001)$ - (2×3) film, Sec. 5.4. This finding led us to infer enhanced In migration on this surface.

Further analysis concentrated on the effect of strain on In diffusivity on the bare GaAs(001)- $c(4 \times 4)$ surface (Chapter 6) which is often used as substrate for InAs deposition, cf. Figure 5.1. In particular, we quantified the strain dependence of the diffusion barrier ΔE for the indium adatom, Sec. 6.4. Our atomistic calculations yielded a maximum increase of the In diffusion barrier on GaAs(001)- $c(4 \times 4)$ of 30 meV for isotropic compressive strain. Since at the relevant growth condition this value is of the order of $k_{\text{B}}T$, the effect on the diffusion coefficient is small. However the strain field resulted in a pronounced strain dependence of the In binding along the main diffusion route. This gives rise to a significant repulsive interaction between a strained island and an adatom diffusing towards the island, Figure 6.11, which appears to be the dominant

effect of strain on the adatom migration. The In interaction with the surface As dimers was also investigated in Sec. 6.3. We do not find convincing evidence for considerably more stable adsorption sites for indium due to As-As bond splitting.

Finally, in Chapter 7, a simple 1D model problem was employed to demonstrate that strain-limited diffusion can lead to self-limiting growth of strained islands. The discussion presented in this work, however, referred to diffusivity of a single adatom, the so-called tracer diffusion (Sec. 4.1.2). Concluding, we would like to emphasize that if any collective effects are to be included, one has to calculate interaction parameters between diffusing adatoms, and consider adatom concentrations where these interactions are effective. Nevertheless our microscopic results could serve as an input, for example, to kinetic Monte Carlo simulations (see, *e.g.*, Sec. 6.2.3) in order to shed more light on the effect of strain on adatom diffusivity in this important material system.



Kurzfassung

Ziel der vorliegenden Arbeit ist es, Einblicke in die Oberflächendiffusion in der Heteroepitaxie von InAs auf GaAs(001) auf atomarer Skala zu liefern. Aufgrund der Gitterfehlانpassung kommt es in diesem Materialsystem zur spontanen Ausbildung kohärenter dreidimensionaler Inseln im Stranski-Krastanov Wachstumsmodus. Diese so genannten Quantenpunkte verleihen diesem System große technologische Bedeutung in Hinblick auf die potentielle Anwendung in optoelektronischen Bauelementen. Die Methode, die wir benutzt haben, um das Problem der Oberflächendiffusion von In anzugehen, basiert auf der Dichtefunktionaltheorie (Abschnitt 2.2), die heutzutage unentbehrlich bei der Untersuchung von mikroskopischen Prozessen im Kristallwachstum ist.

Da das Problem der Oberflächendiffusion eng verbunden ist mit der Morphologie der Oberfläche, auf der die Diffusion stattfindet, haben wir im ersten Teil der Arbeit (Abschnitt 5.2) die thermodynamische Stabilität und die elastischen Eigenschaften der reinen (001)-Oberfläche von GaAs und InAs untersucht. Das Besondere an der vorliegenden Arbeit ist, dass wir eine neuartige $\zeta(4 \times 2)$ Struktur [174] der InAs(001)-Oberfläche unter In-reichen Bedingungen berücksichtigt haben. Wir haben gezeigt, dass diese Rekonstruktion stabil für InAs(001) ist und haben damit einen theoretischen Beweis der Existenz einer stabilen (4×2) Rekonstruktion an der As-armen Grenze im Oberflächenphasendiagramm von InAs(001) geliefert. Darüber hinaus wurde in Abschnitt 5.2.3 die Spur des Oberflächenspannungstensors für die reine Oberfläche berechnet und gezeigt, dass für die reinen binären Oberflächen unter schwach As-reichen Bedingungen die dominante Komponente einer Zugspannung entspricht, während für die kationreiche Phase eine Druckspannung dominiert.

Bei der Untersuchung des Wachstums von InAs/GaAs(001) haben wir uns auf die Legierungsbildung konzentriert, die experimentellen Hinweisen zufolge im Anfangsstadium der Ausbildung der Adsorbatschicht stattfindet, Abschnitt 5.3. Unsere Analyse der Stabilität bestätigt das experimentell vorgeschlagene Modell der InGaAs(001)-Oberfläche. Ein wichtiges Ergebnis ist, dass der pseudomorphe $\text{In}_{2/3}\text{Ga}_{1/3}\text{As}(001)-(2 \times 3)$ -Film unter isotroper Druckspannung beträchtlich destabilisiert ist und bei einer Druckspannung von $|\varepsilon| = 3 \%$ ein Rekonstruktionsübergang $(2 \times 3) \rightarrow (1 \times 3)$ stattfinden kann. Dieser Teil der Arbeit ging über die Analyse von Wang *et al.* [107, 148, 150] insofern hinaus, als auch die $\alpha 2(2 \times 4)$ Rekonstruktion als Benetzungsschicht betrachtet wurde. Als Resultat wurde ein Diagramm der Oberflächenphasen der Benetzungsschicht erstellt (Abbildung 5.14), das veranschaulicht, dass die (2×3) -Rekonstruktion die günstigste unter As-reichen Bedingungen bis zu einer Dicke der Adsorbatschicht von $\theta \simeq 1\text{--}1.5$ ML ist, während bei ausgewogenem III-V-Verhältnis eine $\alpha 2(2 \times 4)$ -Phase dominiert. Die Legierungsbildung und das pseudomorphe Wachstum führen zu einer relativ "glatten" Potentialfläche für die In-Diffusion auf dem $\text{In}_{2/3}\text{Ga}_{1/3}\text{As}(001)-(2 \times 3)$ Film, Abschnitt 5.4. Dieses Ergebnis deutet auf eine verstärkte In-Migration auf der Oberfläche hin.

Desweiteren wurde der Effekt einer mechanischen Verspannung auf die In-Diffusivität auf der reinen GaAs(001)- $c(4 \times 4)$ -Oberfläche untersucht, die oft als Substrat für die Deposition von InAs dient, cf. Abbildung 5.1. Unsere Berechnungen ergeben einen maximalen Anstieg

der In-Diffusionsbarriere von 30 meV bei isotroper Druckspannung, Abschnitt 6.4. Da unter den relevanten Wachstumsbedingungen dieser Wert von der Größenordnung $k_B T$ ist, ist der Effekt auf den Diffusionskoeffizienten klein. Allerdings führt das Verzerrungsfeld zu einer deutlichen Abhängigkeit der Bindung des Indium-Adatoms entlang des Diffusionspfades. Dies verursacht eine stark repulsive Wechselwirkung zwischen der verspannten Insel und dem Adatom, Abbildung 6.11, das zur Insel diffundiert. Diese Wechselwirkung stellt den dominierenden Effekt der Verspannung auf die Adatommigration dar. Die Wechselwirkung von Indium mit den As-Oberflächendimeren wurde auch berücksichtigt, Abschnitt 6.3. Wir haben keinen Hinweis auf die Existenz eines deutlich stabileren Adsorptionsplatzes für In durch die Aufspaltung der As-As-Bindung gefunden.

Schließlich wurde in Kapitel 7 ein einfaches eindimensionales Modell benutzt, um zu zeigen, dass die Diffusion auf verspannten Oberflächen ein Grundprinzip des sich selbst begrenzenden Wachstums verspannter Inseln ist. Allerdings bezieht sich die Diskussion in dieser Arbeit auf die Diffusion eines einzelnen Adatoms, auf den so genannten "Tracer"-Diffusionskoeffizienten (Abschnitt 4.1.2). Abschließend wollen wir betonen, dass zur Berücksichtigung kollektiver Effekte die Wechselwirkungsparameter zwischen diffundierenden Adatomen berechnet werden müssen, und zwar mit Adatom-Konzentrationen, bei denen diese Wechselwirkungen relevant sind. Unsere mikroskopischen Ergebnisse können jedoch als Eingangsparameter einer kinetischen Monte-Carlo-Simulation dienen, um den Effekt der Verspannung auf die Adatom-Diffusivität in diesem technologisch wichtigen System zu untersuchen.



Резюме

Целта на настоящата работа беше да се постигне разбиране на атомно ниво на повърхностната дифузия при хетероепитаксиалното израстване на InAs върху GaAs(001). Самоорганизирането на кохерентни тримерни островчета при Странски-Кръстанов режим на израстване превърна тази материална система с решетъчно несъотвещаващо от първостепенно значение с оглед на потенциалното приложение на тези квантови точки в оптоелектронните уреди. Методът, който бе използван за изучаване на повърхностната дифузия на In, се базира на теорията на функционала на плътността (Раздел 2.2), която в днешно време е незаменима при изследването на микроскопичните процеси в кристалния растеж като цяло.

Тъй като проблемът за повърхностна дифузия е тясно свързан с морфологията на повърхността, върху която се реализира дифузионният процес, ние трябваше първо да разгледаме (Раздел 5.2) термодинамичната стабилност и еластичните свойства на чистите (001) повърхности на GaAs и InAs. Новият елемент в настоящата работа е включването на новия $\zeta(4 \times 2)$ модел [174] и за InAs(001) повърхност при бедни на In условия на израстване. Ние показахме, че тази реконструкция е стабилна за InAs(001), и по този начин приведохме доказателство от първи принципи, че наистина съществува стабилна (4×2) реконструкция в бедната на As гранична област от фазовата диаграма на InAs(001) повърхност. В Раздел 5.2.3 пресметнахме следата на тензора на повърхностно напрежение за чистите повърхности и показахме, че за чистите бинарни (001) повърхности при умерено богати на As условия на растеж доминантната компонента на напрежение съответства на разтягане, докато за катионно богатата $\zeta(4 \times 2)$ фаза доминантната компонента съответства на свиване.

При разглеждането на самия процес на израстване на InAs върху GaAs(001) ние се концентрирахме върху образуването на повърхностна сплав, експериментално наблюдавано в началния стадий на формиране на мокреция слой, Раздел 5.3. Нашият анализ на стабилността на последния поддържа експериментално предложения (2×3) структурен модел за тернарната InGaAs(001) повърхност. Важно е да се отбележи, че установихме значителна дестабилизация на псевдоморфния $\text{In}_{2/3}\text{Ga}_{1/3}\text{As}(001)-(2 \times 3)$ филм при изотропна деформация на свиване; също така, при приблизително $|\varepsilon| = 3\%$ свиване би могъл да се реализира $(2 \times 3) \rightarrow (1 \times 3)$ преход в реконструкцията. Тази част от работата разшири предишния анализ на Wang *et al.* [107, 148, 150] включвайки и $\alpha 2(2 \times 4)$ реконструкция за мокреция слой. В резултат на това построихме диаграма на повърхностните фази на мокреция слой (фиг. 5.14), демонстрирайки чрез нея, че при богати на As условия (2×3) реконструкцията е енергетично най-изгодната за дебелини на мокреция слой до $\theta \simeq 1\text{--}1.5$ монослоя, а $\alpha 2(2 \times 4)$ е доминираща при умерени стойности на химичния потенциал на As. Образуването на повърхностна сплав и присъщия ѝ псевдоморфизъм се оказаха, че водят до относително “равна” потенциална повърхност за дифузия на индий върху $\text{In}_{2/3}\text{Ga}_{1/3}\text{As}(001)-(2 \times 3)$ филм, Раздел 5.4.

По-нататъшният анализ бе фокусиран върху ефекта от деформацията върху дифузията на индий върху чистата GaAs(001)-с(4×4) (Глава 6) повърхност, която често се използва като подложка за отлагането на InAs, вж. фиг. 5.1. В частност, ние определихме количествено зависимостта на дифузионната бариера ΔE за индиевия атом от приложената деформация, Раздел 6.4. Нашите микроскопични изчисления дадоха 30 meV максимално нарастване на ΔE при изотропна деформация на свиване. Тъй като при типичните условия на израстване тази стойност е от порядъка на $k_B T$, ефектът върху дифузионния коефициент е слаб. Деформационното поле обаче доведе до изразена деформационна зависимост на енергията на връзка на индиевия атом по главния дифузионен канал. Това поражда значително отблъскващо взаимодействие между един напрегнат остров и атом, дифундиращ към него, фиг. 6.11, което се явява доминантен ефект от деформацията върху повърхностното мигриране на атома. Разгледано беше подробно и взаимодействието на In с повърхностните As димери. Ние не установихме доказателства за значително по-стабилни адсорпционни възли за индий в резултат на разкъсване на As-As димерни връзки.

Накрая, в Глава 7 беше използван опростен едномерен модел, за да се демонстрира, че деформационно ограничената дифузия съдържа прототип на самоограничаващия се растеж на напрегнати острови. Дискусията, предложена в настоящата работа обаче, се отнасяше за дифузията на един изолиран атом, така наречената “tracer” дифузия (Раздел 4.1.2). В заключение искаме да подчертаем, че за включването на каквито и да е колективни ефекти е необходимо да се пресметнат параметрите на взаимодействие между дифундиращите атоми и да се разглеждат такива атомни концентрации, за които тези взаимодействия са ефективни. Независимо от това нашите микроскопични резултати биха могли да се използват като входни данни например за кинетични Монте Карло симулации, за да се хвърли повече светлина върху ефекта от еластичните деформации за повърхностната дифузия в тази важна материална система.



Appendix A

Structural and cohesive properties of Ga, In, As, GaAs and InAs

Ga, In, As

The atomic structure of bulk Ga, In, and As metals employed in this work is shown in Figure A.1. Geometry optimization was carried out at $E_{\infty} = 10$ Ry, within the LDA, and the Monkhorst-Pack sets $\{(\frac{1}{2}, \frac{1}{2}, \frac{1}{2}), 5 \times 5 \times 5\}$ for Ga and In, and $\{(\frac{1}{4}, \frac{1}{4}, \frac{1}{4}), 5 \times 5 \times 5\}$ for As. In optimizing the structure of α -Ga, Figure A.1 (a), and bct In, Figure A.1 (b), only the lattice constant a_0 was varied, while all other degrees of freedom were kept fixed at their experimental values [92].

Full optimization was performed for bulk rhombohedral As (A7 structure). As a first step the total energy of the supercell was sampled as a function of its volume V and fitted by the Murnaghan's equation of state, Eq. (C.1). In this set of runs the total energy for a given V_i values was determined by full optimization of all internal degrees of freedom (cf. Figure A.1 (c)),

$$E(V) = \min_{a_0, u} E(V, a_0, u) \Big|_{V=\text{const}}.$$

At the so determined equilibrium volume further optimization of a_0 and u was carried out, cf. Figure A.1 (c).

In order to calculate cohesive energies of these elemental metals one needs access to the total energy of the isolated Ga, In, and As atoms. The latter was calculated by putting the atom in a large cubic supercell of volume $12 \times 12 \times 12 \text{ \AA}^3$, and using \mathbf{k} -point mesh consisting of the Γ -point only. Account of the spin polarization lowers the energy of the free atom by ΔE_{σ} , as given in Table A.1.

Table A.1: Structural parameters of bulk Ga, In, and As metals. Numbers in brackets indicate the experimental values kept fixed in the structure optimization. Cohesive energy E_{coh} and the spin correction [231] to the total energy of the corresponding free atom ΔE_{σ} are given in eV/atom.

	a_0 [Å]		c/a_0		E_{coh}		ΔE_{σ}
	LDA	Exp.	LDA	Exp.	LDA	Exp.	
Ga	4.34	4.52	[1.692]		3.50	2.81	-0.15
In	3.17	3.24	[1.525]		3.06	2.52	-0.13
As	3.74	3.76	2.721	2.777	4.05	2.96	-1.41

GaAs, InAs

Bulk GaAs and InAs have the zincblende crystal structure (see, *e.g.*, Figure 2.3 (a) on page 13). It can be described as fcc lattice + diatomic basis: one of the species is located at (0,0,0) and the other is

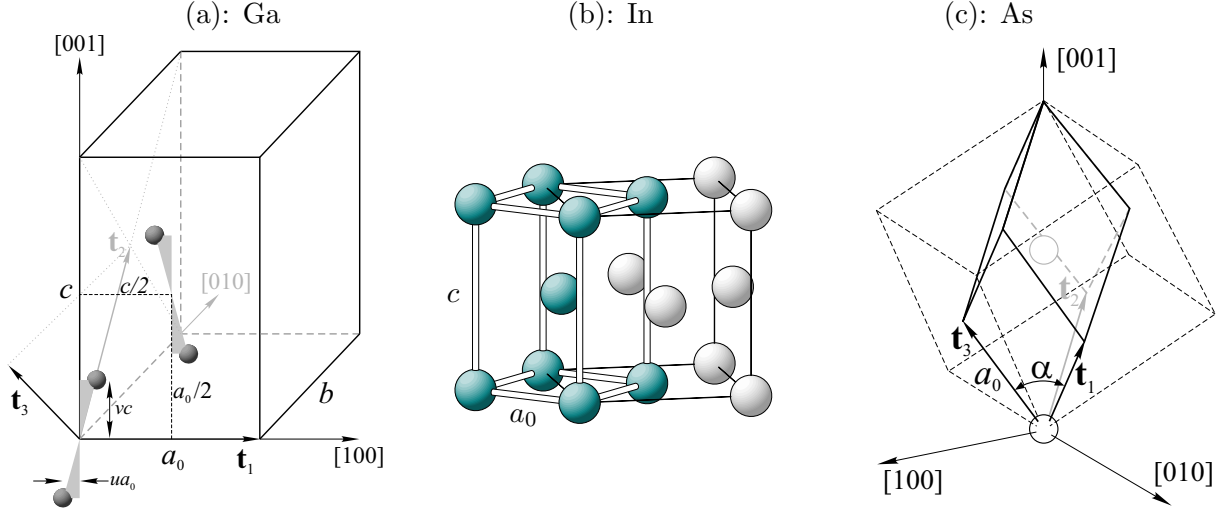


Figure A.1: (a) Base centered orthorhombic structure of α -Ga. The coordinates of the four atoms basis in units of the corresponding conventional unit cell edges (a_0, b, c) reads $(\pm u, 0, \pm v)$, and $(\frac{1}{2} \pm u, 0, \frac{1}{2} \pm v)$. The translation vectors \mathbf{t}_i are given by $\mathbf{t}_1 = (a_0, 0, 0)$, $\mathbf{t}_{2,3} = (0, \pm b/2, c/2)$; (b) Body centered tetragonal unit cell (highlighted atoms) of In. It can be considered also as a face centered tetragonal lattice (thin lines). Note that the c/a_0 ratio of the bct unit cell is $\sqrt{2}$ larger than that of the fct structure; (c) Rhombohedral (A7) structure of As. The diatomic basis (open circles) reads $(0, 0, 0)$, and $u \sum_i \mathbf{t}_i$. The length of the translation vectors \mathbf{t}_i is a_0 and the angle between them is α . One can alternatively describe the structure by defining α and the c/a_0 ratio of the unit cell [232].

Table A.2: Cohesive energy E_{coh} and formation enthalpy $\Delta H_f(0, 0)$ in eV/atom of bulk GaAs and InAs. Experimental values are taken from Ref. [92]. $d_{\text{III-V}} = \sqrt{3} a_0/4$ is the nearest-neighbor cation-anion distance.

	$d_{\text{III-V}} [\text{\AA}]$		E_{coh}		ΔH_f	
	LDA	Exp.	LDA	Exp.	LDA	Exp.
GaAs	2.40	2.45	4.12	3.26	-0.68	-0.84
InAs	2.61	2.62	3.75	3.10	-0.38	-0.44

shifted $1/4$ along the body diagonal $a_0(\frac{1}{4}, \frac{1}{4}, \frac{1}{4})$. However, in the present work these bulk compounds were represented by a simple cubic unit cell and details of the actual optimization procedure are given in Appendix C. The cohesive energy of these binary compounds is calculated from the expression

$$E_{\text{coh}}^{\text{III-V}} = E_2^{\text{III-V}} - E_{\text{atom}}^{\text{III}} - E_{\text{atom}}^{\text{V}}, \quad (\text{A.1})$$

where $E_2^{\text{III-V}}$ is the total energy *per pair* of the III-V crystal, and E_{atom} is the total energy of the free atom including ΔE_σ . The formation enthalpy (heat of formation) at zero temperature and pressure $\Delta H_f^{\text{III-V}}(0, 0)$ is given by a similar expression,

$$\Delta H_f^{\text{III-V}}(0, 0) = E_2^{\text{III-V}} - E_{\text{bulk}}^{\text{III}} - E_{\text{bulk}}^{\text{V}}, \quad (\text{A.2})$$

where E_{bulk} is the total energy *per atom* of the bulk elemental metals. The calculated values of E_{coh} and $\Delta H_f(0, 0)$ are given in Table A.2.

Appendix B

Scaling hypothesis for corrections to total energy and pressure

Following Rignanese *et al.* [84], assume that $\overline{N}_{\text{PW}}^d$ is the mean number of plane waves used in an *actual* calculation for given $E_{>\epsilon}$ and supercell volume V . For simplicity \overline{N}_{PW} can be defined either as geometric or arithmetic mean of the actual number of plane waves for each \mathbf{k} -point $N_{\text{PW},\mathbf{k}}^d$, *i.e.*

$$\overline{N}_{\text{PW}}^d(E_{>\epsilon}, V) = \prod_{\mathbf{k}} [N_{\text{PW},\mathbf{k}}^d(E_{>\epsilon}, V)]^{w_{\mathbf{k}}}, \quad \text{or} \quad \overline{N}_{\text{PW}}^d(E_{>\epsilon}, V) = \sum_{\mathbf{k}} w_{\mathbf{k}} N_{\text{PW},\mathbf{k}}^d(E_{>\epsilon}, V), \quad (\text{B.1})$$

with $\sum_{\mathbf{k}} w_{\mathbf{k}} = 1$. Let also denote by $\overline{N}_{\text{PW}}^c$ the *ideal* number of plane waves for the same $E_{>\epsilon}$ and V , determined according to the number of states in the reciprocal space comprised in a sphere of radius $\sqrt{2E_{>\epsilon}}$,

$$\overline{N}_{\text{PW}}^c(E_{>\epsilon}, V) = \frac{V}{(2\pi)^3} \times \frac{4}{3}\pi(2E_{>\epsilon})^{3/2}. \quad (\text{B.2})$$

Thus, $\overline{N}_{\text{PW}}^c$ is a smooth function of its arguments while $\overline{N}_{\text{PW}}^d$ changes discontinuously due to the discrete nature of the reciprocal space.¹ Consider now the total energy from a computer run as a function of \overline{N}_{PW} used and the supercell volume V , $E[\overline{N}_{\text{PW}}, V]$. Then an actual run at $E_{>\epsilon}$ will give as a result

$$E^d(E_{>\epsilon}, V) = E[\overline{N}_{\text{PW}}^d(E_{>\epsilon}, V), V], \quad (\text{B.3})$$

while the calculated value in a “hypothetical” ideal run at the same $E_{>\epsilon}$ would be

$$E^c(E_{>\epsilon}, V) = E[\overline{N}_{\text{PW}}^c(E_{>\epsilon}, V), V]. \quad (\text{B.4})$$

It is the latter quantity that one should use in reality to determine the materials properties. The main objective of a correction scheme is thus to extrapolate the actual output $E^d(E_{>\epsilon}, V)$ to the smooth “ideal” function $E^c(E_{>\epsilon}, V)$. On the basis of Eqs. (B.3) and (B.4) trivial relation can be obtained for the correction at cutoff energy $E_{>\epsilon}$ and volume V ,

$$E^c(E_{>\epsilon}, V) = E^d(E_{>\epsilon}, V) + \left\{ E[\overline{N}_{\text{PW}}^c(E_{>\epsilon}, V), V] - E[\overline{N}_{\text{PW}}^d(E_{>\epsilon}, V), V] \right\}. \quad (\text{B.5})$$

The function $E[\overline{N}_{\text{PW}}, V]$, however, is *a priori* unknown, so the common sense tells us that we need to sample the total energy for a set of $(\overline{N}_{\text{PW}}, V)$ values and to interpolate the energy values, which is not always the most enlightening idea.

Rignanese *et al.* [84] have proposed a different approach which allows the interpolation to be performed for a single reference volume V_0 . Their technics relies on the hypothesis that *the difference between energy at V_1 and V_0 for fixed $E_{>\epsilon}$ is independent of $E_{>\epsilon}$* , which can be “encrypted” in the form

$$E^c(E_{>\epsilon}, V_1) \approx E^c(E_{>\epsilon}, V_0) + f(V_1 - V_0), \quad \forall E_{>\epsilon}. \quad (\text{B.6})$$

¹The etymology of the superscripts ^c and ^d used by Rignanese *et al.* is “continuous” and “discontinuous”.

This supposition is referred to as the scaling hypothesis. An immediate consequence from Eq. (B.6) is that also the partial derivatives $\partial E^c(E_{>\epsilon}, V)/\partial E_{>\epsilon}$ at constant volume are independent of V ,

$$\left. \frac{\partial E^c(E_{>\epsilon}, V)}{\partial E_{>\epsilon}} \right|_{V=V_1} \approx \left. \frac{\partial E^c(E_{>\epsilon}, V)}{\partial E_{>\epsilon}} \right|_{V=V_0}. \quad (\text{B.7})$$

Using this property we can now differentiate Eq. (B.4),

$$\frac{\partial E^c(E_{>\epsilon}, V)}{\partial E_{>\epsilon}} = \left. \frac{\partial E[\bar{N}_{\text{PW}}, V]}{\partial \bar{N}_{\text{PW}}} \right|_{\bar{N}_{\text{PW}} = \bar{N}_{\text{PW}}^c(E_{>\epsilon}, V)} \frac{\partial \bar{N}_{\text{PW}}^c(E_{>\epsilon}, V)}{\partial E_{>\epsilon}}, \quad (\text{B.8})$$

and use Eq. (B.2) to calculate $\partial \bar{N}_{\text{PW}}^c / \partial E_{>\epsilon} = (V/2\pi^2) \sqrt{2E_{>\epsilon}}$. Inserting Eq. (B.8) into Eq. (B.7) we get the relation

$$\left. \frac{\partial E[\bar{N}_{\text{PW}}, V]}{\partial \bar{N}_{\text{PW}}} \right|_{\substack{V=V_1 \\ \bar{N}_{\text{PW}} = \bar{N}_{\text{PW}}^c(E_{>\epsilon}, V_1)}} \approx \frac{V_0}{V_1} \left. \frac{\partial E[\bar{N}_{\text{PW}}, V]}{\partial \bar{N}_{\text{PW}}} \right|_{\substack{V=V_0 \\ \bar{N}_{\text{PW}} = \bar{N}_{\text{PW}}^c(E_{>\epsilon}, V_0)}}, \quad (\text{B.9})$$

being valid whenever

$$\bar{N}_{\text{PW}}^c(E_{>\epsilon}, V_0) = \frac{V_0}{V_1} \bar{N}_{\text{PW}}^c(E_{>\epsilon}, V_1). \quad (\text{B.10})$$

Now addressing the correction to the energy one can formally cast the second term in the right-hand side of Eq. (B.5) in integral form (changing also V to V_1 for consistency),

$$E^c(E_{>\epsilon}, V_1) = E^d(E_{>\epsilon}, V_1) + \int_{\bar{N}_{\text{PW}}^d(E_{>\epsilon}, V_1)}^{\bar{N}_{\text{PW}}^c(E_{>\epsilon}, V_1)} \left. \frac{\partial E[\bar{N}_{\text{PW}}, V]}{\partial \bar{N}_{\text{PW}}} \right|_{\substack{V=V_1 \\ \bar{N}_{\text{PW}} = \bar{N}_{\text{PW}}^1}} d\bar{N}_{\text{PW}}, \quad (\text{B.11})$$

where a simplified notation is introduced, $\bar{N}_{\text{PW}}^1 = \bar{N}_{\text{PW}}^c(E_{>\epsilon}, V_1)$. With the account of Eq. (B.9) and the condition for its validity (B.10) Rignanese *et al.* have derived the following final expression,

$$E^c(E_{>\epsilon}, V_1) \approx E^d(E_{>\epsilon}, V_1) + E \left[\frac{V_0}{V_1} \bar{N}_{\text{PW}}^c(E_{>\epsilon}, V_1), V_0 \right] - E \left[\frac{V_0}{V_1} \bar{N}_{\text{PW}}^d(E_{>\epsilon}, V_1), V_0 \right]. \quad (\text{B.12})$$

From pragmatic point of view this expression is fairly convenient and has simple meaning: for a reference volume V_0 one calculates $E[\bar{N}_{\text{PW}}, V]$ for a few values of \bar{N}_{PW} . Usually it is $E_{>\epsilon}$ that is used as input parameter to the programs (the `ecut` input parameter in the `fhi98md` program [81]) rather than \bar{N}_{PW} , so a set of computer runs are performed for a few values of $E_{>\epsilon}$. The resulting output energy values are then interpolated in order to get the sacramental curve $E[\bar{N}_{\text{PW}}, V_0]$. Once we have it, Eq. (B.12) is directly used to work out the correction to total energy value calculated at different volume V_1 .

Corrections to pressure, $P(V) = -\partial E / \partial V$, follow from Eq. (B.12) by differentiating it with respect to volume at constant $E_{>\epsilon}$,

$$P^c(E_{>\epsilon}, V_1) \approx P^d(E_{>\epsilon}, V_1) - \frac{V_0}{V_1^2} \bar{N}_{\text{PW}}^d(E_{>\epsilon}, V_1) \left. \frac{\partial E[\bar{N}_{\text{PW}}, V]}{\partial \bar{N}_{\text{PW}}} \right|_{\substack{V=V_0 \\ \bar{N}_{\text{PW}} = \frac{V_0}{V_1} \bar{N}_{\text{PW}}^d(E_{>\epsilon}, V_1)}}. \quad (\text{B.13})$$

By very similar considerations Eqs. (B.12) and (B.13) can be generalized also for the case when, apart of the volume dependence, the total energy depends on the shape of the supercell as well [84]. Equation (B.13) is then reformulated in terms of corrections to the stress tensor $\sigma_{ik}(E_{>\epsilon}, V)$. In Appendix C we demonstrate a practical procedure for implementing the corrections to total energy as given by Eq. (B.12).

Appendix C

Calculation of elastic moduli

As a first step we calculate the equilibrium lattice constant a_0 of the bulk compounds by performing total energy calculations of a simple cubic unit-cell varying its size a so as to sample the expected minimum of $E(V)$, *e.g.*, for GaAs a was changed between 9.0 a.u. and 11.5 a.u., and 11.0–12.8 a.u. for InAs when using the PBE exchange-correlation functional. For fixed E_{sc} the calculated total energies are fitted with the Murnaghan's equation of state [233].

$$E(V) = E(V_0) + \frac{VB_0}{B'_0} \left[\frac{(V_0/V)^{B'_0}}{B'_0 - 1} + 1 \right] - \frac{V_0B_0}{B'_0 - 1}, \quad (\text{C.1})$$

valid for pressures $p < 10^{10}$ Pa; B_0 and B'_0 are, respectively, the bulk modulus and its pressure derivative at V_0 ,

$$B_0(T) = B(T, V_0) = -V \left(\frac{\partial p(T, V)}{\partial V} \right)_{T, V=V_0}, \quad B'_0(T) = \left(\frac{\partial B(T, V(T, p))}{\partial p} \right)_{T, V=V(T, p=0)}. \quad (\text{C.2})$$

Once we have a_0 determined similar procedure is applied to calculate the elastic moduli. Below we describe all steps in the form of ready-to-use MATHEMATICA[®] notebook [200] (version 4.0) which contains also comments on the specific implementation aspects.

Calculation of elastic moduli

This notebook calculates the c_{11} bulk elastic modulus of GaAs. First the total energy was sampled for 11 values of the supercell volume $V = V_0 (1 + \varepsilon_{zz})$, with $\varepsilon_{zz} \in [-4\%, +4\%]$. The set of runs of the **fhi98md** program employed LDA and 8 Ry cutoff energy. In order to correct the total energy according to the scaling hypothesis (Appendix B) only an additional set of 4 runs was performed at V_0 for $E_{\text{cut}} = 6, 7, 9$, and 10 Ry.

Required input:

- file with $E=E(V)$ in the format (the input file GaAs.zz_LDA_8Ry.npw):

$$\begin{array}{ccc} V & \bar{N}_{\text{PW}} & E \end{array}$$
- file with $E = E[\bar{N}_{\text{PW}}, V = V_0]$ in the format (the input file GaAs.LDA_V8_gauge.dat):

$$\begin{array}{ccc} \bar{N}_{\text{PW}} & & E \end{array}$$
- V_0 , $E(V_0)$, and E_{cut}

The notebook can be easily customized to calculate any of the elastic moduli and to evaluate corrections according to the scaling hypothesis.

■ Pre-settings and input

First, because we use lots of similar variables names, we switch off the **General::spell1** message since it's somewhat irritating. The two input files are then read in and displayed by using the postfix version of **TableForm**.

```
Off[General::spell1]
```

```
$DefaultFont = {"Times-Roman", 8};
```

```
path = "~/Math/GaAs/dat/";
```

```
file1 = "GaAs.zz_LDA_8Ry.npw";  
file2 = "GaAs.LDA_V8_gauge.dat";
```

```
bulkDat = ReadList[path<>file1, Real, RecordLists → True];  
bulkDat // TableForm
```

1096.65	419.726	-34.4299
1108.08	423.483	-34.4311
1119.5	427.74	-34.4322
1128.07	430.613	-34.4324
1136.63	434.486	-34.433
1142.35	434.862	-34.4317
1148.06	438.358	-34.4328
1156.63	441.744	-34.4325
1165.19	445.621	-34.4322
1176.62	448.87	-34.4302
1188.04	453.735	-34.429

```
gaugeBulk = ReadList[path<>file2, Real, RecordLists → True];  
gaugeBulk // TableForm
```

281.986	-34.2918
355.979	-34.3669
434.862	-34.4317
518.2	-34.4878
612.72	-34.5387

Here we define the other input parameters: **V0** is the equilibrium supercell volume in a_B^3 , $V_0 = V(T, p = 0)$, **E0** is the corresponding total energy $E_0 = E(V_0)$ in Ha and **Ecut** is the cutoff energy (in Ry) of the plane waves basis set used in the main set of runs.

```
V0 = 1142.35; (* equilibrium supercell volume *)
```

```
E0 = -34.4317; (* total energy at V0 *)
```

```
Ecut = 8.0; (* cutoff energy at which E0 is calculated *)
```

Let us also define two simple auxiliary functions **f2[]** and **f3[]** for fitting, respectively, with second and third order polynomials employing the built-in *Mathematica* function **Fit[]**.

```
f2[dat_?ListQ, var_] := Fit[dat, {1, x, x^2}, x] /. {x → var}
```

```
f3[dat_?ListQ, var_] :=  
Fit[dat, {1, x, x^2, x^3}, x] /. {x → var}
```

The following function is nothing but Eq. (B.2), i.e. the ideal number of plane waves \bar{N}_{PW}^c for the specified **Ecut**.

```
Npwc[ecut_, v_] := (v / (6 Pi ^ 2)) ecut ^ 1.5
```

With the above definitions one can easily get the wanted analytic curve $E[\bar{N}_{\text{PW}}, V_0]$ as required by the scaling hypothesis, see Eq. (B.12). Second order polynomial fit provides very good representation of the $E - \bar{N}_{\text{PW}}$ dependence.

```
fitBulk = f2[gaugeBulk, x]
```

```
-33.9201 - 0.00158718 x + 9.44191 × 10-7 x2
```

In order to visualize the above function together with the calculated points we plot separately the list **gaugeBulk** to which we assigned the data in **file2**, and the analytic fit **fitBulk**. As we are interested only in the combined graphics each individual graphics output is suppressed by setting **DisplayFunction → Identity** in the plotting functions.

```
bgpl = ListPlot[gaugeBulk,  
  Axes → False,  
  Frame → True,  
  GridLines → Automatic,  
  PlotStyle → PointSize[0.02],  
  DisplayFunction → Identity  
]
```

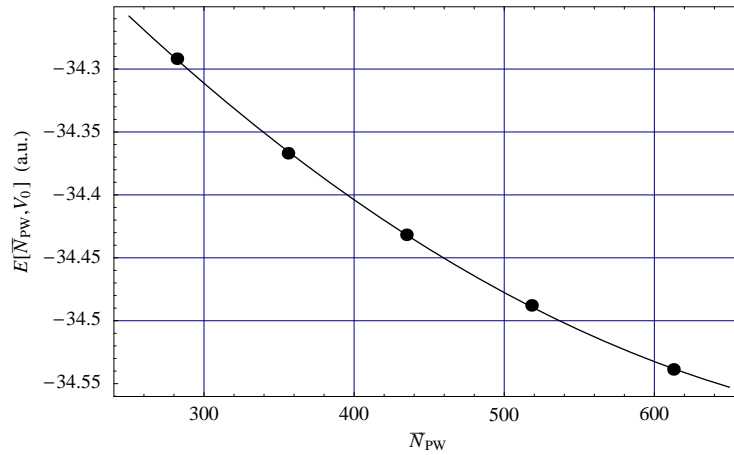
```
- Graphics -
```

```
fbgpl = Plot[fitBulk, {x, 250, 650},  
  DisplayFunction → Identity  
]
```

```
- Graphics -
```

Using **Show[]** the graphics objects generated with the two previous inputs are rendered together to the default display.

```
gcurveBulk = Show[bgpl, fbgpl,  
  FrameLabel → {" $\bar{N}_{\text{PW}}$ ", " $E[\bar{N}_{\text{PW}}, V_0]$  (a.u.)"},  
  DisplayFunction → $DisplayFunction  
]
```



- Graphics -

■ Correction to the total energy according to the scaling hypothesis (Appendix B).

First we define function that simply eliminates the hard-coded variable \mathbf{x} used in the fitting. A simple replacement rule is used, $\{\mathbf{x} \rightarrow \mathbf{Npw}\}$, similar to the definitions of `f2[]` and `f3[]`.

```
Ebulk[Npw_] := fitBulk /. {x → Npw}
```

Next we just transcribe the final expression for the corrections to total energy, Eq. (B.12), into *Mathematica* syntax. To be more specific, the following function represents only the difference of the last two terms in the right-handside of Eq. (B.12), which is, in effect, the wanted correction to the calculated total energy $E^d(E_{cut}, V)$ (the third column of the list `bulkDat`).

```
EcorSHbulk[V_, Npw_] :=  
  Ebulk[(V0/V) Npw] - Ebulk[(V0/V) Npw]
```

With the help of the above function we can obtain the corrected total energy values and to prepare at the same time suitable list of points to be plotted. This employs the concept of a *pure function*. We `Map[]` (via the shorter synonym `/@`) the pure function $\{ \dots, \dots \} \&$ to the raw data stored in `bulkDat`. The first part of the list gives the relative change of the volume which is nothing but the strain value, while the second part takes the corresponding fields from the input data and calculates the corrected total energy density measured with respect to $E(V_0)/V_0$.

```
bulkSHcor = {(#[[1]] - V0) / (V0),  
             (#[[3]] + EcorSHbulk[#[[1]], #[[2]]] - E0) / V0} & /@ bulkDat;
```

Now we would like to compare the raw and the corrected total energy density values. The raw data are first centered to $(V_0, E_0/V_0)$ and then we fit both the raw and corrected data in order to get plotable expressions.

```
bulkRaw = {(#[[1]] - V0) / (V0), (#[[3]] - E0) / V0} & /@ bulkDat;
```



```
curveRaw = f3[bulkRaw, x]
```

$$-8.70381 \times 10^{-7} + 4.04007 \times 10^{-6} x + 0.00178951 x^2 + 0.00455226 x^3$$

```
curveFit = f3[bulkSHcor, x]
```

$$-1.15771 \times 10^{-6} + 6.6329 \times 10^{-6} x + 0.00206542 x^2 - 0.00258827 x^3$$

The next four cells produced the graphical output displaying the calculated and corrected data points along with the polynomial fits to them. The **MultipleListPlot** package is used to render the discrete points on a single graphics.

```
apl = Plot[{curveRaw, curveFit}, {x, -0.05, 0.05},
  PlotStyle -> {
    GrayLevel[0.5],
    RGBColor[1, 0, 0]
  },
  DisplayFunction -> Identity
]
```

- Graphics -

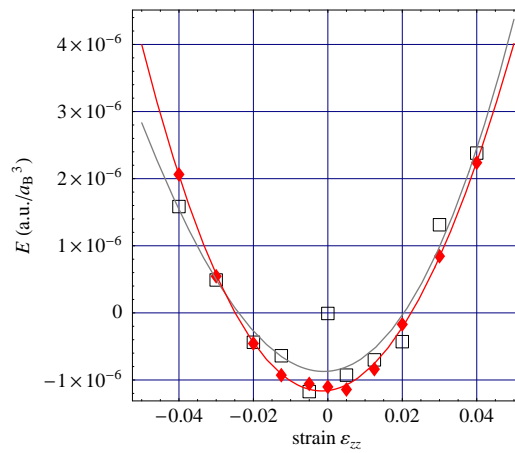
```
<< Graphics`MultipleListPlot`
```

```
lpl = MultipleListPlot[bulkRaw, bulkSHcor,
  Axes -> False,
  Frame -> True,
  SymbolShape -> {
    PlotSymbol[Box, Filled -> False],
    PlotSymbol[Diamond, 3]
  },
  SymbolStyle -> {
    GrayLevel[0],
    RGBColor[1, 0, 0]
  },
  GridLines -> Automatic,
  AspectRatio -> 1,
  DisplayFunction -> Identity
]
```

- Graphics -

The calculated points are shown as open squares (\square), and the corrected ones as solid diamonds (\diamond).

```
Show[lpl, apl,
  FrameLabel -> {"strain  $\varepsilon_{zz}$ ", "E (a.u./ $a_B^3$ )"},
  DisplayFunction -> $DisplayFunction
]
```



- Graphics -

■ Calculation of c_{11}

The last two expressions (**curveRaw**, **curveFit**) represent, in fact, the elastic free energy density as a function of strain for the case where the deformation is realized only along the z axis, i.e. $\varepsilon_{zz} \neq 0$, and $\varepsilon_{xx} = \varepsilon_{yy} = \varepsilon_{ik} \equiv 0$. In this way we obtain, according to Eq. (3.16), the c_{11} elastic constant just from the doubled coefficient in the above expressions. A simple function is defined to extract the proper coefficient and to convert the units to 10^{11} dyn/cm⁻² usually used to measure the elastic constants, please see Table 3.1.

```
ToDyne[fit_] := Coefficient[fit, x^2] * 2942
```

This is the c_{11} value calculated from the corrected total energy values,

```
c11 = 2 ToDyne[curveFit]
```

12.153

whereas the value that one would obtain from the calculated total energy values, if uncorrected, is

```
c11raw = 2 ToDyne[curveRaw]
```

10.5295

The two numerical values differ by 13%, which is, in fact, nicely seen in the above plot where the two polynomial fits have different curvatures at V_0 :

```
Abs[(c11-c11raw)/c11]
```

0.133586

At least within LDA the use of the scaling hypothesis at this low energy cutoff results in a very good agreement with the experimental value of c_{11} (Table 3.1)

Appendix D

Geometry of the $\text{In}_{2/3}\text{Ga}_{1/3}\text{As}(001)-(2 \times 3)$ surface

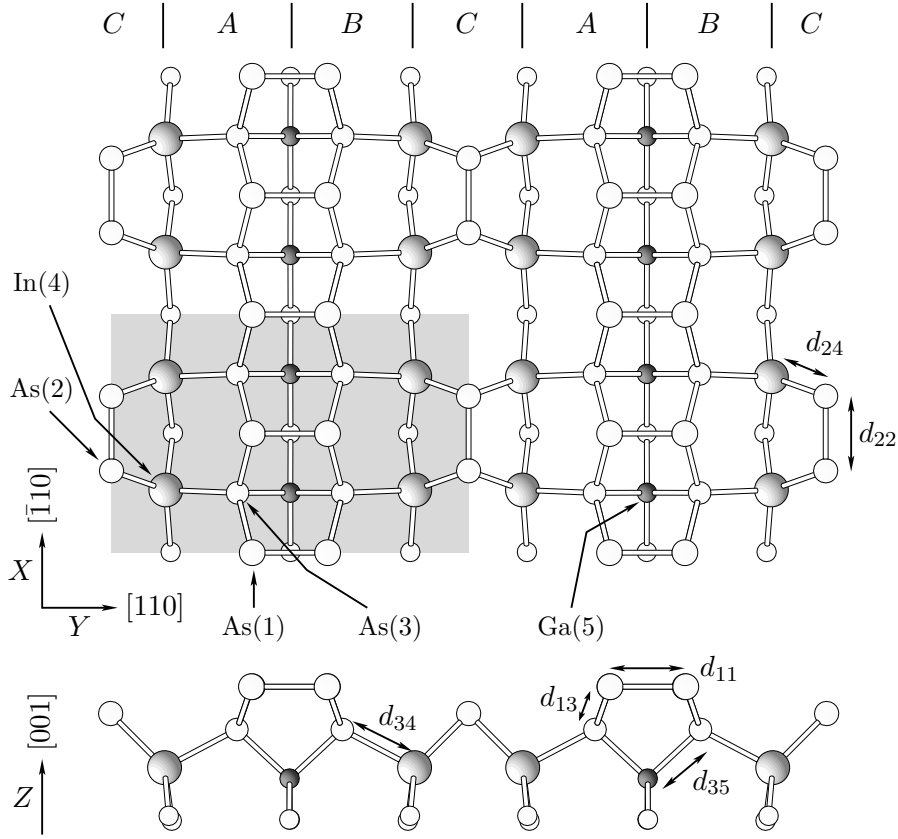


Figure D.1: Atomic structure and geometry parameters of the commensurate $\text{In}_{2/3}\text{Ga}_{1/3}\text{As}(001)-(2 \times 3)$ surface, see Table D.1.

The commensurate (2×3) -reconstructed $\text{In}_x\text{Ga}_{1-x}\text{As}(001)$ surface alloy is characterized with In-Ga ordering which locks the In concentration in the topmost cation layer to $x = 2/3$ [145, 193]. The integer “by-3” periodicity along $[110]$ direction can be represented as a repetition of three structural blocks (A, B, C) each of width $a_0/\sqrt{2}$, a_0 being the lattice constant of bulk GaAs: $ABCABCAB\dots$, Figure D.1. The values of the bond lengths and atomic coordinates indicated in Figure D.1 obtained from LDA and PBE-GGA optimized slab geometries are collected in Table D.1 and compared with the X-ray diffraction (XD) data due to Garreau *et al.* [145]. Previously Bellaiche *et al.* [234] considered only a (2×2) fictitious reconstruction (mimicking part of the (2×3) model) within the LDA and found very

Table D.1: Atomic coordinates and bond lengths as indicated in Figure D.1. X and Y are measured in units $2 \times a_0/\sqrt{2}$ and $3 \times a_0/\sqrt{2}$, respectively, while Z is given in units of the bulk lattice constant a_0 with respect to the Z coordinate of Ga(5). Experimental XD data are those reported by Garreau *et al.* [145] with an error bar of ± 0.004 for the in-plane coordinates, and ± 0.005 for the Z coordinate.

Atom	LDA			GGA			XD			[Å]	LDA	GGA	XD
	X	Y	Z	X	Y	Z	X	Y	Z				
As(1)	0.	0.395	0.544	0.	0.397	0.534	0.	0.398	0.519	d_{11}	2.48	2.52	2.44
As(2)	0.343	0.	0.385	0.347	0.	0.383	0.343	0.	0.384	d_{22}	2.45	2.50	2.51
As(3)	0.25	0.353	0.290	0.25	0.353	0.291	0.25	0.35	0.275	d_{13}	2.46	2.55	2.49
In(4)	0.262	0.151	0.065	0.264	0.150	0.060	0.267	0.151	0.063	d_{34}	2.68	2.82	2.69
Ga(5)	0.25	0.5	0.	0.25	0.5	0.	0.25	0.5	0.	d_{35}	2.36	2.47	2.40
										d_{24}	2.59	2.71	2.63

good agreement with the earlier XD experiment by Sauvage-Simkin *et al.* [193] regarding especially the lateral coordinates of As(2) and In(4).

Incommensurate phases

The incommensurate $(2 \times m)$ reconstruction with $m < 3$ (*e.g.*, (2×2.5) , (2×2.7) [145]) is accounted for in terms of randomly missing C blocks leading to local $ABAB\dots$ sequences, Figure D.2 (a). And vice versa: for the In-enriched surface incommensurate reconstructions with $m > 3$ occur (*e.g.*, (2×3.33) [145]) associated with a CC “stacking fault” shown in Figure D.2 (b): $ABCCAB\dots$

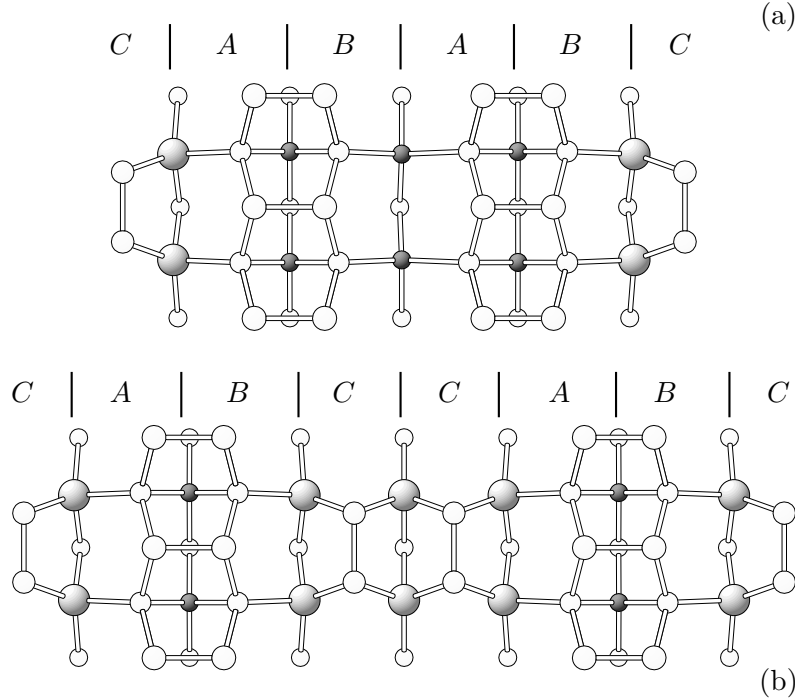


Figure D.2: Sample “stacking faults” in the surface cation ordering along $[110]$ direction as proposed by Garreau *et al.* [145]. Note that an $ABABAB\dots$ stacking would reproduce the GaAs(001)- $c(4 \times 4)$ reconstruction if the proper chemisorbed As(1)-As(1) dimers are removed. Similarly, the $ABCCABCCA\dots$ results in the (2×4) reconstruction observed for lattice matched $\text{In}_{0.53}\text{Ga}_{0.47}\text{As}/\text{InP}(001)$ [235].

Bibliography

- [1] R. W. Keyes, Miniaturization of electronics and its limits, *IBM J. Res. Dev.* **44**, 84–88 (2000). (reprinted from *IBM J. Res. Develop.* **32** (1988)).
- [2] O. Leifeld. *Ge quantum dot formation on the C-alloyed Si(001) surface: a scanning tunneling microscopy study*. PhD thesis, Département de Physique, Ecole Polytechnique Fédérale de Lausanne (EPFL), CH-1015 Lausanne, 1999. Thèse 2030.
- [3] O. Leifeld, E. Müller, D. Grützmacher, B. Müller, and K. Kern, *In situ* scanning tunneling microscopy study of C-induced Ge quantum dot formation on Si(001), *Appl. Phys. Lett.* **74**, 994–996 (1999).
- [4] S. Chandrasekhar, Stochastic problems in physics and astronomy, *Rev. Mod. Phys.* **15**, 1–89 (1943).
- [5] A. Kley. *Theoretische Untersuchungen zur Adatomdiffusion auf niederindizierten Oberflächen von GaAs*. PhD thesis, Technische Universität, Berlin, 1997.
- [6] N. Moll. *Theorie der Form und Stabilität von Quantenpunkten auf III-V-Halbleitern*. PhD thesis, Technische Universität, Berlin, 1998.
- [7] W. F. Brinkman and D. V. Lang, Physics and the communications industry, *Rev. Mod. Phys.* **71**, S480–S488 (1999).
- [8] Y. Arakawa and H. Sakaki, Multidimensional quantum well laser and temperature dependence of its threshold current, *Appl. Phys. Lett.* **40**, 939–941 (1982).
- [9] L. Goldstein, F. Glas, J. Y. Marzin, M. N. Charasse, and G. LeRoux, Growth by molecular beam epitaxy and characterization of InAs/GaAs strained-layer superlattices, *Appl. Phys. Lett.* **47**, 1099–1101 (1985).
- [10] D. J. Eaglesham and M. Cerullo, Dislocation-free Stranski-Krastanov growth of Ge on Si(100), *Phys. Rev. Lett.* **64**, 1943–1946 (1990).
- [11] Y. W. Mo, D. E. Savage, B. S. Swartzentruber, and M. G. Lagally, Kinetic pathway in Stranski-Krastanov growth of Ge on Si(001), *Phys. Rev. Lett.* **65**, 1020 (1990).
- [12] S. Guha, A. Madhukar, and K. C. Rajkumar, Onset of incoherency and defect introduction in the initial stages of molecular beam epitaxial growth of highly strained $\text{In}_x\text{Ga}_{1-x}\text{As}$ on GaAs(001), *Appl. Phys. Lett.* **57**, 2110–2112 (1990).
- [13] J. M. Moison, F. Houzay, F. Barthe, L. Leprince, E. André, and O. Vatel, Self-organized growth of regular nanometer-scale InAs dots on GaAs, *Appl. Phys. Lett.* **64**, 196–198 (1994).
- [14] D. Leonard, K. Pond, and P. M. Petroff, Critical layer thickness for self-assembled InAs islands on GaAs, *Phys. Rev. B* **50**, 11687–11692 (1994).
- [15] J. Tersoff, C. Teichert, and M. G. Lagally, Self-organization in growth of quantum dot superlattices, *Phys. Rev. Lett.* **76**, 1675–1678 (1996).
- [16] N. Kirstaedter, N. N. Ledentsov, M. Grundmann, D. Bimberg, V. M. Ustinov, S. S. Ruvimov, M. V. Maximov, P. S. Kop'ev, Zh. I. Alferov, U. Richter, P. Werner, U. Gösele, and J. Heydenreich, Low threshold, large T_0 injection laser emission from (InGa)As quantum dots, *Electron. Lett.* **30**, 1416–1418 (1994).

- [17] N. N. Ledentsov, V. M. Ustinov, A. Yu. Egorov, A. E. Zhukov, M. V. Maximov, I. G. Tabatadze, and P. S. Kop'ev, Optical properties of heterostructures with InGaAs-GaAs quantum clusters, *Semiconductors* **28**, 832–834 (1994).
- [18] D. Bimberg, M. Grundmann, and N. N. Ledentsov. *Quantum dot heterostructures*. John Wiley & Sons Ltd., 1998.
- [19] V. A. Shchukin and D. Bimberg, Spontaneous ordering of nanostructures on crystal surfaces, *Rev. Mod. Phys.* **71**, 1125–1171 (1999).
- [20] M. Sugawara, editor. *Self-assembled InGaAs/GaAs quantum dots*. Academic Press, 1999.
- [21] I. V. Markov. *Crystal growth for beginners (Fundamentals of nucleation, crystal growth and epitaxy)*. World Scientific, Singapore, 1995.
- [22] E. Bauer, Phänomenologische Theorie der Kristallabscheidung an Oberflächen. I, *Z. Kristallogr.* **110**, 372–394 (1958).
- [23] M. Volmer and A. Weber, Keimbildung in übersättigen Dämpfen, *Z. Phys. Chem.* **119**, 277–301 (1926).
- [24] F. C. Frank. and J. H. van der Merwe, One dimensional dislocations. I Static theory, *Proc. Roy. Soc. (London) A* **198**, 205–216 (1949). This is a full reference only to the first out of three successive publications by the same authors; parts II and III are respectively: *ibid.* 216–225, and *ibid.* **200**, 125–134 (1950).
- [25] I. N. Stranski and L. Krastanov, Zur Theorie der orientierten Ausscheidung von Ionenkristallen aufeinander, *Sitzungsber. Akad. Wiss. Wien, Math.-naturwiss. Kl. Iib* **146**, 797–810 (1938).
- [26] G. Springholz, V. Holy, M. Pinczolis, and G. Bauer, Self-organized growth of three-dimensional quantum-dot crystals with fcc-like stacking and a tunable lattice constant, *Science* **282**, 734–737 (1998).
- [27] C. T. Foxon and B. A. Joyce, Interaction kinetics of As₂ and Ga on {100} GaAs surface, *Surf. Sci.* **64**, 293–304 (1977).
- [28] T. R. Ramachandran, R. Heitz, P. Chen, and A. Madhukar, Mass transfer in Stranski-Krastanov growth of InAs on GaAs, *Appl. Phys. Lett.* **70**, 640–642 (1997).
- [29] M. Volmer and I. Estermann, Über den Verdampfungskoeffizienten von festem und flüssigem Quecksilber, *Z. Phys.* **7**, 1–12 (1921).
- [30] P. Kratzer, C. Morgan, and M. Scheffler, Density-functional theory studies on microscopic processes of GaAs growth, *Prog. Surf. Sci.* **59**, 135–147 (1998).
- [31] S. V. Ghaisas, Study of the kinetics of Ga on strained GaAs(001) surfaces using atomic potentials, *Surf. Sci.* **223**, 441–448 (1989).
- [32] C. C. Matthai and G. A. Moran, Adsorption and diffusion of Ga, In and As adatoms on (001) and (111) GaAs surfaces: a computer simulation study, *Appl. Surf. Sci.* **123/124**, 653–657 (1998).
- [33] R. Gomer, Diffusion of adsorbates on metal surfaces, *Rep. Prog. Phys.* **53**, 917–1002 (1990).
- [34] H. Brune, K. Bromann, H. Röder, K. Kern, J. Jacobsen, P. Stoltze, K. Jacobsen, and J. Nørskov, Effect of strain on surface diffusion and nucleation, *Phys. Rev. B* **52**, R14380–R14383 (1995).
- [35] C. Ratsch, A. P. Seitsonen, and M. Scheffler, Strain dependence of surface diffusion: Ag on Ag(111) and Pt(111), *Phys. Rev. B* **55**, 6750–6753 (1997).
- [36] P. H. Dederichs and K. Schroeder, Anisotropic diffusion in stress fields, *Phys. Rev. B* **17**, 2524–2536 (1978).
- [37] J. Philibert. *Atom movements: diffusion and mass transport in solids*. Les Edition de Physique, Les Ulis, 1991.
- [38] K. Ohno, K. Esfarjani, and Y. Kawazoe. *Computational Materials Science (From Ab initio to Monte Carlo Methods)*. Springer, Berlin, 1999.

- [39] M. Born and R. Oppenheimer, Zur Quantentheorie der Molekeln, *Ann. Phys. (Leipzig)* **84**, 457–484 (1927).
- [40] L. D. Landau and E. M. Lifchitz. *Quantum Mechanics (nonrelativistic theory)*, volume III of *Course on Theoretical Physics*. Pergamon, 1st edition, 1957.
- [41] M. Born and K. Huang. *Dynamic theory of crystall lattices*. Oxford University Press, 1968.
- [42] G. R. Darling and S. Holloway, The dissociation of diatomic molecules at surfaces, *Rep. Prog. Phys.* **58**, 1595–1672 (1995).
- [43] R. M. Dreizler and E. K. U. Gross. *Density Functional Theory: an approach to the quantum many-body problem*. Springer-Verlag, Berlin, 1990.
- [44] R. G. Parr and W. Yang. *Density-functional theory of atoms and molecules*. Oxford University Press, 1994.
- [45] P. Ruggerone, C. Ratsch, and M. Scheffler. *Density-functional theory of epitaxial growth of metals*, volume 8 of *The Chemical Physics of Solid Surfaces*, pages 490–544. Elsevier, Amsterdam, 1997.
- [46] C. Ratsch, P. Ruggerone, and M. Scheffler. *Density-Functional Theory of surface diffusion and epitaxial growth of metals*, volume 360 of *NATO ASI B*, pages 83–101. Plenum Press, New York, 1997.
- [47] P. Hohenberg and W. Kohn, Inhomogeneous electron gas, *Phys. Rev.* **136**, B 864–B 871 (1964).
- [48] W. Kohn and L. J. Sham, Self-consistent equations including exchange and correlation effects, *Phys. Rev.* **140**, A1133–A1138 (1965).
- [49] E. Wigner, On the interaction of electrons in metals, *Phys. Rev.* **46**, 1002–1011 (1934).
- [50] M. Gell-Mann and K. A. Brueckner, Correlation energy of an electron gas at high density, *Phys. Rev.* **106**, 364–368 (1957).
- [51] D. M. Ceperley and B. J. Alder, Ground-state of the electron-gas by a stochastic method, *Phys. Rev. Lett.* **45**, 566–569 (1980).
- [52] J. P. Perdew and A. Zunger, Self-interaction correction to density-functional approximations for many-electron systems, *Phys. Rev. B* **23**, 5048–5079 (1981).
- [53] D. M. Ceperley, Ground-state of the fermion one-component plasma - Monte-Carlo study in 2 and 3 dimensions, *Phys. Rev. B* **18**, 3126–3138 (1978).
- [54] R. O. Jones and O. Gunnarsson, The density functional formalism, its applications and prospects, *Rev. Mod. Phys.* **61**, 689–746 (1989).
- [55] A. D. Becke, Density-functional exchange-energy approximation with correct asymptotic behavior, *Phys. Rev. A* **38**, 3098–3100 (1988).
- [56] J. P. Perdew, Density-functional approximation for the correlation energy of the inhomogeneous electron gas, *Phys. Rev. B* **33**, 8822–8824 (1986).
- [57] C. Lee, W. Yang, and R. G. Parr, Development of the Colle-Salvetti correlation-energy formula into a functional of the electron density, *Phys. Rev. B* **37**, 785–789 (1988).
- [58] J. P. Perdew. *Electronic Structure of Solids '91*, pages 11–20. Akademie-Verlag, Berlin, 1991.
- [59] J. P. Perdew and Y. Wang, Accurate and simple analytic representation of the electron-gas correlation energy, *Phys. Rev. B* **45**, 13244–13249 (1992).
- [60] J. P. Perdew, K. Burke, and M. Ernzerhof, Generalized gradient approximation made simple, *Phys. Rev. Lett.* **77**, 3865–3868 (1996).
- [61] M. Fuchs, J. L. F. da Silva, C. Stampfl, J. Neugebauer, and M. Scheffler, Cohesive properties of group III nitrides: A comparative study of all-electron and pseudopotential calculations using the generalized gradient approximation. unpublished.

- [62] A. Zupan, K. Burke, M. Ernzerhof, and J. P. Perdew, Distribution and averages of electron density parameters: Explaining the effect of gradient corrections, *J. Chem. Phys.* **106**, 10184–10193 (1997).
- [63] E. Penev, P. Kratzer, and M. Scheffler, Effect of the cluster size in modeling the H₂ desorption and dissociative adsorption on Si(001), *J. Chem. Phys.* **110**, 3986–3994 (1999).
- [64] D. J. Doren. *Advances in chemical physics*, volume 95, pages 1–60. Wiley & Sons, New York, 1996.
- [65] B. Hammer, K. W. Jacobsen, and J. K. Nørskov, Role of nonlocal exchange correlation in activated adsorption, *Phys. Rev. Lett.* **70**, 3971–3974 (1993).
- [66] B. Hammer, M. Scheffler, K. W. Jacobsen, and J. K. Nørskov, Multidimensional potential energy surface for H₂ dissociation over Cu(111), *Phys. Rev. Lett.* **73**, 1400–1403 (1994).
- [67] L. D. Landau and E. M. Lifchitz. *Statistical Physics, Part II*, volume IX of *Course on Theoretical Physics*. Pergamon, 1st edition, 1957.
- [68] W. Pickett, Pseudopotential methods in condensed matter applications, *Comp. Phys. Rep.* **9**, 115–198 (1989).
- [69] M. Fuchs and M. Scheffler, Ab initio pseudopotentials for electronic structure calculations of polyatomic systems using density-functional theory, *Comp. Phys. Commun.* **119**, 67–98 (1999). Source and documentation available on-line (www.FHI-Berlin.MPG.DE/th/fhi98md/fhi98PP/).
- [70] D. R. Hamann, Generalized norm-conserving pseudopotentials, *Phys. Rev. B* **40**, 2980–2987 (1989).
- [71] N. Troullier and J. L. Martins, Efficient pseudopotentials for plane-wave calculations, *Phys. Rev. B* **43**, 1993–2006 (1991).
- [72] G. B. Bachelet, D. R. Hamann, and M. Schlüter, Pseudopotentials that work: from H to Pu, *Phys. Rev. B* **26**, 4199–4228 (1982).
- [73] D. Vanderbilt, Optimally smooth norm-conserving pseudopotentials, *Phys. Rev. B* **32**, 8412–8415 (1985).
- [74] S. Louie, S. Froyen, and M. L. Cohen, Nonlinear ionic pseudopotentials in spin-density-functional calculations, *Phys. Rev. B* **26**, 1738–1742 (1982).
- [75] M. Fuchs, M. Bockstedte, E. Pehlke, and M. Scheffler, Pseudopotential study of binding properties of solids with generalized gradient approximations: The role of core-valence exchange correlation, *Phys. Rev. B* **57**, 2134–2145 (1998).
- [76] L. Kleinman and D. M. Bylander, Efficacious form for model pseudopotentials, *Phys. Rev. Lett.* **48**, 1425–1428 (1982).
- [77] X. Gonze, R. Stumpf, and M. Scheffler, Analysis of separable potentials, *Phys. Rev. B* **44**, 8503–8513 (1991).
- [78] J. C. Slater. *Quantum theory of molecules and solids, Vol. II*. McGraw-Hill, New York, 1965.
- [79] N. W. Ashcroft and N. D. Mermin. *Solid state physics*. Saunders College Publishing, Philadelphia, 1976.
- [80] H. J. Monkhorst and J. D. Pack, Special points for Brillouin-zone integrations, *Phys. Rev. B* **13**, 5188–5192 (1976).
- [81] P. Kratzer, C. G. Morgan, E. Penev, A. L. Rosa, A. Schindlmayr, L. G. Wang, and T. Zywietz. *FHI98MD. Computer code for density-functional theory calculations for poly-atomic systems • User's Manual*. Fritz-Haber-Institut der Max-Planck-Gesellschaft, Berlin, 1999. Available on-line (www.fhi-berlin.mpg.de/th/fhi98md/doc/FHI98md.pdf).
- [82] S. Froyen and M. L. Cohen, Structural-properties of NaCl and KCl under pressure, *J. Phys. C* **19**, 2623–2632 (1986).
- [83] G. P. Francis and M. C. Payne, Finite basis set corrections to total energy pseudopotential calculations, *J. Phys.: Condens. Matter* **2**, 4395–4404 (1990).

- [84] G.-M. Rignanese, Ph. Ghosez, J.-C. Charlier, J.-P. Michenaud, and X. Gonze, Scaling hypothesis for corrections to total energy and stress in plane-wave-based *ab initio* calculations, *Phys. Rev. B* **52**, 8160–8178 (1995).
- [85] M. Bockstedte, A. Kley, J. Neugebauer, and M. Scheffler, Density-functional theory calculations for poly-atomic systems: electronic structure, static and elastic properties and *ab initio* molecular dynamics, *Comp. Phys. Commun.* **107**, 187–222 (1997). Available on-line (www.fhi-berlin.mpg.de/th/publications/CPC-107-187-1997.pdf).
- [86] R. Car and M. Parrinello, Unified approach for molecular dynamics and density-functional theory, *Phys. Rev. Lett.* **55**, 2471–2474 (1985).
- [87] M. C. Payne, M. P. Teter, D. C. Alan, T. A. Arias, and J. D. Joannopoulos, Iterative minimization techniques for *ab initio* total energy calculations: molecular dynamics and conjugate gradients, *Rev. Mod. Phys.* **64**, 1045–1097.
- [88] M. Scheffler, J. P. Vigneron, and G. B. Bachelet, Total-energy gradients and lattice distortions at point defects in semiconductors, *Phys. Rev. B* **31**, 6541–6551 (1985).
- [89] L. D. Landau and E. M. Lifchitz. *Elasticity Theory*, volume VII of *Course on Theoretical Physics*. Pergamon, 1st edition, 1957.
- [90] Y. I. Sirotnin and M. P. Shaskol'skaya. *Fundamentals of physics of crystals*. Nauka, Moskva, 1979. in russian.
- [91] O. H. Nielsen and R. M. Martin, Stress in semiconductors: *Ab initio* calculations on Si, Ge, and GaAs, *Phys. Rev. B* **32**, 3792–3805 (1985).
- [92] K.-H. Hellwege, editor. *Semiconductors*, volume III/17a of *Landolt-Börnstein • Numeric Data and Functional Relationships in Science and Technology*. Springer-Verlag, Berlin, 1982.
- [93] O. H. Nielsen and R. M. Martin, Quantum-mechanical theory of stress and force, *Phys. Rev. B* **32**, 3780–3891 (1985).
- [94] A. Dal Corso, A. Pasquarello, A. Baldereschi, and R. Car, Generalized-gradient approximations to density-functional theory: A comparative study for atoms and solids, *Phys. Rev. B* **53**, 1180–1185 (1996).
- [95] C. Filippi, D. J. Singh, and C. J. Umrigar, All-electron local-density and generalized-gradient calculations of the structural properties of semiconductors, *Phys. Rev. B* **50**, 14947–14951 (1994).
- [96] A. Zangwill. *Physics at surfaces*. Cambridge University Press, 1988.
- [97] J. W. Gibbs. *The collected works of J. Willard Gibbs*, volume 1, pages 55–353. Yale University Press, New Haven, 3rd edition, 1948.
- [98] R. Shuttleworth, The surface tension of solids, *Proc. Phys. Soc.* **A63**, 444–457 (1950).
- [99] C. Herring. *Structure and properties of solid surfaces*, chapter I, pages 5–72. The University of Chicago Press, 1953.
- [100] R. Defay, I. Prigogine, and A. Bellemans. *Surface tension and adsorption*. Longmans, London, 1966.
- [101] C. Herring, Some theorems on the free energy of crystal surfaces, *Phys. Rev.* **82**, 87–93 (1951).
- [102] C. Rottmann and M. Wortis, Statistical mechanics of equilibrium crystal shape: interfacial phase diagrams and phase transitions, *Phys. Rep.* **103**, 59–79 (1984).
- [103] D. Wolf, Should all surfaces be reconstructed?, *Phys. Rev. Lett.* **70**, 627–630 (1993).
- [104] N. Moll, M. Scheffler, and E. Pehlke, Influence of stress on the equilibrium shape of strained quantum dots, *Phys. Rev. B* **58**, 4566–4571 (1998).
- [105] N. Moll, A. Kley, E. Pehlke, and M. Scheffler, GaAs equilibrium crystal shape from first principles, *Phys. Rev. B* **54**, 8844–8855 (1996).

- [106] E. Pehlke, N. Moll, A. Kley, and M. Scheffler, Shape and stability of quantum dots, *Appl. Phys. A* **65**, 525–534 (1997).
- [107] L. G. Wang, P. Kratzer, N. Moll, and M. Scheffler, Size, shape, and stability of InAs quantum dots on the GaAs(001) substrate, *Phys. Rev. B* **62**, 1897 (2000).
- [108] J. Márquez, L. Geelhaar, and K. Jacobi, Atomically resolved structure of InAs quantum dots, *Appl. Phys. Lett.* **78**, 2309–2311 (2001).
- [109] Q.-K. Xue, Y. Hasegawa, H. Kiyama, and T. Sakurai, Atomic structure of faceted planes of InAs quantum dots on GaAs(001) studied by scanning tunneling microscopy, *Jpn. J. Appl. Phys.* **38**(1B), 500–503 (1999).
- [110] H. Eisele, O. Flebbe, T. Kalka, C. Preinesberger, F. Heinrichsdorff, A. Krost, D. Bimberg, and M. Dähne-Prietsch, Cross-sectional scanning-tunneling microscopy of stacked InAs quantum dots, *Appl. Phys. Lett.* **75**, 106–108 (1999).
- [111] H. Eisele, O. Flebbe, T. Kalka, and M. Dähne-Prietsch, Cross-sectional STM study of InAs quantum dots for lasers, *Surf. Interface Anal.* **27**, 537–541 (1999).
- [112] J. Tersoff and R. M. Tromp, Shape transition in growth of strained islands: spontaneous formation of quantum wires, *Phys. Rev. Lett.* **70**, 2782–2785 (1993).
- [113] A. A. Maradudin and R. F. Wallis, Elastic interactions of point defects in a semi-infinite medium, *Surf. Sci.* **91**, 423–439 (1980).
- [114] Q. Xie, P. Chen, and A. Madhukar, InAs island-induced-strain driven adatom migration during GaAs overlayer growth, *Appl. Phys. Lett.* **65**, 2051–2053 (1994).
- [115] Q. Xie, A. Madhukar, P. Chen, and N. Kobayashi, Vertically self-organized InAs quantum box islands on GaAs(001), *Phys. Rev. Lett.* **75**, 2542–2545 (1995).
- [116] N. N. Ledentsov, V. A. Shchukin, M. Grundmann, N. Kirstaedter, J. Böhrer, O. Schmidt, D. Bimberg, V. M. Ustinov, A. Yu. Egorov, A. E. Zhukov, P. S. Kop'ev, S. V. Zaitsev, N. Yu. Gordeev, Zh. I. Alferov, A. I. Borovkov, A. O. Kosogov, S. S. Ruvimov, P. Werner, U. Gösele, and J. Heydenreich, Direct formation of vertically coupled quantum dots in Stranski-Krastanow growth, *Phys. Rev. B* **54**, 8743–8750 (1996).
- [117] O. L. Alerhand, D. Vanderbilt, R. D. Maede, and J. D. Joannopoulos, Spontaneous formation of stress domains on crystal surfaces, *Phys. Rev. Lett.* **61**, 1973–1976 (1988).
- [118] V. Bortolani, N. H. March, and M. P. Tosi, editors. *Interaction of atoms and molecules with solid surfaces*. Plenum Press, New York, 1990.
- [119] J. W. Haus and K. W. Kehr, Diffusion in regular and disordered lattices, *Phys. Rep.* **150**, 263–406 (1987).
- [120] E. W. Montroll and G. H. Weiss, Random walks on lattices. II, *J. Math. Phys.* **6**, 167–181 (1965).
- [121] V. T. Binh, editor. *Surface Mobilities on Solid Materials*, volume 86 of *NATO ASI B*, New York, 1983. Plenum Press.
- [122] H. Risken. *The Fokker-Planck equation*. Springer, Berlin, 2nd edition, 1996.
- [123] A. Natori and R. W. Godby, Surface diffusion on a stepped surface, *Phys. Rev. B* **47**, 15816–15822 (1993).
- [124] T. Mishonov and E. Penev, Tight-binding modelling of the electronic band structure of layered superconducting perovskites, *J. Phys.: Condens. Matter* **12**, 143–159 (2000). cond-mat/0001049.
- [125] J. Schnakenberg, Network theory of microscopic and macroscopic behavior of master equation systems, *Rev. Mod. Phys.* **48**, 571–585 (1976).
- [126] V. I. Smirnov. *Course of Higher Mathematics*, volume III, Part 2. Franklin Book Co., 1964. see Chapter III, Secs. 78 and 79.

- [127] R. Festa and E. Galleani d'Agliano, Diffusion coefficient for a Brownian particle in a periodic field of force, *Physica A* **90**, 229–244 (1978).
- [128] M. v. Smoluchowski, Über Brownsche Molekularbewegung unter Einwirkung äußerer Kräfte und deren Zusammenhang mit der verallgemeinerten Diffusionsgleichung, *Ann. Phys. (Leipzig)* **48**, 1103–1112 (1915).
- [129] P. Hänggi, P. Talkner, and M. Borkovec, Reaction-rate theory: fifty years after Kramers, *Rev. Mod. Phys.* **62**, 251–341 (1990).
- [130] S. Glasstone, K. J. Laidler, and H. Eyring. *The Theory of Rate Processes*. McGraw-Hill Book Co, New York, 1941.
- [131] G. H. Vineyard, Frequency factors and isotope effects in solid state rate processes, *J. Phys. Chem. Solids* **3**, 121–127 (1957).
- [132] H. Eyring, The activated complex in chemical reactions, *J. Chem. Phys.* **3**, 107–115 (1935).
- [133] S. Arrhenius, Über die Reaktionsgeschwindigkeit bei der Inversion von Rohrzucker durch Säuren, *Z. Phys. Chem.* **4**, 226–248 (1889).
- [134] U. Kürpick, A. Kara, and T. S. Rahman, Role of lattice vibrations in adatom diffusion, *Phys. Rev. Lett.* **78**, 1086–1089 (1997).
- [135] G. Boisvert, N. Mousseau, and L. J. Lewis, Comment on "Role of lattice vibrations in adatom diffusion", *Phys. Rev. Lett.* **80**, 203 (1998).
- [136] C. Ratsch and M. Scheffler, Density-functional theory calculations of hopping rates of surface diffusion, *Phys. Rev. B* **58**, 13163–13166 (1998).
- [137] D. J. Fisher. *The Meyer-Neldel Rule*. Trans Tech Publications, Uetikon-Zürich, 2001.
- [138] G. Boisvert, L. J. Lewis, and A. Yelon, Many-body nature of the Meyer-Neldel compensation law for diffusion, *Phys. Rev. Lett.* **75**, 469–472 (1995).
- [139] P. B. Joyce, T. J. Krzyzewski, G. R. Bell, T. S. Jones, E. C. Le Ru, and R. Murray, Optimizing the growth of 1.3 μm InAs/GaAs quantum dots, *Phys. Rev. B* **64**, 235317:1–6 (2001).
- [140] B. A. Joyce, D. D. Vvedensky, G. R. Bell, J. G. Belk, M. Itoh, and T. S. Jones, Nucleation and growth mechanism during MBE of III-V compounds, *Mater. Sci. Eng.* **B67**, 7–16 (1999).
- [141] J. G. Belk, J. L. Sudijono, D. M. Holmes, C. F. McConville, T. S. Jones, and B. A. Joyce, Spatial distribution of In during the initial stages of growth of InAs on GaAs(001)-c(4 \times 4), *Surf. Sci.* **365**, 735–742 (1996).
- [142] J. G. Belk, C. F. McConville, J. L. Sudijono, T. S. Jones, and B. A. Joyce, Surface alloying at InAs-GaAs interfaces grown on (001) surfaces by molecular beam epitaxy, *Surf. Sci.* **387**, 213–226 (1997).
- [143] B. A. Joyce, J. L. Sudijono, J. G. Belk, H. Yamaguchi, X. M. Zhang, H. T. Dobbs, A. Zangwill, D. D. Vvedensky, and T. S. Jones, A scanning tunneling microscopy-reflection high energy electron diffraction-rate equation study of the molecular beam epitaxial growth of InAs on GaAs(001), (110) and (111)A-quantum dots and two-dimensional modes, *Jpn. J. Appl. Phys.* **36**, 4111–4117 (1997).
- [144] B. A. Joyce, D. D. Vvedensky, A. R. Avery, J. G. Belk, H. T. Dobbs, and T. S. Jones, Nucleation mechanism during MBE growth of lattice-matched and strained III-V compound films, *Appl. Surf. Sci.* **130–132**, 357–366 (1998).
- [145] Y. Garreau, K. Aïd, M. Sauvage-Simkin, R. Pinchaux, C. F. McConville, T. S. Jones, J. L. Sudijono, and E. S. Tok, Stoichiometry and discommensuration on $\text{In}_x\text{Ga}_{1-x}\text{As}/\text{GaAs}(001)$ reconstructed surfaces: A quantitative x-ray diffuse-scattering study, *Phys. Rev. B* **58**, 16177–16185 (1998).
- [146] B. A. Joyce, D. D. Vvedensky, T. S. Jones, M. Itoh, G. R. Bell, and J. G. Belk, In situ studies of III-V semiconductor film growth by molecular beam epitaxy, *J. Cryst. Growth* **201/202**, 106–112 (1999).

- [147] P. B. Joyce, T. J. Krzyzewski, G. R. Bell, B. A. Joyce, and T. S. Jones, Composition of InAs quantum dots on GaAs(001): Direct evidence for (In,Ga)As alloying, *Phys. Rev. B* **58**, R15981–R15984 (1998).
- [148] L. G. Wang, P. Kratzer, M. Scheffler, and N. Moll, Formation and stability of self-assembled coherent islands in highly mismatched heteroepitaxy, *Phys. Rev. Lett.* **82**, 4042–4045 (1999).
- [149] For a nice introduction see, Compositional modulation and ordering in semiconductors, *Mater. Res. Bull.* **22**(7), 20–43 (1997).
- [150] L. G. Wang, P. Kratzer, and M. Scheffler, Energetics of InAs thin films and islands on the GaAs(001) substrate, *Jpn. J. Appl. Phys.* **39**(7B), 4298–4301 (2000).
- [151] C. B. Duke, Semiconductor surface reconstruction: The structural chemistry of two-dimensional surface compounds, *Chem. Rev.* **96**, 1237–1259 (1996).
- [152] G. P. Srivastava, Theory of semiconductor surface reconstruction, *Rep. Prog. Phys.* **60**, 561–613 (1997).
- [153] F. Bechstedt and R. Enderlein. *Semiconductor surfaces and interfaces*. Akademie-Verlag, Berlin, 1988.
- [154] E. A. Wood, Vocabulary of surface crystallography, *J. Appl. Phys.* **35**, 1306–1312 (1964).
- [155] M. D. Pashley, Electron counting model and its application to island structures on molecular-beam epitaxy grown GaAs(001) and ZnSe(001), *Phys. Rev. B* **40**, 10481–10487 (1989).
- [156] L. J. Whitman, P. M. Thibado, S. C. Erwin, B. R. Bennett, and B. V. Shanabrook, Metallic III-V (001) surfaces: Violation of the electron counting model, *Phys. Rev. Lett.* **79**, 693–696 (1997).
- [157] D. K. Biegelsen, R. D. Bringans, J. E. Northrup, and L.-E. Swartz, Surface reconstructions of GaAs(001) observed by scanning tunneling microscopy, *Phys. Rev. B* **41**, 5701–5706 (1990).
- [158] L. Däweritz and R. Hey, Reconstruction and defect structure of vicinal GaAs(001) and $\text{Al}_x\text{Ga}_{1-x}\text{As}(001)$ surfaces during MBE growth, *Surf. Sci.* **236**, 15–22 (1990).
- [159] Q.-K. Xue, T. Hashizume, and T. Sakurai, Scanning tunneling microscopy of III-V compound semiconductor (001) surfaces, *Prog. Surf. Sci.* **56**, 1–131 (1997).
- [160] Q.-K. Xue, T. Hashizume, and T. Sakurai, Scanning tunneling microscopy study of GaAs(001) surfaces, *Appl. Surf. Sci.* **141**, 244–263 (1999).
- [161] J. M. Márquez. *Struktur von GaAs-Oberflächen und ihre Bedeutung für InAs-Quantenpunkten*. PhD thesis, Technische Universität, Berlin, 2000. Available on-line: edocs.tu-berlin.de/diss/2000/marquez_juan.pdf.
- [162] P. K. Larsen, J. H. Neave, J. F. van der Veen, P. J. Dobson, and B. J. Joyce, GaAs(001)- $c(4 \times 4)$: A chemisorbed structure, *Phys. Rev. B* **27**, 4966–4977 (1983).
- [163] M. Sauvage-Simkin, R. Pinchaux, J. Massies, P. Calverie, N. Jedrecy, J. Bonnet, and I. K. Robinson, Fractional stoichiometry of the GaAs(001) $c(4 \times 4)$ surface: An *in-situ* x-ray scattering study, *Phys. Rev. Lett.* **62**, 563–566 (1989).
- [164] D. J. Chadi, Atomic structure of GaAs(100)- (2×1) and (2×4) reconstructed surfaces, *J. Vac. Sci. Technol. A* **5**, 834–837 (1987).
- [165] H. H. Farrell and C. J. Palmstrøm, Reflection high energy electron diffraction characteristic absence in GaAs(001)- (2×4) -As: A tool for determining the surface stoichiometry, *J. Vac. Sci. Technol. B* **8**, 903–907 (1990).
- [166] V. P. LaBella, H. Yang, D. W. Bullock, P. M. Thibado, P. Kratzer, and M. Scheffler, Atomic structure of the GaAs(001)- (2×4) surface resolved using scanning tunneling microscopy and first-principles theory, *Phys. Rev. Lett.* **83**, 2989–2992 (1999).
- [167] J. E. Northrup and S. Froyen, Structure of GaAs(001) surfaces: The role of electrostatic interactions, *Phys. Rev. B* **50**, 2015–2018 (1994).

- [168] Y. Garreau, M. Sauvage-Simkin, N. Jedrecy, R. Pinchaux, and M. B. Veron, Atomic structure and faulted boundaries in the GaAs(001) $\beta(2 \times 4)$ surface as derived from x-ray diffraction and line-shape analysis, *Phys. Rev. B* **54**, 17638–17646 (1996).
- [169] L. D. Broekman, R. C. G. Leckey, J. D. Riley, A. Stampf, B. F. Usher, and B. A. Sexton, Scanning-tunneling-microscope study of the α and β phases of the GaAs (001)- (2×4) reconstruction, *Phys. Rev. B* **51**, 17795–17799 (1995).
- [170] W. G. Schmidt, S. Mirbt, and F. Bechstedt, Surface phase diagram of (2×4) and (4×2) reconstructions of GaAs(001), *Phys. Rev. B* **62**, 8087–8091 (2000).
- [171] C. Ratsch, W. Barvosa-Carter, F. Grosse, J. H. G. Owen, and J. J. Zinck, Surface reconstructions for InAs(001) studied with density-functional theory and STM, *Phys. Rev. B* **62**, R7719–R7722 (2000).
- [172] L. G. Wang, P. Kratzer, and M. Scheffler. unpublished.
- [173] R. H. Miwa and G. P. Srivastava, Structure and electronic states of InAs(001)- (2×4) surfaces, *Phys. Rev. B* **62**, 15778–15787 (2000).
- [174] S.-H. Lee, W. Moritz, and M. Scheffler, GaAs(001) surface under conditions of low As pressure: Evidence for a novel surface geometry, *Phys. Rev. Lett.* **85**, 3890–3893 (2000).
- [175] T. Hashizume, Q.-K. Xue, A. Ichimiya, and T. Sakurai, Determination of the surface structures of the GaAs(001)- (2×4) As-rich phase, *Phys. Rev. B* **51**, 4200–4212 (1995).
- [176] P. Kratzer. private communication.
- [177] Q. Xue, T. Hashizume, J. M. Zhou, T. Sakata, T. Ohno, and T. Sakurai, Structures of the Ga-rich 4×2 and 4×6 reconstructions of the GaAs(001) surface, *Phys. Rev. Lett.* **74**, 3177–3180 (1995).
- [178] C. Kumpf, D. Smilgies, E. Landemark, M. Nielsen, R. Feidenhans'l, O. Bunk, J. H. Zeysing, Y. Su, R. L. Johnson, L. Cao, J. Zegenhagen, B. O. Fimland, L. D. Marks, and D. Ellis, Surface structure of metal-rich (001) surfaces of III-V compound semiconductors, *Phys. Rev. B* **64**, 075307:1–10 (2001).
- [179] K. Kanisawa and H. Yamaguchi, Extremely long surface diffusion of Ga and critical nucleation on As-rich GaAs(001) surfaces caused by phase transitions, *Phys. Rev. B* **56**, 12080–12083 (1997).
- [180] G. R. Bell, J. G. Belk, C. F. McConville, and T. S. Jones, Species intermixing and phase transitions on the reconstructed (001) surfaces of GaAs and InAs, *Phys. Rev. B* **59**, 2947–2955 (1999).
- [181] H. Yamaguchi and Y. Horikoshi, Surface structure transitions on InAs and GaAs (001) surfaces, *Phys. Rev. B* **51**, 9836–9854 (1995).
- [182] M. Göthelid, Y. Garreau, M. Sauvage-Simkin, R. Pinchaux, A. Cricenti, and G. Le Lay, Atomic structure of the As-rich InAs(100) $\beta 2(2 \times 4)$ surface, *Phys. Rev. B* **59**, 15285–15289 (1999).
- [183] S. Ohkouchi and N. Ikoma, Role of steps in GaAs heteroepitaxial growth on InAs(001) surfaces, *Jpn. J. Appl. Phys.* **33**(6B), 3710–3714 (1994).
- [184] C. Kendrick, G. LeLay, and A. Kahn, Bias-dependent imaging of the In-terminated InAs(001) $(4 \times 2)/c(8 \times 2)$ surface by STM: Reconstruction and transitional defect, *Phys. Rev. B* **54**, 17877–17883 (1996).
- [185] K. Shiraishi, A new slab model approach for electronic-structure calculation of polar semiconductor surface, *J. Phys. Soc. Jpn.* **59**, 3455–3458 (1996).
- [186] C. Ratsch, Strain-induced change of surface reconstructions for InAs(001), *Phys. Rev. B* **64**, 161306:1–4 (2001).
- [187] J. Dąbrowski, E. Pehlke, and M. Scheffler, Calculation of the surface stress anisotropy for the buckled Si(001) (1×2) and $p(2 \times 2)$ surfaces, *Phys. Rev. B* **49**, 4790–4793 (1994).
- [188] J. P. Silveira and F. Briones, In situ observation of reconstruction related surface stress during molecular beam epitaxy (MBE) growth of III-V compounds, *J. Cryst. Growth* **201/202**, 113–117 (1999).

- [189] N. Ikoma and S. Ohkouchi, InAs island formation aligned along the steps on a GaAs(001) vicinal surfaces., *Jpn. J. Appl. Phys.* **34**(6B), L724–L726 (1995).
- [190] N. Grandjean, J. Massies, and O. Tottereau, Surface segregation in (Ga,In)As/GaAs quantum boxes, *Phys. Rev. B* **55**, R10189–R10192 (1997).
- [191] J. M. Moison, C. Guille, and M. Bensoussan, Commensurate and incommensurate phase transition of the (001) InAs surface under changes of bulk lattice constant, As chemical potential, and temperature, *Phys. Rev. Lett.* **58**, 2555–2558 (1987).
- [192] J. M. Moison, C. Guille, M. Van Rompay, F. Barthe, F. Houszay, and M. Bensoussan, Buildup of III-V-compound semiconductor heterojunctions: Structural and electronic properties of monolayer-thick III-V overlayers on III-V substrates, *Phys. Rev. B* **39**, 1772–1785 (1989).
- [193] M. Sauvage-Simkin, Y. Garreau, R. Pinchaux, M. B. Véron, J. P. Landesman, and J. Nagle, Commensurate and incommensurate phases at reconstructed (In,Ga)As(001) surfaces: X-ray diffraction evidence for a composition lock-in, *Phys. Rev. Lett.* **75**, 3485–3488 (1995).
- [194] M. Sauvage-Simkin, Y. Garreau, R. Pinchaux, A. Cavanna, M. B. Véron, N. Jedrecy, J. P. Landesman, and J. Nagle, Reconstruction and chemical ordering at the surface of strained (In,Ga)As epilayers, *Appl. Surf. Sci.* **104/105**, 646–651 (1996).
- [195] S. Ohkouchi and A. Gomyo, Scanning tunneling microscopy observations of surface structures on ordered GaInAs layers grown on InP, *Appl. Surf. Sci.* **130–132**, 447–451 (1998).
- [196] T. Kita, K. Tachikawa, H. Tango, K. Yamashita, and T. Nishino, Self-assembled growth of InAs-quantum dots and postgrowth behaviour studied by reflectance-difference spectroscopy, *Appl. Surf. Sci.* **159–160**, 503–507 (2000).
- [197] T. Kita, H. Tango, K. Tachikawa, K. Yamashita, T. Nishino, T. Nakayama, and M. Murayama. Optical anisotropy of Stranski-Krastanov growth surface of InAs on GaAs(001). In N. Miura and T. Ando, editors, *Proceedings of the 25th international conference on the physics of semiconductors (Osaka, 2000)*, pages 365–366, Berlin, 2001. Springer.
- [198] L. Geelhaar, J. Márquez, P. Kratzer, and K. Jacobi, GaAs(2 5 11) : A new stable surface within the stereographic triangle, *Phys. Rev. Lett.* **86**, 3815–3818 (2001).
- [199] A. Kley, P. Ruggerone, and M. Scheffler, Novel diffusion mechanism on the GaAs(001) surface: the role of adatom-dimer interaction, *Phys. Rev. Lett.* **79**, 5278–5281 (1997).
- [200] S. Wolfram. *The MATHEMATICA[®] Book*. Cambridge University Press, 4th edition, 1999.
- [201] K. A. Fichtorn and M. Scheffler, Island nucleation in thin-film epitaxy: A first-principles investigation, *Phys. Rev. Lett.* **84**, 5371–5374 (2000).
- [202] M. Schroeder and D. E. Wolf, Diffusion on strained surfaces, *Surf. Sci.* **375**, 129–140 (1997).
- [203] C. Roland and G. H. Gilmer, Epitaxy on surfaces vicinal to Si(001). I. Diffusion of silicon adatoms over the terraces, *Phys. Rev. B* **46**, 13428–13436 (1992).
- [204] H. Spjut and D. A. Faux, Computer simulation of strain-induced diffusion enhancement of Si adatoms on the Si(001) surface, *Surf. Sci.* **306**, 233–239 (1994).
- [205] E. Zoethout, O. Gürlü, H. J. W. Zandvliet, and B. Poelsema, The influence of strain on the diffusion of Si dimers on Si(001), *Surf. Sci.* **452**, 247–252 (2000).
- [206] E. Penev, P. Kratzer, and M. Scheffler, Effect of strain on surface diffusion in semiconductor heteroepitaxy, *Phys. Rev. B* **64**, 085491:1–9 (2001).
- [207] J. G. LePage, M. Alouani, D. L. Dorsey, J. W. Wilkins, and P. E. Blöchl, *Ab initio* calculations of binding and diffusion of a Ga adatom on the GaAs(001)-c(4 × 4) surface, *Phys. Rev. B* **58**, 1499–1505 (1998).
- [208] J. G. LePage. *Projector augmented wave method calculation of Ga adatom diffusion and local density of states for GaAs and Si surfaces*. PhD thesis, The Ohio State University, Columbus, 1997. Available on-line: <ftp://ftp.physics.ohio-state.edu/pub/jglepage/mythesis.ps.gz>.

- [209] D. R. Lide, editor. *Handbook of Chemistry and Physics*. CRC Press, New York, 1995.
- [210] S. Clarke and D. D. Vvedensky, Origin of reflection high-energy electron-diffraction intensity oscillations during molecular-beam epitaxy: A computational modeling approach, *Phys. Rev. Lett.* **58**, 2235–2238 (1987).
- [211] P. Kratzer, E. Penev, and M. Scheffler, First-principles studies of kinetics in epitaxial growth of III-V semiconductors, *Appl. Phys. A* (2002). to be published.
- [212] A. Madhukar, A unified atomistic and kinetic framework for growth front morphology evolution and defect initiation in strained epitaxy, *J. Cryst. Growth* **163**, 149–164 (1996).
- [213] H. T. Dobbs, A. Zangwill, and D. D. Vvedensky. *Surface Diffusion: Atomistic and Collective Processes*, volume 360 of *NATO ASI Series B*, pages 263–275. Plenum Press, New York, 1998.
- [214] H. M. Koduvely and A. Zangwill, Epitaxial growth kinetics with interacting coherent islands, *Phys. Rev. B* **60**, R2204–R2207 (1999).
- [215] N. N. Ledentsov, V. M. Ustinov, V. A. Shchukin, P. S. Kop'ev, and Zh. I. Alferov, Quantum dot heterostructures: fabrication, properties, lasers (Review), *Semiconductors* **32**, 343–365 (1998).
- [216] C. Priester and M. Lannoo, Origin of self-assembled quantum dots in highly mismatched heteroepitaxy, *Phys. Rev. Lett.* **75**, 93–96 (1995).
- [217] M. Meixner, E. Schöll, V. A. Shchukin, and D. Bimberg, Self-assembled quantum dots—Crossover from kinetically controlled to thermodynamically limited growth, *Phys. Rev. Lett.* **87**, 236101:1–4 (2001).
- [218] C. S. Kim, M. Kim, J. K. Furdyna, M. Dobrowolska, S. Lee, H. Rho, L. M. Smith, H. E. Jackson, E. M. James, Y. Xin, and N. D. Browning, Evidence for 2D precursor and interdiffusion in the evolution of self-assembled CdSe quantum dots on ZnSe, *Phys. Rev. Lett.* **85**, 1124–1127 (2000).
- [219] H. T. Dobbs, D. D. Vvedensky, A. Zangwill, J. Johansson, N. Carlsson, and W. Seifert, Mean-field theory of quantum dot formation, *Phys. Rev. Lett.* **79**, 897–900 (1997).
- [220] Y. Chen and J. Washburn, Structural transition in large-lattice-mismatch heteroepitaxy, *Phys. Rev. Lett.* **77**, 4046–4049 (1996).
- [221] I. Daruka and A.-L. Barabási, Island formation and critical thickness in heteroepitaxy, *Phys. Rev. Lett.* **78**, 3027 (1997). See also the Chen and Washburn's reply, *Phys. Rev. Lett.* **78**, 3028 (1997).
- [222] D. E. Jesson, G. Chen, K. M. Chen, and S. J. Pennycook, Self-limiting growth of strained faceted islands, *Phys. Rev. Lett.* **80**, 5156–5159 (1998).
- [223] M. Kästner and B. Voigtländer, Kinetically self-limiting growth of Ge islands on Si(001), *Phys. Rev. Lett.* **82**, 2745–2748 (1999).
- [224] D. J. Srolovitz, On the stability of surfaces of stressed solids, *Acta. Metall.* **37**, 621–625 (1989).
- [225] V. Holý, G. Springholz, M. Pinczolit, and G. Bauer, Strain induced vertical and lateral correlations in quantum dot superlattices, *Phys. Rev. Lett.* **83**, 356–359 (1999).
- [226] C. Priester and M. Lannoo, Growth aspects of quantum dots, *Current Opinion in Solid State & Materials Science* **2**, 716–721 (1997).
- [227] E. Steimetz. *In-situ Wachstumsuntersuchungen zur selbstorganisierten Ausbildung von InAs-Quantenpunkten auf GaAs(001)-Oberflächen*. PhD thesis, Technische Universität, Berlin, 2002.
- [228] W. K. Burton, N. Cabrera, and F. C. Frank, The growth of crystals and the equilibrium structure of their surfaces, *Philos. Trans. R. Soc. London, Ser. A* **243**, 299–358 (1951).
- [229] J. Tersoff, M. D. Johnson, and B. G. Orr, Adatom densities on GaAs: Evidence for a near-equilibrium growth, *Phys. Rev. Lett.* **78**, 282–285 (1997).
- [230] M. Meixner, E. Schöll, M. Schmidbauer, H. Raidt, and R. Köhler, Formation of island chains in SiGe/Si heteroepitaxy by elastic anisotropy, *Phys. Rev. B* **64**, 245307:1–4 (2001).

- [231] S. Kotochigova, Z. Levine, E. Shirley, M. Stiles, and C. Clark. Atomic reference data for electronic structure calculations, 1997. (math.nist.gov/DFTdata/atomdata/narrative.html).
- [232] R. J. Needs, R. M. Martin, and O. H. Nielsen, Total-energy calculations of the structural properties of the group-V element arsenic, *Phys. Rev. B* **33**, 3778–3784 (1986).
- [233] F. D. Murnaghan, The compressibility of media under extreme pressures, *Proc. Nat. Acad. Sci. U.S.A.* **30**, 244–247 (1944).
- [234] L. Bellaiche, K. Kunc, M. Sauvage-Simkin, Y. Garreau, and R. Pinchaux, Local aspects of the As-stabilized 2×3 reconstructed (001) surface of strained $\text{In}_x\text{Ga}_{1-x}\text{As}$ alloys: a first-principles study, *Phys. Rev. B* **53**, 7417–7420 (1996).
- [235] K. Aïd, Y. Garreau, M. Sauvage-Simkin, and R. Pinchaux, Atomic structure of the (2×4) $\text{In}_{0.53}\text{Ga}_{0.47}\text{As}/\text{InP}(001)$ reconstructed surface. A study of average strain and growth temperature effects on the indium segregation, *Surf. Sci.* **425**, 165–173 (1999).

Index

- absolute rate theory, 38
- activated complex, 39
- Ag/Ag(111), 41, 67, 78
- approximation
 - adiabatic –, 6, 31
 - Born-Oppenheimer (BO) –, 6, 18, 31
 - flat island –, 28, 82, 83
 - harmonic –, 6, 40
 - Hartree-Fock (HF) –, 7
- Atomic Force Microscopy (AFM), 1
- beam-equivalent pressure (BEP), 46
- biorthogonal set, 35
- Bravais lattice, 22, 32, 33, 68
- Brillouin zone (BZ), 16–17, 50, 61
- Car-Parrinello method, 18
- classical limit, 40
- cohesive energy (E_{coh}), 11, 51, 53, 71, 95, 96
- compensation effect*, 40
- Darken relation, 34
- de Broglie’s wavelength, iv
- Debye temperature (Θ_{D}), 40, 65
- density of states, 1
- Density-Functional Theory (DFT), v, 7–10, 12
- diffusion
 - kernel (\mathfrak{G}), 37
 - barrier, 40, 89
- dividing surface*, 25
- effective-medium theory, 78
- Einstein summation convention, 12
- electron counting rule (ECR), 46–50, 59, 61
- energy cutoff (E_{c}), 13, 14, 22–24, 50, 97–99
 - input parameter `ecut`, 18, 98
- enhancement factor, 11
- Fermi energy/level, 16, 61
- `fhi98md` program, 17, 22, 98, 99
- `fhi98PP` program, 14–16
- `fhi98start` starting utility, 17
- force
 - Hellmann-Feynman –, 18
 - residual \sim s, 18
 - variational \sim s, 18
- Fourier series/transform, 13, 35
- free energy
 - Gibbs –, 20, 26
 - Helmholtz –, 20, 26, 39
 - of activation, 39
- GaAs(001), 3–4, 13, 27, 38, 43–61
 - $\alpha 2(2 \times 4)$, 47, 52–56
 - $\beta 2(2 \times 4)$, 47–55, 60, 72, 76
 - $\zeta(4 \times 2)$, 49, 52–55
 - $c(4 \times 4)$, 46–49, 52, 54–56, 58, 61, 68–72, 76–79, 82, 86, 89, 106
 - $c(8 \times 2)$, 48
- GaAs(2511), 59
- GaSb(001), 46
- Generalized Gradient Approximation (GGA), 10–12, 16, 23, 24, 51, 62, 84, 106
- ghost states, 15
- Gibbs adsorption equation, 25
- Grüneisen parameter, 85
- heat of formation (ΔH_{f}), 26, 52, 96
- $\text{In}_x\text{Ga}_{1-x}\text{As}(001)$, 4, 44
 - (1×3) , 56, 60, 89
 - (2×3) , 45, 56–63, 66, 69, 85, 89, 105
 - (4×3) , 56
 - $\alpha 2(2 \times 3)$, 56
 - $\alpha 2(2 \times 4)$, 57, 59–61
 - $\beta 2(2 \times 4)$, 59–61
- InAs(001), 44–46, 49, 52–55, 57, 86, 89
 - $\alpha 2(2 \times 4)$, 49, 52–55
 - $\alpha 3(2 \times 4)$, 53
 - $\beta 2(2 \times 4)$, 49, 52–55
 - $\zeta(4 \times 2)$, 49, 52–55, 89
 - $c(4 \times 4)$, 49
 - $c(8 \times 2)$, 49
 - $I(4 \times 2)$, 53
- InP(001), 56
 - $\text{In}_{0.53}\text{Ga}_{0.47}\text{As}/-$, 106
- Kleinman-Bylander form, 15
- Kohn-Sham equations, 9, 12, 18
- law
 - Fick’s first –, 34
 - Fick’s second –, 34, 37
- Local-Density Approximation (LDA), 10–12, 16, 23, 24, 50–52, 62, 71, 95, 99, 104–106
- Low-Energy Electron Diffraction (LEED), 56

- Markoff process*, 34
 master equation, 35, 36, 63
mesoscopics, iii
 Metal-Organic Chemical Vapor Deposition (MOCVD), 3
 Meyer-Neldel energy, 41
 Meyer-Neldel rule, 40, 79, 82
 modulus
 bulk – (B), 21, 99
 shear – (G), 21
 Young’s – (Y), 21
 Molecular Beam Epitaxy (MBE), iv, 3, 27, 44, 47, 85
 Monkhorst-Pack scheme, 16–17, 50, 57, 62, 95
 Murnaghan’s equation of state, 95, 99

 norm-conserving pseudopotentials, 14

 partial core density ($\tilde{n}_0^{\text{core}}$), 15
 partition function, 39
 PbSe/Pb_{1-x}Eu_xTe, 3
 plane-wave expansion, 13, 14
 potential energy surface (PES), 6–7, 32, 62–63, 69, 71, 75–77, 86
pre-pairing scenario, 11
psgen tool, 15
pswatch utility, 14

 radius
 cutoff – (r^{c}), 14
 ionic –, 71, 76
 Wigner-Seitz – (r_s), 10
 ratio
 As:Ga flux –, 46
 aspect –, 27, 30
 c/a_0 – (of the unit cell), 96
 diffusion anisotropy –, 66, 70
 Poisson’s – (ν), 21–23
 Reflectance-Difference Spectroscopy (RDS), 56
 Reflection High-Energy Electron Diffraction (RHEED), 43, 46–48

 scaling hypothesis, 17, 22, 98, 102
 Scanning Tunneling Microscopy (STM), iv, 27, 43, 44, 47–49, 53, 56, 61
 Si(001), iii, 10–12
 Ag/–, 28
 Ge/–, 27, 85, 87
 H₂/–, 11
 Si_xGe_{1-x}/–, 3
 Slater determinant, 7
 Smoluchowski equation, 37, 83
 spectral decomposition, 36
 spin correction, 95
 sticking coefficient, 3
 stoichiometry, 26, 46, 47, 53, 61

 Stranski-Krastanov (SK) growth mode, 2–4, 43, 44, 89
 supercell, 12, 17, 22, 50, 51, 53, 59
 surface energy, 24, 26, 46, 49–51

 tensor
 ω_{ik} , 19
 chemical diffusion – ($D_{\alpha\beta}$), 34
 elastic compliance – (s_{iklm}), 20
 elastic constants – (c_{iklm}), 20
 elastic distortions – (γ_{ik}), 19
 elastic Green’s – (χ_{ik}), 21
 Levi-Civita’s – (ε_{ijk}), 12
 strain – (ε_{ik}), 20
 surface – – ($\varepsilon_{\alpha\beta}$), 25, 27, 68
 stress – (σ_{ik}), 20
 surface – – ($\tau_{\alpha\beta}$), 25, 26, 53
 tracer diffusion – ($D_{\alpha\beta}^*$), 32–37, 63, 70, 72
 theorem
 Bloch –, 12, 16
 Gauss’s –, 20
 Hohenberg-Kohn –, 8
 sampling –, 18
 stress –, 23, 26
 thermodynamic factor, 34
 Thomas-Fermi model, 8
 transition rate matrix, 35, 63, 72
 transition-state theory, 38

 Voigt notations, 20, 22

 Wood’s notations, 45

 X-ray diffraction, 47–49, 53, 56, 62, 63, 105